Universal three- and four-body phenomena in an ultracold gas of cesium atoms

DISSERTATION

by

Martin Berninger

submitted to the Faculty of Mathematics, Computer Science and Physics of the University of Innsbruck

in partial fulfillment of the requirements for the degree of doctor of science

Advisor:
Univ.Prof. Dr. Rudolf Grimm,
Institute of Experimental Physics, University of Innsbruck,
Institute for Quantum Optics and Quantum Information
of the Austrian Academy of Sciences

Innsbruck, October 2011

ABSTRACT

Physical systems that appear to be completely different at first glance can, under certain conditions, exhibit the same behavior. This is the essence of the concept of universality, which enables ultracold atoms to be employed as a versatile model system. The unique controllability of interparticle interactions between ultracold atoms allows one to investigate fundamental questions of universal few-body physics also arising in various other quantum systems.

This thesis presents experimental studies of universal three- and four-body phenomena performed in an ultracold quantum gas of cesium atoms by trap-loss spectroscopy. By varying the magnetic field, we exploit the large tunability of the effective two-body interaction strength resulting from broad and narrow scattering resonances. These so-called Feshbach resonances make cesium a prime candidate for exploring universal few-body physics.

The main part of this thesis examines the Efimov scenario, which predicts the existence of an infinite series of universally related three-body bound states for resonant two-body interactions. For attractive effective interactions, these trimer states couple to the free-atom continuum or, for repulsive ones, to the atom-dimer threshold. Both situations lead to experimentally detectable enhancements of the particle loss, which are referred to as tri-atomic and atom-dimer Efimov resonances, respectively. We investigate the latter in an ultracold sample of atoms and weakly bound dimers. These measurements yield the first evidence of an atom-dimer Efimov resonance. We observe a slight shift of the resonance position in comparison to what universal theory would lead us to expect. In another experiment, the properties of the three-body parameter, which incorporates all unknown short-range interactions in universal theories, are studied in an atomic cesium gas. For this, three-body losses are investigated in the vicinity of different Feshbach resonances. We observe several Efimov features, including three tri-atomic Efimov resonances. The analysis of our findings shows that the three-body parameter stays essentially constant for the Feshbach resonances investigated.

Utilizing an ultracold atom-dimer sample, we observe a magnetically controllable exchange process. This experiment represents the first demonstration of an elementary reaction process in the regime of universal interactions. Complete

control is achieved by tuning the effective interaction strength.

Universal four-body processes in pure dimer and atom samples are another focus of research covered in this thesis. A collisional study based on universal dimers reveals a pronounced loss minimum. This phenomenon, which offers insight into an elementary four-body process, is still not completely understood. We extend our investigations by including non-universal dimer states and detect several narrow loss resonances. Due to the shape of the resonances, we can conclude that these features are induced by coupling of the dimers to tetramer states; so far, the properties of these states remain unknown.

A recent theoretical study suggests the existence of two universal four-body states accompanying each Efimov trimer state. To verify this study, we analyze four-body losses in an ultracold atomic sample, thereby identifying two resonances representing the first evidence for these universal four-body states. This result is in good agreement with the expectations from theory.

ZUSAMMENFASSUNG

Physikalische Systeme, die auf den ersten Blick völlig unterschiedlich wirken, können unter bestimmten Bedingungen das gleiche Verhalten aufweisen. Auf dieser Eigenschaft beruht das Konzept der Universalität, welches die Verwendung ultrakalter Atome als vielseitiges Modellsystem erlaubt. Die einzigartige Kontrollmöglichkeit der interatomaren Wechselwirkungen ultrakalter Atome ermöglicht die Untersuchung grundlegender Fragen der universellen Mehrteilchenphysik, die auch in verschiedenen anderen Quantensystemen von Relevanz sind.

Diese Doktorarbeit präsentiert experimentelle Studien universeller Drei- und Vierkörperphänomene, die unter Verwendung eines ultrakalten atomaren Cäsium-Quantengases mittels "Fallen-Verlust"-Spektroskopie durchgeführt wurden. Durch Variation des Magnetfeldes machen wir uns die große Abstimmbarkeit der effektiven Zweikörperwechselwirkungsstärke zunutze, die aus breiten und schmalen Zweikörperresonanzen resultiert. Diese sogenannten Feshbach-Resonanzen machen Cäsium zu einem erstklassigen Kandidaten für die Erforschung von Mehrteilchenphysik im universellen Wechselwirkungsbereich.

Der Hauptteil dieser Arbeit behandelt das Efimov Szenario, welches die Existenz einer unendlichen Serie von universell zusammenhängenden, gebundenen Dreikörperzuständen vorhersagt. Diese Trimerzustände koppeln für effektiv anziehende Zweikörperwechselwirkungen mit dem Kontinuum freier Atome, und für abstoßende Wechselwirkungen mit der Atom-Dimer-Schwelle. In beiden Fällen kommt es zu experimentell nachweisbaren Verlustresonanzen, die dementsprechend als dreiatomige beziehungsweise als Atom-Dimer Efimov-Resonanzen bezeichnet werden. Wir weisen experimentell erstmals die Existenz einer Atom-Dimer Efimov-Resonanz unter Verwendung eines ultrakalten Atom-Dimer-Gemisches nach. Die ermittelte Resonanzposition weicht geringfügig von jener ab, welche laut universeller Theorie zu erwarten wäre. In einem weiteren Experiment werden in einem atomaren Cäsiumgas die Eigenschaften des Dreikörperparameters studiert, der in universellen Theorien die unbekannten, kurzreichweitigen Wechselwirkungen beinhaltet. Dazu untersuchen wir Dreikörperverluste in der Nähe unterschiedlicher Feshbach-Resonanzen. Bei dieser Messung werden einige Efimov-verwandte Phänomene entdeckt, unter anderem drei dreiatomige Efimov-Resonanzen. Die Auswertung unserer Ergebnisse zeigt, dass der Drei-

körperparameter für die betrachteten Streuszenarien im Wesentlichen konstant ist.

Mit Hilfe eines ultrakalten Atom-Dimer-Gemisches studieren wir einen magnetisch steuerbaren Austauschprozess. Dieses Experiment stellt die erste Demonstration eines elementaren Reaktionsprozesses im Regime universeller Wechselwirkungen dar. Die Kontrolle über diesen Vorgang wird mittels der magnetischen Abstimmbarkeit der Wechselwirkungsstärke ausgeübt.

Ein weiterer Forschungschwerpunkt dieser Arbeit liegt auf universellen Vierkörperprozessen in reinen Atom- beziehungsweise Dimer-Quantengasen. Die Untersuchung inelastischer Zweikörperkollisionen in einem Gas schwach gebundener Dimere enthüllt ein ausgeprägtes Verlustminimum. Dieses Phänomen, welches Einsicht in einen elementaren Vierkörperprozess gibt, entzieht sich derzeit noch unserem Verständnis. Eine Erweiterung dieser Studie unter Einbeziehung nichtuniverseller Dimerzustände bringt mehrere schmale Verlustresonanzen zum Vorschein, die auf die Kopplung mit komplexen molekularen Strukturen hinweisen. Aufgrund der Form der Resonanzen gehen wir davon aus, dass diese durch Tetramerzustände verursacht werden, deren Eigenschaften noch nicht vollständig bekannt sind.

Eine vor kurzem veröffentlichte theoretische Arbeit deutet auf die Existenz zweier universeller Vierkörperzustände hin, die jeweils mit einem Efimov-Zustand einhergehen. Zur Überprüfung dieses Szenarios werden Vierkörperverlustmessungen in einem ultrakalten atomaren Gas durchgeführt. Wir finden dabei zwei Resonanzen, die mit den theoretischen Erwartungen übereinstimmen und einen ersten Beweis für die Existenz dieser universellen Vierkörperzustände darstellen.

CONTENTS

CHAPTER 1

INTRODUCTION

Experiments on ultracold atomic quantum gases have led to a tremendous progress in the understanding of few- and many-body phenomena in the past two decades. This success is closely linked to the unique degree of control of such systems, which allows to investigate the fundamental behavior of quantum matter under various conditions[1].

The major motivation for experimental investigation of few-body physics with ultracold atoms is related to the concept of *universality*. In physics, universality generally refers to a situation in which systems that are different at short distances have identical long-distance behavior [Bra06]. Based on this concept, ultracold atoms are an ideal model system for exploring few-body phenomena that also appear in various fields that are, at first sight, completely different, such as nuclear and molecular physics. Even though the typical energy regime for experiments on ultracold atoms (peV) differs by many orders of magnitude from the one connected to nuclear matter (MeV), both systems can be described in the same theoretical framework within the universal regime.

In the field of few-body physics, a theoretical milestone was reached in the early seventies by V. Efimov, who discovered several fundamental properties of the universal quantum three-body system [Efi70]. Most intriguing was the existence of an infinite series of universal three-body bound states, occurring in systems of three identical bosons with resonant pair-wise interactions. These so-called *Efimov states* feature several peculiar properties that are described in detail in Sec. 1.2. V. Efimov originally proposed nuclear systems as prime candidates for the experimental observation of Efimov states. Unfortunately, no clear proof was found and those states remained elusive for more than 35 years. In fall 2005, Kraemer *et al.* delivered the first evidence for universal Efimov quantum states in an ultracold sample of ^{133}Cs atoms [Kra06b]. Since then, Efimov states have been observed in an increasing number of experiments on ultracold quantum gases [Kra06b, Ott08, Huc09, Kno09, Zac09, Bar09, Gro09, Pol09a, Wil09, Nak10, Gro10, Lom10a, Lom10b, Nak11, Ber11b, Fer11]. Two

[1] This introduction is partly based on Ref. [Fer11].

of these publications are part of this thesis; see Chapters 2 and 4.

Efimov's fascinating three-body states are not the only universal few-body system by far. Concerning the four-body sector, Efimov's scenario has recently been extended by two theoretical studies [Ham07b, Ste09], proclaiming that each Efimov trimer is closely related to the appearance of two universal four-body states. The first experimental evidence for these states was also obtained in an ultracold sample of ^{133}Cs atoms and is presented in Chapter 6 of this thesis (see also Ref. [Fer09a]). Additional atom experiments have as well observed indications for these four-body states [Zac09, Pol09a, Ber11b].

There are numerous phenomena in the field of few-body physics that require additional experimental and theoretical investigation. A deeper understanding of (universal) few-body physics would allow to bridge the gap to many-body physics and result in a clearer view on phenomena encountered in different fields of physics.

This thesis presents experiments performed with ultracold bosonic samples of ^{133}Cs atoms in order to study universal three- and four-body phenomena. Several of these experiments can be satisfactorily explained in the framework of universal theory. Some results deviate slightly from simple universal theory models, indicating that a more realistic description might be necessary. Other findings show unexpected results and open up new fields of few-body physics, which still elude adequate understanding.

In Sec. 1.1, the basic elements of two-body scattering and the concept of two-body universality are introduced. Sec. 1.2 describes the Efimov scenario, being the most prominent situation for three-body universality. The extension to the four-body sector is outlined in Sec. 1.3. In Sec. 1.4, ultracold atom experiments focussing on universal three- and four-body physics are summarized, including the contributions of this PhD thesis. An overview of the thesis is given in Sec. 1.5.

1.1. Two-body scattering physics

In this section, the basic concepts of two-body scattering physics for neutral and indistinguishable atoms are introduced, which are necessary for understanding the universal few-body phenomena presented in this thesis.

Interaction potentials and the s-wave scattering length

The basic scattering properties are a consequence of the shape of the two-body interaction potentials, which result from the overall effect of the *exchange*, *spin-dipole* and *van der Waals* interactions. The (exponentially decreasing) short-range exchange interaction originates from the antisymmetry of the electronic wave function and leads to a splitting into *singlet* and *triplet* Born-Oppenheimer potentials, as shown in Fig 1.1. The weak spin-dipole interaction results from the interaction of the electronic spins and is modified by second-order spin-orbit coupling [Köh06b]. On a long-range scale, the dominant contribution to

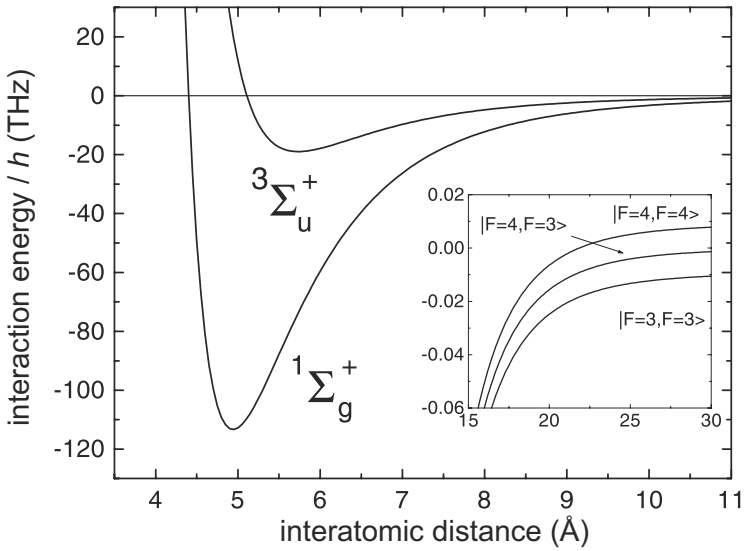

Figure 1.1.: Singlet $^1\Sigma_g^+$ and triplet $^3\Sigma_u^+$ Born-Oppenheimer ground state potential-energy curves for the Cs_2 dimer. The exchange energy, which lowers (raises) the singlet (triplet) potential, is dominant for small interparticle distances, given in the unit angstrom Å. In the long-range regime, the van der Waals interaction $\propto R^{-6}$ describes the behavior of the potential curves. Inset: In the asymptotic limit $R \to \infty$, the energy curves split into three distinct hyperfine scattering potentials, which result from possible values of the total atomic angular momentum $F = 3, 4$. The energy difference between these potential curves is defined by the atomic hyperfine splitting. Taken from Ref. [Chi01] with small modifications.

elastic scattering stems from the van der Waals interaction, representing the induced dipole-dipole interaction via $V_{\mathrm{vdW}} = -C_6/R^6$, with the van der Waals coefficient C_6 and the interparticle distance R. The natural length and energy scales associated with the van der Waals interaction are the van der Waals length R_{vdW} and energy E_{vdW}, which are defined as [Chi10]

$$R_{\mathrm{vdW}} = \frac{1}{2}\left(\frac{mC_6}{\hbar^2}\right)^{1/4} \quad \text{and} \quad E_{\mathrm{vdW}} = \frac{\hbar^2}{m}\frac{1}{R_{\mathrm{vdW}}^2}, \tag{1.1}$$

with the reduced Planck constant $\hbar = h/(2\pi)$ and the atomic mass m. As for neutral atoms the van der Waals interaction is the most far reaching contribution to the interaction potential, R_{vdW} determines the characteristic range of the interaction $r_{\mathrm{int}} = R_{\mathrm{vdW}}$.

In principle, determining two-body scattering properties requires solving the Schrödinger equation, including the interaction potentials, for an incoming plane wave with atomic wave vector k, which relates to the relative collision energy of the two atoms by $E_{\mathrm{rel}} = \hbar^2 k^2/m$. Unfortunately, the deep scattering potentials are usually never known with sufficient accuracy to permit precise calculations on threshold scattering properties. Especially the fast oscillations of the scattering

wave function, which are induced by the exchange interaction, crucially depend on exact knowledge of the potentials. However, in most situations only the long-range behavior is of interest, and therefore it is sufficient to know the effective influence of the interaction potentials on the scattered wave function in the asymptotic limit of large particle distances ($R \to \infty$).

In the asymptotic limit, the two-body scattering process can be described for spherical symmetric potentials as the superposition of an incoming plane wave and an outgoing spherical wave, which are related via the scattering amplitude. This problem is typically reformulated by expanding the in- and outgoing waves into contributions from different angular momenta ℓ via a *partial wave expansion*. To each of these partial waves, denoted by ℓ, a scattering phase shift $\delta_\ell(k)$ is assigned, which describes the phase shift of the outgoing partial wave with respect to the incoming one. If inelastic processes are present, these phase shifts can be complex-valued with positive imaginary part [Bra06]. The centrifugal potential $\hbar^2\ell(\ell+1)/(mR^2)$ sets an energy dependent limit for the partial waves taking part in the scattering process. For atomic collisions in the ultracold regime, where the atomic wave vector $k \to 0$, the phase shifts $\delta_\ell(k)$ approach zero according to $k^{2\ell+1}$ [Bra06]. Therefore, elastic collisions of (indistinguishable) bosons in the ultracold regime[2] are entirely described by the s-wave phase shift $\delta_0(k)$.

For colliding atoms, the phase $\delta_0(k)$ is generally a function of the momentum $\hbar k$. At sufficiently low energies, $\delta_0(k)$ can be written by the so-called *effective-range expansion* as [Chi10]

$$k \cot \delta_0(k) = -\frac{1}{a} + \frac{1}{2} r_0 k^2. \tag{1.2}$$

The s-wave scattering length a is the main parameter for the description of universal few-body phenomena in the ultracold regime. The effective range r_0 is directly related to the long-range behavior of the van der Waals interaction [Chi10]. In the low energy limit $k \to 0$, it follows that $k \cot \delta_0(k) = -1/a$. For low particle momenta in the order of $\hbar/r_0$, the large size of the de Broglie wavelength $\lambda_{\mathrm{dB}} = \sqrt{2\pi\hbar^2/(mk_BT)}$, with k_B being Boltmann's constant and T the temperature of the sample, prevents the atoms from resolving the internal structure of the real interaction potential. Therefore, in the long-distance regime the effect of this interaction potential is indistinguishable from the one resulting from a differently shaped (model) potential which yields an equal value for a, as, for example, an adjusted zero-range potential.

The s-wave scattering length is connected with the elastic collision cross section $\sigma_0(k)$ via [Chi10]

$$\sigma_0(k) = \frac{8\pi a^2}{1+k^2a^2} \overset{ka\ll 1}{\longrightarrow} 8\pi a^2 \tag{1.3}$$

$$\overset{ka\gg 1}{\longrightarrow} 8\pi/k^2. \tag{1.4}$$

[2] Because of exchange symmetry, only even (odd) partial waves are allowed for indistinguishable bosons (fermions), independent of the collision energy.

For $ka \gg 1$, elastic collisions are *unitarity limited* by the collision energy.

For a Bose-Einstein condensate (BEC), the s-wave scattering length defines the mean-field energy of the system $E_{\mathrm{mf}} = 4\pi\hbar^2 na/m$ [Ket99], with the particle density n, and thereby other properties, such as the size of the BEC.

Universal regime

The significance of the s-wave scattering length a is revealed in the *universal regime*, which is entered when a is much larger than the characteristic range of interaction. For ultracold atom collisions, this typically corresponds to a situation where $|a| \gg r_0, R_{\mathrm{vdW}}$. In this case, the properties of the two-body system depend only on a and not on the particular details of the interaction potential. This independence on the short-range properties of the system is the key characteristic of universal theories. Hence, even though systems have distinct short-range interactions, for identical values of a the important long-range properties are the same. This is the concept of universality.

One of the universal properties is the existence of a shallow universal bound state for positive and large a with a binding energy E_b given as

$$E_b = \frac{\hbar^2}{ma^2}. \tag{1.5}$$

The wave function of this so-called *halo dimer state* extends far into the classically forbidden region, with only a small fraction being within the short-range region [Jen04, Köh06b]; see Fig. 1.2. This state has a halo character with a mean distance of the atoms $\langle r \rangle = a/2$, which by far exceeds the classical turning point of the interaction potential. According to Eq. (1.1), the condition $a \gg R_{\mathrm{vdW}}$ translates to $E_b \ll E_{\mathrm{vdW}}$.

There are many situations in real-world systems where a is indeed the largest length scale, but does not considerably exceed the characteristic interaction range. In this intermediate regime some of the universal properties are maintained by taking into account non-universal correction. For example, the binding energy for a weakly bound system can be refined by introducing finite range corrections associated with the mean scattering length $\bar{a}$ and the so-called Feshbach resonance parameter R^* [Chi10],

$$E_b = \frac{\hbar^2}{m(a - \bar{a} + R^*)^2}. \tag{1.6}$$

The mean scattering length $\bar{a}$ relates to the van der Waals length via $\bar{a} = 4\pi R_{\mathrm{vdw}}/\Gamma(1/4)^2 = 0.955978\ldots R_{\mathrm{vdw}}$,[3] which corresponds to an energy scale defined by $\bar{E} = \hbar^2/(m\bar{a}^2) = 1.09422\ldots R_{\mathrm{vdW}}$ [Gri93]. The Feshbach resonance parameter $R^* = \bar{a}/s_{\mathrm{res}}$, with the resonance strength s_{res} defined in Eq. (1.8) [Pet04a]. It is quite interesting how non-universal contributions can have an impact on universal quantities in this intermediate regime. Especially in the three-body sector, this is a partly unsolved question.

[3] Here, $\Gamma(x)$ refers to the gamma function.

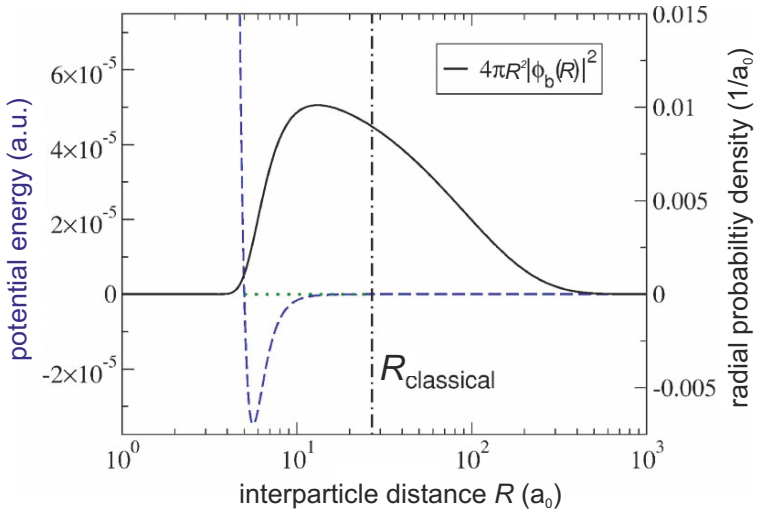

Figure 1.2.: Helium dimer interaction potential (dashed curve) and radial probability density (solid curve) as an example of a halo dimer state. For the shallow bound state (dotted line), the major fraction of the wavefunction is outside the classical turning point $R_{\text{classical}} = 27\,a_0$ (dot-dashed line) at large interparticle distances R (given on a logarithmic scale). Taken from Ref. [Köh06b] with small modifications.

Universal two-body systems in nature

For neutral atoms, the magnitude of the s-wave scattering length is typically in the order of R_{vdW}. Nature, however, offers some universal systems where a exceeds the characteristic interaction range. Generally, for atomic systems, a changes considerably for different species as well as for different isotopes.

The ^{4}He atom features a large positive scattering length of $a \sim 197\,a_0$ [Gri00b], exceeding the van der Waals length $R_{\text{vdW}} \approx 10.2\,a_0$. Therefore the ^{4}He interaction potential has a weakly bound universal dimer state with $E_b \sim h \times 28$ MHz [Sch94, Luo93, Köh06b]; see Fig. 1.2.

One of the earliest examples of universality, originating from nuclear physics, is the deuteron, which in the 1930s motivated theoretical approaches to exploiting the separation of length scales [Bet35a, Bet35b]. It is a weakly bound state with a binding energy of 2.2 MeV, which is considerably lower than the natural low-energy scale of the interaction potential[4] $E_\pi \sim 21$ MeV [Bra06]. For this system the natural energy scale E_π is related to the range of the one-pion-exchange potential $R_\pi \approx \hbar/(m_\pi c) = 1.4$ fm.

For neutron-neutron scattering of opposite spin states, the s-wave scattering length $a = -18.5$ fm is also larger than the effective range $r_0 = 2.8$ fm and the range of the one-pion-exchange potential.

In principle, the scattering process of two α particles, where α stands for the

[4]This corresponds to the s-wave scattering length being larger than the characteristic interaction range.

^{4}He nucleus, features a large s-wave scattering length [Efi90] $a \approx 5$ fm, which exceeds the effective range $r_0 \approx 2.5$ fm [Bra06]. Here, the Coulomb force between the α particles does not allow for a bound state, and shifts the ground state energy to about 0.1 MeV above the α-α scattering threshold [Bra06]. Therefore, the ^{8}Be nucleus is short-lived.

Feshbach resonances

Even though several nuclear systems exist where nature provides a large s-wave scattering length, a fixed a hinders the study of universal physics. The major success of atomic quantum gases originates from the tunability of a via the *Feshbach resonance* phenomenon. This phenomenon, arising from the coupling of a discrete state (molecular state) to the continuum (scattering states), was first theoretically treated by Feshbach and Fano independently of each other [Fes58, Fes62, Fan35, Fan61, Fan05]. Feshbach described this phenomenon in the context of nuclear physics, whereas Fano approached the problem from the side of atomic physics.

To understand Feshbach resonances it is useful to introduce the concept of scattering *channels*. In the asymptotic limit $R \to \infty$, two atoms can be definitely specified by their internal quantum numbers, typically their atomic spin quantum numbers. The two-body scattering (Born-Oppenheimer) potentials which relate to these quantum numbers and the rotational quantum number are referred to as their scattering channel. The channel in which atoms are initially prepared with an energy E is called the *entrance-channel*. For bosons in the ultracold regime, the entrance-channel is an s-wave channel, as only scattering in the lowest partial wave ($\ell = 0$) takes place. Channels can be classified by their energy E_c in the limit $R \to \infty$, as either *closed channels* with $E_c > E$ or *open channels*[5], where $E_c < E$. The exchange and dipole-dipole interactions feature off-diagonal elements in this channel basis, which lead to coupling of different channels.

The most prominent way to experimentally induce a Feshbach resonance is related to the magnetic field dependent Zeeman shift, which allows to energetically shift different channels against each other. When a molecular state belonging to a closed channel is tuned in resonance with the atomic scattering state in the entrance channel, a magnetic Feshbach resonance[6] is induced [Chi10][7]. The coupling of the states leads to resonant interaction, which allows to magnetically tune a from plus to minus infinity, with a divergence at the center of the

[5] Those names result from the fact that only open channels are energetically allowed for separated atoms.

[6] Feshbach resonances can also be induced by means of optical [Fed96a, Fat00, The04] or rf coupling [Moe96, Han10, Kau09] of the scattering state to a molecular state. Large inevitable losses, which have been experimentally encountered, are the downside of these methods.

[7] Contrary to a Feshbach resonance, a *shape resonance* is induced when the scattering state is coupled to a metastable state behind a potential barrier of an open channel.

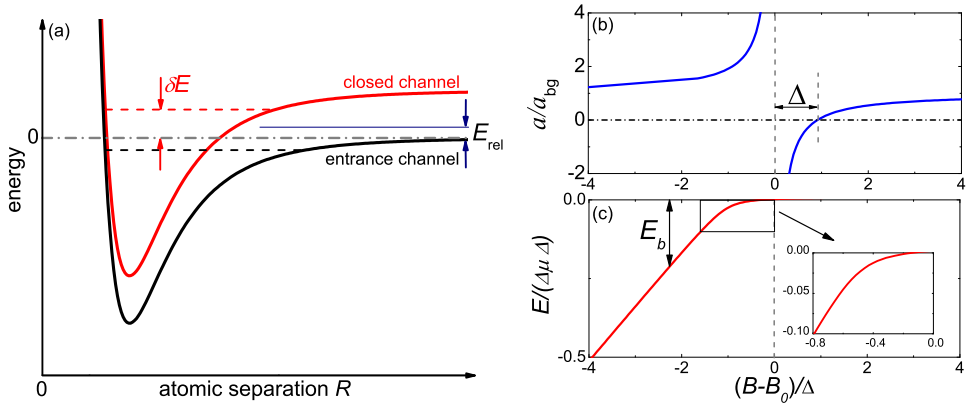

Figure 1.3.: Magnetically tunable Feshbach resonance scenario in an ultracold collision. (a) Basic entrance (black solid line) and closed-channel (red solid line) model for a Feshbach resonance. The last bound state (black dashed line) in the entrance channel defines the background scattering length a_{bg}. The energy difference δE between the zero energy (grey dash-dotted line) and the closed channel molecular bound state (red dashed line) can be magnetically tuned. In the ultracold regime, the collision energy $E_{\mathrm{rel}} \to 0$. For ultracold collisions, the coupling of the two channels induces a Feshbach resonance when $\delta E \to 0$. The right-hand panel shows the Feshbach resonance properties. (b) s-wave scattering length a in terms of a_{bg} and (c) binding energy E_b of the halo dimer state in the vicinity of a magnetically tunable Feshbach resonance with width Δ. Far out from the resonance, the energy dependence of the molecular state is related to the magnetic moment difference $\Delta\mu$ of the closed and entrance channel. The inset shows the universal regime, where the binding energy can be appropriately described by Eq. (1.5). A similar figure can be found in Ref. [Chi10].

resonance. This behavior is conveniently parametrized by [Chi10]

$$a(B) = a_{\mathrm{bg}}\left(1 - \frac{\Delta}{B - B_0}\right), \tag{1.7}$$

where B_0 and Δ are the pole and the width of the Feshbach resonance, respectively, and a_{bg} is the background scattering length, which is the "natural" scattering length of the entrance channel. This scenario is depicted in Fig 1.3.

The channel coupling mixes the closed and open channels near the center of the resonance, and the closed-channel molecular state takes over the character of the open channel. For $1/a \to 0$, this leads to a quadratic dependence of the binding energy E_b (Eq. (1.5)) on the magnetic detuning $B - B_0$; see Fig 1.3(c). The strength of this mixing determines the magnetic field range for which universality is applicable. For this, it is helpful to define the resonance strength s_{res} according

to [Chi10]

$$s_{\mathrm{res}} = \frac{a_{\mathrm{bg}}}{\bar{a}} \frac{\Delta\mu\,\Delta}{\bar{E}}, \tag{1.8}$$

with the magnetic moment difference $\Delta\mu$ between the open and closed channel. This allows to classify Feshbach resonances in the limiting cases as either *entrance channel dominated resonances* with $s_{\mathrm{res}} \gg 1$ or *closed channel dominated resonances* with $s_{\mathrm{res}} \ll 1$. For entrance channel dominated resonances, the near-threshold scattering and bound states inherit the spin character of the entrance channel. Thereby, the universal regime, where Eq. (1.5) is applicable, extends to magnetic field strengths for which the detuning from the resonance pole $|B - B_0|$ corresponds to a large fraction of the resonance width Δ. These resonances are typically called *broad resonances* and are well described by Eq. (1.7). For closed channel dominated resonances, which are called *narrow resonances*, the bound state is universal only for a small fraction of Δ near B_0; the resonance has to be modeled by a *coupled-channel* approach, which takes into account the properties of both channels and their coupling [Chi10].

In the following, Feshbach resonances will be labeled according to the rotational angular momentum quantum number ℓ of the molecular state in the closed channel that induces the resonance. The common notation is used, denoting states with $\ell = 0, 2, 4, \ldots$ as $s, d, g, \ldots$ [Rus29].

Cesium scattering properties

Even before the link between universal few-body physics and the benefical properties of ultracold atoms was found, the intriguing scattering properties of cesium raised major interest in the physics community. Initially, the motivation was to perform Bose-Einstein condensation (BEC) of this alkali species, which only offers one stable isotope, the naturally existent ^{133}Cs. First studies focused on the magnetically trappable states, starting with the doubly polarized state $|F = 4, m_F = 4\rangle$. Here, F and m_F refer to the total atomic angular momentum quantum number[8] and its magnetic projection number. For this state, Arndt *et al.* [Arn97] found a large s-wave scattering length hindering Bose-Einstein condensation due to strong enhancement of inelastic two-body losses [Söd98]. Attempts to condense cesium in the $|F = 3, m_F = -3\rangle$ state were also in vain for the same reason [GO98], raising the question whether condensation in the absolute ground state, $|F = 3, m_F = 3\rangle$ is possible. In the absolute atomic ground state inelastic two-body losses are energetically forbidden. However, this state is not magnetically trappable and three-body losses, which scale as a^4, could inhibit the formation of a stable condensate.

In 2003, Bose-Einstein condensation of cesium was successfully achieved by Weber *et al.* in the Innsbruck group[9] [Web03b]. For this, an atom sample was prepared in the absolute ground state $|F = 3, m_F = 3\rangle$ by means of optical trapping. This method allowed to independently tune the magnetic fields and

[8] Note that F is also referred to as the hyperfine state of the atom.

[9] The experiments presented in this PhD thesis were performed in the same laboratory.

adjust the s-wave scattering length during the experimental stages for optimizing the evaporation conditions. A key feature in this experiment was the existence of a broad Feshbach resonance, situated at -12 G (see Appendix A), which provided a large tunability of a in the magnetic low-field region. This broad s-wave Feshbach resonance results from the coupling to an $\ell = 0$ closed channel state.

Still, the absolute ground state is the most favorable state of cesium for performing ultracold atom experiments and therefore chosen as initial state for all experiments presented in this PhD thesis. All the ongoing discussion of cesium refers to this state.

There are two key features making cesium a prime candidate for the observation of universal few-body phenomena. First, a weakly bound state with $E_b \sim h \times 10$ kHz in the open channel gives rise to an extremely large background scattering length of about $a_{\mathrm{bg}} \sim 2000\, a_0$, greatly exceeding the van der Waals length of $101\, a_0$ [Chi04b][10]. This factor leads, according to Eq. (1.8), to large values for the resonance strength for occurring Feshbach resonances and thereby large universal windows. Secondly, the spin-dipole interaction, incorporating the second order spin-orbit coupling interaction, are particularly strong for heavy atoms such as cesium [Mie96, Kot00, Köh06b]. This effect enhances the coupling to molecular states stemming from higher-order partial wave channels. For this reason, cesium features a variety of many broad, intermediate and narrow Feshbach resonances, which create a suitable playground for the study of few-body phenomena.

The first experimental studies of the scattering properties of cesium were performed at Stanford University [Chi00, Chi04b][11]. Intense investigations of the near-threshold molecular structure were carried out by our group in Innsbruck [Mar07a] up to magnetic field strengths of 60 G (see Fig F.3).

Most remarkable are three broad s-wave resonances with poles near -12 G, 549 G and 787 G as shown in Fig. 1.4. The resonance positions were derived in Refs. [Chi10, Chi04b] and Appendix F. These three resonances are strongly entrance channel dominated with $s_{\mathrm{res}} > 100$ and thereby offer a broad universal regime[12].

A main part of this PhD work was the extension of the magnetic field system, in order to take advantage of the broad resonances at 549 G and 787 G. The former setup was suitable for reaching a magnetic field strength of about 150 G, allowing to perform measurement at the low-field resonance. As the center of this resonance (-12 G) cannot be accessed with the $|F = 3, m_F = 3\rangle$ state, the s-wave scattering length was limited to a tuning range between approximately $-2500\, a_0$ (0 G) and $1600\, a_0$ (150 G). After a major upgrade, which is described in Appendix B, the maximum for experimentally achievable magnetic field strengths is increased to about 1400 G, which allows to utilize the full tunability provided by the broad s-wave Feshbach resonance in the magnetic

[10] The van der Waals coefficient for cesium is $C_6 = 6860\, E_h a_0^6$ [Chi04b], where E_h is a hartree.
[11] Note that these studies were not limited to the $|F = 3, m_F = 3\rangle$ state.
[12] For the resonance at 787 G, $s_{\mathrm{res}} > 1000$.

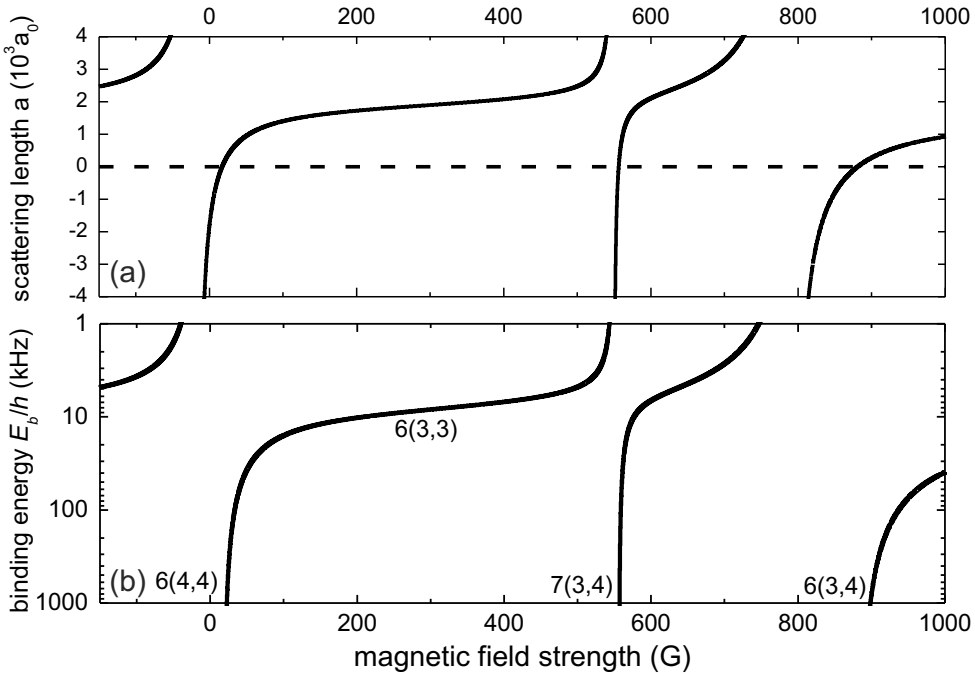

Figure 1.4.: Cesium scattering properties in the absolute atomic ground state $|F = 3, m_F = 3\rangle$ and near threshold s-wave molecular open and closed channel bound states. (a) The interesting scattering properties of cesium result from three broad s-wave Feshbach resonances with poles near -12 G, 549 G and 787 G, in combination with a large background scattering length originating from a weakly bound state in the open channel. Feshbach resonances resulting from the coupling to molecular states with $\ell > 0$ are neglected in this figure. (b) The near threshold s-wave dimer states are responsible for the broad s-wave Feshbach resonances shown in (a). The molecular states are labeled according to $f(F_1, F_2)$, with $f = |\mathbf{F}_1 + \mathbf{F}_2|$ and the indices (1,2) referring to the two atoms. The background scattering length results from the weakest bound 6(3,3) state, whereas the 6(4,4), 7(3,4) and 6(3,4) states induce the broad Feshbach resonances.

high-field region. The experiments presented in Chapter 4 and Appendix F were performed with the upgraded magnetic field system[13]. A recent experimental study of Feshbach resonances and binding energies in the magnetic high-field region up to 1000 G is part of this thesis, presented in Appendix F. These results will soon be published in a separate article [Ber11a].

[13]Bose-Einstein condensates were also created in the magnetic high-field region. The collapse of these condensates was used to determine the positions of the zero-crossings of the broad s-wave Feshbach resonances [Zen11].

1.2. Universality in three-body systems

The Efimov scenario represents a solution for the quantum three-body problem in the universal regime. This section gives an overview of this scenario and its implications, being a main research topic of this thesis.

The Efimov effect

In 1970, Vitaly Efimov discovered the first strong evidence of universality in a three-body system [Efi70]. He investigated theoretically the 3-body spectrum of identical bosons with resonant pairwise interactions ($|a| \to \infty$) that are induced by short range potentials. This study brought up several astonishing and counterintuitive predictions, the most striking of them being the existence of an infinite series of "giant" trimer states in the resonant limit $a \to \pm\infty$. This scenario is depicted in Fig. 1.5. In the resonant limit, the binding energy of the nth *Efimov trimer state* $E_{\mathrm{T}}^{(n)}$ relates to the consecutive trimers according to a strict geometric scaling law [Bra06],

$$\frac{E_{\mathrm{T}}^{(n+1)}}{E_{\mathrm{T}}^{(n)}} = e^{-2\pi/s_0} \approx \frac{1}{515.03}, \tag{1.9}$$

where $s_0 \approx 1.0062378$ for identical bosons. Consequentially, there is an infinite number of arbitrarily shallow Efimov states accumulating at $E_{\mathrm{T}}^{(\mathrm{n}\to\infty)} \to 0$. As the binding energies decrease, the size of each successively shallower Efimov trimer increases by a factor $e^{\pi/s_0} \approx 22.7$. Even though these bizarre predictions were strongly debated, the Efimov effect was subsequently theoretically confirmed shortly after its discovery [Ama71, Ama72].

The Efimov trimer states connect the domain of negative scattering length ($a < 0$), where no weakly bound dimer exists, with the one of positive scattering length ($a > 0$) via $a = \pm\infty$. The region of $a < 0$ is also referred to as the *Borromean region*. This expression originates from the similarities of the trimer states, persisting in the absence of weakly bound dimer states, to the Borromean rings: removal of any one of the three components destroys the whole system. In the Borromean region, the Efimov states become unbound as they cross the tri-atomic[14] zero-energy threshold. In the crossing region, three particles can resonantly couple to an Efimov trimer in a low-energy collision (red arrows in Fig. 1.5). The value of the s-wave scattering length at which the nth Efimov trimer crosses the threshold is referred to as $a_-^{(n)}$. In the region of $a > 0$, the Efimov states of non-Borromean character couple to the atom-dimer threshold at $a_*^{(n)}$ (blue arrows in Fig. 1.5). The crossing points of successive Efimov states are determined by the geometric scaling factor as [Bra06]

$$\frac{a_-^{(n+1)}}{a_-^{(n)}} = \frac{a_*^{(n+1)}}{a_*^{(n)}} = e^{\pi/s_0} \approx 22.7. \tag{1.10}$$

[14] Although the Efimov scenario is, due to universality, valid for all kinds of systems, we refer only to atomic systems in this description, for reasons of simplicity.

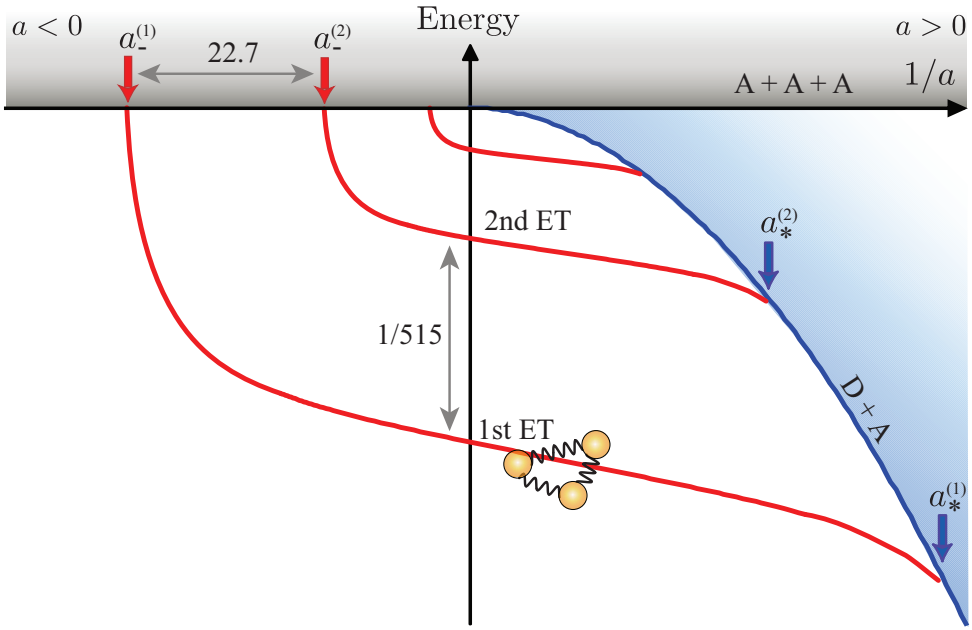

Figure 1.5.: Visualization of a series of universal trimer states in the Efimov scenario. The plot shows the binding energies of the trimer states (red lines) as a function of the inverse scattering length $1/a$. The horizontal line corresponds to the three atom threshold (A+A+A). For $a > 0$ a universal dimer state exists, which defines the atom-dimer (D+A) threshold (blue line). The shaded regions symbolize the scattering continuum for three atoms and for an atom plus a dimer. For resonant interactions $1/a \to 0$, the Efimov scenario predicts an infinite number of trimer states with an energy scaling factor of 1/515. The trimer states connect the free atom threshold at $a < 0$ with the atom-dimer threshold at $a > 0$ via $a = \pm\infty$. The arrows mark the positions where the trimer becomes unbound at the atom threshold (red) at a_- and the atom-dimer threshold (blue) at a_*. The values for a_-, where consecutive trimers become unbound, are related via the universal scaling factor 22.7. Features on the positive and negative side are connected via the universal relations given in Eq. (1.14). Only three Efimov states are depicted in the figure, and the scaling factor is artificially reduced from 22.7 to 2. Taken from Ref. [Fer11].

Furthermore, universality relates $a_-^{(n)}$ and $a_*^{(n)}$ by $a_-^{(n)} = -\frac{22.7}{1.06}\, a_*^{(n)}$ [Bra06]. These relations are important cornerstones for the verification of experimentally observed Efimov states.

Near the atom-dimer threshold, the Efimov trimer state can be understood as an atom-dimer system, with a size $a_{\mathrm{AD}}^2/3$ defined by the atom-dimer scattering length a_{AD}. Furthermore, a_{AD} diverges as $a \to a_*$ if effects from deeply bound dimers are ignored. The qualitative behavior of a_{AD} is one of the remarkable universal results on low-energy 3-body observables derived by V. Efimov [Efi71, Efi79]. Over the years, a quantitative derivation of a_{AD}, parameterizing the decay to deeply bound states by the introduction of the inelasticity parameter

η_*, was performed, which resulted in [Sim81, Bra03, Bra06]

$$a_{\mathrm{AD}} = (1.46 + 2.15 \cot[s_0 \ln(a/a_*) + i\eta_*])\, a. \tag{1.11}$$

Here, the index n on a_* has been dropped, as Eq. (1.11) is independent on the definite value of n. This follows from the geometric scaling law, which is responsible for the periodicity of a_{AD}. In the following, for quantities that are independent of n due to their periodicity, this index is neglected.

Following from the discussion above, it is clear that only a finite number of bound trimer states exists for finite a. This number is in the order of $N_b = (s_0/\pi) \ln(|a|/r_{\mathrm{int}})$ [Bra06], thereby limiting the number of observable trimer states for experimental systems where the tunability of a is limited.

Theoretical approaches to the three-body problem

One intuitive route to analyzing the three-body problem is by starting from a convenient set of coordinates, the hyperspherical coordinates[15] [Nie01, Bra06]. Using this description, the Schrödinger equation reduces to six independent coordinates in the center of mass frame, five hyperangular variables and the hyperradius R_{hyp}. The hyperradius relates to the size of the three particle system via $R_{\mathrm{hyp}}^2 = \frac{1}{3}(R_{12}^2 + R_{23}^2 + R_{31}^2)$, where R_{ij} refers to the interparticle distance of atoms i and j. Similar to the well-known two-body problem, the essence of this method is to treat R_{hyp} as a parameter and to solve the Schrödinger equation for a fixed R_{hyp}. This results in Born-Oppenheimer-like three-body potential curves that feature an R_{hyp}^{-2}-dependence, with the bound states being the Efimov states.

As early as 1935, Thomas analyzed the quantum three-body problem for a two-body potential supporting a single bound state in the zero-range limit, where $r_{\mathrm{int}} \to 0$ simultaneously with the two-body potential depth $V_0 \to -\infty$ in such a way that the energy of the two-body bound state is kept fixed [Tho35]. He showed that such a two-body potential leads to a 3-body spectrum that is unbounded from below, the so-called *Thomas collapse*. This behavior follows from the unphysical assumption of a zero-range potential and does not appear in real systems. The Thomas effect is closely related to the Efimov effect [Adh88], where r_{int} is fixed and $a \to \pm\infty$.

After the findings of Efimov, major interest arose in the universal three-body problem [Ama71, Ama72]. In 1993, Federov *et al.* found a simple derivation to solve the coordinate space Faddeev equations involved [Fad61, Fed93]. Within the last years, several (partly) new approaches for the investigation of the universal three-body problem led to a tremendous growth of the field, including, for example, numerically solving the Schrödinger equation with model potentials [Sun02, D'I04, D'I05a] or treating the problem in the framework of effective field theory [Bed99a, Bed99b]. Each approach is based on the assumption that the effective two-body interaction is much larger than the characteristic two-body

[15] It is beyond the scope of this introduction to give a detailed description of the derivation of the Efimov effect. The main aim here is to give a basic understanding of the three-body problem. For a detailed discussion, see for example Ref. [Bra06].

interaction range, $a \gg r_{\mathrm{int}}$. Similar to the two-body case, this condition defines the universal regime for three interacting particles. For neutral atoms, where the van der Waals interaction dominates the long-range tail of the interaction potential, this condition is typically fulfilled for $a \gg R_{\mathrm{vdW}}$. In the derivation of the Efimov effect, genuine three-body interactions are usually ignored in order to simplify matters, and only pair-wise interactions are taken into account.

Limitations of universal theory - The three-body parameter

All theoretical approaches used so far are based on the possibility of simplifying the three-body problem in the universal regime. Even though the real short-range interaction potentials are not known with sufficient accuracy to perform *ab initio* calculations, universal theory allows to solve the problem by substituting these unknown potentials by "handier" model potentials or adequate boundary conditions to reproduce the long-range behavior defined by a. This reflects the big advantage of universal theories. However, there is a drawback. Though the different theoretical approaches yield the correct scaling behavior, there remains one free parameter, the so-called *three-body parameter*. It includes all effects resulting from short-range physics, which have been ignored in simplified approaches. In dependence on the theoretical approach, there are several ways to define this three-body parameter. Furthermore, different theoretical approaches yield different three-body parameters, even for equal values of a. In the Efimov scenario, this corresponds to an arbitrary shift of the "ladder" of trimer bound state energies, which simultaneously shifts the positions of a_- and a_*. In nuclear physics, this phenomenon is well known from calculations of the triton binding energy and referred to as the *Phillips line* [Phi68]. In this way, the Thomas collapse can be understood as resulting from the removal of the only non-universal length scale, r_{int}, which would fix the three-body parameter.

Candidates for Efimov trimers in nature

Until 2006, when the first experimental evidence of an Efimov state was reported in an ultracold atomic quantum gas of ^{133}Cs [Kra06b], the most promising candidate was actually ^{4}He [Jen04]. First, a theoretical study by Lim *et al.* [Lim77] suggested that the excited trimer state of ^{4}He is an Efimov state. Even though this interpretation is widely accepted, the existence of this state has not yet been confirmed experimentally [Brü05]. Some discussion arose whether the ground state trimer of ^{4}He, which was observed in 1994 [Sch96], could be called an Efimov state [Esr96, Bra03]. According to a study by Esry *et al.* [Esr96] this state does not completely fulfill the properties of an Efimov state.

Other systems where states with Efimovian character can be found are halo nuclei [Jen04]. In particular systems with two valence nucleons, such as ^{18}C and ^{20}C, which both consist of a core nucleus and two valence neutrons, are possible candidates for Efimov states [Fed94, Bra06]. The triton, consisting of one proton and two neutrons, can, according to Refs. [Bra06, Efi81], be defined as an Efimov state. In nuclear systems such as the ^{3}He core, the Coulomb interaction due to

proton-proton repulsion is not short-range, thereby complicating the theoretical analysis [Bra06].

Although some of the trimers mentioned above might have Efimovian character, the lack of tunability of the interaction strength limits the possibility of studying the Efimov scenario in these cases. The smoking gun for experimentally verifying this scenario is based on showing that universal relations hold for real systems. The main benefit of ultracold atom experiments is the tunability of the interaction strength in the vicinity of a Feshbach resonance. This is the key ingredient for the success story of ultracold atom experiments for the study of Efimov physics. Moreover, ultracold atomic gases allow for several other adjustments to the system. One of them is the temperature, which is typically between a few nK and hundreds of μK and allows to investigate Efimov states above the scattering threshold [Yam07]. The dimensionality of atomic systems can be changed by means of optical lattices [Blo08]. Low-dimensional systems have highly non-trivial properties, where, for identical bosons, the Efimov effect only appears in three dimensions [Nie01, Bra06].

Several predictions resulting from universal theory concern the situation of general three-body systems, with unequal scattering lengths and/or unequal masses. The Efimov effect does not occur in a situation where only one pair features a large scattering length, but it does if two pairs are resonantly interacting [Ama72, Efi72, Efi73, D'I05b, Bra06]. In the situation of distinguishable particles, the mass ratio determines the value of s_0 and thereby the universal scaling factor [Ama72, Efi72, Efi73, D'I06b, D'I06a]. Mixture experiments of bosonic and/or fermionic atoms allow to extend the study of the Efimov effect. These investigations may help to learn more about trimer properties in other universal systems, such as the ones mentioned above. In the following discussion, the focus is on atomic systems in the universal regime, although the universally derived properties are valid for other systems as well.

Three-body recombination

The key link connecting Efimov's early predictions and ultracold atom experiments is the process of three-body recombination. In this process, three particles collide and successively recombine to a deeply bound dimer (D) and a free atom (A), $A + A + A \to D + A$. The energy released in this process is typically much larger than the trap depth, leading to loss of the three particles. Three-body recombination, which can be described by

$$\frac{dn_A}{dt} = -L_3 n_A(t)^3, \tag{1.12}$$

features a strong dependency on the atomic density n_A. Therefore, it is an obstacle to the achievement of Bose-Einstein condensation, even in a situation where one- or two-particle loss processes are suppressed. The understanding of the three-body loss rate L_3 in the framework of universal theory began to emerge more than a decade ago, when several theory groups tried to derive the

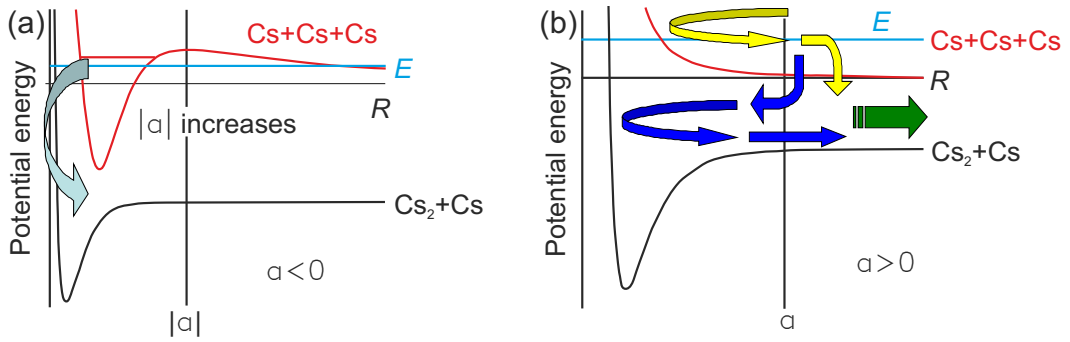

Figure 1.6.: Influence of the Efimov trimer states and potentials on the three-body recombination process in an ultracold atom (Cs) sample. (a) For $a < 0$, the three-body Efimov potential (red line) is the lowest scattering channel for three free atoms with collision energy E (blue horizontal line) and features a repulsive barrier with a maximum at $R_{\mathrm{hyp}} = |a|$. The Efimov trimer (red horizontal line) is a bound state in the three-body potential. Its binding energy can be tuned into resonance with the collision energy of the scattering state by variation of a. The free atoms can tunnel through the repulsive barrier and couple to the trimer state behind the barrier (similar to a shape resonance). The trimer state enhances losses to deeply bound atom-dimer states (indicated by the arrow) as the wave function overlap is increased. The value a_- corresponds to the scattering length, where the Efimov trimer energy coincides with the $E = 0$ threshold. (b) For $a > 0$, the atom-dimer channel, which supports the trimer states, is energetically below the three atom scattering threshold by an amount corresponding to the dimer binding energy. Two distinct pathways, symbolized by the blue and yellow arrows, allow the atoms to recombine into the atom-dimer channel at $R \approx a$. These two paths can interfere constructively and destructively, showing minima and maxima in the three-body recombination rate. The original figure can be found in Ref. [Esr06], the picture shown here is a redrawn version.

dependence of the three-body loss rate. The overall dependence of L_3 on the s-wave scattering length follows from a simple dimensional analysis as [Web03c]

$$L_3 = n_l C(a) \frac{\hbar a^4}{m}, \tag{1.13}$$

where n_l refers to the number of particles lost in this process. Typically, $n_l = 3$. In this equation, the general a^4-scaling is separated from the non-trivial physics embedded in the $C(a)$-parameter.

First calculations performed by Fedichev *et al.* in 1996 for large and positive values of a resulted in a fixed value of $C(a) = 3.9$ [Fed96b]. This value was doubted by Nielsen *et al.*, who, in a different approach for the same regime, derived an upper boundary of $C(a) \leq 68.4$ [Nie99]. This value is close to the experimentally determined $C(a) \approx 75$ by Weber *et al.* [Web03c]. In 1999, a numerical study by Esry *et al.* [Esr99] based on model potentials revealed

the connection of three body recombination with the Efimov scenario for large postive and negative scattering lengths. The results of this study are still in agreement with experimental findings. A qualitative picture of these recombination processes based on hyperspherical potential curves is given in the next paragraphs and shown in Fig. 1.6.

For negative s-wave scattering lengths, the three-body potential is deep enough to support at least one Efimov trimer bound state if $a < a_-^{(1)}$. At $a = a_-^{(n)}$, the nth trimer state has the same energy as the scattering threshold for three free atoms, see Fig. 1.6(a). The three-body potential features a repulsive barrier, with a maximum at $R_{\mathrm{hyp}} = |a|$. Therefore, the Efimov state leads to a shape resonance for three free atoms and low collision energies. The coupling to trimer states drastically enhances three-body recombination due to the fact that the wave function overlap to deeply bound atom-dimer states is strongly increased. This scenario induces a tri-atomic Efimov resonance [Efi79], which is the prime observable for Efimov physics in ultracold atom experiments.

In the case of a large and positive scattering length, the behavior is even more fascinating. The lowest three-body channel, which supports Efimov trimer bound states for $a > a_*^{(1)}$, is energetically shifted by the dimer binding energy from the repulsive entrance channel of the three scattering atoms; see Fig. 1.6(b). Two distinct paths allow the system to transition from the entrance to the Efimov channel at $R_{\mathrm{hyp}} \approx a$. In the first path (yellow arrow in Fig. 1.6(b)), the atoms bounce off the repulsive barrier of the entrance channel and recombine for increasing R_{hyp}. Whereas in the second path (blue arrow in Fig. 1.6(b)), recombination happens for decreasing R_{hyp}, then the system rebounds off the Efimov channel. These two pathways interfere constructively and destructively, which is reflected by three-body recombination minima and maxima. The s-wave scattering length, where the nth recombination minimum is observed, is labeled $a_+^{(n)}$. Successive minima follow the Efimov scaling law and appear at $a_+^{(n+1)}/a_+^{(n)} = e^{\pi/s_0} \approx 22.7$. They are universally related to a_- and a_* according to [Bra06]

$$a_-^{(n)} = -\frac{22.7^{(n-m+1)}}{1.06} a_*^{(m)} = -4.9 \times 22.7^{(n-m)} a_+^{(m)}. \tag{1.14}$$

Observation of recombination minima and the universal relations provides a strong evidence for the verification of Efimov physics. Interestingly, even before the first Efimov related observation was reported in 2006, a recombination minimum at $+210\,a_0$ was utilized for efficient evaporation cooling in an ultracold sample of ^{133}Cs, without knowledge of the origin of this benefit [Kra04].

A major step in the interpretation of three-body recombination measurements followed from effective field theory, which provided analytic expressions for $C(a)$

given as [Bra04, Bra01, Bed00, Bra06]

$$C(a) = \begin{cases} \dfrac{4590\,\sinh(2\eta_-)}{\sin^2[s_0\ln(a/a_-)] + \sinh^2\eta_-} & \text{for } a<0, \quad (1.15a) \\ 67.1\,e^{-2\eta_+}(\sin^2[s_0\ln(a/a_+)] + \sin^2\eta_+) & \\ \qquad +16.8\,(1-e^{-4\eta_+}) & \text{for } a>0. \quad (1.15b) \end{cases}$$

The inelasticity parameters[16] $\eta_\pm$ originate from the non-universal decay rate to deeply bound molecules and are therefore not accessible by universal theory. The log-periodic oscillatory behavior of $C(a) = C(e^{\pi/s_0}a) \approx C(22.7a)$ reflects the periodicity of the Efimov scenario.

Atom-dimer relaxation

Conceptually similar to three-body recombination is the two-body loss process observed in an atom-dimer system for a large and positive s-wave scattering length. During an atom-dimer collision, the weakly bound dimer (D^*) relaxes into a more deeply bound dimer state (D), $A + D^* \to A + D$. This collisional relaxation, also known as vibrational quenching, results in a loss of the atom and dimer from the trap due to the conversion of the dimer binding energy into kinetic energy distributed among the particles involved. This process is strongly favored in the vicinity of a_*, where the Efimov trimer couples to the atom dimer threshold and the atom-dimer cross section is resonantly enhanced (Eq. (1.11)). The loss process can be described by

$$\frac{dn_D}{dt} = \frac{dn_A}{dt} = -\beta(a) n_D(t) n_A(t), \tag{1.16}$$

with the relaxation rate coefficient $\beta(a)$ and the dimer density n_D. The universal expression for $\beta(a)$ is provided by effective field theory and, in the zero-temperature limit, reads as [Bra04, Bra07, D'I05b, Hel09][17]

$$\beta = C_{\mathrm{AD}}(a)\frac{\hbar a}{m}, \tag{1.17}$$

with

$$C_{\mathrm{AD}}(a) = \frac{20.3\sinh(2\eta_*)}{\sin^2\left[s_0\ln(a/a_*)\right] + \sinh^2\eta_*}. \tag{1.18}$$

As for $C(a)$, the log-periodic oscillatory behavior of $C_{\mathrm{AD}}(a)$ follows from the periodicity of the Efimov effect, resulting in an atom-dimer loss resonance each time an Efimov trimer couples to the atom-dimer threshold.

[16] These parameters are sometimes referred to as the imaginary part of the three-body parameter [Bra06, Mar08a].

[17] Note that in Ref. [Bra07] the temperature effect was studied as well. Due to an error in the thermal averaging procedure, the height of the resonance peaks were not correctly determined [Bra09a].

Unitarity limit

In principle, recombination loss measurements in the vicinity of a Feshbach resonance would allow to observe the infinite ladder of Efimov states successively intersecting with the atom threshold. Unfortunately, two experimental limitations considerably narrow the number of detectable trimer states. First, magnetic field instabilities, which are normally in the mG regime, translate into a strong variation of the s-wave scattering length near the pole. For this reason, broad Feshbach resonances are favorable for the experimental investigation of few-body phenomena. The more crucial restriction is connected to the unitarity limit in few-body collisions. Similar to the elastic two-body collision cross-section (Eq. (1.3)), the limitation of the scattering matrix sets a natural border for three body recombination losses. In Ref. [D'I04] this limit has been derived as a function of the temperature according to

$$L_3^{\max} = \frac{36\sqrt{3}\pi^2\hbar^5}{(k_B T)^2 m^3}. \tag{1.19}$$

The unitarity limit for four-body recombination is given in a similar manner as [Gre11]

$$L_4^{\max} = \frac{256\sqrt{2}\pi^{7/2}\hbar^8}{(k_B T)^{7/2} m^{9/2}}. \tag{1.20}$$

In general, recombination losses follow a strong temperature dependence, according to $L_N \propto T^{-\frac{3N-5}{2}}$ [Gre11]. In order to observe a recombination loss resonance, the visibility of the structure demands that the background losses are smaller than the unitarity limit. This restriction limits the number of observable Efimov features to one or two in experiments with atoms of the same mass. Experiments on atomic mixtures with a more advantageous mass ratio and scaling factor would allow the observation of more resonances before the unitarity limit is reached [D'I06b].

Open questions

The possibility to observe Efimov physics experimentally raises several questions about the predictive power of universal theories for real-world systems and motivated the experiments presented in this PhD thesis, as well as experimental and theoretical work of other groups. One of the key questions is, what happens in the transition regime between the universal $a \gg R_{\mathrm{vdw}}$ and the non-universal region $a \sim R_{\mathrm{vdw}}$? How sensitive are the universal relations and scaling behaviors? One way to approach this interesting regime theoretically is by incorporating finite-range corrections in the universal theory [Ham07a, Pla09, Thø08b]. It is still unclear whether these corrections can explain the experimental findings presented in Sec. 1.4 and Chapter 2.

Another important issue concerns the properties of the three-body parameter. Because it incorporates unknown effects resulting from the details of two- and real three-body potentials, it cannot be determined by the simplified universal

theories[18] and has to be obtained experimentally. This parameter determines the values of a_- and the universally related observables. Therefore, a_- is an experimentally appropriate way to define the three-body parameter. The key question is how this parameter varies in different scattering scenarios for Feshbach resonances stemming from different molecular levels. Even a magnetic field dependence of the three-body parameter cannot be excluded a priori [D'I09c]. Little is known about the effects of genuine three-body forces on universal theories. D'Incao *et al.* performed a model calculation incorporating a unique three-body force via the Axilrod-Teller potential [Axi43], which led to a small shift of the resonance position a_-. Generally, three-body forces are expected to play a minor role, as they modify the three-body potentials at length scales much smaller than R_{vdW} [Sol03]. However, this issue is still not fully resolved. If three-body forces are assumed to have a negligible effect on the constancy of the three-body parameter, it is sufficient to understand the role of pair-wise two-body interactions. Theoretical work suggests that for closed-channel dominated Feshbach resonances with $R^* \gg a$ the three-body parameter is expected to be fixed by the length scale set by R^* [Pet04a, Gog08]. However, this result is still discussed [Wan11a]. For open-channel dominated resonances, the largest non-universal length scale is connected to R_{vdW}. This raises hope that a refined theoretical approach, for example by including several bound states [Lee07], might be able to describe the three-body scattering properties in the universal regime sufficiently well. Even if approaches are found that satisfactorily explain the scattering physics at broad and narrow resonances, the question remains how they connect to a situation encountered at intermediate Feshbach resonances.

Some of these issues raised above have been addressed in this thesis and other experimental work on ultracold atomic gases, as outlined in Sec. 1.4.

1.3. Universality in four-body systems

Shortly after Efimov's prediction of the existence of an infinite number of universal three-body bound states, it was questioned whether this intriguing phenomenon also occurs for four and more bodies. Amado and Greenwood showed that there is no "true" Efimov effect for $N \geq 4$ [Ama73], meaning that the tuning of an $(N-1)$-bound state to zero energy cannot produce an infinite number of N-body bound states accumulating at zero energy. However, this conclusion does not prohibit the appearance of other classes of universal four-body states.

One class of universal four-body states with Efimovian character can be found in the vicinity of the atom-dimer Efimov resonance position a_*. There, the atom-dimer scattering length diverges $a_{\mathrm{ad}} \to \infty$ (Eq. (1.11)), giving rise to an Efimov scenario involving the atom-atom-dimer system [Bra06]. In this case, the four-body problem is reduced to three interacting particles with unequal masses.

[18] In effective field theory, the three-body parameter typically enters as a regulator to ensure that the momentum integral in the Skorniakov-Ter-Martirosian equation is independent on the definite value of the ultraviolet cutoff [Bra06].

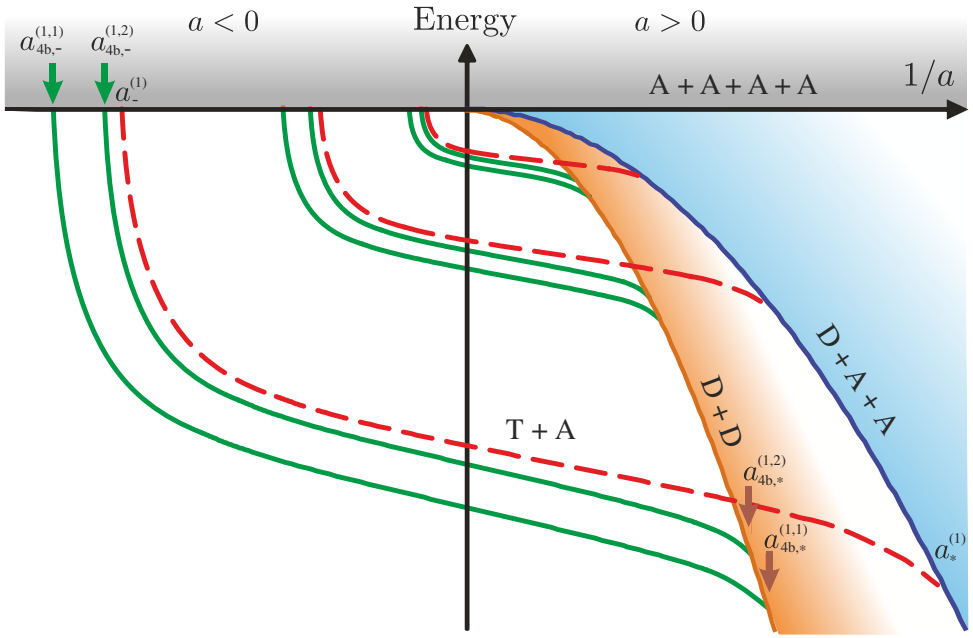

Figure 1.7.: Extended Efimov scenario showing the universal tetramer states. This figure is an extension of Fig. 1.5, where the dashed lines correspond to the Efimov trimer plus atom (T+A) thresholds. Note that in comparison to Fig. 1.5, one particle is added to each threshold. In the four-body picture each Efimov trimer is accompanied by two four body states (green solid lines), which cross the four atom threshold (A+A+A+A) at $a_{4b,-}^{(n,1)}$ and $a_{4b,-}^{(n,2)}$ and merge with the dimer-dimer threshold (D+D) (orange line) at $a_{4b,*}^{(n,1)}$ and $a_{4b,*}^{(n,2)}$. The arrows symbolize the positions where the tetramers couple to the free atom threshold (green) and the dimer-dimer threshold (brown). Taken from Ref. [Fer11].

Open questions

There has been a growing number of studies on the four (and more) body problem [Adh81, Nau87, Sø02, Pla04, Yam06, Han06, Thø08a]. Besides the issue of applicability of universal theory to real-world four-body systems, one particular question is whether a *four-body parameter* in addition to the three-body parameter is needed for the description of universal tetramer states [Yam06, Pla04].

One hint towards answering this questions comes from the field of nuclear physics. There, a well known correlation exists between three- and four-body observables, the *Tjon line* [Tjo75], which connects the binding energy of the triton with the binding energy of the α particle, without the necessity of introducing a genuine four-body force term.

The extended Efimov scenario

A fundamental step in understanding the four-body problem resulted from two articles published by theory groups in Bonn/Ohio [Ham07b] and at JILA in

Boulder [Ste09]. They predicted that the four-body potential created by an Efimov trimer and an atom is capable of supporting two universal tetramer states. Therefore, exactly two universal tetramer states are tied to each Efimov trimer, as depicted in Fig. 1.7. In this extended Efimov scenario, the values $a_{4b,-}^{(n,1)}$ and $a_{4b,-}^{(n,2)}$, where the tetramer states cross the free atom threshold, are universally related to $a_{-}^{(n)}$ by [Ste09]

$$a_{4b,-}^{(n,1)} = 0.43 a_{-}^{(n)} \qquad \text{and} \qquad a_{4b,-}^{(n,2)} = 0.90 a_{-}^{(n)}. \tag{1.21}$$

Furthermore, both tetramer states connect to the dimer-dimer threshold at [D'I09d]

$$a_{4b,*}^{(n,1)} = 2.37 a_{*}^{(n)} \qquad \text{and} \qquad a_{4b,*}^{(n,2)} = 6.6 a_{*}^{(n)}. \tag{1.22}$$

For the derivation of Eqs. (1.21) and (1.22) no four-body parameter was necessary, indicating that their experimental verification anwers the question of necessity of such a parameter in this particular case.

Similar to the Efimov scenario, enhancement of four-body recombination at $a_{4b,-}^{(n,1)}$ and $a_{4b,-}^{(n,2)}$ leads to losses in an atomic sample according to

$$\frac{dn_A}{dt} = -L_4 n_A(t)^4, \tag{1.23}$$

with the four-body loss coefficient L_4. A small indication for this process was already found in the publication concerning the first observation of an Efimov trimer by Kraemer *et al.* in 2006. One publication presented in this thesis (Chapter 6) examines this issue in a separate experiment. This study, which is outlined in Sec. 1.4, verifies the universal relations given in Eq. (1.21).

For positive scattering lengths, the tetramer is expected to couple to the dimer-dimer threshold. This process should lead to a variation of the dimer-dimer scattering length, similar to a Feshbach resonance scenario, allowing to magnetically tune dimer-dimer interactions. So far, no clear evidence for dimer-dimer resonances has been reported[19].

1.4. Few-body phenomena in ultracold atom experiments

Here, ultracold atom gas experiments related to the (extended) Efimov scenario are presented. Unless stated differently, all measurements were based on recombination or relaxation loss measurements in the vicinity of broad Feshbach resonances. To begin with, Efimov-related experiments performed by the Innsbruck group, utilizing an ultracold cesium sample, are outlined. Except for the publication by Kraemer *et al.* [Kra06b], all of these experiments were performed

[19] In Ref. [Pol09a], the authors report the observation of two loss resonances at a value where the dimer-dimer resonances are expected. The process leading to this observation is still not fully understood as the measurements were performed with an atomic instead of a dimer sample.

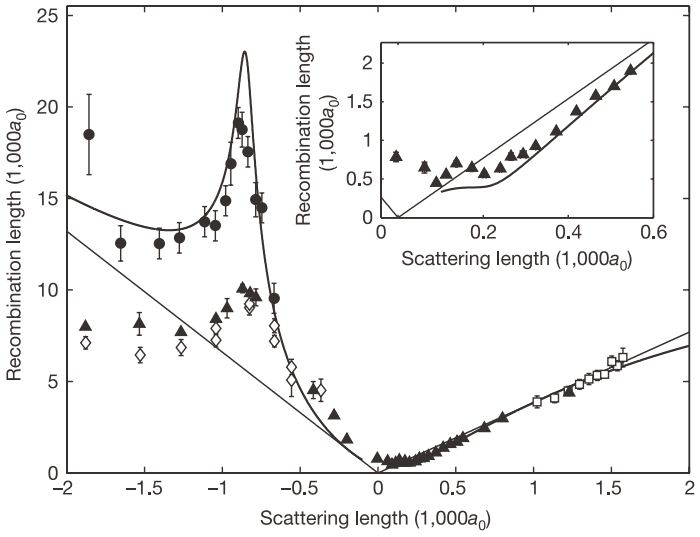

Figure 1.8.: First evidence of an Efimov trimer, obtained in three-body recombination measurements by Kraemer *et al.* [Kra06b]. For convenience, the recombination length $\rho_3 \propto L_3^{1/4}$ (instead of L_3) is displayed as a function of the scattering length in this figure. For a definition of ρ_3 see for example Chapter 4. The dots and triangles correspond to measurements performed with initial temperatures around 10 nK and 200 nK, respectively. The open diamonds are data from another setup with a temperature of 250 nK. The open squares are data taken from Ref. [Web03c]. For $a < 0$, a loss resonance at $a_-^{(1)} = -872(22)\,a_0$ was observed, originating from an Efimov trimer crossing the atom threshold. The higher-temperature samples yield a less-pronounced loss maximum due to the unitarity limit (Eq. (1.19)). At positive scattering lengths a recombination minimum was found at $a_+^{(1)} = 210(10)\,a_0$. The straight lines visualize the general a^4 scaling of L_3, which corresponds to a linear behavior for ρ_3. The curve represents a fit to the low temperature data according to the universal theory given in Eqs. (1.15a) and (1.15b). The inset shows a zoom on the minimum. The values given here differ slighly from the ones in Ref. [Kra06b] due to an improved $a(B)$ conversion, see Appendix F.

during the PhD work of the author of this thesis and are presented in detail in the following chapters. In order to avoid a thematic overlap, Ref. [Fer11] is omitted in this thesis, as this publication mainly focusses on an introduction to the Efimov scenario in a similar way as in the introduction given here. A summary of experiments performed by other groups, with atomic systems different from cesium, is given in the second part of this section.

Observations in an ultracold quantum gas of cesium atoms

The first evidence for an Efimov trimer was obtained in an ultracold atomic gas of cesium by the Innsbruck group[20] [Kra06b] in fall 2005. The large tunability of the s-wave scattering length, which was the basis for these findings, resulted from an entrance channel dominated Feshbach resonance with the pole at -12 G (as discussed in Sec. 1.1), allowing for a broad universal window of $a = [-2500\,a_0,\, 1600\,a_0]$, accessible even at relatively low magnetic field strengths. For $a < 0$, a tri-atomic Efimov resonance was observed in three-body recombination measurements at $a_-^{(1)} = -872(22)\,a_0$. For $a > 0$, a recombination minimum was found at[21] $a_+^{(1)} = +210(10)\,a_0$; see Fig. 1.8. Furthermore, a temperature dependent shift of the tri-atomic Efimov resonance was found [Näg06], which agreed with theoretical expectations [Yam07]. This shift relates to the existence of the trimer state above the free atom threshold; see Fig. 1.6(a).

The confirmation of the universal relation linking these two resonances was the smoking gun for relating the experimental findings to Efimov physics. The experimentally obtained value, $a_-^{(1)}/a_+^{(1)} = -4.2(2)$, agrees nicely with the theoretical expectation, $a_-^{(n)}/a_+^{(n)} = -4.9$ (Eq. (1.14)). The small deviation might originate from non-universal corrections, as the magnitude of $a_+^{(1)}$ was in the order of $R_{\mathrm{vdW}} = 101\,a_0$. The quantitative agreement led to the conclusion that this experiment was the first indication of the existence of the Efimov scenario in real systems. However, the results were strongly disputed [D'I09c], as the connection from $a < 0$ to $a > 0$ was via a zero-crossing ($a = 0$) and not a pole ($a = \pm\infty$) as in the original Efimov scenario. The authors of Ref. [D'I09c] claimed that due to variations in the three-body parameter an accidental correlation of the experimental findings could not be excluded. Contrary to that, Refs. [Lee07, Pla08] found good agreement of their model calculations with the experimental observations. The investigation of this issue was an important motivation for this PhD thesis.

Another experimental cornerstone for verifying the Efimov scenario was the confirmation of an Efimov trimer state coupling to the atom-dimer threshold. For this, we prepared an ultracold atom-dimer cesium sample and measured the atom-dimer relaxation rate $\beta(a)$. These measurements revealed the first observation of an atom-dimer Efimov resonance at $a_*^{(2)} = 367(13)$, which is connected to the first excited trimer state[22], as presented in Chapter 2 (see also Ref. [Kno09]). Good qualitative agreement with the theoretically expected shape of the loss resonance was found (Eq. (1.18)), even though the overall value of the relaxation rate was smaller than calculations in the zero-temperature limit suggested. An extension of universal theory considering finite-temperature effects partly resolved this issue [Bra07, Bra09a, Hel09]. Still, quite puzzling is the

[20] This experiment was performed at the same lab where the experiments presented in this PhD thesis were carried out.

[21] These values differ slightly from the ones given in Ref. [Kra06b], as the data has been refitted according to a new conversion of $a(B)$, as described in detail in Appendix F.

[22] Note that in Chapter 2 the excited Efimov trimer state is labeled as $n = 1$, and the ground trimer state as $n' = 0$.

universal relation between the atom-dimer and the tri-atomic Efimov resonance, $a_*^{(2)}/|a_-^{(1)}| \approx 0.4$, which deviates from the universal value of 1.06 (Eq. (1.14)) by a factor of 2. Studies on finite-range corrections show that these non-universal contributions decrease the value of $a_*^{(n+1)}/|a_-^{(n)}|$ [Ham07a, Pla09, Thø08b]. The question remains whether this effect by itself explains the experimental findings.

The properties of the three-body parameter, which, experimentally, can be conveniently parametrized by the resonance position a_-, are a controversial issue [D'I09c]. The questions whether the three-body parameter is magnetic field dependent, and whether it changes for different Feshbach resonances, still have no definite answer. In order to shed light on this matter, we investigated three-body recombination in the vicinity of several Feshbach resonances, including the high-field s-wave resonances at 549 G and 787 G. The study was extended to an overlapping g-wave ($\ell = 4$) Feshbach resonance[23] of intermediate strength ($s_{\rm res} \sim 1$) situated at 553.3 G. This experiment is described in detail in Chapter 4 (see also Ref. [Ber11b]). At the 787 G Feshbach resonance, which is the broadest of the resonances, we found a tri-atomic Efimov resonances for $a < 0$ and a recombination minimum for $a > 0$, with $a_-^{(1)}/a_+^{(1)} = -3.5(3)$ being not far from the expectations of universal theory (Eq. (1.14)). Furthermore, two more tri-atomic Efimov resonances were observed at the overlapping g- and s-wave Feshbach resonances around 550 G. Comparison of the measured resonance positions $a_-^{(1)}$, including the one reported by Kraemer *et al.* [Kra06b], yielded an astonishing result. These four Efimov resonances, resulting from different Feshbach resonance scenarios, delivered matching values of $a_-^{(1)}$ within a few percent of an Efimov period. This shows that the three-body parameter is almost constant over a magnetic field range spanning more than 800 G across a series of Feshbach resonances. This result excludes strong variation of the three-body parameter, as suggested in Ref. [D'I09c]. Interestingly, the values for $a_-^{(1)}$, normalized to the mean scattering length, $a_-^{(1)}/\bar{a} = -9.5(4)$, agree well with the ones derived in experiments on ^{7}Li [Pol09a, Gro10] and ^{6}Li [Wil09, Ott08, Huc09, Wen09], which vary between -8 and -10. This points to a deeper connection of the van der Waals length with the three-body parameter in the case of open-channel dominated Feshbach resonances.

Further investigations of the magnetic high-field region revealed another recombination minimum in the vicinity of the 549 G s-wave Feshbach resonance, agreeing nicely with the assumption of a constant three-body parameter; see Ref. [Fer11]. During this study, we found two tri-atomic Efimov resonances at two relatively broad d-wave Feshbach resonances ($\ell = 2$). Unfortunately, the $a(B)$ conversion was not accurate enough to determine the values of a_- in these cases.

Concerning the four-body sector, we could in 2008 announce the first evidence for two universal tetramer states as proposed in Ref. [Ste09]. These states were observed in recombination measurements in the magnetic low field region, close to the tri-atomic Efimov resonance reported in Ref. [Kra06b]. The obtained universal ratios, $a_{\rm 4b,-}^{(1,1)}/a_-^{(1)}$ and $a_{\rm 4b,-}^{(1,2)}/a_-^{(1)}$, were measured for the ground and the

[23] Appendix F describes the determination of the according Feshbach resonance properties.

excited tetramer state, yielding 0.47 and 0.84, respectively. These values are remarkably close to the universally derived values of 0.43 and 0.9 (Eq. (1.21)). Moreover, it was possible to experimentally distinguish between three- and four-body recombinations, showing that the observed loss resonances truly relate to a four-body process. These results verified the extended Efimov scenario of Ref. [Ste09] and demonstrated that no four-body parameter is needed to describe this universal scenario.

Before Ref. [Ste09] was published, we performed measurements in the magnetic low-field region, investigating collisions between tunable halo dimers; see Chapter 5 (and also Ref. [Fer08]). For this elementary four-boson process, we found a pronounced loss minimum in the dimer-dimer relaxation rate, which still lacks an adequate description. In 2009, D'Incao *et al.* suggested that the observed phenomena might be related to the universal tetramer states of the extended Efimov scenario coupling to the dimer-dimer threshold [D'I09d]. However, the expected positions of these resonances do not agree with those experimental data. Due to the constrained tunability of a in the magnetic low-field region, this issue could not be investigated any further. The new high-field setup allows to investigate this question in the near future, possibly revealing whether the observed resonance is connected to an universal tetramer state.

Observations in other ultracold quantum gas experiments

The first test of Efimov's universal scaling law was carried out in experiments on ^{39}K by the Florence group [Zac09] by observation of consecutive Efimov resonances. For $a > 0$, two recombination minima were found with a ratio $a_+^{(2)}/a_+^{(1)} = 25(4)$, which is in agreement with the universal scaling factor of 22.7. Furthermore, two small loss maxima were found, which were related to atom-dimer Efimov resonances via an "avalanche effect"[24]. These atom-dimer related loss maxima reproduced the universal scaling behavior quite well, with a scaling factor of 30.6(14). For $a < 0$, a single tri-atomic resonance was observed. Furthermore an indication for the related ground state tetramer state, connected to this Efimov state, was found. Interestingly, the resonances obtained for positive and negative a deviated substantially (by about $\sim 50\%$) from the universal predictions. The authors expected effective range corrections to be responsible for this variation, as the first recombination minimum and atom-dimer resonance are not (far) in the universal regime.

Another experiment reporting on the observation of consecutive Efimov resonances was performed by the Rice group [Pol09a]. An ultracold sample of ^{7}Li in its absolute atomic ground state was utilized for the observation of 11 Efimov and Efimov-related resonances. These results included for $a < 0$ two tri-atomic

[24] In this process, atoms decay by three-body recombination to the weakly bound dimer state. In the second step, these dimers scatter resonantly with several atoms before the dimers leave the trap. These scattering processes are enhanced due to the resonance in the elastic atom-dimer cross section near the atom-dimer Efimov resonance; see Eq. (1.11). As the dimer's kinetic energy greatly exceeds the trap depth, several atoms are lost in this process, leading to an atomic loss resonance.

loss resonance as well as the related four tetramer resonances and for $a > 0$ two recombination minima and an atom-dimer resonance, caused by the "avalanche effect". Furthermore, this group reported the discovery of two dimer-dimer resonances connected to the universal tetramer states. The process behind these resonances is still unknown, as the experiments were performed with a pure atom sample. All the scaling factors and universal relations on either side of the Feshbach resonance were in good agreement with universal theory. However, the connection between both sides featured an systematic discrepancy, deviating from the theoretically expected value by a factor of 2. The authors suggested a variation of the three-body parameter as being responsible for this deviation, which is in opposite direction as compared to the one observed in Ref. [Zac09].

Shortly after the Rice group published their data, measurements were performed by the Bar Ilan group [Gro10], utilizing the same atomic system (^{7}Li) as the Rice group in the absolute atomic ground state, $|F = 1, m_F = 1\rangle$. The Bar Ilan group found one recombination minimum and one tri-atomic Efimov resonance, confirming the universal relation between positive and negative a, in contradiction to the results of the Rice group. Even though the resonance positions in terms of the magnetic field strength were in agreement with the results of the Rice group, it was pointed out that the used $a(B)$ conversion featured strong discrepancies, when comparing the analysis of these two groups. The Bar Ilan group used molecular spectroscopy in combination with a coupled channel calculation for determining the properties of the Feshbach resonance, whereas the Rice group relied on *in-situ* BEC size measurements [Pol09b]. As spectroscopy is generally expected to yield more accurate results[25], the results of Ref. [Gro10] suggest a reinterpretation of the Rice data. The $a(B)$ conversion derived in Ref. [Gro10] calls in question the observation of the second tri-atomic resonance, which is likely not Efimov-related, but can be attributed to an enhancement of losses at the pole of the Feshbach resonance instead. In another experiment, the Bar Ilan group analyzed three-body recombination in the second lowest state ($|F = 1, m_F = 0\rangle$)[26] [Gro09]. In this atomic state, they found also a recombination minimum and a tri-atomic Efimov resonance, which agree well with the universal relations.

Furthermore, these two experiments allowed to study the three-body parameter for a situation of two different states of the same atomic species. They found equal resonance positions $a_-^{(1)}$ and $a_+^{(1)}$, and therefore equal three-body parameters, for both atomic states [Gro10]. As the ^{7}Li-measurements were performed at magnetic field strengths of about 800 G, the atoms were well described by the Paschen-Back effect. The two analyzed states feature a different nuclear spin, but similar electron spin, resulting in very similar two-body potentials. The nuclear-spin independence of the three-body parameter suggests that unique three-body forces are either nuclear-spin independent or make only a minor con-

[25] For the characterization of the high-field Feshbach resonances in our cesium sample we used the same method; see Appendix F.

[26] Chronologically, the experiment in the $|F = 1, m_F = 0\rangle$-state was performed before the one utilizing the $|F = 1, m_F = 1\rangle$-state.

tribution to the three-body parameter.

The first evidence of Efimov resonances in a bosonic mixture experiment was reported by the Florence group [Bar09]. The measurements were performed with an ultracold sample of ^{41}K and ^{87}Rb in the vicinity of a broad interspecies Feshbach resonance. This mixture exhibits two heteronuclear three-body channels: KKRb and KRbRb with scaling factors of $e^{\pi/s_0} = 3.51 \times 10^5$ and 131, respectively. Even though these scaling factors are not favorable for the observation of Efimov physics, the Florence group found two tri-atomic Efimov resonances, one attributed to the KKRb combination and one to the KRbRb channel. More favorable scaling factors are expected for light-heavy-heavy combinations of LiYbYb ($e^{\pi/s_0} = 4.5$), LiCsCs (5.5) and LiRbRb (7.9) [Bar09, Efi73].

Major interest was aroused by a series of experiments exploring Efimov physics in a three-component spin mixture of fermionic ^{6}Li by three groups in Heidelberg, at Penn State University and in Tokyo. The intriguing scattering properties result from three very broad overlapping Feshbach resonances at $B_0 = 690$ G, 811 G and 834 G [Bar05], which allow to tune the three different s-wave scattering lengths to large values simultaneously. Furthermore, the background scattering lengths change from very small values at zero magnetic field to about $-2000\,a_0$ at magnetic fields strengths exceeding 1000 G. Therefore, the scattering lengths decrease at first for increasing magnetic fields and then increase due to the Feshbach resonances. Initially, the magnetic low-field side, $B < B_0$, of these Feshbach resonances was investigated. Here, two tri-atomic resonances were found, which are connected to the same Efimov ground state [Ott08, Huc09]. Shortly afterwards, a study on the high-field side, $B > B_0$, of the Feshbach resonances revealed another tri-atomic resonance, originating from an excited Efimov trimer state [Wil09]. These results were studied theoretically, verifying the connection to Efimov physics [Bra09b, Nai09, Flo09, D'I09b]. Interestingly, for the Efimov ground state resonances, a change of the width of the loss resonances, which is related to the inelasticity parameter η, was observed. As the width depends on the lifetime of the Efimov trimers, which decay into a deeply bound dimer plus an atom, η is expected to depend on the decay probability of the trimer state. Wenz *et al.* suggested introducing an energy-dependent $\eta(E_b)$, which is a simple function of the binding energy E_b of the energetically nearest dimer states [Wen09]. This simple model was able to reproduce the measured data quite well. Furthermore, two studies performed on atom-dimer samples revealed two atom-dimer Efimov resonances [Lom10a, Nak10], as predicted in Ref. [Bra10]. Even though the tri-atomic resonances supported the idea of a fixed three-body parameter, the positions of the atom-dimer resonances disagreed with this assumption. Hence, the authors of Refs. [Lom10a, Nak10, Nai11] concluded an energy- and possible magnetic field dependence of the three-body parameter. A conceptually different route to studying Efimov trimers has been introduced in Refs. [Lom10b, Nak11]. Instead of measuring the value at which the trimer becomes unbound at the atomic or the atom-dimer threshold, rf-spectroscopy was used to determine its binding energy below the threshold[27].

[27] This method favors fermionic systems, due to the lifetime of the initial atom-dimer sample.

Due to the limited lifetime of the trimers, which is estimated to range between a few nanoseconds to microseconds [Bra10], no macroscopic samples of Efimov trimers could be produced with this method. Nevertheless, the binding energy measurements indicated a non-trivial energy or magnetic field dependence of the three-body parameter, similar to the results obtained in the observations of atom-dimer resonances.

1.5. Overview

This thesis includes six publications primarily investigating universal three- and four-body physics. Some of these articles examine open questions connected to the applicability of universal theory to real-world systems, whereas others report on the observation of unexpected phenomena motivating the search for theoretical explanations. The author of the present PhD thesis also contributed to a conference proceeding [Kno09] and a review article on Efimov physics [Fer11], which are not presented here.

All experiments presented in the following chapters were performed with an ultracold bosonic ^{133}Cs sample, most of them utilizing the absolute atomic ground state, $|F = 3, m_F = 3\rangle$. The publications presented in Chapters 2, 3, 5, 6 and 7 are based on exploiting the tunability of the broad -12 G Feshbach resonance in the magnetic low-field region. The experimental setup for these experiments is described in detail in the theses of the PhD and diploma students working prior to and temporarily with the author of the present thesis in the lab: Tino Weber [Web03a], Jens Herbig [Her05], Tobias Kraemer [Kra06a], Michael Mark [Mar03, Mar08b] and Harald Schöbel [Sch07][28]. In order to to take advantage of the (theoretically) unlimited tunability of the broad high-field Feshbach resonances at 549 G and 787 G, a major technical upgrade has been accomplished, which allows to access the magnetic high-field region up to 1400 G. The technical advances necessary for these upgrade are described in the appendices of this PhD thesis and, partly, in the diploma thesis of Walter Harm [Har10], who worked with the author of the present thesis on the realization of the newly implemented magnetic field system. The experiments presented in Chapter 4 were performed utilizing the new experimental high-field setup.

Chapter 2, *Observation of an Efimov-like trimer resonance in ultracold atom-dimer scattering*, reports on the first evidence of an atom-dimer Efimov loss resonance. This experiment was performed with an atom-dimer sample by determining the relaxation rate in dependence on a. The observed loss resonance is in good qualitative agreement with the expectations from universal theory. A puzzling shift of the expected position of the atom-dimer resonance in comparison to universal theory (Eq. (1.14)) might be the consequence of non-universal effects.

Chapter 3, *Magnetically controlled exchange process in an ultracold atom-*

[28]For the sake of completeness, note that the diploma thesis of Johann Danzl [Dan07] was also carried out in this lab, although it concerns a separate project.

dimer mixture, describes an exchange process $A_2 + B \rightarrow A + AB$ in an ultracold mixture of weakly bound dimers (A_2) and free atoms (B). This is an elementary proof-of-principle experiment, showing the first evidence for a reaction process controlled by the s-wave scattering length in the regime of universal interactions.

Chapter 4, *Universality of the three-body parameter for Efimov states in ultracold cesium*, investigates the properties of the three-body parameter in the vicinity of different Feshbach resonances. Three tri-atomic Efimov resonances and a recombination minimum in the magnetic high-field region were obtained and compared with the resonance reported in Kraemer *et al.* [Kra06b]. This study suggests that in this situation the three-body parameter is essentially independent on the magnetic field. Moreover, this publication presents the first evidence for an Efimov resonance observed in the vicinity of a g-wave Feshbach resonance, originating from a molecular state with higher-order rotational angular momentum.

Chapter 5, *Collisions between tunable halo dimers: exploring an elementary four-body process with identical bosons*, presents results on inelastic collisions in a pure sample of universal dimers. In this experiment, a pronounced loss minimum is identified while tuning the s-wave scattering length. These results give insight into an elementary four-body process. It is still an open question whether this minimum is related to a universal tetramer approaching the dimer-dimer threshold.

Chapter 6, *Evidence for universal four-body states tied to an Efimov trimer*, presents the first observation of two universal tetramer states coupling to the free atom threshold in the vicinity of the tri-atomic Efimov resonance, reported by Kraemer *et al.* [Kra06b]. These measurements verify the extended Efimov scenario as presented in Ref. [D'I09d].

Chapter 7, *Collisions of ultracold trapped cesium Feshbach molecules*, contains a collisional study of universal and non-universal dimer states. This chapter reports on several narrow loss resonances, which indicate the coupling to (non-universal) tetramer states. This process can be understood as a Feshbach-like resonance for ultracold molecules.

Chapter 8 gives an outlook on some future directions of research in the field of universal few-body physics.

The appendices give an overview of the technical modifications implemented in order to access the magnetic high-field region. Appendix A describes the energy level structure of ^{133}Cs in the ground and excited state manifold. Appendix B covers technical details of the new magnetic field system, which allows to achieve magnetic field strengths up to 1400 G. Appendix C discusses the experimental setup for the new absorption imaging system suitable for the magnetic high-field region. Appendix D describes the upgrade of the micro-wave setup for the high-field region. Appendix E explains the method for determining binding energies of weakly bound dimers as well as the technical setup. Appendix F presents new data on Feshbach resonances and dimer binding energies in the magnetic high-field region. This appendix explains the derivation of the $a(B)$ conversion, which is the basis for the publications related to the high-field region.

CHAPTER 2

PUBLICATION

Observation of an Efimov-like trimer resonance in ultracold atom-dimer scattering[†]

Nature Phys. **5**, 227 (2009)

S. Knoop,[1] F. Ferlaino,[1] M. Mark,[1] M. Berninger,[1] H. Schöbel,[1] H.-C. Nägerl,[1] and R. Grimm[1,2]

[1] *Institut für Experimentalphysik und Zentrum für Quantenphysik, Universität Innsbruck, 6020 Innsbruck, Austria*

[2] *Institut für Quantenoptik und Quanteninformation, Österreichische Akademie der Wissenschaften, 6020 Innsbruck, Austria*

The field of few-body physics has originally been motivated by understanding nuclear matter. New model systems to experimentally explore few-body quantum systems can now be realized in ultracold gases with tunable interactions [Kra06b, Bra06, Chi10]. Albeit the vastly different energy regimes of ultracold and nuclear matter (peV as compared to MeV), few-body phenomena acquire universal properties for near-resonant two-body interactions [Bra06]. Efimov states represent a paradigm for universal quantum states in the three-body sector [Efi70]. After decades of theoretical work, a first experimental signature of such a weakly bound trimer state was recently found under conditions where a weakly bound dimer state [Jen04, Köh06b, Fer08] is absent. Here we report on a trimer state in the opposite regime where such a dimer state exists. The trimer state manifests itself in a resonant enhancement of inelastic collisions in a mixture of atoms and dimers. Our observation is closely related to an atom-dimer resonance as predicted by Efimov [Efi79, Nie02, Bra07], but occurs in the theoretically challenging regime where the trimer spectrum reveals effects beyond the universal limit.

[†]The primary contribution of the author of the present thesis to this publication was the maintenance and improvement of the experimental setup together with M.M. and H.S. The author performed the measurements together with S.K. and F.F. The data analysis was carried out by S.K.

Trimer states arise as a natural consequence of two-body binding forces, but the general understanding of a quantum system of three interacting particles is a remarkably difficult task. For resonant two-body interactions, however, the energy spectrum follows simple, yet surprising rules as manifested in Efimov's scenario describing a series of trimer states [Efi70]. Systems in nuclear physics [Jen04] and molecular physics [Brü05, Bac00] were considered as candidates for Efimov states, but only recently ultracold atomic gases have opened up the possibility to realize and explore the required interaction conditions in a controlled way [Kra06b, Chi10]. In view of these new developments, the question becomes particulary important how idealized few-body scenarios are connected to near-universal systems existing in the real world.

A universal three-body system of identical bosons can be fully characterized by two parameters, the two-body scattering length a and an additional three-body parameter; the latter results from short-range physics [Bra06]. In principle, knowledge on one Efimov trimer state, as for example its binding energy for a given value of a, is sufficient to determine the three-body parameter and thus to predict the complete spectrum. A test of universality in a real three-body system is possible, when at least two different pieces of information on the trimer spectrum become experimentally available. For the caesium system, information was obtained by measuring three-body recombination [Kra06b]. The observation of a triatomic resonance marked the particular value of the negative scattering length where a trimer state of Borromean character [Jen04] reaches the threshold for dissociation into three free atoms. Observations at positive scattering lengths revealed a decay minimum, but an interpretation in terms of universal arguments is questionable because of ambiguities concerning the origin of this feature [D'I09c].

Here we follow a new experimental approach and show that an atom-dimer mixture provides experimental access to the situation where a non-Borromean trimer state couples to the threshold for dissociation into a free atom and a dimer. The phenomenon that we observe is a resonance in atom-dimer scattering, which manifests itself in resonantly enhanced inelastic decay. The resonance location provides an unambiguous piece of information which complements the previous results on caesium and facilitates a comparison with universal predictions concerning the spectrum of trimer states.

For caesium atom in the lowest internal state (hyperfine and projection quantum numbers $F = 3$ and $m_F = 3$) the s-wave scattering length a shows a pronounced dependence on the magnetic field in the low-field region below 50 G; see inset of Fig. 2.1. Over a wide range, $|a|$ is very large and exceeds the range of the attractive van der Waals potential, which can be characterized [Chi10] by a length $r_{\mathrm{vdW}} \simeq 100\, a_0$, where a_0 is Bohr's radius, and a corresponding energy $E_{\mathrm{vdW}} \simeq h \times 2.7$ MHz. Universality in general requires scattering lengths much larger than r_{vdW} and energies much smaller than E_{vdW}. For caesium, a near-universal halo dimer state [Jen04, Köh06b, Fer08] exists for large positive a with a binding energy of $E_{\mathrm{b}} = \hbar/(ma^2) \ll E_{\mathrm{vdW}}$, where m is the atomic mass.

A schematic of the relevant three-body energy spectrum is shown in Fig. 2.1,

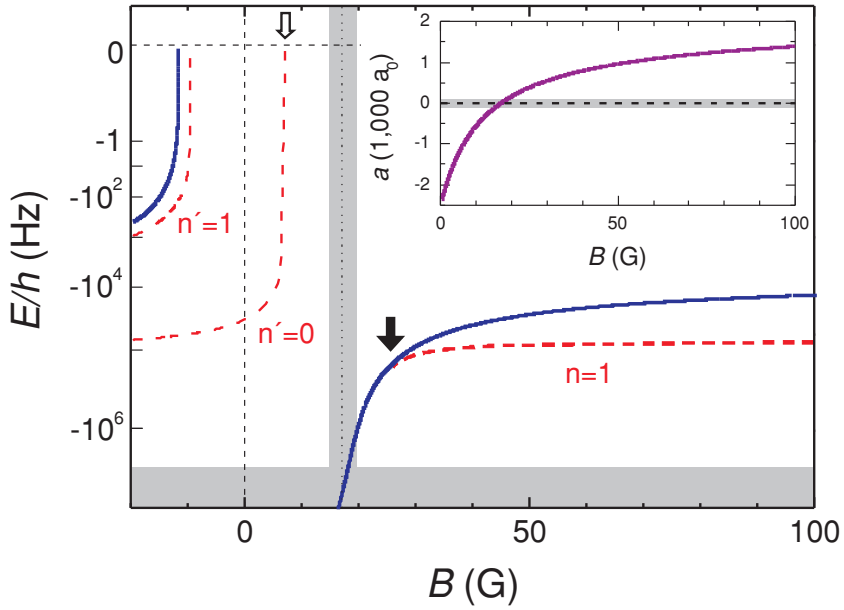

Figure 2.1.: Three-body spectrum of caesium. The energies E of the atom-dimer thresholds (blue solid curves) are shown as function of the magnetic field B. The red dashed lines illustrate Efimov-like trimer states, which are labelled by n' and n on the left- and right-hand side of the zero crossing of the scattering length at 17 G, respectively. For the trimer states the energy dependence is not precisely known. The giant three-body loss resonance found at 7.5 G [Kra06b] has pinpointed the intersection of an Efimov state with the three-atom threshold (open arrow). The intersection of an Efimov state with an atom-dimer threshold (filled arrow) leads to a resonance in atom-dimer relaxation. Zero energy corresponds to three atoms in the lowest spin state, labelled by the total spin quantum number $F = 3$ and its projection $m_F = 3$. The inset shows the scattering length a as a function of the magnetic field B. The grey areas represent the non-universal regions, where $|a| < r_{\mathrm{vdW}} = 100\, a_0$ or $E_{\mathrm{b}} > E_{\mathrm{vdW}} = h \times 2.7$ MHz.

illustrating the energies of trimer states (red dashed curves) and atom-dimer thresholds (blue solid curves). The energy dependencies of the thresholds are well known, because of the precise knowledge the caesium two-body spectrum [Mar07a]. The dimer state that corresponds to the atom-dimer threshold at positive magnetic fields has near-universal halo character in a wide magnetic-field range above 20 G [Fer08]. The trimer states are located in the regime where $|a|$ exceeds r_{vdW}, with binding energies well below E_{vdW}. We therefore refer to them as Efimov states [Efi70], although sometimes more strict definitions are used [Lee07]. An Efimov trimer intersects the three-atom threshold, at which three free atoms couple resonantly to a trimer. Similarly, an Efimov trimer couples to a halo dimer and a free atom at the atom-dimer threshold.

The energy spectrum of trimer states is not precisely known, but their appearance at the thresholds can give clear signatures of their locations. The observation of a giant three-body recombination loss resonance in an ultracold atomic

caesium sample at 7.5 G, corresponding to $a = -850\,a_0$, has pinpointed the location at which one of the Efimov states (labelled $n' = 0$) hits the three-atom threshold [Kra06b]; see open arrow. The next Efimov resonance in three-body recombination loss (as caused by the state with $n' = 1$) is predicted at negative magnetic fields, in principle accessible with atoms in the $F = 3$, $m_F = -3$ state. Unfortunately, in practice its observation will be obscured by fast two-body losses [Chi10]. Several studies have suggested the intersection of a trimer state with the atom-dimer threshold for positive magnetic fields below 50 G (Refs. [Köh06a, Esr07, Mas08]); see filled arrow. Note that in our case the regions with $a < 0$ and $a > 0$ are connected via a zero crossing and not via a pole. Therefore the states with $n = 1$ and $n' = 1$ are not adiabatically connected as they would in a complete realization of Efimov's scenario.

The appearance of an Efimov trimer at the atom-dimer threshold is predicted to manifest itself in a resonant enhancement of atom-dimer relaxation [Nie02, Bra07]. Relaxation is energetically possible because of the presence of deeply bound dimer states and leads to loss of both the atom and the dimer from the trap, as the corresponding release of energy generally exceeds the trap depth. The resonant coupling of an atom and a dimer to a trimer opens up strong loss channels as the trimer state decays rapidly into a deeply bound dimer state plus a free atom. The particle loss is described by the rate equation $\dot{n}_\mathrm{D} = \dot{n}_\mathrm{A} = -\beta n_\mathrm{D} n_\mathrm{A}$, where $n_\mathrm{D}(n_\mathrm{A})$ is the molecular (atomic) density and β denotes the loss rate coefficient for atom-dimer relaxation. In the non-universal regime, relaxation loss in ultracold atom-dimer samples has been studied in various systems [Muk04, Sta06, Zah06, Sya06] and was found to be essentially independent of the magnetic field. In the universal regime, suppression of loss has been observed in systems involving fermions [Ing08].

The experimental realization of an ultracold sample of simultaneously trapped atoms and dimers is a challenging task and requires special trap conditions (see Methods section). We prepare an ultracold atomic sample in a crossed-beam optical dipole trap, after which a part of the atomic ensemble is converted into dimers by means of Feshbach association [Her03, Köh06b] using a 200-mG-wide Feshbach resonance at 48 G [Mar07a, Fer08]. For our lowest temperatures of 30 nK we obtain a mixture of about 3×10^4 atoms and 4×10^3 dimers. After preparation of the mixture we ramp to a certain magnetic field and wait for a variable storage time. Then we switch off the trap and let the sample expand before ramping back over the 48-G resonance to dissociate the molecules, after which standard absorption imaging is performed. During the expansion a magnetic field gradient is applied to spatially separate the atomic and molecular cloud (Stern-Gerlach separation) [Her03]. In this way we simultaneously monitor the number of remaining atoms and dimers, see Fig. 2.2a. A typical loss measurement is shown in Fig. 2.2b. We observe loss of dimers on the timescale of a few tens of milliseconds. To obtain β we have set up a dimer loss model based on the above-mentioned rate equation (see Methods section). Because the number of atoms greatly exceeds the number of dimers, a simple analytic expression can be derived, which is fitted to the data. The loss of dimers due

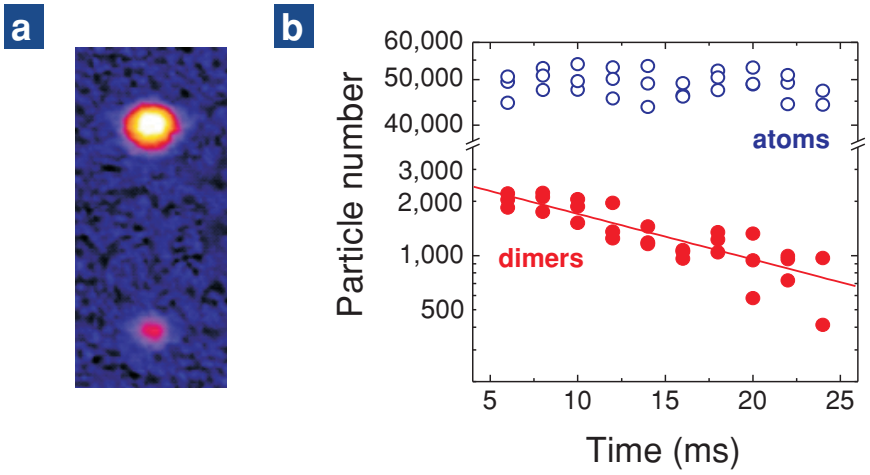

Figure 2.2.: Measuring the atom-dimer relaxation loss rate. (a) Absorption image of the atom-dimer mixture after release from the trap and Stern-Gerlach separation. (b) Time evolution of the number of atoms and dimers at 35 G. Here the loss of dimers can be fitted with an exponential decay curve with a $1/e$ lifetime proportional to β^{-1}, as the atom number greatly exceeds the dimer number and loss due to the dimer-dimer relaxation can be neglected (see Methods).

to dimer-dimer relaxation is small and is taken into account; the corresponding loss rate for this process was measured independently using a pure dimer sample [Fer08].

The relaxation rate coefficient β is shown in Fig. 2.3 as a function of the two-body scattering length a; the inset shows the same data as a function of the magnetic field. For $a < 0$ ($B < 17$ G) we observe an essentially constant β of about 1.5×10^{-11} cm^{3}s^{-1}. In this region, the atom-dimer system is non-universal and its properties are not directly related to the scattering length. With increasing a, β exhibits a strikingly different behavior. We first observe a sharp rise in β, which reaches its maximum value at about $a = 400\,a_0$ ($B = 25$ G), and a subsequent smooth decrease towards values similar to those in the non-universal region. We interpret the observed resonant enhancement as being caused by the appearance of a three-body bound state at the atom-dimer threshold. Due to the presence of the near-threshold trimer state, the atom-dimer scattering length is expected to diverge [Bra06]. In analogy with a usual two-body Feshbach resonance, such a three-body resonance could offer the unique possibility to tune the atom-dimer interaction from attractive to repulsive while the atomic two-body scattering length a stays always positive.

An intriguing question is whether the observed resonance is related to a trimer state that crosses the atom-dimer threshold or emerges from it. The behavior of the relaxation rate with temperature can provide further insight on this subject. For crossing states, the trimers also exist in quasi-bound states in the continuum above the atom-dimer threshold, and the location of the loss maximum will show

a related shift with temperature. For a trimer state merging with the threshold such a shift will not occur. Efimov's scenario predicts that in the Borromean region an Efimov trimer crosses the three-atom threshold, and measurements on the triatomic resonance position have indeed revealed a shift with temperature [Näg06]. In contrast, for the non-Borromean region an Efimov trimer is expected to merge with the atom-dimer threshold, as illustrated in Fig. 2.1. Figure 2.3 shows two data sets at different temperatures, namely at 40(10) nK (blue open triangles) and 170(20) nK (red closed squares). We observe β to be independent of the temperature of the mixture. We do not observe any shift of the resonance position supporting the expectation from Efimov's scenario that the trimer state exists only below the atom-dimer threshold. In addition, also the magnitude of the loss rate is not affected by the temperature change, indicating that the measurements are in the threshold regime and not unitarity limited.

At large scattering length trimer states are expected to have Efimovian character. In the non-Borromean region, Efimov physics manifests itself as a series of asymmetric resonances in the atom-dimer relaxation rate, in the universal limit separated by the factor $e^{\pi/s_0} \approx 22.7$, where $s_0 = 1.00624$. In the zero-temperature universal limit, an analytic expression of β has been found within an effective field theory [Bra07]. The loss rate coefficient has the form $\beta = C_{\mathrm{AD}}(a)\hbar a/m$ with $C_{\mathrm{AD}}(a) = D\left[\sinh(2\eta_*)/\left(\sin^2\left[s_0\ln(a/a_*)\right] + \sinh^2\eta_*\right)\right]$. The parameters a_* and η_*, corresponding to the resonance position and the decay parameter respectively, are both free in the theory since the short-range physics of realistic three-body system is usually largely unknown. We compare our findings with the universal predictions by fitting the analytic expression of β to our 170 nK data in the region where $a > r_{\mathrm{vdW}} = 100a_0$, with a_*, η_* and D as free parameters. As shown in Fig. 2.3, we observe a good qualitatively agreement, in particular regarding the characteristic shape of the observed loss feature. From the fit we obtain $a_* = 367(13)\,a_0$, $\eta_* = 0.30(4)$, and $D = 2.0(2)$. In Ref. [Bra07], D is a fixed value, which is predicted to be 20.3 in the zero-temperature universal limit.

In the ideal Efimov scenario, the locations of the resonance features in atom-dimer relaxation at $a_*^{(n)} > 0$ and those in three-body recombination at $a_-^{(n')} < 0$ are connected via the relation $a_*^{(n)}/|a_-^{(n')}| \approx 1.06 \times 22.7^{(n-n'-1)}$ [Bra06, Gog08]. With the observation of $a_-^{(0)} = -850(20)\,a_0$ [Kra06b] and our present finding of $a_*^{(1)} = 367(13)\,a_0$ we obtain $a_*^{(1)}/|a_-^{(0)}| = 0.43(2)$, which is significantly smaller than the value 1.06 in the ideal scenario. Theoretical models that take the finite range of the two-body potential into account [Ham07a, Thø08b, D'I09c, Pla09] have shown that finite-range corrections, which are particularly important for low-lying Efimov states, lead to shifts of the resonance positions. A downshift of $a_*^{(n)}$ is expected along with an upshift of $|a_-^{(n')}|$. This would indeed result in a smaller $a_*^{(1)}/|a_-^{(0)}|$. An alternative explanation would be a change in the three-body parameter between the $a < 0$ and $a > 0$ regions, which may occur in our case where these regions are connected via a zero crossing instead of a pole in a.

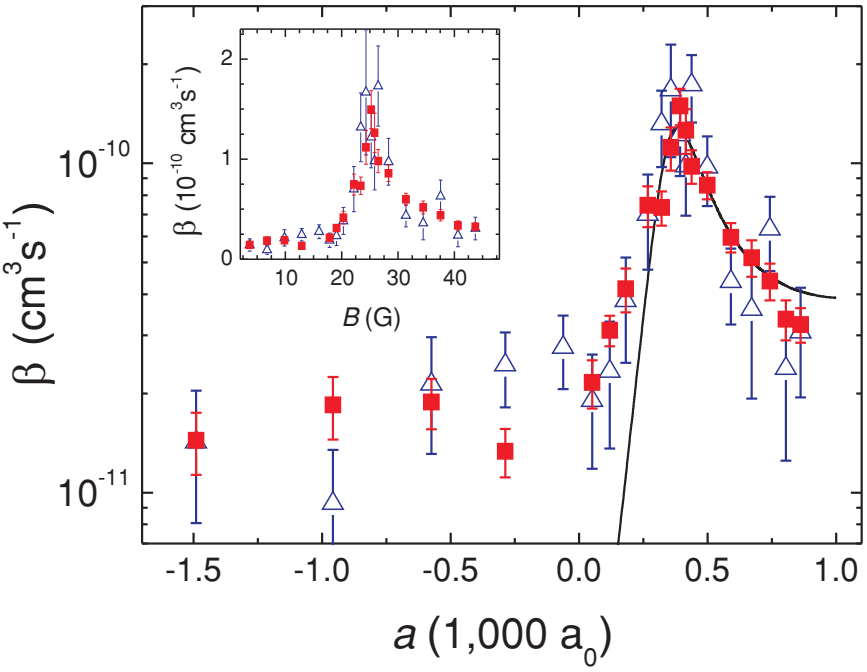

Figure 2.3.: Loss resonance in atom-dimer relaxation. The loss rate coefficient β for atom-dimer relaxation is shown as a function of the scattering length a (main figure) and the magnetic field B (inset); measurements are taken at temperatures of 40(10) nK (blue open triangles) and 170(20) nK (red closed squares). The error bars on β contain all statistical uncertainties (one standard deviation) from the fit of the time evolution as well as the trap frequencies and the temperature measurements (see Methods). The solid curve is a fit of an analytic model from effective field theory (see text) to the data for $a > r_{\mathrm{vdW}} = 100\, a_0$.

We have observed a strong loss resonance in an ultracold atom-dimer mixture, induced by a weakly bound trimer state. Our work demonstrates that atom-dimer relaxation measurements can provide information on the three-body spectrum in a complementary way to three-body atomic recombination. To resolve the open issues regarding the relation between different resonance features, more efforts, both experimentally and theoretically, are necessary. On the experimental side, the realization of the complete Efimov scenario requires a Feshbach resonance in which both sides of the resonance are accessible. For caesium a broad Feshbach resonance at 800 G is an excellent candidate for this purpose [Lee07]. A full understanding of the three-body sector in real-world systems near universality is required as a prerequisite to explore more complex few-body phenomena [Bra06, Ham07b, Thø08a, Ste09], such as the four-body scenario on which present experiments are beginning to shed new light [Fer08, Ste09].

Methods

Preparation

Our ultracold atom-dimer mixture is trapped in a crossed-beam optical dipole trap generated by two 1,064-nm laser beams with waists of about 250 μm and 36 μm [Fer08]. Since atoms and dimers in general have different magnetic moments the application of a levitation field is not appropriate and a sufficiently high optical gradient in the vertical direction to hold the atoms and dimers against gravity is required. However, to obtain very low temperatures and not too high densities a tight trap is not advantageous. Here we use an adjustable elliptic trap potential with weak horizontal confinement and tight confinement in the vertical direction. The ellipticity is introduced by a rapid spatial oscillation of the 36-μm waist beam in the horizontal plane with the use of an acousto-optic modulator, creating a time-averaged optical potential. The final temperature of the atomic and molecular sample can be set by varying the ellipticity and the laser power of the laser beam in the final trap configuration, and is in the range of 30-250 nK. For the lowest temperature samples, the final time-averaged elliptic potential is characterized by trap frequencies of 10 Hz and 20 Hz in the horizontal plane, and 80 Hz in the vertical direction.

Dimer loss model

We measure the atom-dimer relaxation loss rate β by recording the time evolution of the dimer number N_D and atom number N_A. In a harmonic trap the atomic and molecular samples can be described by Gaussian density distributions, where the width depends on the trap frequencies, the temperature and the mass. Because the polarizability of the halo dimers is twice that of the atoms, the trap frequencies of the atoms and the dimers are the same. We find that the atomic and molecular samples have the same temperature [Fer08]. The time evolution of N_D can then be described by the following rate equation:

$$\dot{N}_\mathrm{D} = -\frac{8}{\sqrt{27}}\beta\bar{n}_\mathrm{A}N_\mathrm{D} - \alpha\bar{n}_\mathrm{D}N_\mathrm{D}, \tag{2.1}$$

with $\bar{n}_\mathrm{A} = [m\bar{\omega}^2/(4\pi k_\mathrm{B}T)]^{3/2}N_\mathrm{A}$ and $\bar{n}_\mathrm{D} = [m\bar{\omega}^2/(2\pi k_\mathrm{B}T)]^{3/2}N_\mathrm{D}$ the mean atomic and molecular density, respectively, m the atomic mass, $\bar{\omega}$ the geometric mean of the trap frequencies and T the temperature. Here loss of dimers due to dimer-dimer relaxation is also taken into account via the dimer-dimer relaxation loss rate coefficient α. Because of the unequal mass, the density distributions of the atomic and molecular samples are not the same. As a result, an effective atomic density experienced by the molecular cloud has to be considered, which is taken into account by the factor $\frac{8}{\sqrt{27}}$ in front of the atom-dimer loss term [Sta06].

Our experiments are carried out in the regime in which $N_\mathrm{A} \gg N_\mathrm{D}$ and loss of atoms as a result of atom-dimer relaxation is negligible. Three-body recombination leads to atom loss on a much longer timescale compared to the molecular

lifetime. Therefore N_{A} can be taken as a constant and equation (2.1) has the following solution:

$$N_{\mathrm{D}}(t) = \frac{bN_{\mathrm{A}}N_{\mathrm{D},0}}{(bN_{\mathrm{A}} + aN_{\mathrm{D},0})e^{bN_{\mathrm{A}}t} - aN_{\mathrm{D},0}}, \tag{2.2}$$

where $N_{\mathrm{D},0} \equiv N_{\mathrm{D}}(t=0)$, $b \equiv \frac{8}{\sqrt{27}}\beta[m\bar{\omega}^2/(4\pi k_{\mathrm{B}}T)]^{3/2}$ and $a \equiv \alpha[m\bar{\omega}^2/(2\pi k_{\mathrm{B}}T)]^{3/2}$. If $\beta N_{\mathrm{A}} \gg \alpha N_{\mathrm{D}}$, i.e. dimer-dimer relaxation loss is negligible compared to atom-dimer relaxation loss, equation (2.2) simplifies to

$$N_{\mathrm{D}}(t) = N_{\mathrm{D},0}e^{-bN_{\mathrm{A}}t}, \tag{2.3}$$

and N_{D} shows an exponential decay with a $1/e$ lifetime of $(bN_{\mathrm{A}})^{-1}$. In our experiments dimer-dimer relaxation loss can be neglected for $B > 20\,\mathrm{G}$ and equation (2.3) is fitted to the data. For $B < 20\,\mathrm{G}$, β is much smaller than α [Fer08] and the application of equation (2.2) is required, taking α from independent loss measurements of a pure dimer sample [Fer08]. For each measurement of β the trap frequencies and the temperature are determined by sloshing mode and time-of-flight measurements, respectively.

Acknowledgments

We thank T. Köhler, B. D. Esry and P. Massignan for many fruitful discussions. We acknowledge support by the Austrian Science Fund (FWF) within SFB 15 (project part 16). S. K. is supported within the Marie Curie Intra-European Program of the European Commission. F. F. is supported within the Lise Meitner program of the FWF.

CHAPTER 3

PUBLICATION

Magnetically controlled exchange process in an ultracold atom-dimer mixture[†]

Phys. Rev. Lett. **104**, 053201 (2010)

S. Knoop,[1] F. Ferlaino,[1] M. Berninger,[1] M. Mark,[1] H.-C. Nägerl,[1]
R. Grimm,[1,2] J. P. D'Incao,[3] and B. D. Esry[4]
[1]*Institut für Experimentalphysik und Zentrum für Quantenphysik, Universität Innsbruck, 6020 Innsbruck, Austria*
[2]*Institut für Quantenoptik und Quanteninformation, Österreichische Akademie der Wissenschaften, 6020 Innsbruck, Austria*
[3]*JILA, University of Colorado and NIST, Boulder, Colorado 80309-0440, USA*
[4]*Department of Physics, Kansas State University, Manhattan, Kansas 66506, USA*

We report on the observation of an elementary exchange process in an optically trapped ultracold sample of atoms and Feshbach molecules. We can magnetically control the energetic nature of the process and tune it from endoergic to exoergic, enabling the observation of a pronounced threshold behavior. In contrast to relaxation to more deeply bound molecular states, the exchange process does not lead to trap loss. We find excellent agreement between our experimental observations and calculations based on the solutions of three-body Schrödinger equation in the adiabatic hyperspherical representation. The high efficiency of the exchange process is explained by the halo character of both the initial and final molecular states.

The full control of reactive processes on the quantum level is a major prospect of ultracold chemistry. The strong current efforts to produce samples of trapped

[†]The primary contribution of the author of the present thesis to this publication was the maintenance and improvement of the experimental setup together with M.M. The author performed the measurements together with S.K. and F.F. S.K. analyzed the data based on the theoretical description of the exchange process provided by J.P.D'I. and B.D.E.

ultracold molecules [Kre09, Dan08, Dei08, Lan08b, Ni08, Dan10] are providing experimentalists with new systems, where fundamental questions in this emerging field can be addressed [Car09]. Molecules can be prepared at ultralow temperatures in a single internal state, i.e. within a specific quantum state of its vibrational, rotational or spin quantum numbers. This allows quantum-state selective studies of elastic, inelastic, and even chemically reactive collisions. The application of external electromagnetic fields opens up unique possibilities for controlling the interacting processes, thus leading to a controlled ultracold chemistry [Kre08].

Elementary interaction processes in ultracold molecular gases have been studied experimentally, with the observation of intriguing phenomena such as the stability of Feshbach molecules created from fermionic atoms [Str03, Cub03, Joc03b] and the observation of collisional resonances caused by the presence of trimer [Kno09] and tetramer states [Chi05b, Fer10]. Inelastic collisions are commonly probed in a trap-loss regime where the products leave the trap following a large release of internal energy; see e.g. [Muk04, Sta06, Zah06, Sya06, Zir08a, Hud08]. Such trap loss represents a readily detectable signature of the interactions, but it does not provide information on the reaction products. The situation changes, however, when the energies of the initial and final state are nearly degenerate, and the small amount of energy released allow the reaction products to remain in the trap. Such a scenario provides unique access to study the dynamics of the reaction but has, to our knowledge, not been observed yet in ultracold gases.

In this Letter, we report on the observation of a controllable exchange process $A_2 + B \rightarrow A + AB$ in an ultracold mixture of weakly bound dimers (A_2) and free atoms (B). Our experiments provide a proof-of-principle demonstration of an elementary exchange reaction in the ultracold regime, including the direct observation of A atoms as a reaction product. Magnetic tuning allows to vary the energetic nature from endoergic over resonant to exoergic. We theoretically study the process by numerically solving the three-body Schrödinger equation in the adiabatic hyperspherical representation [Sun02] using a model potential. The calculations highlight the important role of large scattering lengths in the universal halo regime where both the A_2 and the AB dimers are very weakly bound [Köh06b, Fer09b]. Our results can be interpreted as the first observation of a reaction in the regime of universal interactions [Bra06].

The two atomic constituents A and B are represented by Cs atoms in different hyperfine states. More specifically, A represents the lowest hyperfine sublevel $|F = 3, m_F = 3\rangle$, and B one of the upper $|F = 4, m_F\rangle$ hyperfine sublevels, with $m_F = 2$, 3 or 4; the quantum number F denotes the total spin and m_F its projection. The characterization of the weakly bound dimer states according to the atomic hyperfine spin states is possible as the molecular binding energies are much smaller than the atomic hyperfine and Zeeman splitting. Since A and B only differ by their spin state, atom exchange is indistinguishable from spin exchange and the exchange process generally represents a coherent sum of both.

The magnetic field dependencies of the relevant molecular states play a crucial role for the exchange process. In Fig. 3.1(a) we schematically show the Zeeman

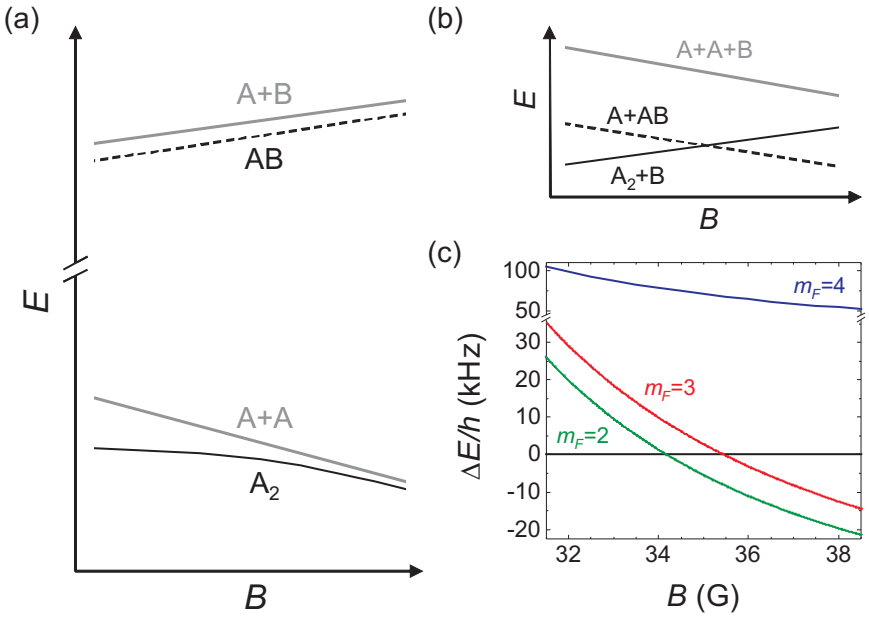

Figure 3.1.: (a) Zeeman diagram of the most weakly bound dimer states A_2 and AB below the A+A and A+B dissociation thresholds, respectively; here A and B are two hyperfine sublevels of Cs. (b) Schematic representation of a crossing between the A_2+B and A+AB channels. (c) The energy difference ΔE between the A_2+B(m_F) and A+AB(m_F) channels, with $m_F = 2$, 3 or 4, showing channel crossings around 35 G for $m_F = 2$ and 3.

diagram of the most weakly bound states A_2 and AB below the A+A and A+B dissociation thresholds, respectively. The magnetic field dependence of the A_2 binding energy has been studied both experimentally and theoretically [Chi04b, Mar07a]. Towards lower magnetic fields the A_2 state bends away from the A+A threshold, and its binding energy increases from $h\times 30$ kHz at 45 G to $h\times 150$ kHz at 30 G. The AB binding energies are essentially independent of the magnetic field and amount to about $h \times 5$ kHz for $m_F = 4$, and $h \times 80$ kHz for $m_F = 2$ and $m_F = 3$. We obtain these values from scattering length calculations [Jul08], using a generalized relation between the scattering length and the binding energy derived from quantum defect theory [Gao04].

As a result of the different magnetic field dependencies of the A_2 and AB binding energies, the A_2+B and A+AB channels can cross each other, which is depicted in Fig. 3.1(b). Such a scenario provides the opportunity to magnetically tune the exchange process into resonance. A quantitative picture is shown in Fig. 3.1(c), showing the energy difference ΔE between the A_2+B and A+AB channels. The channels cross for $m_F = 2$ and 3 around 35 G, and for higher magnetic fields the exchange process $A_2 + B \rightarrow A + AB$ is exoergic and thus energetically allowed. For $m_F = 4$ the exchange process remains endoergic in the investigated magnetic field range.

The experimental setup has been described earlier [Fer08, Kno09]. In brief, we

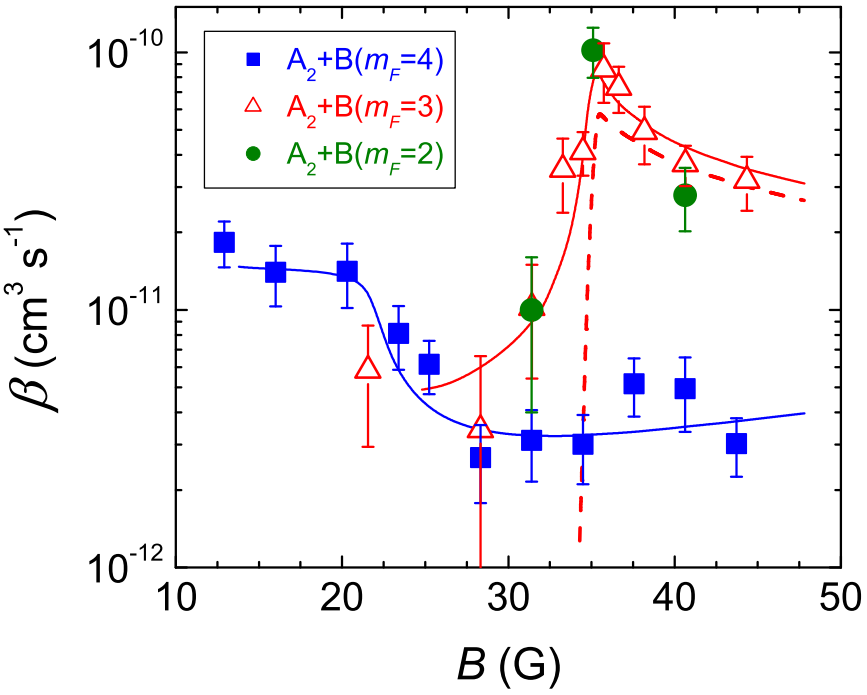

Figure 3.2.: Rate coefficient β for inelastic atom-molecule collisions for the B+A_2 mixtures at a temperature of 50(10) nK as function of the magnetic field B, comparing the experimental results (symbols) with the model calculations (lines). The solid curves represent the total A_2 loss rate including relaxation to more deeply bound states, whereas the dashed curve shows the contribution of the exchange process. The error bars contain the uncertainties of the trap frequencies and temperature measurements, required to convert the measured particle numbers into densities.

prepare an ultracold thermal sample of Cs atoms at temperatures of 50-100 nK in state A in a crossed-beam optical dipole trap, with a mean trap frequency of typically 30 Hz. Feshbach association at a narrow Feshbach resonance at 48 G results in an A+A_2 atom-molecule mixture consisting of 4000 molecules and 30 000 atoms. By applying a 3-ms microwave (MW) pulse we transfer the atoms from state A to state B with an efficiency of better than 95% and without any observable effect on the A_2 molecules. After preparation of the B+A_2 mixture we ramp to a certain magnetic field and wait for a variable storage time. Then we switch off the trap and let the sample expand before ramping back over the 48-G resonance to dissociate the remaining A_2 molecules, after which standard absorption imaging is performed. During expansion we apply the Stern-Gerlach technique to spatially separate the different atomic and molecular states.

In a first set of experiments, we measure the atom-molecule inelastic collision rates by recording the time evolution of the number of A_2 molecules and B atoms. In order to extract a rate coefficient β from the data we set up a loss model, similar to the one described in Ref. [Kno09]. The model includes loss by

molecule-molecule collisions [Fer08] and atomic loss due to two-body hyperfine-changing collisions. We derive an analytic expression, which we fit to the data. We show the results in Fig. 3.2, showing β as function of the magnetic field. The measured loss rate coefficient includes all atom-molecule collisions that lead to the loss of A_2 molecule from the sample, i.e. both the exchange process as well as relaxation to more deeply bound vibrational states.

In parallel, we theoretically determine the loss rates for A_2+B collisions. We model the two-body interactions with short-range potentials that have only a few bound states. Their strength is chosen in such a way to reproduce the energy of the weakly bound molecular A_2 and AB states at each magnetic field. The results of our calculations are shown in Fig. 3.2 for $m_F = 3$ and 4. The solid curves display the total loss rate of A_2 molecules, including both the exchange process and relaxation to more deeply bound states. The dashed curve shows the contribution that results from the exchange process. Because of the simplicity of the model potential the calculations are not expected to have accurate predictive power regarding the absolute total loss rate. Therefore the calculations are normalized to the experimental data to facilitate the comparison. The comparison between theory and experiment shows excellent agreement in the dependencies of the total loss rates on the magnetic field.

The most striking observation is the resonant enhancement that the rate coefficient β shows for both $m_F = 2$ and 3 around 35 G. The calculations show that the resonance is caused by opening up the possibility for the exchange process. Once energetically allowed, it contributes to 80% of all the inelastic atom-molecule collisions. Within the theoretical model the results for $m_F = 2$ (not shown in Fig. 3.2) are exactly the same as for $m_F = 3$, but simply shifted in magnetic field by 1.3 G because of the slight difference in AB binding energy.

A "smoking gun" for the exchange process is the appearance of atoms in state A. They show up as a reaction product and remain in the trap because of the small energy release. In a second set of experiments, we measure the number of A_2 molecules and A atoms in a small magnetic field range around 35 G after holding the A_2+B mixtures for $m_F = 2$ and 3 for a fixed storage time. The results are shown in Figs. 3.3(a) and 3.3(b), for the fraction of remaining A_2 molecules and A atoms, respectively. We indeed observe the onset of the appearance of A atoms around 35 G, providing clear evidence for the exchange process. Most of lost A_2 molecules are accompanied by the appearance of A atoms, indicating that the molecular loss is dominated by the exchange process. The curves in Figs. 3.3(a) and 3.3(b) are obtained from the theoretical total loss and exchange rates, respectively. The number of A atoms is consistent with the calculations[1].

The observation of A atoms implies that also AB molecules are produced.

[1] We attribute the small amount of A atoms present at lower magnetic field values to the imperfect MW transfer. However, because the MW transfer is done at a fixed magnetic field value, the number of non-transferred A atoms is independent of the magnetic field at which the measurement is performed. Therefore we expect a constant background, which is added to the theoretical results to obtain the curves of Fig. 3.3(b).

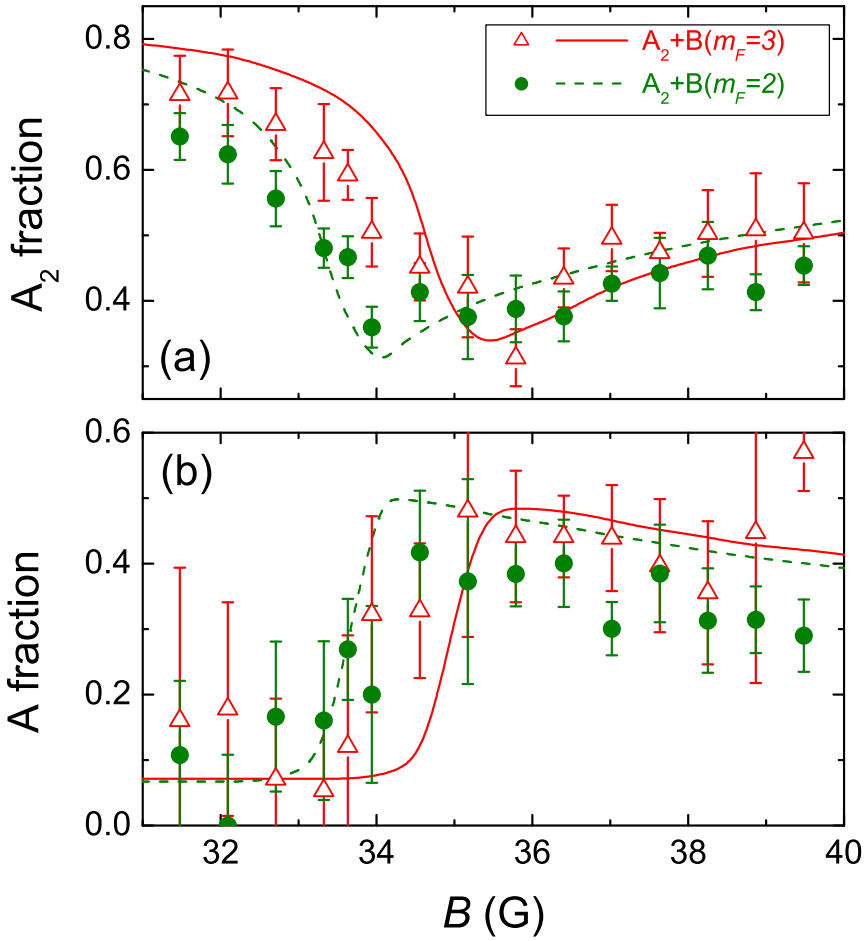

Figure 3.3.: Measurement of the fraction of A_2 molecules (a) and A atoms (b), after a fixed storage time of 22 ms of the B+A_2 mixtures at a temperature of 100(10) nK. The fractions are defined as the A_2 molecule and A atom number normalized to the initial A_2 molecule number (about 4000). The data points are averaged over three to five measurement runs and the error bars represent the statistical uncertainty. The lines are obtained from the rate equations using the theoretical results for the total loss rates (a) and exchange rates (b), as shown in Fig. 3.2.

However, we cannot observe trapped AB molecules because of the absence of Feshbach resonances in the present magnetic field region to dissociate the AB molecules [Jul08]. Furthermore, the AB molecule is expected to very rapidly decay via spin relaxation [Mar07a].

A remarkable finding is the dominance of the exchange process over inelastic decay to more deeply bound states. This can be explained by the fact that the exchange process takes place in a regime where the relevant two-body scattering lengths are very large and the dimer A_2 and AB are in the quantum halo regime [Bra06]. The relevant scattering lengths are shown in Fig. 3.4; they are all in the universal regime for $B > 20$ G. Near and above the magnetic fields at

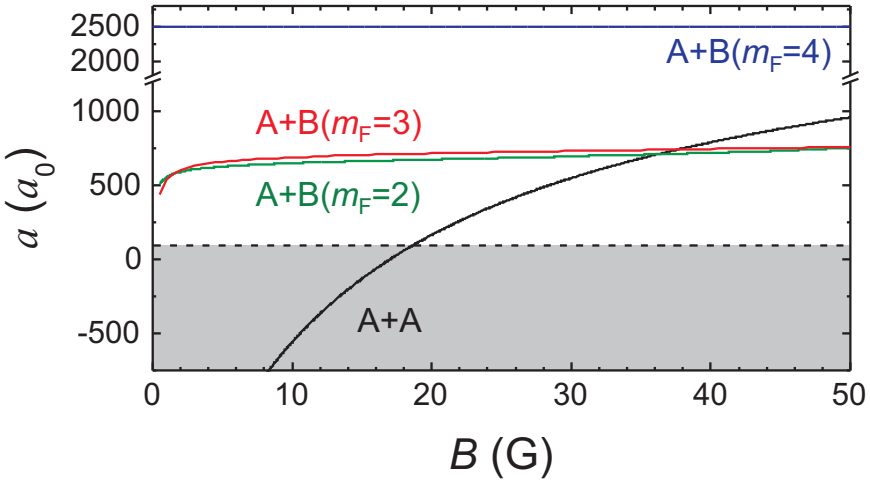

Figure 3.4.: Magnetic field dependence of the two-body scattering lengths for the A+A and the three A+B channels, in units of the Bohr radius a_0. The non-shaded region represents the universal regime, which for Cs is realized for $a \gg 100a_0$ [Köh06b]. Narrow Feshbach resonances resulting from higher partial waves are neglected here.

which the A_2+B and A+AB channels cross, the dominance of the exchange process can be attributed to the large wavefunction overlap between these two channels resulting from the large and similar extent of the A_2 and AB states. That is in contrast to the small overlap between the A_2+B channel to more deeply bound channels because of the small extent of the deeply bound states. In our calculations we were able to verify that, when the channel crossing occurs at small scattering lengths, all processes have the same importance and the exchange process is not favored.

Our theoretical analysis also indicates that for large scattering lengths the exchange process occurs predominantly when all three atoms are within distances comparable to the scattering lengths and, therefore, none of the atoms "see" the short-range details of the interatomic interactions. In contrast, atom-molecule collisions that populate more deeply bound states require all three atoms to approach to short distances. Therefore, our theoretical findings suggest that the dominance of the exchange process is a consequence of the universal regime of halo dimers. In fact, the nearly equal experimental rates for the $m_F = 2$ and $m_F = 3$ cases are consistent with our expectation that, near the channel crossing, the main collisional behavior depends only on the scattering lengths. Therefore we also expect atom exchange to be the dominant process in heteronuclear systems when both the heteronuclear and one of the homonuclear scattering lengths are large and positive. The possible high efficiency of atom exchange for halo molecules was already pointed out long time ago [Stw78, Stw04].

Finally we turn to our observations for the $m_F = 4$ case (see Fig. 3.2). Here we observe no resonance, but instead very small loss rates for $B > 20\,\mathrm{G}$. We find that this is well reproduced by the model calculations. Although the A_2+B and

A+AB channels do not cross on the present range of magnetic fields, the fact that both scattering lengths are large does affect the collisional behavior. In our numerical calculations we find a strong coupling between between the A_2+B and A+AB channels at interatomic separations comparable to the A+A scattering length. Such a coupling manifests itself in the appearance of a repulsive barrier in both channels, leading to the observed suppression of A_2+B collisions [D'I09a].

To summarize, we have observed an exchange process in an optically trapped ultracold sample of atoms and Feshbach molecules. In a mixture of A_2 molecules and B atoms, where A and B are two hyperfine sublevels of Cs, we observe the appearance of free atoms in state A once the exchange process is magnetically tuned to be exoergic. This lead to a resonant enhancement near threshold. In contrast to relaxation to more deeply bound molecular states, the exchange process does not lead to trap loss. The magnetic field dependence of the measured total inelastic collision and exchange rates are in excellent agreement with model calculations. The high efficiency of the exchange process is explained by the halo character of both the initial and final molecular states.

Our observation represents an elementary example for the possibility to control a reaction that involves ultracold molecules. Since field-dependent resonance and threshold phenomena are ubiquitous in molecular gases, we expect that similar possibilities will arise in many situations and offer intriguing possibilities in the developing field of ultracold molecular quantum gases and controlled ultracold chemistry.

We thank P. S. Julienne for helpful discussions and providing us the scattering length calculations. We acknowledge support by the Austrian Science Fund (FWF) within SFB 15 (project part 16). S. K. was supported within the Marie Curie Intra-European Program of the European Commission. F. F. was supported within the Lise Meitner program of the FWF. J. P. D. and B. D. E. acknowledge support from U. S. NSF.

CHAPTER 4

PUBLICATION

Universality of the three-body parameter for Efimov states in ultracold cesium[†]

Phys. Rev. Lett. 107, 120401 (2011)

M. Berninger,[1] A. Zenesini,[1] B. Huang,[1] W. Harm,[1] H.-C. Nägerl,[1]
F. Ferlaino,[1] R. Grimm,[1,2] P. S. Julienne,[3] and J. M. Hutson[4]

[1]*Institut für Experimentalphysik und Zentrum für Quantenphysik, Universität Innsbruck, 6020 Innsbruck, Austria*

[2]*Institut für Quantenoptik und Quanteninformation, Österreichische Akademie der Wissenschaften, 6020 Innsbruck, Austria*

[3]*Joint Quantum Institute, NIST and the University of Maryland, Gaithersburg, Maryland 20899-8423, USA*

[4]*Department of Chemistry, Durham University, South Road, Durham, DH1 3LE, United Kingdom*

We report on the observation of triatomic Efimov resonances in an ultracold gas of cesium atoms. Exploiting the wide tunability of interactions resulting from three broad Feshbach resonances in the same spin channel, we measure magnetic-field dependent three-body recombination loss. The positions of the loss resonances yield corresponding values for the three-body parameter, which in universal few-body physics is required to describe three-body phenomena and in particular to fix the spectrum of Efimov states. Our observations show a robust universal behavior with a three-body parameter that stays essentially constant.

[†]The author of the present thesis made essential contributions to deriving the concept of the experiment. In particular, he constructed and implemented the magnetic field system capable of reaching magnetic field strengths exceeding 1400 G. In this he was supported by W.H. and A.Z. The author of the present thesis recorded the data and performed the analysis together with A.Z. and B.H.. A.Z. and B.H. made important contributions to the improvement of the experimental setup. J.M.H. and P.S.J. derived the magnetic field dependence of the scattering length via a coupled-channel calculation based on experimentally obtained data.

The concept of universality manifests itself in the fact that different physical systems can exhibit basically the same behavior, even if the relevant energy and length scales differ by many orders of magnitude [Bra06]. Universality thus allows us to understand in the same theoretical framework physical situations that at first glance seem completely different. In ultracold atomic collisions, the universal regime is realized when the s-wave scattering length a, characterizing the two-body interaction in the zero-energy limit, is much larger than the characteristic range of the interaction potential. Then the essential properties of the two-body system such as the binding energy of the most weakly bound dimer state and the dominating part of the two-body wave function can simply be described in terms of a, independent of any other system-dependent parameters. In the three-body sector, the description of a universal system requires an additional parameter, which incorporates all relevant short-range interactions not already included in a. In few-body physics, this important quantity is commonly referred to as the three-body parameter (3BP).

In Efimov's famous scenario [Efi70, Bra06], the infinite ladder of three-body bound states follows a discrete scaling invariance, which determines the relative energy spectrum of the states. The 3BP fixes the starting point of the ladder and thus the absolute energies of all states. The parameter enters the theoretical description as a short-range boundary condition for the three-body wave function in real space or as a high-frequency cut-off in momentum space. To determine the 3BP from theory would require precise knowledge of both the two-body interactions and the genuine three-body interactions at short range. In real systems, this is extremely difficult and the 3BP needs to be determined experimentally through the observation of few-body features such as Efimov resonances.

In the last few years, ultracold atomic systems have opened up the possibility to explore Efimov's scenario experimentally and to test further predictions of universal theory [Kra06b, Kno09, Zac09, Pol09a, Gro09, Huc09, Ott08, Wil09, Bar09, Gro10, Lom10a, Nak10]. The key ingredient of such experiments is the possibility to control a by an external magnetic field B via the Feshbach resonance phenomenon [Chi10]. This naturally leads to the important question whether the 3BP remains constant or whether it is affected by the magnetic tuning, in particular when different Feshbach resonances are involved.

The current status of theoretical and experimental research does not provide a conclusive picture on possible variations of the 3BP. A theoretical study [D'I09c] points to strong possible variations when different two-body resonances are exploited in the same system, and even suggests a change of the 3BP on the two sides of a zero crossing of the scattering length. Other theoretical papers point to the importance of the particular character of the Feshbach resonance [Chi10]. While closed-channel dominated ("narrow") resonances involve an additional length scale that may fix the 3BP [Pet04a, Mas08, Wan11a], the case of entrance-channel dominated ("broad") resonances leaves the 3BP in principle open. However, predictions based on two-body scattering properties exist that apparently fix the 3BP for broad resonances as well [Lee07, JL10, Nai11]. The

available experimental observations provide only fragmentary information. The first observation of Efimov physics in an ultracold Cs gas [Kra06b] is consistent with the assumption of a constant 3BP on both sides of a zero crossing. A later observation on ^{39}K [Zac09] indicated different values of the 3BP on both sides of a Feshbach resonance. A similar conclusion was drawn from experiments on ^{7}Li [Pol09a], but other experiments on ^{7}Li showed universal behavior with a constant 3BP for the whole tuning range of a single resonance [Gro09] and for another spin channel [Gro10]. Besides these observations on bosonic systems, experiments on fermionic gases of ^{6}Li [Ott08, Huc09, Wil09] can be interpreted based on a constant 3BP [Wen09]. A recent experiment on ^{6}Li, however, indicates small variations of the 3BP [Nak11].

In the present work, we investigate universality in an ultracold gas of Cs atoms, which offers several broad Feshbach resonances in the same spin channel and thus offers unique possibilities to test for variations of the 3BP. In the lowest hyperfine and Zeeman sublevel $|F=3, m_F=3\rangle$, Cs features a variety of broad and narrow Feshbach resonances in combination with a large background scattering length [Chi04b]. Of particular interest are three broad s-wave Feshbach resonances in the range up to 1000 G [1], with poles near -10 G, 550 G, and 800 G [Chi04b, Lee07, Chi10]. The character of these three resonances is strongly entrance-channel dominated, as highlighted by the large values of their resonance strength parameter s_{res} [Chi10] of 560, 170, and 1470, respectively. The resulting magnetic-field dependence $a(B)$ is illustrated in Fig. 4.1. In our previous work [Kra06b, Kno09] we have focussed on the low-field region up to 150 G. After a major technical upgrade of our coil set-up, we are now in the position to apply magnetic fields B of up to 1.4 kG with precise control down to the 20 mG uncertainty level and thus to explore the resonance regions at 550 G and 800 G [2].

Our ultracold sample consists of about 2×10^4 optically trapped ^{133}Cs atoms, close to quantum degeneracy. The preparation is based on an all-optical cooling approach as presented in Refs. [Kra04, Mar07a]. The final stage of evaporative cooling is performed in a crossed-beam dipole trap (laser wavelength 1064 nm) and stopped shortly before Bose-Einstein condensation is reached. Finally, the trap is adiabatically recompressed to twice the initial potential depth to suppress further evaporation loss. At this point, the mean trap frequency is about 10 Hz and the temperature is typically 15 nK.

Our experimental observable is the three-body loss coefficient L_3, which in the framework of universal theory is conveniently expressed as $L_3 = 3C(a)\frac{\hbar a^4}{m}$ [Web03c], where m denotes the atomic mass. The expression separates a log-periodic function $C(a)$ from the general a^4-scaling of three-body loss. For $a<0$, effective field theory [Bra06] provides the analytic expression

$$C(a) = 4590\,\frac{\sinh(2\eta_-)}{\sin^2[s_0\ln(a/a_-)]+\sinh^2\eta_-}, \tag{4.1}$$

[1] Units of gauss instead of the SI unit tesla (1 G $= 10^{-4}$ T) are used to conform to conventional usage in this field.

[2] The upgrade of the magnetic field system is described in detail in Appendix B.

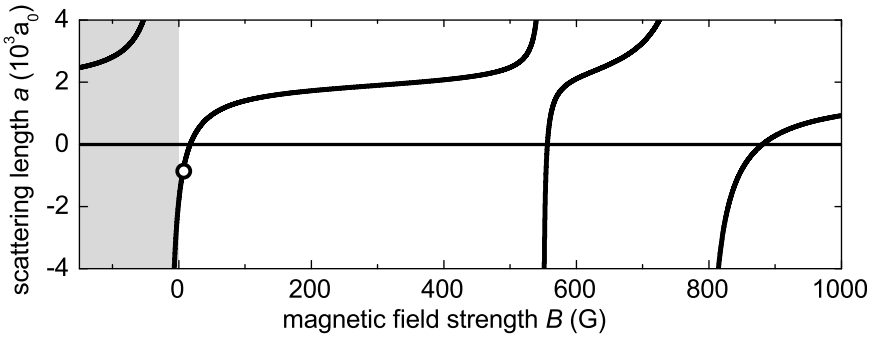

Figure 4.1.: Illustration of the three broad s-wave Feshbach resonances for Cs in the absolute atomic ground state $|F=3, m_F=3\rangle$. The open circle corresponds to the previous observation of a triatomic Efimov resonance at 7.6 G [Kra06b]. The many narrow Feshbach resonances resulting from d- and g-wave molecular states [Chi04b] are not shown for the sake of clarity. The region with $B < 0$ corresponds to the state $|F=3, m_F=-3\rangle$, which is not stable against two-body decay. Scattering lengths are given in units of Bohr's radius a_0.

with $s_0 \approx 1.00624$ for identical bosons. The decay parameter η_- is a non-universal quantity that depends on the deeply-bound molecular spectrum [Wen09]. The scattering length a_- marks the situation where an Efimov state intersects the three-atom threshold and the resulting triatomic Efimov resonance leads to a giant three-body loss feature. In the following, the quantity a_- will serve us as the representation of the 3BP.

To measure L_3 we record the time evolution of the atom number after quickly (within 10 ms) ramping B from the evaporation to the target field strength. We determine the atom number N by absorption imaging. One-body decay, as caused by background collisions, is negligible under our experimental conditions. Furthermore, two-body decay is energetically suppressed in the atomic state used. We can therefore model the decay by $\dot{N}/N = -L_3\langle n^2\rangle$, where the brackets denote the spatial average weighted with the atomic density distribution n. Additional, weaker loss contributions caused by four-body recombination [Fer09a] can be described in terms of an effective L_3 [Ste09]. For fitting the decay curves and extracting L_3 we use an analytic expression that takes into account the density decrease resulting from anti-evaporation heating [Web03c].

The experimental results are a function of B whereas theory expresses L_3 as a function of a. It is thus crucial to have a reliable conversion function $a(B)$. We have obtained $a(B)$ from full coupled-channel calculations on a Cs-Cs potential obtained by least-squares fitting to extensive new measurements of binding energies, obtained by magnetic-field modulation spectroscopy [Lan09b], together with additional measurements of loss maxima and minima that occur at resonance poles and zero crossings. The new potential provides a much improved representation of the bound states and scattering across the whole range from low field to 1000 G. The experimental results and the procedures used to fit them will be described in a separate publication.

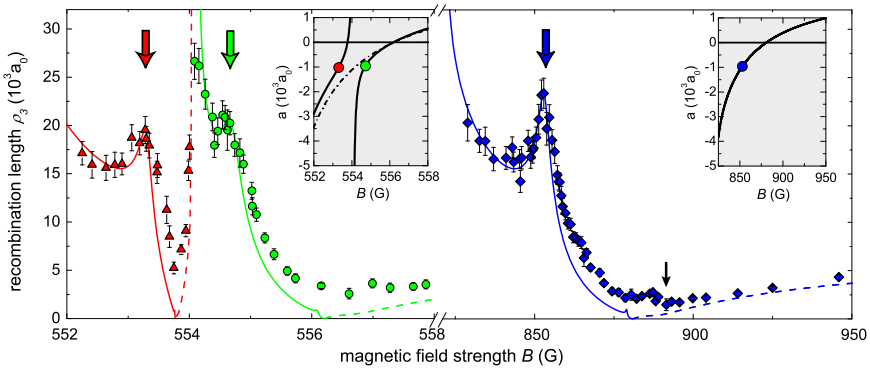

Figure 4.2.: Recombination loss in the vicinity of the high-field Feshbach resonances. The measured recombination length ρ_3 is shown for three different regions (▲, 552 G $< B <$ 554 G; ●, 554 G $< B <$ 558 G; ♦, 830 G $< B <$ 950 G), which are separated by the poles of different Feshbach resonances. The error bars indicate the statistical uncertainties. For all three regions, the solid lines represent independent fits to the data at negative a. The dashed lines show the predictions of effective field theory for $a > 0$ [Bra06], using the parameters obtained in the same region at $a < 0$. The insets show $a(B)$ (solid line, full calculation; dash-dot line, s-wave states only). The arrows in the main figure and the corresponding dots in the insets refer to the triatomic Efimov resonances. The small arrow indicates a recombination minimum.

Figure 4.2 shows our experimental results on the magnetic-field dependent recombination loss near the two broad high-field Feshbach resonances (550 G and 800 G regions). For convenience we plot our data in terms of the recombination length $\rho_3 = (2mL_3/(\sqrt{3}\hbar))^{1/4}$ [Esr99]. The three filled arrows indicate three observed loss resonances that do not coincide with the poles of two-body resonances. We interpret these three features as triatomic Efimov resonances.

In the 800 G region, a single loss resonance shows up at 853 G, which lies in the region of large negative values of a. We fit the L_3 data based on Eq. (4.1) [3] and using the conversion function $a(B)$ described above. The fit generally reproduces the experimental data well, apart from a small background loss that apparently does not result from three-body recombination[4]. For the 3BP the fit yields the resonance position of $a_- = -955(28)\, a_0$, where the given error includes all statistical errors. For the decay parameter the fit gives $\eta_- = 0.08(1)$.

For the 550 G region, Fig. 4.1 suggests a qualitatively similar behavior as found in the 800 G region. The experimental data, however, reveal a more complicated structure with three loss maxima and a pronounced minimum. This behavior is explained by a g-wave resonance (not shown in Fig. 4.1) that overlaps with the broader s-wave resonance. We have thoroughly investigated this region

[3] The fits include an additional free scaling factor λ to account for possible systematic errors in the number density. For the 800 G region, we obtain $\lambda = 0.89$. For the lower and upper 550 G region, we obtain $\lambda = 0.46$ and $\lambda = 1.06$, respectively.

[4] The smallest values obtained for ρ_3 correspond to one-body lifetimes exceeding 100 s.

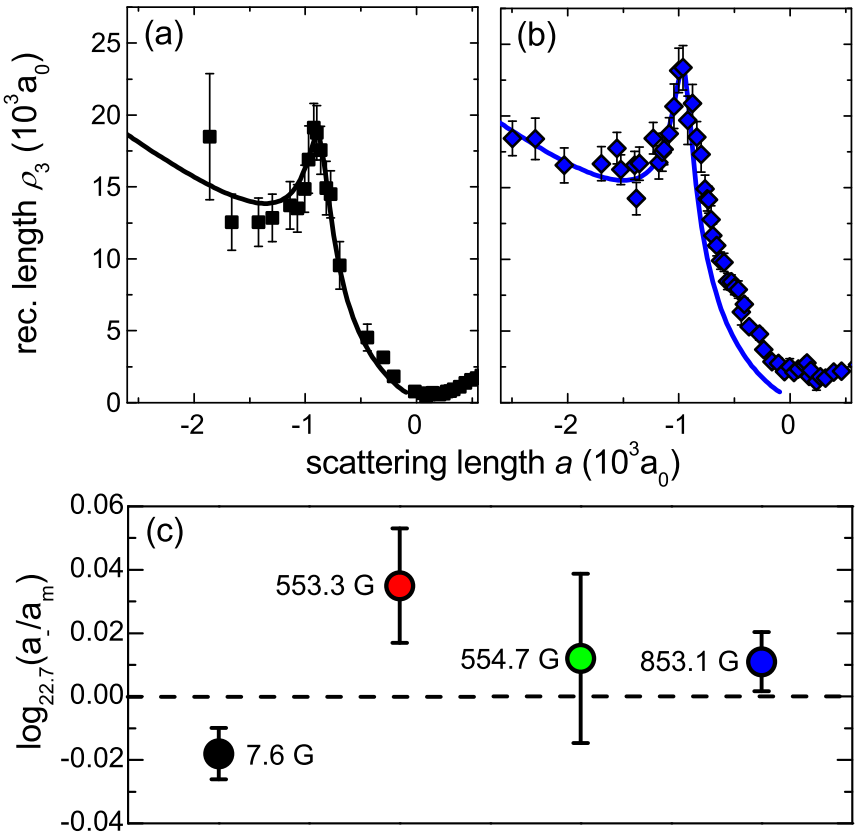

Figure 4.3.: Efimov resonances and the 3BP. In (a) and (b), we compare the resonance previously observed [Kra06b] at 7.6 G to the one found at 853 G. In (c), we plot the 3BPs obtained for all four resonances measured in Cs. The dashed line corresponds to a mean value of $a_m = -921\,a_0$, calculated as a weighted average of the four different values. The logarithmic scale (to the basis of 22.7) covers one tenth of the Efimov period.

by Feshbach spectroscopy. These studies clearly identify the central maximum (554.06 G) and the deep minimum (553.73 G) as the pole and zero crossing of the g-wave resonance (see inset). With $s_{\rm res} = 0.9$, this resonance is an intermediate case between closed-channel and entrance-channel dominated.

The g-wave resonance causes a splitting that produces two Efimov resonances instead of one in this region. This explains the upper and the lower loss maxima, which are found at 553.30(4) G and 554.71(6) G (arrows in Fig. 4.2). To determine the parameters of these Efimov resonances, we independently fit the two relevant regions of negative scattering length using Eq. (4.1) [5]. This yields $a_- = -1029(58)\,a_0$ and $-957(80)\,a_0$ for the lower and the upper resonances, respectively.

[5] The fits include an additional free scaling factor λ to account for possible systematic errors in the number density. For the 800 G region, we obtain $\lambda = 0.89$. For the lower and upper 550 G region, we obtain $\lambda = 0.46$ and $\lambda = 1.06$, respectively.

$B_{\rm res}$ (G)	a_-/a_0	δ_1/a_0	δ_2/a_0	δ_3/a_0	η_-
7.56(17)	−872(22)	21	3	6	0.10(3)
553.30(4)	−1029(58)	43	28	27	0.12(1)
554.71(6)	−957(80)	57	25	49	0.19(2)
853.07(56)	−955(28)	27	1	4	0.08(1)

Table 4.1.: Parameters of the four triatomic Efimov resonances. The first and second column give the magnetic field values $B_{\rm res}$ at the resonance centers and the corresponding 3BPs together with their full statistical uncertainties. The individual error contributions δ_1, δ_2, and δ_3 refer to the statistical uncertainties from the fit to the L_3 data, from the determination of the magnetic field strength, and from the $a(B)$-conversion, respectively.

We now compare all our observations on triatomic Efimov resonances in Cs. We also include the previous data of Ref. [Kra06b] on the low-field resonance (7.6 G), which we have refitted using our improved $a(B)$ conversion. The relevant parameters for the four observed Efimov resonances are given in Table 4.1. Figures 4.3(a) and 4.3(b) show the recombination data for the low-field resonance and the 853 G resonance, using a convenient $\rho_3(a)$ representation. This comparison illustrates the striking similarity between both cases. For all four Efimov resonances, Fig. 4.3(c) shows the 3BP on a logarithmic scale, which relates our results to the universal scaling factor 22.7. Note that the full scale is only one tenth of the Efimov period, i.e. a factor $22.7^{\frac{1}{10}} \approx 1.37$. The error bars indicate the corresponding uncertainties (1 standard deviation), resulting from all statistical uncertainties [6]. The data points somewhat scatter around an average value of about $-921\,a_0$ (dashed line) with small deviations that stay within a few percent of the Efimov period. Taking the uncertainties into account, our data are consistent with a constant 3BP for all four resonances. However, between the values determined for the two broad resonances at 7.6 and 853 G we find a possible small aberration of about 2.5 standard deviations. This may be accidental but it may also hint at a small change in the 3BP.

Let us briefly discuss our findings on further few-body observables. For $a > 0$, three-body recombination minima are well known features related to Efimov physics [Bra06, Kra04, Zac09, Pol09a]. In the 800 G region, we observe a minimum at $B = 893(1)$ G (small arrow in Fig. 4.2), corresponding to $a = +270(30)\,a_0$, which is very similar to the minimum previously observed in the low-field region [Kra04] and consistent with a universal connection to the $a < 0$ side. In general, however, these minima are difficult to access in Cs and dedicated experiments will be needed to provide stringent tests also for the $a > 0$ side. Also atom-dimer resonances [Kno09, Zac09, Pol09a] have not yet been ob-

[6] Systematic uncertainties are not included in our error budget. They may result from model-dependent errors in the determination of the scattering length from binding energy and scattering data and from finite-temperature shifts. All these errors, however, stay well below the statistical uncertainties.

served in the high-field region. Additional measurements in the 800 G region (not shown) reveal a pair of four-body resonances at 865.4(5) G and 855.0(2) G, corresponding to scattering lengths of $-444(8)\,a_0$ and $-862(9)\,a_0$. This excellently fits to universal relations [Ste09] and our previous observations at low magnetic fields [Fer09a].

Our observations show that universality persists in a wide magnetic-field range across a series of Feshbach resonances in the same spin channel and that the 3BP shows only minor variations, if any. This rules out a scenario of large variations as suggested by the model calculations of Ref. [D'I09c]. The apparent fact that the relevant short-range physics is not substantially affected by the magnetic field may be connected to the strongly entrance-channel dominated character [Chi10] of the broad resonances in Cs. However, even the case of overlapping s- and g-wave Feshbach resonances, where the latter one has intermediate character, is found to exhibit universal behavior consistent with an essentially constant 3BP. Our observation that universality is robust against passing through many poles and zero crossings of the scattering length also implies a strong argument in favor of a universal connection of both sides of a single Feshbach resonance. This supports conclusions from experiments on ^{7}Li as reported in Refs. [Gro09, Gro10], in contrast to Ref. [Pol09a] and related work on ^{39}K [Zac09].

With the present experimental data there is growing experimental evidence that theories based on low-energy two-body scattering and the near-threshold dimer states [Lee07, JL10, Nai11] can provide reasonable predictions for the 3BP without invoking genuine short-range three-body forces, which are known to be substantial for all the alkali metal trimers [Sol03]. We also stress a remarkable similarity [Gro09] between the Cs data and experimental results on both Li isotopes. When the 3BP is normalized to the mean scattering length $\bar{a}$ of the van der Waals potential [Chi10], our actual Cs value $a_-/\bar{a} = -9.5(4)$ is remarkably close to corresponding values for ^{7}Li [Gro10, Pol09a] and ^{6}Li [Ott08, Huc09, Wil09, Wen09], which vary in the range between -8 and -10.

Universality in tunable atomic quantum gases near Feshbach resonances appears to be rather robust, but the understanding of the particular reasons and conditions remains a challenge to few-body theories.

We thank M. Ueda, T. Mukaiyama, P. Naidon, and S. Jochim for discussions. We acknowledge support by the Austrian Science Fund FWF within project P23106. A.Z. is supported within the Marie Curie Intra-European Program of the European Commission. P.S.J. and J.M.H. acknowledge support from an AFOSR MURI grant.

CHAPTER 5

PUBLICATION

Collisions between tunable halo dimers: exploring an elementary four-body process with identical bosons[†]

Phys. Rev. Lett. **101**, 023201 (2008)

F. Ferlaino,[1] S. Knoop,[1] M. Mark,[1] M. Berninger,[1] H. Schöbel,[1] H.-C. Nägerl,[1] and R. Grimm[1,2]

[1] *Institut für Experimentalphysik und Zentrum für Quantenphysik, Universität Innsbruck, 6020 Innsbruck, Austria*

[2] *Institut für Quantenoptik und Quanteninformation, Österreichische Akademie der Wissenschaften, 6020 Innsbruck, Austria*

We study inelastic collisions in a pure, trapped sample of Feshbach molecules made of bosonic cesium atoms in the quantum halo regime. We measure the relaxation rate coefficient for decay to lower-lying molecular states and study the dependence on scattering length and temperature. We identify a pronounced loss minimum with varying scattering length along with a further suppression of loss with decreasing temperature. Our observations provide insight into the physics of a few-body quantum system that consists of four identical bosons at large values of the two-body scattering length.

Few-body quantum systems in halo states exhibit unique properties [Jen04]. A quantum halo is a very weakly bound state whose wave function extends far into the classically forbidden range. Halo systems are much larger than one would expect from the characteristic interaction range of their constituents.

[†]The primary contribution of the author of the present thesis to this publication was the construction and implementation of an optical dipole trap with adjustable ellipticity, together with M.M. and H.S. He also worked on maintaining the experimental setup. He recorded the data together with F.F. and S.K. F.F. performed the data analysis.

Many examples for halo states are known in nuclear physics, with the deuteron being a prominent example [Bla52]. In molecular physics, the He dimer has for many years served as the prime example of a halo state [Luo93, Sch94].

A particular motivation to study halo states is given by the concept of universality in few-body systems [Bra06]. Since, in a halo state, short-range details of the interaction become irrelevant, the system is described by very few parameters and shows universal behavior in its low-energy observables. A halo dimer is the elementary two-body halo system. Here the only relevant length scale is given by the scattering length a, which describes the s-wave interaction between its two constituents. The size of the halo dimer is directly related to a and the binding energy is $E_b = \hbar^2/(2\mu a^2)$, where μ is the reduced mass. For three-body halo systems, universal Efimov states can exist [Efi70, Kra06b]. Here one additional parameter is required to fully describe the system in the universal limit. A natural further step is to investigate the universal physics of systems composed of four identical bosons. The fundamental properties of such systems are unexplored terrain, with the existence of an additional four-body parameter [Yam06, Ham07b], the scaling and threshold behavior, and the binding energies of four body-states [Ham07b] being open issues.

In the field of ultracold gases, the Feshbach association technique [Köh06b] has provided experimentalists with unprecedented possibilities to create and study halo dimers. In the case of certain Feshbach resonances, a considerable range of universality exists, where halo dimers can be conveniently controlled by a magnetic bias field to vary their binding energy and size. Such *tunable halo dimers* are unique probes to explore quantum phenomena related to universality. A binary collision between two halo dimers can be seen as an *elementary four-body process*. For a special kind of halo dimers such a four-body process has already attracted considerable attention: halo dimers made of fermionic atoms in different spin states allow to create molecular Bose-Einstein condensates and to study the crossover to a fermionic superfluid [Ing08]. Here a key point is the Pauli suppression effect that, in combination with the halo nature of the dimer, leads to stability against decay into lower-lying molecular states and favors elastic processes [Pet04b].

In this Letter, we study binary collisions in a pure, trapped sample of tunable halo dimers made of *bosonic* atoms. Halo dimers of this class have so far received much less experimental attention than their fermionic counterparts, although they represent an important link to universal few-body phenomena in systems of few interacting bosons; for three particles, an early example is the predicted atom-dimer "Efimov" resonances [Efi79]. Halo dimers of bosonic atoms have been realized in ultracold gases of ^{85}Rb and ^{133}Cs [Tho05a, Mar07a] and properties of the individual dimers, like binding energies, magnetic moments, and spontaneous decay rates, have been measured. In contrast, their collision properties have remained unexplored terrain. Because of the absence of a Pauli suppression effect, substantial inelastic decay to lower-lying molecular states can be expected. The observation of loss serves as a probe for dimer-dimer interactions [Jen04, Köh06b].

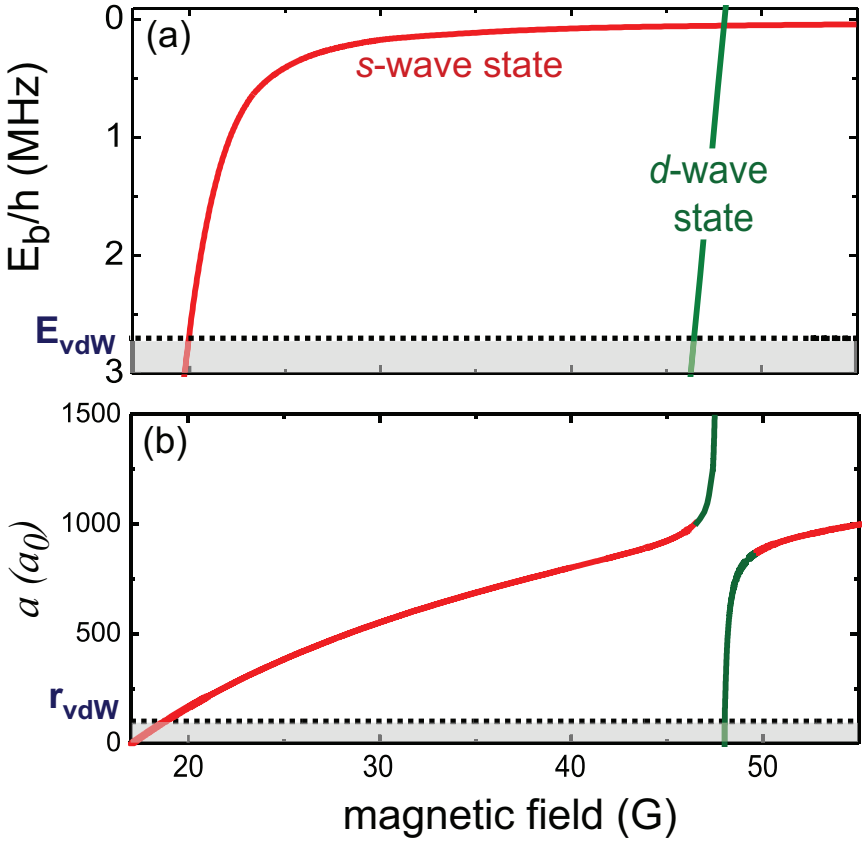

Figure 5.1.: Weakly bound Cs_2 molecular states at low magnetic fields. (a) Binding energies of the relevant Cs_2 dimer states. The zero-energy level is the s-wave threshold of two colliding Cs atoms in their absolute hyperfine ground state sub-level. (b) s-wave scattering length a versus the magnetic field (see text). The shaded regions in (a) and (b) indicate the non-halo regime with $E_b > E_{\mathrm{vdW}}$, and $a < r_{\mathrm{vdW}}$, respectively.

Our experiments are performed with ^{133}Cs atoms, which represent an excellent system to study few-body physics with bosons at large scattering lengths [Kra06b] because of the unique scattering properties [Chi04b]. In the lowest spin state at low magnetic fields, one finds a broad entrance-channel dominated s-wave Feshbach resonance [Web03b, Köh06b] along with an extraordinarily large background scattering length. The scattering properties of ultracold atoms are governed by the last bound s-wave state below the dissociation threshold as displayed in Fig. 5.1. In a wide magnetic-field range, this state carries a quantum halo character, where the two-body scattering length far exceeds the classical interaction range of the van der Waals potential, r_{vdW} ($\approx 100\, a_0$), and the binding energy E_b is much smaller than the corresponding E_{vdW} ($\approx h \times 2.7$ MHz) [1]. Here a_0 is Bohr's radius.

[1] The van der Waals length and energy can be defined as $r_{\mathrm{vdW}} = \frac{1}{2}(mC_6/\hbar^2)^{1/4}$ and $E_{\mathrm{vdW}} = \hbar^2/mr_{\mathrm{vdW}}^2$, respectively [Köh06b].

Our experimental procedure to produce an optically trapped sample of tunable halo dimers involves several stages. We initially prepare ultracold trapped ^{133}Cs atoms in their absolute hyperfine ground state sublevel $|F, m_F\rangle = |3, 3\rangle$, similarly to Ref. [Mar07a]. The atoms are optically trapped by two crossed 1064-nm laser beams with waists of about 250 μm and 36 μm, while a magnetic field levitates the atoms against gravity [Web03b, Her03]. The levitation field ensures an optimized evaporative cooling of the atoms, which is realized by lowering the optical power in the trapping beams. We stop the cooling just before the onset of Bose-Einstein condensation to avoid too high atomic densities. At our lowest temperature of 20 nK, we obtain about 1.5×10^5 non-condensed atoms.

In the next stage, we create the halo dimers by Feshbach association. Here, the application of the levitation field is not appropriate since atoms and dimers in general have different magnetic moments. This leads to special requirements for the trap design. On the one hand, we need a sufficiently high optical gradient in the vertical direction to hold the atoms and dimers against gravity. On the other hand, we want to avoid the high density of a tight trap, which causes fast losses driven by atom-dimer collisions. These two requirements can be simultaneously fulfilled by using an elliptic trap potential with weak horizontal confinement and tight confinement in the vertical direction. Shortly before molecule production, we adiabatically convert the levitated trap to a non-levitated trap by simultaneously changing the levitation field, the optical power, and the trap ellipticity. The latter is modified by a rapid spatial oscillation of the 36-μm waist beam in the horizontal plane with the use of an acousto-optic modulator at a frequency of about 100 kHz, which greatly exceeds the typical trap frequencies, and thus creates a time-averaged optical potential [Mil01, Fri01, Alt07b]. The adiabatic change of the trap shape is set in a way to keep the peak density, the temperature, and thus the phase-space density constant[2]. Right after converting the trap, we associate the halo dimers by sweeping the magnetic field across the 200 mG wide d-wave Feshbach resonance located at approximately 48 G [Mar07a], (see Fig. 5.1).

The molecular temperature can be set by adjusting the temperature of the initial atomic sample. To selectively measure the atomic and molecular temperatures, we spatially separate the two components with the Stern-Gerlach technique, and we perform a subsequent time-of-flight imaging, as described in Refs. [Her03, Mar07a]. In Fig. 5.2(a), we compare the atomic and the molecular temperatures for a wide range of the initial temperatures. In spite of some overall heating in the conversion process, we observe that the dimers and the atoms have the same translational temperature in the trap. This observation may indicate an elastic interaction between atoms and dimers on the 10 ms time scale of our preparation sequence and it allows us to conveniently use the atomic sample to determine the temperature of the molecular gas.

In the last step of the preparation sequence, we selectively remove the atoms from the dipole trap. This is done by using a double-resonant purification

[2]For the lowest temperature samples, the final time-averaged elliptic potential has trap frequencies of 10 Hz and 20 Hz in the horizontal plane, and 80 Hz in the vertical direction.

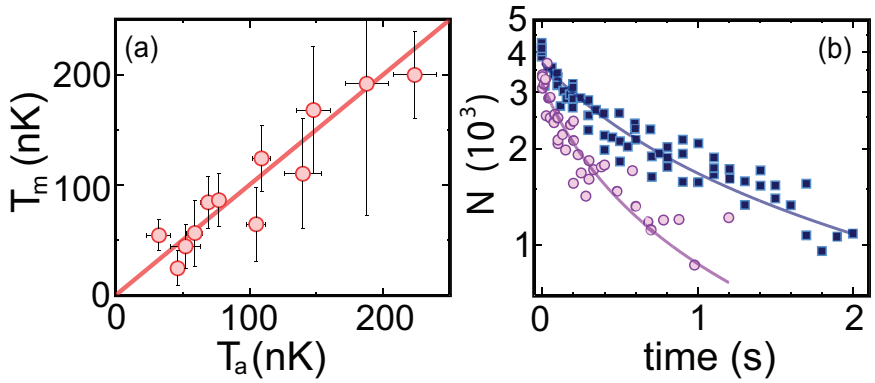

Figure 5.2.: Measurements on the trapped molecular sample. (a) Comparison between the atomic and molecular temperatures T_a and T_m at 35 G, where $E_b \simeq h \times 87$ kHz. The solid line indicates equal temperatures for atoms and molecules. (b) Number of halo dimers N as a function of the holding time in trap at 28.3 G ($a = 500\,a_0$, squares) and at 45.6 G ($a = 900\,a_0$, circles). The solid lines are fits to the data (see text).

scheme, which combines microwave excitation with resonant light[3], similarly to Ref. [Tha06]. By absorption imaging after the Stern-Gerlach technique we verify that no atoms are remaining. We do not observe heating or loss of molecules as induced by the purification sequence.

We then use the pure, trapped sample of tunable halo dimers to study binary collisions. We measure inelastic decay, resulting from the relaxation into more deeply bound states. In such a process the conversion of internal into kinetic energy by far exceeds the trap depth and leads to immediate trap loss of all particles involved. All our experiments are carried out in a regime of very low temperatures ($k_B T \ll E_b$), where the initial kinetic energy of the colliding dimers is not sufficient to break up the molecules, as observed for ^{6}Li halo dimers in Ref. [Joc03b]. Moreover, spontaneous dissociation observed for ^{85}Rb halo dimers [Tho05a, Köh05] is not possible as there is no energetically open channel. Other density-independent losses, such as background collisions or light-induced losses, can also be neglected under our experimental conditions. We can therefore completely attribute the observed losses to inelastic dimer-dimer collisions. The decay of the trapped dimer sample is thus described by the usual rate equation $\dot{N} = -\alpha_{rel}\bar{n}N$. Here N indicates the number of dimers and α_{rel} the relaxation rate coefficient. The mean molecular density $\bar{n}$ is given by $\bar{n} = [m\bar{\omega}^2/(2\pi k_B T)]^{3/2} N$ with m being the atomic mass and $\bar{\omega}$ denoting the geometric mean of the trap frequencies.

We measure α_{rel} as a function of the scattering length a for a fixed temperature $T = 120$ nK. We ramp the magnetic field to a desired value, and we then perform

[3]The microwave drives the $|3,3\rangle \rightarrow |4,4\rangle$ hyperfine transition, while the resonant light pulse drives the closed optical transition $|4,4\rangle \rightarrow |5,5\rangle$, which pushes the atoms out of the optical trap. The purification is performed at a magnetic field of 35 G.

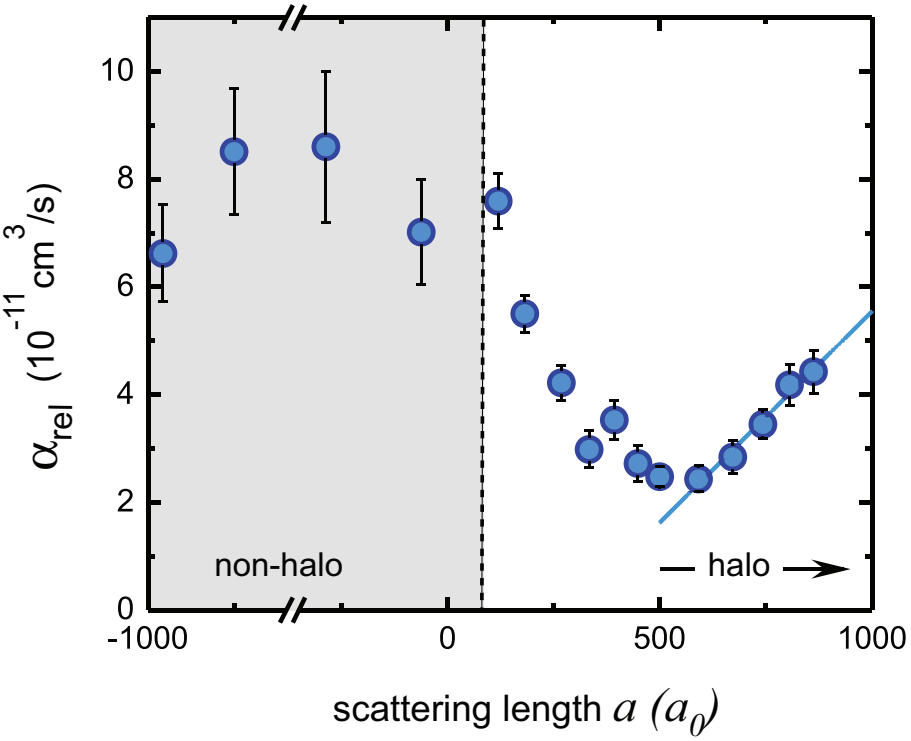

Figure 5.3.: Scattering length dependence of the relaxation rate coefficient α_{rel} at 120 nK. The solid line is a linear fit to the data in the region $a \geq 500\,a_0$ (see text). The error bars refer to the statistical uncertainty. The shaded region indicates the $a < r_{\mathrm{vdW}}$ regime; here the experimental uncertainties are larger because the molecules have to be transferred through several avoided crossings with higher partial-wave states [Mar07a].

a lifetime measurement on the trapped dimers for storing times up to 2 s. As an example, the time evolution of the dimer number in the optical trap is shown in Fig. 5.2(b) at two different values of the magnetic field. We observe the expected non-exponential decay of the dimer number. We extract the value of α_{rel} by fitting the data with the above rate equation. The lifetime measurements are then repeated at different values of the magnetic field in a range from 7 G to 50 G.

The observed dependence of the relaxation rate coefficient on the scattering length reveals an interesting behavior; see Fig. 5.3. Non-halo dimers exhibit a relative large and essentially constant collisional rate coefficient. In contrast, when the dimers enter the halo regime with increasing scattering length ($a > r_{\mathrm{vdW}}$), the rate coefficient first drops to a minimum. The minimum is found at $a \approx 500\,a_0$ ($\sim 5\,r_{\mathrm{vdW}}$). For larger values of a, the rate coefficient increases with a. General considerations [Bra04, D'I05b, Pet08] suggest to first approximation a universal linear scaling law for α_{rel} according to $\alpha_{\mathrm{rel}} = C(\hbar/m)a$ with a dimensionless constant C. From a linear fit for $a > 500\,a_0$ (solid line) we obtain an estimate for C of about 3.

An essentially constant relaxation rate coefficient for varying binding energy

or magnetic field has been previously measured in collisions between non-halo dimers. Class of the non-halo dimers includes $^{23}Na_2$ [Muk04], $^{87}Rb_2$ [Sya06], $^{133}Cs_2$ in various molecular states [Chi05b, Kno08], and also $^6Li_2$ p-wave molecules as a process involving four identical fermions [Ina08]. Our halo dimers composed of bosonic atoms thus show a novel and qualitatively different behavior.

In a second set of experiments, we study the temperature dependence of the relaxation rate coefficient. In the ultracold domain, inelastic two-body collision processes are usually described in terms of a simple rate constant, i.e. a rate coefficient being independent of the particular collision energy. This applies to the case of inelastic atom-atom collisions [Lan65], as well as to collisions between deeply bound dimers [Lee06, Qué08]. In contrast to this usual behavior, we find a strong temperature dependence of the loss rate coefficient of halo dimers, so that a simple rate constant model does not apply.

We have focused our measurements on the temperature-dependence in three different cases: the non-halo regime (120 a_0), the loss minimum in the halo regime (500 a_0), and a more extreme halo case with increased loss (800 a_0). As shown in Fig. 5.4, the dimers exhibit the expected constant relaxation rate outside of the halo regime ($\approx 9 \times 10^{-11}$ cm^3/s). In the halo regime, we observe a clear decrease of the relaxation rate with decreasing temperature, both at 500 a_0 and 800 a_0, roughly following a $\sqrt{T}$-dependence. This surprising behavior raises the question whether the temperature-dependence of the relaxation rate is a property unique to halo states or whether it can also occur for other weakly bound Feshbach molecules. In the latter case, a halo dimer may just be seen as an extreme case of a weakly bound dimer. We speculate that this observation is related to the fact that collisions between weakly bound dimers can involve more complex processes which go beyond simple two-body mechanisms. For instance, the release of binding energy may lead to a fragmentation with three particles in the exit channel, i.e. a more deeply bound molecule and two free atoms. Breakup thresholds may manifest themselves in a more complicated dependence on the collision energy.

The possibility to suppress inelastic loss by controlling temperature and magnetic field leads to a favorable situation, in which halo dimers exhibit a high degree of stability. In particular, at 40 nK and 500 a_0, we measure a loss rate coefficient as low as $\sim 7 \times 10^{-12}$ cm^3/s. This unusually small value corresponds to an order of magnitude improvement in the stability against collisional decay with respect to previously investigated cases of $^{23}Na_2$ [Muk04] and $^{87}Rb_2$ [Sya06].

To conclude, we have studied inelastic collisions between tunable halo dimers composed of bosonic atoms. We have observed a pronounced scattering length dependence, with a minimum in the loss coefficient as a most striking feature. We have also found that inelastic loss is further suppressed by decreasing the temperature. The existence of the minimum raises the question whether this feature can be understood in terms of universal four-body physics, similar to a minimum in three-body recombination at large positive scattering length [Esr99, Nie99, Bra06, Kra06b], which results from the destructive interference of two

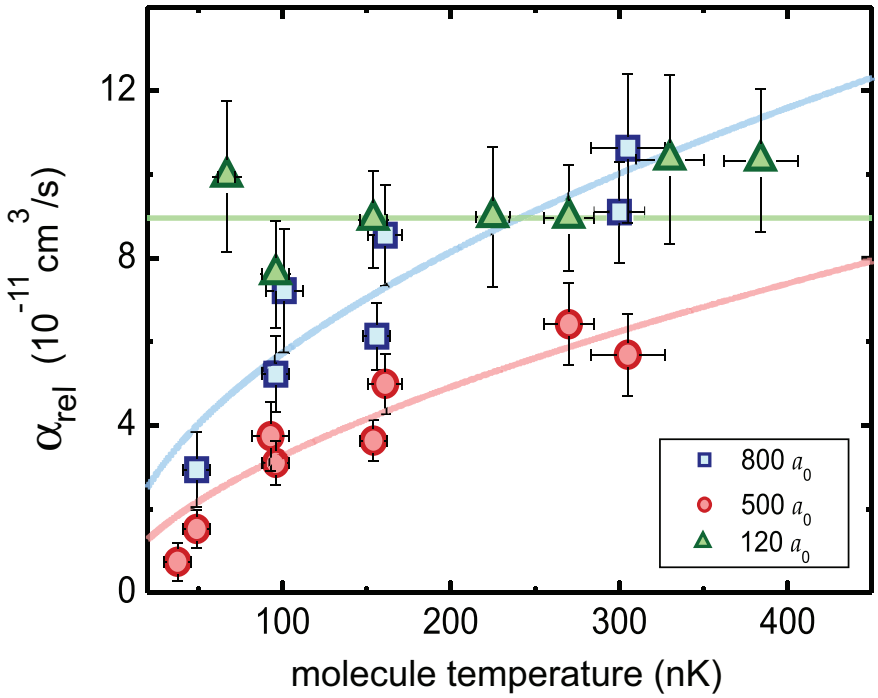

Figure 5.4.: Temperature dependence of the relaxation rate coefficient α_{rel} at 120 a_0 (triangles), 500 a_0 (squares), and 800 a_0 (circles). The solid lines are introduced as guides to the eye.

decay channels. The slow inelastic decay near the minimum may provide us with a favorable situation to study elastic dimer-dimer interactions or to search for universal four-body bound states [Ham07b].

We thank B. Esry, M. Baranov, D. Petrov, G. Shlyapnikov, and T. Köhler for fruitful discussions. We acknowledge support by the Austrian Science Fund (FWF) within SFB 15 (project part 16). S. K. is supported within the Marie Curie Intra-European Program of the European Commission. F. F. is supported within the Lise Meitner program of the FWF.

CHAPTER 6

PUBLICATION

Evidence for universal four-body states tied to an Efimov trimer[†]

Phys. Rev. Lett. **102**, 140401 (2009)

F. Ferlaino,[1] S. Knoop,[1] M. Berninger,[1] W. Harm,[1] J. P. D'Incao,[2,3]
H.-C. Nägerl,[1] and R. Grimm[1,2]

[1]*Institut für Experimentalphysik und Zentrum für Quantenphysik, Universität Innsbruck, 6020 Innsbruck, Austria*

[2]*Institut für Quantenoptik und Quanteninformation, Österreichische Akademie der Wissenschaften, 6020 Innsbruck, Austria*

[3]*JILA, University of Colorado and NIST, Boulder, Colorado 80309-0440, USA*

We report on the measurement of four-body recombination rate coefficients in an atomic gas. Our results obtained with an ultracold sample of cesium atoms at negative scattering lengths show a resonant enhancement of losses and provide strong evidence for the existence of a pair of four-body states, which is strictly connected to Efimov trimers via universal relations. Our findings confirm recent theoretical predictions and demonstrate the enrichment of the Efimov scenario when a fourth particle is added to the generic three-body problem.

Few-body physics produces bizarre and counterintuitive phenomena, with the Efimov effect representing the major paradigm of the field [Efi70]. Early in the 1970s, Efimov found a solution to the quantum three-body problem, predicting the existence of an infinite series of universal weakly bound three-body

[†]The author of the present thesis performed the data analysis, assisted by W.H. For the analysis, the author developed a software program to determine the three-body and four-body loss coefficients and statistical uncertainties, based on a resampling method. He also worked on maintaining and improving the experimental setup. F.F. performed the data acquisition together with S.K. J.P.D'I. provided theoretical support.

states. Surprisingly, these Efimov trimers can even exist under conditions where a weakly bound dimer state is absent [Jen04, Köh06b, Bra06]. An essential prerequisite for the Efimov effect is a large two-body scattering length a, far exceeding the characteristic range of the interaction potential. Ultracold atomic systems with tunable interactions [Chi10] have opened up unprecedented possibilities to explore such few-body quantum systems under well controllable experimental conditions. In particular, a can be made much larger than the van der Waals length r_{vdW} [1], the range of the interatomic interaction.

In the last few years, signatures of Efimov states have been observed in ultracold atomic and molecular gases of cesium atoms [Kra06b, Kno09], and recently in three-component Fermi gases of ^{6}Li [Ott08, Huc09], in a Bose gas of ^{39}K atoms [Zac08], and in mixtures of ^{41}K and ^{87}Rb atoms [Bar09]. In all these experiments, Efimov states manifest themselves as resonantly enhanced losses, either in atomic three-body recombination or in atom-dimer relaxation processes. The recent observations highlight the universal character of Efimov states, and they also point to a rich playground for future experiments.

As a next step in complexity, a system of four identical bosons with resonant two-body interaction challenges our understanding of few-body physics. The extension of universality to four-body systems has been attracting increasing interest both in theory [Pla04, Yam06, Han06, Ham07b, Wan09, Ste09] and experiment [Fer08]. A particular question under debate is the possible relation between universal three- and four-body states [Pla04, Yam06, Han06, Ham07b, Ste09]. In this context, Hammer and Platter predicted the four-body system to support universal tetramer states in close connection with Efimov trimers [Ham07b].

Recently, von Stecher, D'Incao, and Greene presented key predictions for universal four-body states [Ste09]. For each Efimov trimer, they demonstrate the existence of a pair of universal tetramer states according to the conjecture of Ref. [Ham07b]. Such tetramer states are tied to the corresponding trimer through simple universal relations that do not invoke any four-body parameter [Pla04, Han06, Ste09]. The authors of Ref. [Ste09] suggest resonantly enhanced four-body recombination in an atomic gas as a probe for such universal tetramer states. They also find hints on the existence of one of the predicted four-body resonances by reinterpreting our earlier recombination measurements on ^{133}Cs atoms at large negative scattering lengths [Kra06b]. In this Letter, we present new measurements on the Cs system dedicated to four-body recombination in the particular region of interest near a triatomic Efimov resonance. Our results clearly verify the central predictions of Ref. [Ste09]. We observe two loss resonances as a signature of the predicted tetramer pair and we find strong evidence for the four-body nature of the underlying recombination process.

The four-body extended Efimov scenario [Ham07b, Ste09] is schematically illustrated in Fig. 6.1, where the tetramer states (Tetra1 and Tetra2) and the relevant thresholds are depicted as a function of the inverse scattering length

[1] The van der Waals length is defined as $r_{\mathrm{vdW}} = \frac{1}{2}(mC_6/\hbar^2)^{1/4}$, where C_6 is the van der Waals dispersion coefficient [Köh06b]. For Cs, $r_{\mathrm{vdW}} = 100\,a_0$.

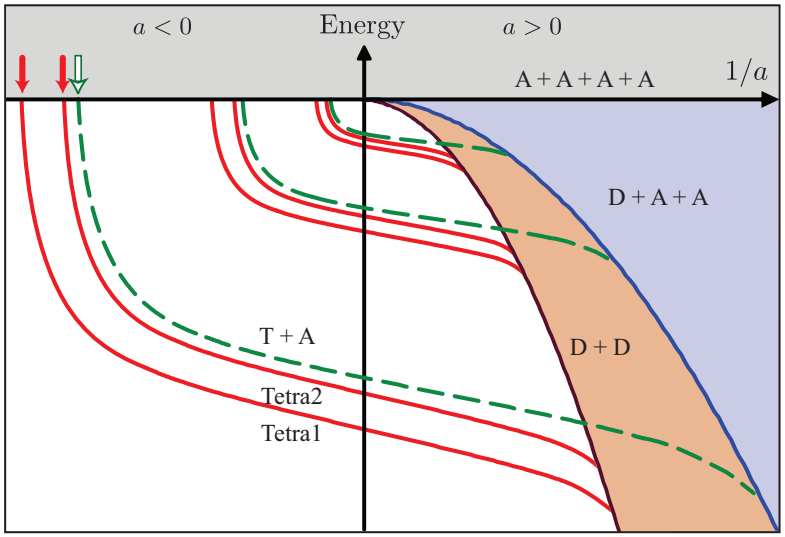

Figure 6.1.: Extended Efimov scenario describing a universal system of four identical bosons; Energies are plotted as a function of the inverse scattering length. The red solid lines illustrate the pairs of universal tetramer states (Tetra1 and Tetra2) associated with each Efimov trimer (T). For illustrative purposes, we have artificially reduced the universal Efimov scaling factor from 22.7 to about 2. The shaded regions indicate the scattering continuum associated with the relevant dissociation threshold. The four-body threshold is at zero energy and refers to four free atoms (A+A+A+A). In the $a > 0$ region, the dimer-atom-atom threshold (D+A+A) and the dimer-dimer threshold (D+D) are also depicted. The weakly bound dimer, only existing for $a \gg r_{\mathrm{vdW}} > 0$, has universal halo character and its binding energy is given by $\hbar^2/(ma^2)$ [Jen04, Fer08]. The open arrow marks the intersection of the first Efimov trimer (T) with the atomic threshold, while the filled arrows indicate the corresponding locations of the two universal tetramer states.

$1/a$. Within the four-body scenario, the Efimov trimers (T) are associated with trimer-atom thresholds (T+A, dashed lines). The pair of universal tetramer states (solid lines) lies below the corresponding T+A threshold. The four-body breakup threshold (A+A+A+A) defines zero energy and refers to the continuum of four free atoms. For completeness, we also show the $a > 0$ region. Here, the picture is even richer because of the presence of the weakly bound dimer state, whichs leads to the dimer-atom-atom threshold (D+A+A) and the dimer-dimer threshold (D+D). In the four-body scenario, the tetramer states emerge at the atomic threshold for $a < 0$ and connect to the D+D threshold for $a > 0$.

The Efimov trimer intersects the atomic threshold at $a = a_{\mathrm{T}}^*$, which leads to the observed triatomic resonance [Kra06b]. The corresponding tetramer states are predicted [Ste09] to intersect the atomic threshold at scattering length values

$$a_{\mathrm{Tetra1}}^* \approx 0.43\ a_{\mathrm{T}}^* \ \text{ and } \ a_{\mathrm{Tetra2}}^* \approx 0.9\ a_{\mathrm{T}}^*. \tag{6.1}$$

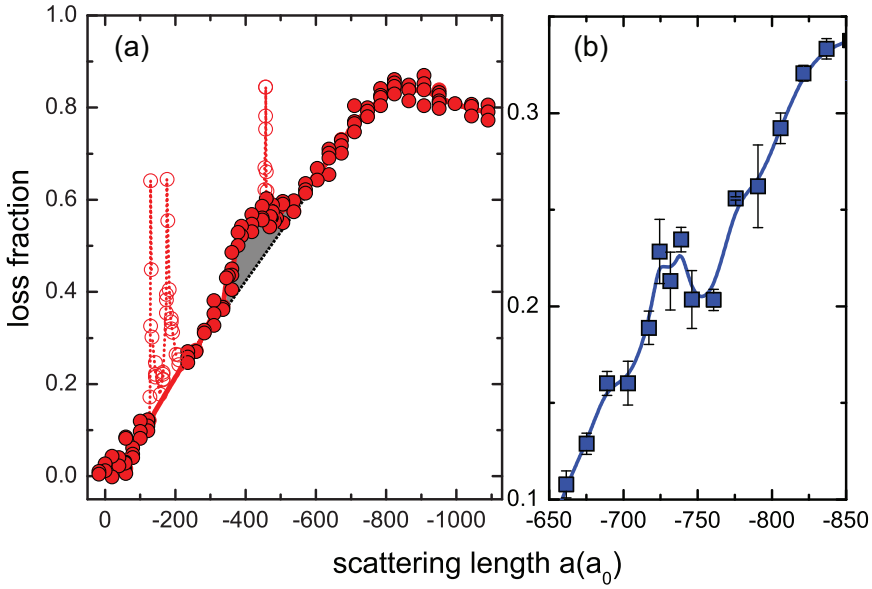

Figure 6.2.: Recombination losses in an ultracold sample of Cs atoms. (a) Loss fraction for a 50-nK sample after a storage time of 250 ms. Here we present all individual measurements to give an impression of the scatter of our data. The broad maximum at about $-870a_0$ is caused by a triatomic Efimov resonance [Kra06b] and the shaded area highlights the resonant loss enhancement that we attribute to the four-body state Tetra1. The three very narrow loss features (open circles) are caused by known g-wave Feshbach resonances [Chi04b], which are irrelevant in the present context. (b) Loss fraction for a 30-nK sample after a storage time of 8 ms. Each data point represents the average values resulting from five individual measurements for a given a together with their statistical errors. The loss enhancement at around $-730a_0$ is caused by the state Tetra2. The solid lines are spline interpolations guiding the eye.

These universal relations, linking three- and four-body resonances, express the fact that no additional parameter, namely, the so-called four-body parameter, is needed to describe the system behavior. In contrast to the connection between universal two- and three-body systems, where a three-body parameter is required to locate the trimer states, the universal properties of the four-body system are thus directly related to the corresponding three-body subsystem.

In analogy to the well-established fact that Efimov trimers lead to loss resonances in an atomic gas [Esr99, Kra06b], universal four-body states can also be expected to manifest themselves in a resonant increase of atomic losses [Ste09]. Resonant coupling between four colliding atoms and a tetramer state ($a \simeq a^*_{\mathrm{Tetra}} < 0$) drastically enhances four-body recombination to lower lying channels. Possible decay channels are trimer-atom, dimer-dimer, and dimer-atom-atom channels. In each of these recombination processes, we expect all the particles to rapidly escape from the trap, as the kinetic energy gained usually exceeds the trap depth.

We prepare an ultracold optically trapped atomic sample in the lowest hyperfine sublevel ($F = 3, m_F = 3$) [2], as described in Ref. [Fer08]. By varying the magnetic field between 6 and 17 G, the scattering length a can be tuned from -1100 to $0\,a_0$ [Web03b], where a_0 is Bohr's radius. For presenting our experimental data in the following, we convert the applied magnetic field into a using the fit formula of Ref. [Kra06b]. After several cooling and trapping stages [Web03b], the atoms are loaded into an optical trap, formed by crossing two infrared laser beams [Fer08]. The trap frequencies in the three spatial directions are about $(\omega_x, \omega_y, \omega_z) = 2\pi \times (10, 46, 65)$ Hz. Similar to [Web03b], we support the optical trap by employing a magnetic levitation field acting against gravity. Evaporative cooling in the levitated trap is stopped just before the onset of Bose-Einstein condensation in order to avoid implosion of the gas. For our typical temperature of 50 nK, we obtain about 8×10^4 non-condensed atoms with a peak density of about 7×10^{12} cm^{-3}.

In a first set of experiments, we record the atom number after a fixed storage time in the optical trap for variable scattering length in the $a < 0$ region. Figure 6.2 shows the observed losses, containing both three- and four-body contributions. The three-body part consists of a background that follows a general a^4-scaling behavior [Fed96b, Esr99, Web03c] and resonant losses caused by the triatomic Efimov resonance, which for a 50-nK sample was observed to occur at $a_T^* = -870(10)\,a_0$ [Kra06b, Näg06]; this is consistent with the large losses shown in Fig. 6.2(a). Beside this expected behavior of the three-body subsystem, we clearly observe two additional loss features, one located at about $-410\,a_0$ [Fig. 6.2(a)] and one at about $-730\,a_0$ [Fig. 6.2(b)]. The observation of the resonance at $-730\,a_0$ is particularly demanding and requires a careful choice of parameters as the signal needs to be discriminated against the very strong background that is caused by three-body losses. Here we use a much shorter hold time of 8 ms, which is the shortest possible time required to ensure precise magnetic field control in our apparatus.

We interpret the two observed resonant loss features as the predicted pair of four-body resonances [Ste09]. For the resonance positions we find $a^*_{\mathrm{Tetra1}}/a^*_T \simeq 0.47$ and $a^*_{\mathrm{Tetra2}}/a^*_T \simeq 0.84$, which are remarkably close to the predictions of Eq. (6.1).

In a second set of experiments, we study the time-dependence of the atomic decay in the optical trap. Here we focus on the region around the resonance at $a^*_{\mathrm{Tetra1}} \simeq -410 a_0$, where the three-body losses are comparatively weak and thus allow for a detailed analysis of the loss curves. Representative loss measurements for three different values of a are shown in Fig. 6.3.

The observed decay can be fully attributed to three-body and four-body recombination collisions. This is due to the fact that inelastic two-body collisions of atoms in the lowest Zeeman sub-level are energetically suppressed, and one-body losses, such as background collisions or light-induced losses, can be completely neglected under our experimental conditions. The corresponding

[2] F and m_F indicate the hyperfine and projection quantum number, respectively.

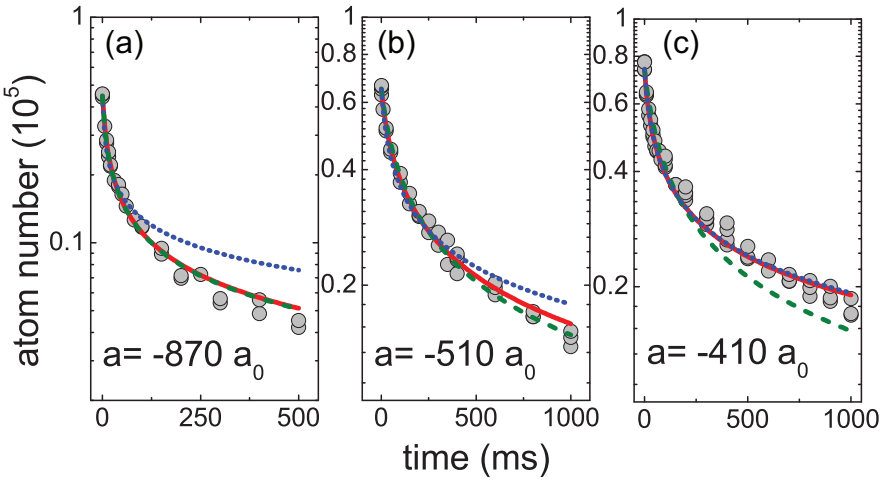

Figure 6.3.: Time evolution of the number of atoms in an optically trapped sample. The solid lines are the fit to the data based on the full numerical solution of Eq. (6.2). The dashed and dotted lines correspond to a pure three-body and pure four-body decay, respectively (see text). (a) For dominant three-body collisions ($a = -870\,a_0$), (b) an intermediate situation ($a = -510\,a_0$), and (c) dominant four-body collisions ($a = -410\,a_0$).

differential equation for the decaying atom number reads as

$$\dot{N}/N = -L_3\langle n^2\rangle - L_4\langle n^3\rangle, \tag{6.2}$$

where L_3 and L_4 denote the three- and the four-body recombination rate coefficient, respectively. The average density is calculated by integrating the density over the volume $\langle n^2\rangle = (1/N)\int n^3 d^3\mathbf{r}$ and $\langle n^3\rangle = (1/N)\int n^4 d^3\mathbf{r}$. By considering a thermal density distribution of gaussian shape in the three-dimensional harmonic trap, we obtain $\langle n^2\rangle = n_p^2/\sqrt{27}$ and $\langle n^3\rangle = n_p^3/8$, with $n_p = N[m\overline{\omega}^2/(2\pi k_{\mathrm{B}}T)]^{3/2}$ the peak density. Here, m is the atomic mass, T the temperature, and $\overline{\omega} = (\omega_x\omega_y\omega_z)^{1/3}$ the mean trap frequency. We determine the trap frequencies and the temperature by sloshing mode and time-of-flight measurements, respectively.

In general Eq. (6.2) is not analytically solvable. An analytic solution can be found in the limit of either pure three-body losses or pure four-body losses.

Therefore we fit our decay curves with a numerical solution of Eq. (6.2), keeping both L_3 and L_4 as free parameters. Note that we have not included anti-evaporation heating [Web03c] in our model because we do not observe the corresponding temperature increase in our experiments. We believe that, for the fast decay observed here, the sample may not have enough time to thermalize.

Our experimental data clearly reveal a qualitative change of the decay curves when a is tuned between a^*_{T} and a^*_{Tetra1}. Fig. 6.3(a) shows that for $a \approx a^*_{\mathrm{T}}$ the loss is dominated by three-body recombination; here the full numerical fitting curve follows the pure three-body solution. A different situation is found at $-410\,a_0$; see Fig. 6.3(c). Here a pure three-body analysis cannot properly describe the

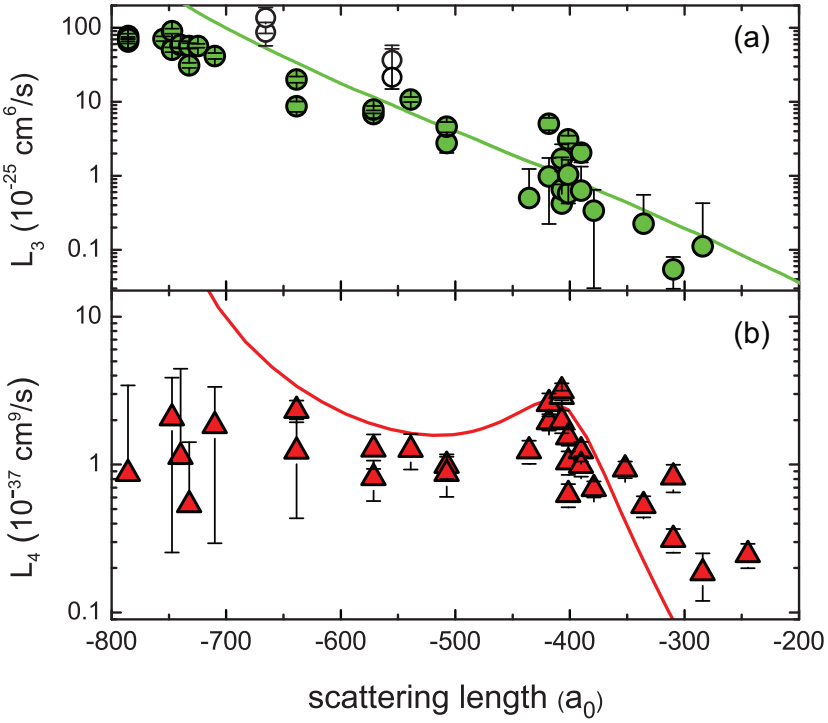

Figure 6.4.: Loss rate coefficient for (a) three- and (b) four-body recombination as a function of the scattering length a. The measurements are taken at temperatures of about 40 nK. The values are obtained by fitting the numerical solution of Eq. (6.2) to the decay curve. The error bars on L_3 and L_4 are the statistical uncertainties from the fit evaluated with a resampling method [Wes93]. The open circles in (a) refer to previous data at 250 nK [Kra06b]. The solid curves result from the theoretical model of Refs. [Ste09, Meh09].

observed behavior and the full numerical solution reveals a predominant four-body character. In intermediate situations, for which an example is shown in Fig. 6.3(b), both three- and four-body processes significantly contribute to the observed decay.

From the decay curves taken at different values of a we determine L_3 and L_4; the results are shown in Figs. 6.4(a) and 6.4(b), respectively. The three-body contribution L_3 follows previously observed behavior [Kra06b], as dictated by the a^4-scaling in combination with the Efimov effect.

Our major result is shown in Fig. 6.4(b), where we plot the rate coefficient L_4. Our data provide the first available quantitative information on L_4, establishing the role of four-body collisions in ultracold gases. For $|a| < |a^*_{\mathrm{Tetra1}}|$, where no universal tetramer states exist, the four-body losses are typically very weak. Here, we measure $L_4 \simeq 0.2 \times 10^{-37}\mathrm{cm}^9/\mathrm{s}$. With increasing $|a|$, the system undergoes a significant change in its behavior, with four-body collisions dominating the atomic decay; see Fig. 6.3(c). We observe a sharp increase of L_4, which reaches its maximum value at $a = -412(2)\,a_0$. This observation is another strong piece of evidence for the predicted universal four-body state at a^*_{Tetra1}

[Ste09]. To directly estimate the relative contributions of three- and four-body recombination, one can compare L_3 with $n_0\,L_4$, where $n_0 \simeq 1.0\times10^{13}\,\mathrm{cm}^{-3}$ is the initial peak density at 40 nK. At resonance, n_0L_4 exceeds L_3 by more than one order of magnitude, with $L_3 = 0.7\times10^{-25}\,\mathrm{cm}^6/\mathrm{s}$ and $n_0L_4 = 3\times10^{-24}\,\mathrm{cm}^6/\mathrm{s}$. With further increasing $|a|$, L_4 decreases and L_3 increases such that $L_3 > n_0L_4$. For $|a| > 700\,a_0$, the very fast three-body decay renders the analysis of the loss curves in terms of L_4 unreliable. In addition to the large statistical fit errors seen in our data in this region, other systematic error sources like a non-thermal evolution of the atomic density distribution can have a strong influence.

Figure 6.4 also includes the theoretical predictions for L_3 and L_4 at 40 nK and demonstrates a remarkable qualitative agreement with our experimental results. The theoretical approach utilizes a solution of the four-body problem in the hyperspherical adiabatic representation [Ste09]; the derivation and associated calculations of L_4, adapted from [Meh09], provide the first quantitative description of the four-body recombination rate. The calculations only require to fix the position of the triatomic Efimov resonance as determined in the previous experiment at 10 nK of Ref. [Kra06b]. The difference in the width and the amplitude of the four-body resonance between experimental and theoretical data may be explained by different coupling to possible decay channels.

Our work leads to important conclusions related to the concept of universality with increasing complexity. The observation of the two four-body resonances close to the predicted positions [Ste09] points to the universal character of the underlying states. This also supports the view or Refs. [Pla04, Han06, Ste09] that a four-body parameter is not required to describe the system. Universal four-body states then emerge as a genuine consequence of the Efimov spectrum. This also provides a novel way to test Efimov physics. The Efimovian character of a three-body resonance can be probed by observing the universal tetramer resonances tied to it, without the necessity to explore the full geometric scaling of Efimov physics by changing the scattering length by orders of magnitude.

While our present work has focussed on four-body phenomena at negative scattering length, a further exciting step will be the exploration of the entire four-body spectrum. For positive scattering lengths, the spectrum becomes richer and new phenomena can be expected such as resonant interactions between four-body states and two-dimer states. In this way, experiments on few-body phenomena in ultracold atoms will keep on challenging our understanding of the universal physics of a few resonantly interacting particles.

We are aware of related results in ^{39}K, in which enhanced losses near a Feshbach resonance may be interpreted as a four-body resonance [Zac09][3].

We acknowledge C. Greene and J. von Stecher for stimulating discussions and for sharing their theoretical curves (Fig. 6.4) with us. We acknowledge support by the Austrian Science Fund (FWF) within SFB 15 (project part 16). F. F. is supported within the Lise Meitner program of the FWF. JPD's contribution was supported in part by the NSF.

[3] In the original article [Fer09a], this reference is quoted as "M. Zaccanti (private communication)", as Ref. [Zac09] was not available until after the publication of Ref. [Fer09a].

CHAPTER 7
PUBLICATION

Collisions of ultracold trapped cesium Feshbach molecules[†]

Laser Phys. **20**, 23 (2010)

F. Ferlaino,[1] S. Knoop,[1] M. Berninger,[1] M. Mark,[1] H.-C. Nägerl,[1] and R. Grimm[1,2]

[1] *Institut für Experimentalphysik und Zentrum für Quantenphysik, Universität Innsbruck, 6020 Innsbruck, Austria*

[2] *Institut für Quantenoptik und Quanteninformation, Österreichische Akademie der Wissenschaften, 6020 Innsbruck, Austria*

We study collisions in an optically trapped, pure sample of ultracold Cs_2 molecules in various internal states. The molecular gas is created by Feshbach association from a near-degenerate atomic gas, with adjustable temperatures in the nanokelvin range. We identify several narrow loss resonances, which point to the coupling to more complex molecular states and may be interpreted as Feshbach resonances in dimer-dimer interactions. Moreover, in some molecular states we observe a surprising temperature dependence in collisional loss. This shows that the situation cannot be understood in terms of the usual simple threshold behavior for inelastic two-body collisions. We interpret this observation as further evidence for a more complex molecular structure beyond the well-understood dimer physics.

[†]The primary contribution of the author of the present thesis to this publication was the maintenance and improvement of the experimental setup, supported by M.M. He performed the measurements together with F.F. and S.K. The data was analyzed by F.F and S.K.

7.1. Introduction

Laser control of atoms and molecules has numerous important applications in physics [Let07]. A major research field emerged from the fascinating possibilities to cool and trap atoms by laser light [Min87, Kaz90, Chu98, CT98, Phi98]. V. S. Letokhov gave very important contributions to the field; here the idea of confining atoms in standing light waves in 1968 [Let68] and the first demonstration of atomic-beam cooling in 1981 [And81] represent two early examples for work that was well ahead of its time. More examples for the pioneering work of the laser cooling group at the Institute of Spectroscopy in Troitsk can be found in Refs. [Bal85, Bal88a, Bal88b, Gri90].

The great advances in the field of cooling and trapping in the 1980's and early 1990's [Ari92] led to the attainment of Bose-Einstein condensation (BEC) in 1995 [And95, Bra95, Dav95] and the production of a degenerate Fermi gases in 1999 [DeM99]. These achievements heralded the advent of a new era in physics, where ultracold atomic systems serve as well-controllable model systems to investigate a wide range of intriguing quantum phenomena [Lew07, Blo08, Gio08, Chi10].

Molecular quantum gases emerged in the last decade. Great breakthroughs were achieved in the years 2002 and 2003, when molecular quantum gases could be produced in various systems of bosons [Don02, Her03, Dür04, Xu03] and fermions [Reg03b, Str03, Cub03, Joc03b]. The key to this success was the method of Feshbach association, where molecules are formed from colliding atom pairs by tuning a magnetic bias field across a Feshbach resonance [Köh06b, Chi10, Kre09]. Molecular BEC was achieved at the end of 2003 [Joc03a, Gre03, Zwi03]. In the last few years great progress has been made in manipulating ultracold molecules, and they have found numerous intriguing applications [Kre09]. Recent highlights are the transfer of Feshbach molecules to very deeply bound states [Dan08] and the creation of rovibrational ground-state molecules [Ni08, Lan08b].

With the experimental availability of ultracold trapped samples of molecules, it has become very important to understand their interaction properties. For Feshbach molecules, the interactions are usually dominated by inelastic processes, as the molecules in a high rovibrational state carry a large amount of internal energy. Here the stability of molecules made of fermionic atoms is a remarkable exception [Pet05, Gio08]. Inelastic collisions between ultracold Feshbach molecules have been studied in various systems [Muk04, Chi05b, Sya06, Kno08, Fer08, Ina08]. Most of these experiments did not show any significant dependence on the applied magnetic bias field. Two experiments on Cs_2, however, revealed novel magnetic-field dependent phenomena. In Ref. [Chi05b] we observed loss resonances in dimer-dimer scattering, and in Ref. [Fer08] we found a suppression of loss for weakly bound dimers in a halo state.

In this Article, we study the collisional interactions between Cs_2 Feshbach molecules in more detail, building on our previous observations in Refs. [Chi05b, Fer08]. Our new results provide further evidence for a more complex molecular structure beyond the well-understood dimer physics. In Sec. 7.2, we start

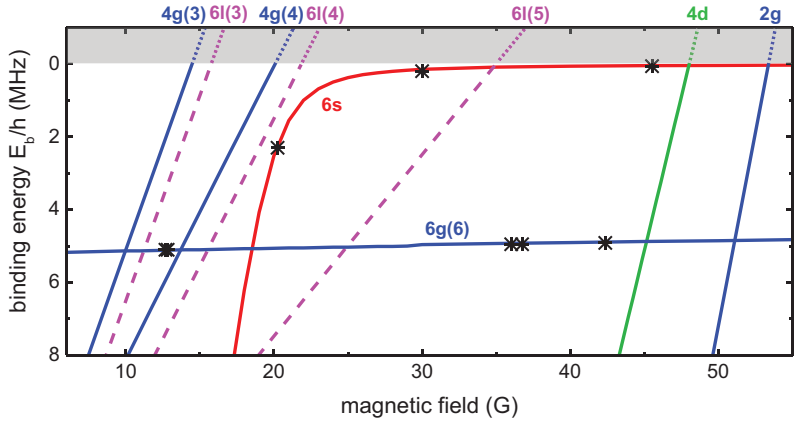

Figure 7.1.: Energy spectrum of weakly bound Cs_2 dimers versus magnetic field. The molecular states are labeled by the quantum numbers $f\ell(m_f)$ as discussed in Sec. 7.2.2; the quantum number m_f is omitted for states with $m_f = f$ and $m_\ell = \ell$. The solid lines represent s-, d-, and g-wave states. The intersections of the d- and g-wave states cause narrow Feshbach resonances, which can be used for molecule production. The dashed lines represent l-wave states; they do not couple to the zero-energy threshold and therefore do not lead to Feshbach resonances. The stars mark the states and positions where we find the narrow collisional resonances discussed in Sec. 7.3.

with giving background information on Cs_2 Feshbach molecules. In Sec. 7.3, we present our results on collisional resonances in inelastic dimer-dimer scattering, which show up in different molecular states. In Sec. 7.4, we report on the observations of a surprising temperature dependence of dimer-dimer collisions, which we find in some, but not all of the dimer states. In Sec. 7.5, we finally discuss our results in view of more complex ultracold molecules.

7.2. Ultracold Feshbach molecules made of cesium atoms

7.2.1. Cesium as a quantum gas: brief history

Cesium, the heaviest stable alkali species, was considered a candidate for Bose-Einstein condensation (BEC) already in the early 1990's [Mon93]. After the attainment of BEC in Rb and Na [And95, Dav95], it turned out that Cs atoms are subject to very special collisional interactions, which lead to anomalously fast spin flips. This inhibited all attempts to reach BEC by the standard magnetic trapping approach [Söd98, GO98, Arl98]. The unusual interactions were understood as a combination of resonant scattering with a very large indirect spin-spin coupling [Leo00].

It took until the year 2002 that BEC of Cs was reached in an optical dipole trap [Web03b]. In such a trap [Gri00a], the atoms can be stored in the lowest

internal state, where they are immune against two-body inelastic decay. It was crucial for the experiment to magnetically tune the s-wave scattering length in a way to optimize the collisional properties for the evaporative cooling process [Kra04, Kra06b]. Since then BEC of cesium has been realized in several other experiments [Ryc04, Gus08b, Hun08].

The successful production of near-degenerate samples or BECs of Cs opened up efficient ways to produce ultracold molecules via Feshbach association [Her03, Mar05, Mar07a, Kno08]. The basic principles and the many applications of this important association method are reviewed in [Köh06b, Kre09, Chi10]. Besides the creation of ultracold dimers, the remarkable scattering properties of Cs have proven very advantageous for the exploration of universal few-body phenomena related to Efimov states [Kra06b, Fer08, Kno09, Fer09a].

7.2.2. Energy structure of Cs_2 Feshbach molecules

The internal structure of Cs_2 Feshbach dimers is particularly rich as compared to other alkali systems, and contributions by higher partial waves play an important role. Figure 7.1 gives an overview of the molecular states relevant to the present work, covering the magnetic field region up to 55 G and binding energies up to $h \times 8\,\mathrm{MHz}$, where h is Planck's constant. Zero energy corresponds to the dissociation threshold into two Cs atoms in the absolute hyperfine ground state sublevel $|F=3, m_F=3\rangle$.

Our notation $f\ell(m_f)$ for the angular momentum of the molecular states is explained in detail in Refs. [Chi04b] and [Mar07a]. The rotational angular momentum and its orientation are denoted by the quantum numbers ℓ and m_ℓ, respectively; we follow the convention of labeling states with $\ell = 0, 2, 4, 6, 8, \ldots$ as $s, d, g, i, l, \ldots$-wave states [Rus29]. The quantum numbers f and m_f refer to the internal spin of the molecular and its orientation, respectively. All molecular states relevant to the present work obey $m_f + m_\ell = 6$, which allows to simplify the notation by omitting one of these numbers. For states with $m_f = f$ and $m_\ell = \ell$, we use the notation $f\ell$ for brevity.

Feshbach resonances in general arise from the intersection of a molecular state with the atomic threshold [Chi10]. For Cs the observation of such resonances together with an elaborate quantum scattering model provided the essential information on the near-threshold molecular structure [Chi04b]. Higher-order interactions are particularly important for Cs [Leo00] and lead to significant couplings between states up to $\Delta\ell = 4$. Therefore states up to g-wave character can couple to the s-wave scattering continuum, leading to observable resonances. The solid lines in Fig. 7.1 represent states up to g waves ($\ell \leq 4$), which were identified in this way [Chi04b]. The dashed lines in Fig. 7.1 represent l-wave states ($\ell = 8$), which do not cause observable Feshbach resonances but which can be populated via avoided crossings with g-wave states [Mar07b, Mar07a, Kno08].

Coupling between molecular states with the same f and ℓ in general leads to very broad avoided crossings between molecular states. The pronounced curvature of the $6s$ state in Fig. 7.1 is a result of such a strong crossing. In

this case, a weakly bound $6s$-state with $F_1 = 3$ and $F_2 = 3$ couples to a $6s$-state with $F_1 = 4$ and $F_2 = 4$. Narrow avoided crossings arise when molecular states of different f and ℓ intersect [Hut08]. Such crossings are not shown in Fig. 7.1, where the molecular states just intersect. Nevertheless, the existence of these weakly avoided crossings between molecular states of different $f\ell$ is crucial for a controlled state transfer by elaborate magnetic field ramps, as described in detail in Ref. [Mar07a].

7.2.3. Tunable halo dimers

The state $6s$ provides experimental access to the "halo" regime [Jen04], which is of particular interest in view of the universal properties of few-body systems [Bra06]. For a halo dimer the only relevant length scale is given by the scattering length a, which describes the s-wave interaction between its two constituents. The size of the halo dimer is directly related to a and the binding energy is $E_b = \hbar^2/(2\mu a^2)$, where μ is the reduced mass. For ultracold gases, the characteristic interaction range is determined by the van der Waals potential and the halo regime is realized for binding energies well below an energy E_{vdW} [Köh06b, Chi10]; for the s-wave scattering length this condition is equivalent to $a \gg r_{\mathrm{vdW}}$, where r_{vdW} a characteristic length. For Cs, $E_{\mathrm{vdW}} \approx h \times 2.7$ MHz and $r_{\mathrm{vdW}} \approx 100\, a_0$, where a_0 is Bohr's radius.

In the $6s$ state of Cs_2 we can conveniently control the binding energy via the magnetic field. The *tunable halo dimers* realized in this way [Mar07a, Fer08] are unique probes to explore universal quantum phenomena [Bra06]. As a recent example, we have observed a scattering resonance in the interaction of tunable halo dimers with free atoms [Kno09], which we interpret as an atom-dimer resonance arising from the coupling to an Efimov trimer state [Efi70, Kra06b].

A binary collision between two halo dimers represents an *elementary four-body process*. Collisional studies on halo dimers thus probe universal four-body physics, as has been demonstrated in the special case of halo dimers made of fermionic atoms in different spin states [Pet04b, Ing08]. As a first step to explore universal four-body physics of identical bosons, we have recently measured collisional decay in a trapped sample of Cs_2 Feshbach molecules in the $6s$ state [Fer08]. The experiments revealed a broad loss minimum around 30 G ($a \approx 500\, a_0$), for which Ref. [D'I09d] presents a possible explanation in terms of universal four-body physics.

The full understanding of four-body systems is a present frontier of universal physics. Theoretical work has predicted pairs of four-body states tied to Efimov trimer states [Ham07b, Ste09]. Very recently we could confirm the existence of these states by measured four-body recombination in an atomic cesium gas [Fer09a]. Studies on dimer-dimer interactions are of great interest for future experiments, as they hold great potential for future investigations, such as the observation of the resonant coupling of colliding dimers to tetramer states and systems of a trimer plus a free atom [D'I09d].

7.2.4. Main experimental procedures

Our experimental procedures to produce an optically trapped sample of Cs_2 Feshbach molecules involve several stages. The main steps can be divided into the preparation of a near-degenerate atomic sample, the Feshbach association of the dimers, the purification of the molecular sample by removing remaining atoms, and the state transfer to the desired molecular state for the present investigation. Here we just give a short account of the main steps; further details can be found in Ref. [Mar07a].

The cesium atoms are first captured from an atomic beam into a standard magneto-optical trap, followed by an optical molasses cooling phase. A degenerate Raman sideband cooling stage [Tre01] then further increases the phase-space density and polarizes the atoms into the hyperfine ground state sublevel $|F = 3, m_F = 3\rangle$. Then the atoms are loaded into a large-volume optical dipole trap, followed by collisional transfer into a much tighter trap [Web03b, Kra04]. The tight trap serves for evaporative cooling; it is formed by two crossed 1064-nm laser beams with waists of about 250 μm and 36 μm. We stop the cooling just before the onset of Bose-Einstein condensation to avoid too high atomic densities.

We magnetically associate the ultracold trapped cesium atoms to dimers on Feshbach resonances [Her03, Xu03, Dür04, Köh06b]. For this purpose we use three different resonances, the two g-wave resonances at $B = 19.8\,\mathrm{G}$ and $53.4\,\mathrm{G}$ and the d-wave resonance at $47.9\,\mathrm{G}$. To prepare a maximum number of molecules in the trap, it is necessary to separate atoms and molecules as fast as possible, since atom-dimer collisions dramatically reduce the lifetime of the molecular sample [Muk04]. We remove the atoms from the dipole trap using a "blast" technique similar to the schemes of Refs. [Xu03, Tha06]; the atoms are pushed out of the trap by resonant light, while the effect on the molecules remains negligible.

The molecular temperature can be set in a range between $40\,\mathrm{nK}$ and $300\,\mathrm{nK}$ by adjusting the temperature of the initial atomic sample. This can be done by variations in the evaporative cooling process and of the trap parameters [Fer08]. The number of trapped molecules is typically around 5000.

Other molecular states than the ones that we can directly access through the Feshbach association schemes can be populated by controlled state transfer [Mar07b, Mar07a, Lan08a]. The experimental key is the precise control of Landau-Zener tunneling at avoided crossings through elaborate magnetic field ramps. By means of the ramp speed we can choose whether a crossing is followed adiabatically (slow ramp) or jumped diabatically (fast ramp). In this way, as demonstrated in Ref. [Mar07a], we can efficiently populate any of the states shown in Fig. 7.1.

To finally detect the molecules, we apply the standard method [Chi10] to dissociate the molecules by a reverse Feshbach ramp and to image the resulting atom cloud.

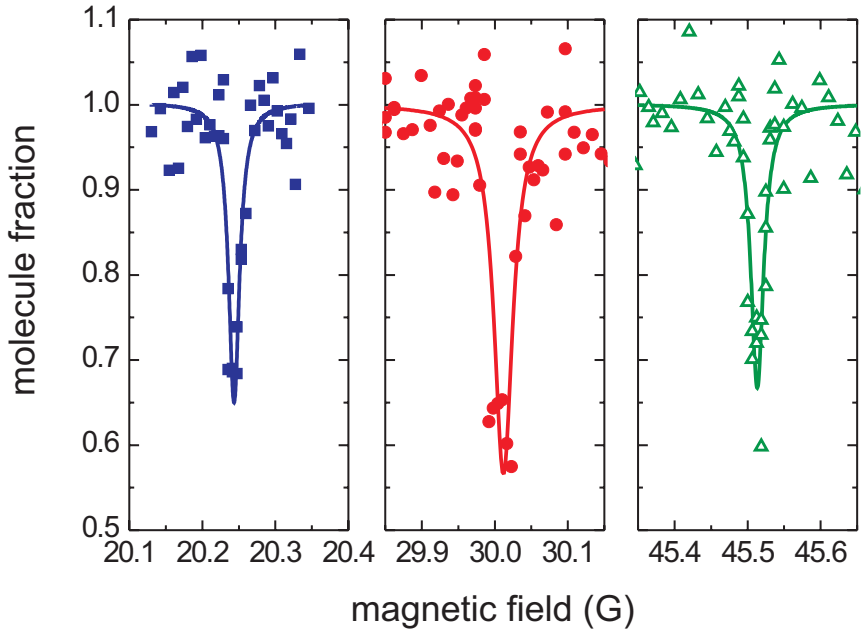

Figure 7.2.: Dimer-dimer resonances in the $6s$ state. The molecule fraction represents the number of $6s$ molecules after a 100-ms hold time in the dipole trap normalized to the corresponding average number detected off any resonance. The initial molecule number is typically 5000 at a temperature of about 150 nK. The loss resonances are fitted with Lorentzian profiles. The results of the fits are listed in Table 7.1.

7.3. Resonances in dimer-dimer scattering

Studies of collisions between molecules can provide essential information on the interaction physics. We probe the system by studying collisionally induced loss in a trapped molecular sample. At ultralow temperatures, the dominant collisional mechanism is relaxation into lower-lying bound states. Feshbach dimers carry a large amount of internal energy, which is in a relaxation event rapidly converted into kinetic energy . Since this released energy usually far exceeds the trap depth, both collisional partners can escape from the trap. The resulting loss signal provides our experimental observable.

The relaxation rate depends on the possible decay channels, i. e. on the available lower-lying molecular state manifolds, and on the wave-function overlap between the initial and the final dimer state. For relaxation into deeply bound states, such a rate does not significantly depend on the applied bias magnetic field. This can be understood in terms of a simple molecular potential picture. The magnetic fields typically used in the experiments lead to energy shifts in the molecular potentials that are usually very small compared to the energy distance between the initial and final state. Consequently, the wave function overlap does not change substantially. Typical relaxation rate constants are on the order of 10^{-10} - 10^{-11} cm^{-3}/s [Muk04, Chi05b, Sya06, Kno08, Ina08].

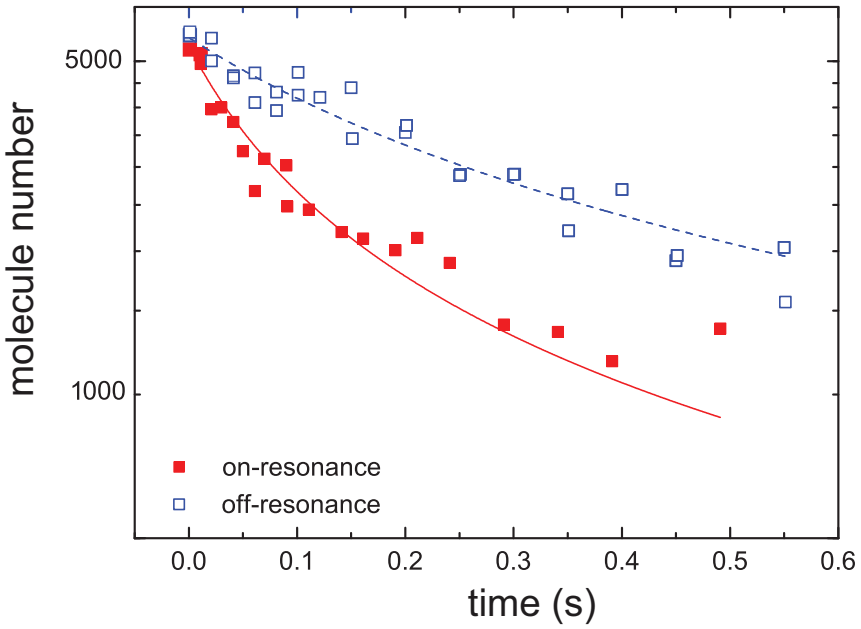

Figure 7.3.: Time evolution of the number of $6s$ dimers at 20.24 G (on resonance, squares) and at 20.11 G (off resonance, open squares). Fits are based on the standard two-body loss equation; see text.

Remarkable exceptions, in which the relaxation rate varies with the applied magnetic field, have been observed in collisions between halo molecules [Joc03a, Gre03, Zwi03, Fer08] and when collisional resonances appear in dimer-dimer scattering [Chi05b]. In the present Section, we focus on the latter case.

Collisional resonances in dimer-dimer scattering occur when the two dimers couple to more complex bound states, involving either tetramer or trimer states. When such a complex state approaches the threshold of two colliding dimers, either by crossing or merging, it induces a resonant enhancement of relaxation events and, consequently a resonant increase of losses. The number of dimers as a function of the magnetic field then shows a sharp loss peak. In analogy to the case of coupling between two atoms and a dimer state, these enhanced losses can be viewed as *Feshbach-like resonances for ultracold molecules*. In a recent experiment, we observed such dimer-dimer resonances in a sample of g-wave Cs_2 dimers [Chi05b].

Here, we carry out a careful and systematic search of dimer-dimer resonances in a number of different molecular states by performing magnetic field scans with a typical step size of 5 mG. In particular, we explore the $6g(6)$ state in a magnetic field range between 10 to 13 G and 25 to 45 G and the $4g(4)$ state, the $4d$ state and the $6s$ halo state up to 5 MHz binding energy.

We measure the collisional resonances in dimer-dimer scattering by following an experimental procedure similar to Ref. [Chi05b]. We first produce a sample of optically trapped dimers in a desired molecular states, as outlined in Sec. 7.2.4. We then hold the dimers in the dipole trap for a certain time, typically 100

to 200 ms. Finally, we record the number of remaining dimers by standard dissociation detection; see Sec. 7.2.4. The measurement is then repeated for various magnetic field values in the range of interest and for various molecular states.

Figure 7.2 shows the three dimer-dimer resonances found in the $6s$ state. The observed loss peaks are typically very pronounced, very narrow, and symmetric. By fitting the loss peaks with Lorentzian profiles, we precisely determine the positions and we extract the widths of the resonances, as listed in Table 7.1. We use the Breit-Rabi formula to determine the magnetic-field value from a measurement of the resonant frequency corresponding to the $|F=3, m_F=3\rangle \rightarrow |F=4, m_F=4\rangle$ atomic hyperfine transition. Differently from Ref. [Chi05b], in which a levitating magnetic field was employed to support the dimers against gravity, we here use a purely optical trap. The present setup does not suffer from the corresponding inhomogeneity and thus improves the magnetic field resolution to about 10 mG, compared to 150 mG resolution obtained with the levitation field.

The enhancement of losses can be characterized by studying the time dependence of the molecular decay in the optical trap. Figure 7.3 shows the decay curve for $6s$ dimers at the 20-G resonance (squares) and slightly below resonance (open squares). Both on and off resonance, we observe a non-exponential decay of the dimer number. The decay of the trapped dimer sample is well described by the usual two-body rate equation

$$\dot{N} = -\alpha_{\mathrm{rel}} \bar{n} N, \tag{7.1}$$

where N indicates the number of dimers and α_{rel} the relaxation rate coefficient. The mean molecular density $\bar{n}$ is given by $\bar{n} = [m\bar{\omega}^2/(2\pi k_B T)]^{3/2} N$ with m being the atomic mass and $\bar{\omega}$ denoting the geometric mean of the trap frequencies. Typically, we observe the relaxation rate coefficient to increase by about a factor of 5 on resonance.

We perform similar magnetic field scans in the states $6g(6)$, $4d$, and $4g(4)$. In the $6g(6)$ state, we both confirm the existence of the resonances observed in previous experiments [Chi05b], and we identify three additional new resonances in the magnetic field range between 25 to 45 G. Up to binding energies of 5 MHz, we do not observe any resonance for dimers in the $4d$ and $4g(4)$ state. Our results are listed in Table 7.1. For illustrative purposes, we also mark the resonance positions in Fig. 7.1 (stars).

An important open question is whether the observed resonances are related to tetramer or trimer states, coupling to the dimer-dimer threshold. The observation of resonance shapes that are symmetric suggests a coupling to a tetramer state. In fact, one can expect that the coupling with a trimer plus a free atom would lead to an asymmetric shape because of the continuum of energy [D'I09d]. However, further investigations are needed to clearly distinguish between these two processes.

Dimer branch	B(G)	ΔB(mG)	$a(a_0)$
$6s$	20.24 (1)	18 (3)	179
	30.01 (1)	31 (4)	552
	45.52 (1)	21 (4)	893
$6g(6)$	12.67 (1)[a]	5 (2)	
	12.82 (1)[a]	19 (2)	
	36.06 (1)	10 (2)	
	36.80 (1)	19 (5)	
	42.43 (1)	9 (2)	

Table 7.1.: Observed dimer-dimer resonances. The resonances are found in the states $6s$ and $6g(6)$, while no resonances are found in the states $4d$ and $4g(4)$. The locations and the widths of the loss signals, together with their statistical errors, are obtained from Lorentzian fits. For the $6s$ state, the Table also gives the corresponding value of the scattering length [Lan09b].
[a]The two resonance positions in the $6g(6)$ state near 13 G slightly differ from the values of Ref. [Chi05b]. In this previous experiment, the levitation field introduced an uncontrolled offset.

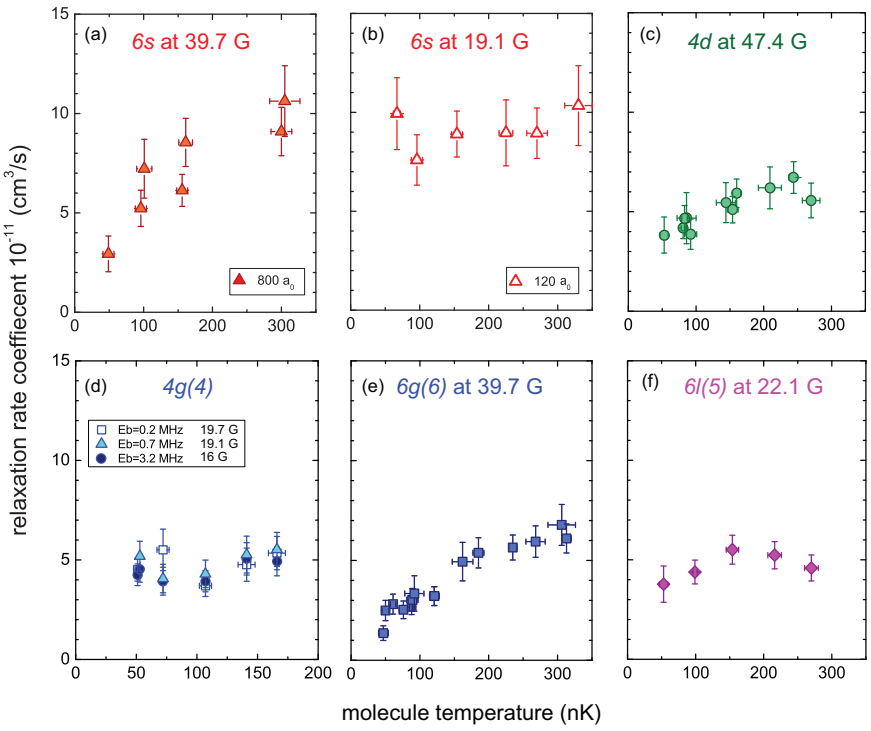

Figure 7.4.: Temperature dependence of the relaxation rate coefficient α_{rel} for different molecular states: the $6s$ state in the halo (a) and non-halo regime (b), the $4d$ state (c), the $4g(4)$ state (d) for different binding energies, the $6g(6)$ state (e), and the $6l(5)$ state (f). The data in (a) and (b) are from [Fer08].

7.4. Temperature dependence of collisional loss

For inelastic processes in the ultracold regime, the relaxation rate coefficient is usually independent of the collision energy, or the temperature T of the sample. This threshold law applies for s-wave collisions and for $k_B T$ smaller than all other energy scales in the system [Wei99]. The essential point behind this threshold law is that relaxation processes into deeply bound states release such a large amount of internal energy that the collisional energy plays no role. This picture breaks down when another state is energetically close to the threshold of the two colliding particles.

In our previous experiments on collisions between $6s$ dimers, we found a surprising temperature dependence of the relaxation rate coefficient [Fer08]. In the non-halo regime, α_{rel} showed the expected constant behavior, while a clear increase with temperature was observed in the halo regime. A recent theoretical work suggests that the temperature dependence observed in the halo state is related to the existence of a universal trimer state, which lies energetically slightly above the zero-energy threshold of two colliding atoms [D'I09d].

We here raise the question whether the unusual temperature behavior is a property unique to halo states or whether it can also occur for other Feshbach molecules. We thus probe the temperature dependence of the relaxation rate coefficient for different dimer states, investigating the states $6s$, $4d$, $4g(4)$, $6g(6)$, and $6l(5)$.

We measure the time dependence of the molecular decay for various temperatures, recording decay curves similar to Fig. 7.3. The relaxation rate coefficient α_{rel} is extracted by fitting the decay curve with the usual two-body rate equation, Eq. (7.1). Our findings are summarized in Fig. 7.4. We observe a clear temperature dependence in two cases, while the other three cases follow the threshold law expectation of a constant rate coefficient. In one case the result is ambiguous. The two cases with a clear temperature dependence are the $6s$ state at about 39.7 G (Fig. 7.4a) and the $6g(6)$ state (Fig. 7.4e); here the relaxation rate increases with temperature, roughly following a $\sqrt{T}$-dependence. Constant rate coefficients are observed in the $6s$ state at about 19.1 G, the $4g(4)$ state, and the $6l(5)$ state. The ambiguous case is the $4d$ state, which seems to show a weak temperature dependence; here the situation may be obscured by the proximity of the d-wave Feshbach resonance at 47.78 G [Lan09b].

Motivated by our previous observation that the temperature dependence of α_{rel} changes with the magnetic field in the $6s$ state [Fer08], we perform similar investigations in the g-wave states. In $4g(4)$, we check three points between 16.0 and 19.7 G, finding essentially the same behavior of a constant rate coefficient; see Fig. 7.4d. In $6g(6)$, we inspect the range between 25 and 45 G (data not shown), the temperature dependence being preserved over the full range. Comparing the observations on the two g-wave states with the behavior of the $6s$ state, which in contrast to all other states has a curvature, we find an interesting systematics. The temperature dependence shows up when the state is parallel to the atomic threshold, which means that threshold and molecular state have

the same magnetic moment. This is the case for the $6g(6)$ state and the $6s$ state in the halo regime. In contrast, we do not observe the temperature dependence when the magnetic moments are different, which is the case for the $4g(4)$ state, the $6l(5)$ state, and for the $6s$ state in the non-halo regime. It is also interesting to note that the two states that show a temperature dependence are also the only two for which resonances in dimer-dimer scattering have been observed. These observations may just be accidental coincidences, but they may also have a deeper physical reason.

7.5. Conclusion and outlook

We have reported on two phenomena where ultracold dimer-dimer collisions point to a more complex structure beyond the two-body physics of dimers. Understanding this structure is not only important from a fundamental point of view, it also holds potential for future experimental applications.

The occurrence of narrow loss resonances is most likely explained by coupling to tetramer states. The analogy of this situation to Feshbach resonances in atom-atom collisions [Chi10] points to potential applications, which can be found in controlling dimer-dimer interactions and in the association of more complex molecules. Because of the many open decay channels such molecules will be inherently unstable, but situations may exist where loss suppression mechanisms [Pet04b, D'I08] will enable observation times long enough for experimental applications. Then it may be possible to perform a magnetic field ramp to associate tetramers from colliding dimers. A related possibility would be a controlled rearrangement reaction where two dimers are converted into a trimer and a free atom [D'I09d]. Further possible applications of collisional resonances arise from the prospect to use strong dissipation in dimer-dimer collisions for realizing strongly correlated states of matter [Sya08].

The temperature dependence observed in some of the investigated collision channels provides hints on the existence of thresholds which are energetically slightly above the zero-energy threshold of two colliding dimers; this again points to the role of more complex molecular states. For the universal $6s$ halo dimer state, the existence of a trimer state indeed provides a plausible explanation for the observed behavior [D'I09d]. For the non-universal $6g(6)$ state, which shows a very similar temperature dependence over a wide magnetic field range, we can only speculate that a non-universal trimer or tetramer state may closely follow the dimer state's energy.

We are only beginning to understand the complex interaction properties of ultracold trapped molecules, but we already see intriguing phenomena with potential applications in this emerging research field.[1]

Acknowledgments

We thank C. Chin, S. Dürr, and J. D'Incao for stimulating discussions. We

[1]The original article includes a personal note by R. Grimm.

acknowledge support by the Austrian Science Fund (FWF) within SFB 15. F. F. was supported within the Lise Meitner program of the FWF, and S. K. was supported by the European Commission with a Marie Curie Intra-European Fellowship.

CHAPTER 8

OUTLOOK

The findings presented in this thesis clearly show the successful interplay of experimental and theoretical work in the universal regime. Experimental research on ultracold atomic quantum gases has contributed greatly to the verification and improvement of universal theories. These achievements motivated to extend the theoretical analysis to more complex systems showing several new few-body phenomena, which still miss experimental verification. Furthermore, the question needs to be answered whether a simple refinement of universal theories by incorporating non-universal properties exists, which would be capable of appropriately describing real-world systems, which are not far in the universal regime. In particular, further studies on Efimov and four-body states in different systems, including observation of consecutive resonances, are necessary in order to get a global overview of the situation in real-world systems. This might help our understanding of observed experimental discrepancies in comparison to the expectations arising from universal theory, such as the indicated deviation of the position of the atom-dimer Efimov resonances.

Up to now, only broad and intermediate Feshbach resonances were utilized for the study of few-body physics. For very narrow resonances, the three-body parameter in the Efimov scenario should be fixed by the Feshbach resonance parameter R^* as derived in Refs. [Pet04a, Gog08]. This prediction still lacks experimental verification, which could offer further insight into the properties of the three-body parameter.

So far, the research on universal phenomena has mainly focused on few-body processes involving samples with equal atomic isotopes, the exception being the observation of Efimov resonances in a bosonic RbK mixture [Bar09]. The rapid growth in the number of atomic mixture experiments allows studying new universal few-body phenomena. Research on (heteronuclear) Bose-Bose, Bose-Fermi and Fermi-Fermi mixtures will increase our knowledge of universality in systems offering different mass ratios, spin states, quantum statistics and interaction strengths. In the Efimov scenario, several theoretical predictions exist for non-identical particle systems [Ama72, Efi72, Efi73, D'I06b, D'I05b, D'I06a],

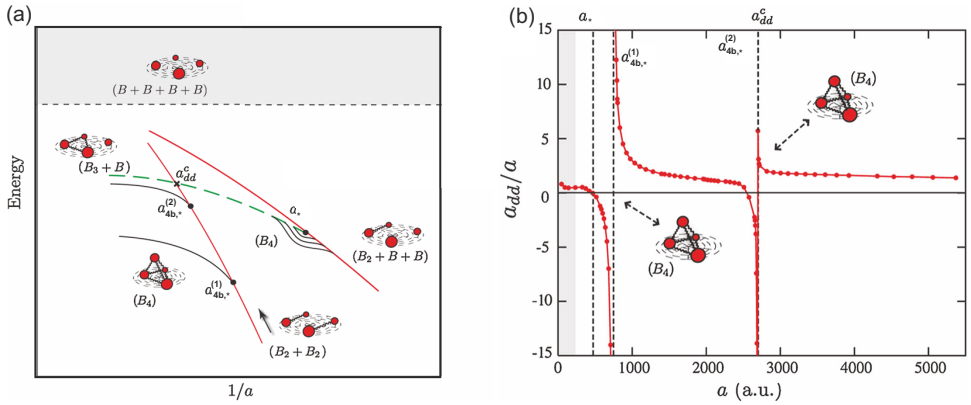

Figure 8.1.: Schematic representation of the universal four-body resonances at the dimer-dimer threshold in the extended Efimov scenario. (a) The plot visualizes the universal tetramer (B_4) states (black solid lines) coupling at $a^{(1)}_{4b,*}$ and $a^{(2)}_{4b,*}$ to the dimer-dimer (B_2+B_2) threshold (lower red curve). The state related to an Efimov trimer plus a free atom (green dashed line) crosses the dimer-dimer threshold at a^c_{dd} and couples to the dimer-atom-atom ($B_2 + B + B$) threshold (upper red curve) at a_*. The resonance of the atom-dimer scattering length at a_* induces an Efimov scenario involving two atoms and a dimer (black curves at a_*). The horizontal dashed line indicates the free atom threshold ($B + B + B + B$). (b) The coupling of the tetramer states to the dimer-dimer threshold leads to a resonant enhancement of the dimer-dimer scattering length a_{dd} at $a^{(1)}_{4b,*}$ and $a^{(2)}_{4b,*}$. Taken from Ref. [D'I09d] with modified labeling.

which haven't been tested yet. For example, it is expected that combinations of light-heavy-heavy particles, such as LiYbYb, LiCsCs and LiRbRb, offer favorable universal scaling factors, facilitating the observation of several consecutive Efimov resonances [Bar09, Efi73].

Furthermore, the conversion of ultracold atomic mixtures into samples of heteronuclear molecules opens up the field of ultracold chemistry, which offers a promising way of studying diverse chemical reactions under controlled circumstances [Car09, Osp10b, Kno10][1].

Universal dimer-dimer collisions present a yet barely explored research topic, which will offer a deeper insight into the properties of elementary four-body processes. Especially the coupling of the Efimov-related universal tetramer states [Ste09, Fer09a][2] to the dimer-dimer threshold are expected to give rise to resonance phenomena in universal dimer samples [D'I09d][3]. This scenario is shown in Fig. 8.1. Experimental verification of this scenario would allow for the creation of a universal dimer sample with tunable interactions. These measurements

[1] See also Chapter 3.
[2] See also Chapter 6.
[3] Possible evidence for this process might have already been observed in the dimer-dimer measurements reported in Chapter 5.

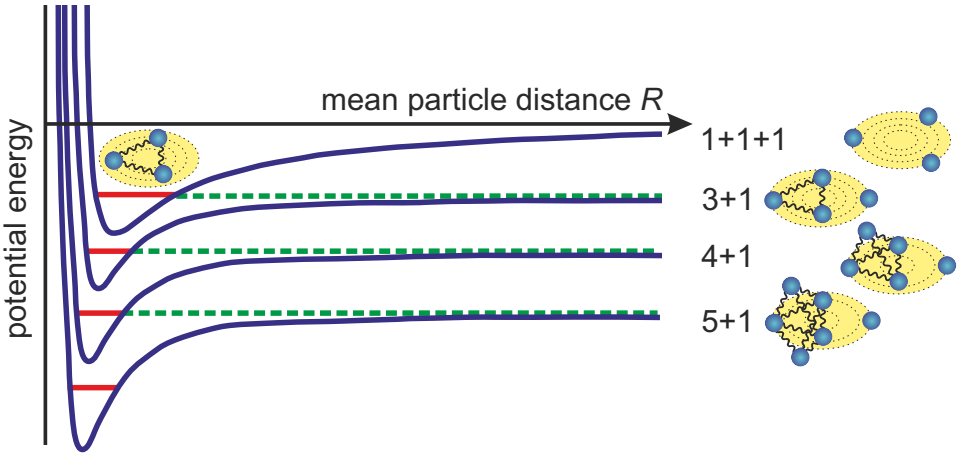

Figure 8.2.: The "cluster plus one atom" scenario of the Efimov family. Each hyperspherical potential curve (blue solid lines) supports a cluster state (red solid line), which creates another cluster-atom potential curve (green dashed line)[Ste10].

would also yield the yet unobserved intersection of the Efimov trimer state at the dimer-dimer threshold.

Another research route leads to the investigation of universal N-body clusters. Recent theoretical studies imply that universality can be extended to a so-called *Efimov family*, where each Efimov state is associated to a series of N-body cluster states, with $N > 3$ [Ste10, Ste11, Han06]. Different types of cluster states are expected to exist, such as clusters binding with one or more atoms to create new clusters. The "cluster plus one atom" scenario, which relates to the extended Efimov scenario, is depicted in Fig. 8.2. There are several questions concerning these cluster states, such as whether other higher-order parameters, besides the s-wave scattering length and the three-body parameter, are needed to fix the spectrum of these clusters. How do non-universal corrections enter the cluster scenario? A recent study suggests that no four- or higher-order parameters are necessary for the determination of five- and six-boson clusters [Ste11]. The observation of such a cluster state would increase the zoo of few-body states and open up a completely new direction of research. During the final stage of writing this thesis, we found experimental indications for the existence of a five-body cluster state connected to an Efimov trimer in the vicinity of the 787 G s-wave Feshbach resonance.

So far, experimental research has focused on few-body phenomena in three dimensions. For the intriguing case of reduced dimensions, no Efimov effect is expected for identical bosons [Nie01]. Nevertheless, there are several classes of systems where the Efimov effect should exist even if the number of dimensions is other than three [Nis11]. Theoretical studies suggest that of the infinite number of Efimov states in three dimensions, only two states survive the transition into the two-dimensional space [Nie97]. Recently, a one-dimensional optical lattice

that allows to study this transition was employed in our experimental setup. Furthermore, atomic mixture experiments make it in principle possible to create the fascinating situation of different dimensionalities for different species. This field is completely unexplored as yet.

The achievement of heteronuclear ground-state molecules in the ultracold regime [Ni08, Osp10a] is the initial step for studying universal few-body physics in dipolar quantum gases. A theoretical work on three interacting bosonic dipoles proposes not only that the Efimov effect persists, but also that dipolar interactions are extremely beneficial for the study of universal trimer states [Wan11b]. The three-body parameter should be defined by the dipolar interaction range, and the Efimov trimers become ever more long-lived for increasing dipolar interaction strengths. Therefore, a system of strongly dipolar particles might provide suitable conditions to directly observe a gas of Efimov trimer states for the first time.

These future studies will lead to a deeper understanding of the fascinating world of few-body phenomena, as well as reveal basic properties of quantum matter.

APPENDIX A

CESIUM ENERGY LEVEL STRUCTURE

In this appendix, an overview of the energy level structure of ^{133}Cs is given, focussing on its characterization in the magnetic high-field region. In the following, the magnetic high-field region refers to magnetic field strengths B between 150 G and 1400 G, which are experimentally accessible after a substantial reconstruction of our magnetic field system; see Appendix B. Precise knowledge of this structure is essential for setting up the high-field imaging system (Appendix C) and performing magnetic-field calibrations by means of microwave-spectroscopy (Appendix D).

Sec. A.1 summarizes the atomic properties resulting from the hyperfine and Zeeman interactions, as described in general textbooks on atomic physics, for example Ref. [Foo05]. In particular, this section focusses on the atomic cesium system[1]. The energy level structure of the ground-state and excited-state manifold is discussed in Sec. A.2 and Sec. A.3.

A.1. Hyperfine and Zeeman energies

The energy levels are described by an appropriate set of so-called "good" quantum numbers[2], which allow for an adequate characterization of the atomic state. This set of "good" quantum numbers is determined by the competition of the energy splittings related to the fine structure and hyperfine structure with the magnetic-field dependent Zeeman energy. As shown below, these sets differ for the ground- and excited-state manifold in the magnetic high-field region.

Cesium, being an alkali atom, has an electronic spin angular momentum quantum number[3] of $S = 1/2$, which leads to a splitting of the excited state into a

[1] An overview of the physical and optical properties of cesium is given in Ref. [Ste03].

[2] In this sense "good" means that the atomic properties can be easily read out from these quantum numbers.

[3] Here, the convention is used that bold letters refer to the angular momentum ($\mathbf{S}, \ldots$), and normal letters ($S, \ldots$) to the magnitude of the eigenvalue $\sqrt{S(S+1)}\hbar, \ldots$ of the angular momentum operators ($\hat{\mathbf{S}}, \ldots$); the eigenvalue of $\hat{S}_z$ is $m_S\hbar$, and so on.

fine-structure doublet with total electronic angular momentum quantum numbers $J = 1/2, 3/2$. Due to the large fine-structure splitting of cesium, it is not possible to observe the Paschen-Back effect for the fine structure, which leaves J as a good quantum number. The transition frequencies and line widths of the D_1 transition[4] ($6\,^2S_{1/2} \rightarrow 6\,^2P_{1/2}$) and the D_2 transition ($6\,^2S_{1/2} \rightarrow 6\,^2P_{3/2}$) can be found in Table A.1.

		D_1 - transition	D_2 - transition
wavelength (Vaccum)	λ	894.592 959 86(11) nm	852.347 275 82(27) nm
frequency	ν	335.116 048 807(41) THz	351.725 718 50(11) THz
natural line width	γ	4.561 2(57) MHz	5.222 7(66) MHz

Table A.1.: Optical transition properties of the D_1-line ($6\,^2S_{1/2} \rightarrow 6\,^2P_{1/2}$) and the D_2-line ($6\,^2S_{1/2} \rightarrow 6\,^2P_{3/2}$) [Ude99, Ude00]. The natural line width refers to the full width at half maximum (FWHM).

		$6\,^2S_{1/2}$	
magnetic dipole constant	A_{hfs}	$h \times 2.298\,157\,942\,5$ GHz	
hyperfine splitting	ΔE_{hfs}	$h \times 9.192\,631\,770$ GHz	
fine structure Landé g-factor	g_J	2.002 540 32(20)	
		$6\,^2P_{1/2}$	$6\,^2P_{3/2}$
magnetic dipole constant	A_{hfs}	$h \times 291.92(2)$ MHz	$h \times 50.275(3)$ MHz
electric quadrupole constant	B_{hfs}	0	$-h \times 0.53(2)$ MHz
fine structure Landé g-factor	g_J	0.665 90(9)	1.334 0(3)
Nuclear g-factor	g_I	$-0.000\,398\,853\,95(52)$	

Table A.2.: Hyperfine structure constants, nuclear g-factor and fine structure Landé factors for ^{133}Cs in the ground- ($6\,^2S_{1/2}$) [Ari77] and excited-states manifold ($6\,^2P_{1/2}$ and $6\,^2P_{3/2}$) [Ude99, Raf97, Tan88, Ari77]. The ground state hyperfine splitting and magnetic dipole constants are exact, resulting from the current definition of the second. For the ground-state manifold $B_{\mathrm{hfs}} = 0$, and the hyperfine splitting is related to the magnetic dipole constant by $\Delta E_{\mathrm{hfs}} = A_{\mathrm{hfs}}(I+1/2)$, which results from Eq. (A.1).

The energy levels feature a hyperfine structure due to the coupling of the nuclear angular momentum $\mathbf{I}$ with $\mathbf{J}$, with $I = 7/2$ for ^{133}Cs. In the approximation that J is a good quantum number, the Hamiltonian that describes the hyperfine interaction is given as [Cor77, Ale93]

$$\hat{H}_{\mathrm{hfs}} = \frac{A_{\mathrm{hfs}}}{\hbar^2}\hat{\mathbf{I}}\cdot\hat{\mathbf{J}} + \frac{B_{\mathrm{hfs}}}{\hbar^4}\frac{3(\hat{\mathbf{I}}\cdot\hat{\mathbf{J}})^2 + \frac{3\hbar^2}{2}\hat{\mathbf{I}}\cdot\hat{\mathbf{J}} - \hat{\mathbf{I}}^2\hat{\mathbf{J}}^2}{2I(2I-1)J(2J-1)}, \tag{A.1}$$

[4]The labeling refers to $n^{2S+1}\mathrm{L}_J$, with the principal quantum number n and L the electronic orbital angular momentum quantum number in the typical spectroscopic assignment, $L = 0, 1, 2, \ldots = S, P, D, \ldots$ [Rus29].

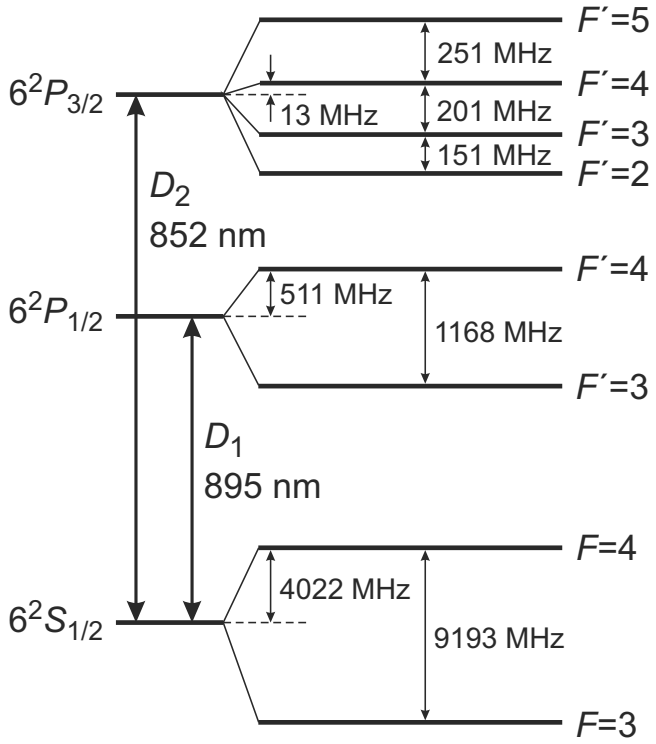

Figure A.1.: Level scheme of ^{133}Cs at zero magnetic field including hyperfine interaction. The dashed lines show the atomic energy levels without hyperfine interaction. The prime ($'$) denotes states of the excited-state manifold. Only D_2 transitions are employed in our experiments, as these transitions offer closed optical cycles. The imaging cycle at zero magnetic field is operated on the $F = 4 \rightarrow F' = 5$ transitions (not shown). Prior to that, the atoms are optically pumped from the $F = 3$ to the $F = 4$ state by a repumper beam resonant on the $F = 3 \rightarrow F' = 3$ transition.

with the magnetic dipole constant A_{hfs} and the electric quadrupole constant B_{hfs}. Table A.2 lists the values for the hyperfine structure constants, nuclear g-factor and fine structure Landé factors g_J of the ground and excited states.

In the low magnetic field regime, where the total atomic angular momentum $F = |\mathbf{J} + \mathbf{I}|$ is a good quantum number, the atomic states can be labeled by a set of good quantum numbers as $|\alpha, LSJIFm_F\rangle$. Here, α denotes all non-angular momentum quantum numbers. Then, the hyperfine interaction energies can easily be calculated using $\hat{\mathbf{I}} \cdot \hat{\mathbf{J}} = \frac{1}{2}(\hat{\mathbf{F}}^2 - \hat{\mathbf{J}}^2 - \hat{\mathbf{I}}^2)$ in Eq. (A.1). The resulting level scheme at zero magnetic field (including hyperfine interaction) is depicted in Fig. A.1.

The interaction with the magnetic field is described by the Zeeman Hamiltonian

$$\hat{H}_B = \frac{\mu_B}{\hbar}(\hat{\mathbf{L}} + g_S\hat{\mathbf{S}} + g_I\hat{\mathbf{I}}) \cdot \mathbf{B}, \tag{A.2}$$

which, for a magnetic field along the z-direction and depending on the atomic

state, becomes

$$|\alpha, Lm_L Sm_s Im_I\rangle \to \hat{H}_B = \frac{\mu_B}{\hbar}(\hat{L}_z + g_S\hat{S}_z + g_I\hat{I}_z)B_z, \quad (A.3)$$

$$|\alpha, LSJm_J Im_I\rangle \to \hat{H}_B = \frac{\mu_B}{\hbar}(g_J\hat{J}_z + g_I\hat{I}_z)B_z, \quad (A.4)$$

$$|\alpha, LSJIFm_F\rangle \to \hat{H}_B = \frac{\mu_B}{\hbar}g_F\hat{F}_z B_z. \quad (A.5)$$

The regime of applicability of Eqs. (A.4) and (A.5) results from the magnetic field dependent competition between hyperfine interaction and Zeeman energy. In the following, it is assumed that $B \simeq B_z$ (see Eq. (B.4)).

For small magnetic field strengths, hyperfine interaction dominates the Zeeman energy and the atomic states are well described in the $|\alpha, LSJIFm_F\rangle$ basis. The energy shift ΔE (with respect to the fine-structure energy levels at zero magnetic fields) is the result of the hyperfine energy $\Delta E_{\rm hfs}$ and the Zeeman energy ΔE_B [Ari77, Ale93],

$$\Delta E = \Delta E_{\rm hfs} + \Delta E_B, \quad (A.6)$$

$$\Delta E_{\rm hfs} = \frac{1}{2}A_{\rm hfs}K + B_{\rm hfs}\frac{\frac{3}{2}K(K+1) - 2I(I+1)J(J+1)}{2I(2I-1)2J(2J-1)}, \quad (A.7)$$

$$\Delta E_B = \mu_B g_F m_F B, \quad (A.8)$$

with

$$K = F(F+1) - I(I+1) - J(J+1). \quad (A.9)$$

The hyperfine Landé factor g_F is

$$g_F = g_J\frac{F(F+1) - I(I+1) + J(J+1)}{2F(F+1)} + g_I\frac{F(F+1) + I(I+1) - J(J+1)}{2F(F+1)} \quad (A.10)$$

$$\simeq g_J\frac{F(F+1) - I(I+1) + J(J+1)}{2F(F+1)}. \quad (A.11)$$

If the Zeeman energy exceeds the hyperfine splitting, the hyperfine Paschen-Back regime is entered, decoupling **J** and **I**. The magnetic field strengths employed in the experiment are large enough for the excited-state manifold to enter the Paschen-Back regime, but not for the ground-state manifold. The Paschen-Back eigenstates are $|\alpha, LSJm_J Im_I\rangle$ and the energy shift ΔE is given by [Ale93]

$$\Delta E = \Delta E_{\rm hfs} + \Delta E_B, \quad (A.12)$$

$$\Delta E_{\rm hfs} = A_{\rm hfs}m_J m_I + B_{\rm hfs}\frac{3(m_J m_I)^2 + \frac{3}{2}m_J m_I - I(I+1)J(J+1)}{I(2I-1)2J(2J-1)}, \quad (A.13)$$

$$\Delta E_B = \mu_B(g_J m_J + g_I m_I)B. \quad (A.14)$$

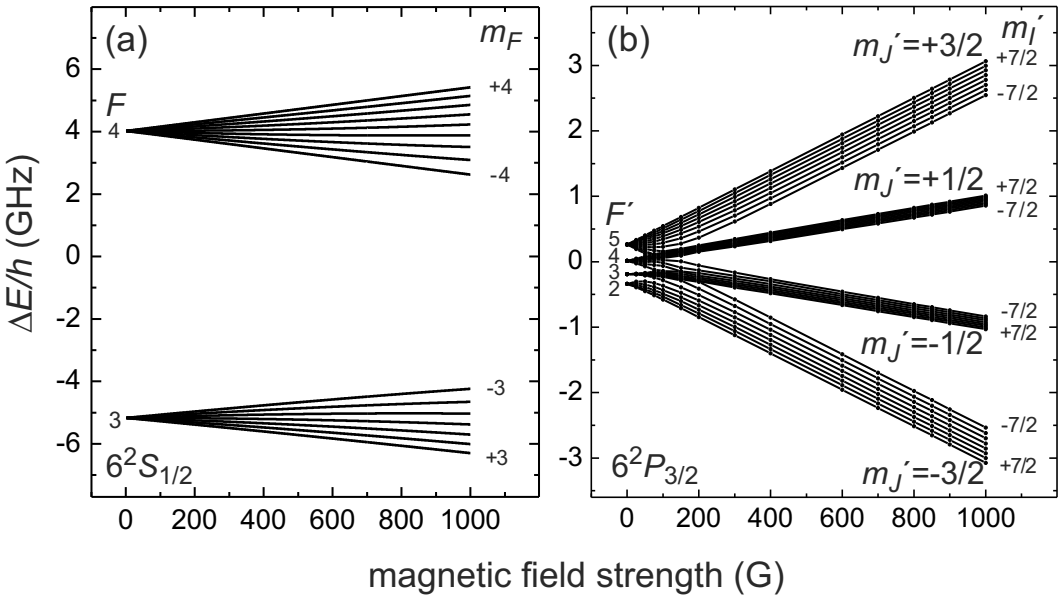

Figure A.2.: Magnetic field dependencies of the ground and excited state manifold hyperfine levels. (a) The ground state manifold ($6\,^2S_{1/2}$) is calculated with the *Breit-Rabi formula* [Bre31]. At zero magnetic field, the hyperfine states $F = 3$ and $F = 4$ feature an energy splitting of $h \times 9.192\ldots$ GHz. This splitting is larger than the Zeeman energy in the experimentally accessible magnetic field range. Therefore, the states are appropriately described in the $|\alpha, LSJIFm_F\rangle$ basis. The lowest line illustrates the absolute atomic ground state $|F = 3, m_F = 3\rangle$. (b) The excited state manifold of $6\,^2P_{3/2}$ is derived by numerical diagonalization of $\hat{H}_{\mathrm{hfs}} + \hat{H}_B$. The four possible hyperfine states $F' = 2, 3, 4, 5$ feature zero-field energy splittings of $h \times 151$ MHz ($F' = 2 \leftrightarrow 3$), $h \times 201$ MHz ($F' = 3 \leftrightarrow 4$) and $h \times 251$ MHz ($F' = 4 \leftrightarrow 5$). The Zeeman energies are comparable to these hyperfine splittings at relatively low magnetic field strengths of about 100 G. For increasing magnetic field strengths these states are in the hyperfine Paschen-Back regime and follow the grouping according to their m'_J quantum number.

A.2. Ground-state manifold

The ground-state manifold can be sufficiently well described in the $|\alpha, LSJIFm_F\rangle$ basis over the whole experimental tuning range of the magnetic field strength because of the large hyperfine splitting; see Fig. A.2(a). However, for precise determination of the atomic energies, state mixing has to be taken into account and $\hat{H}_{\mathrm{hfs}} + \hat{H}_B$ has to be diagonalized. For the ground state manifold, this diagonalization leads to an analytic expression, the *Breit-Rabi formula* [Bre31].

The *Breit-Rabi formula* is valid for both the (anomalous) Zeeman and the

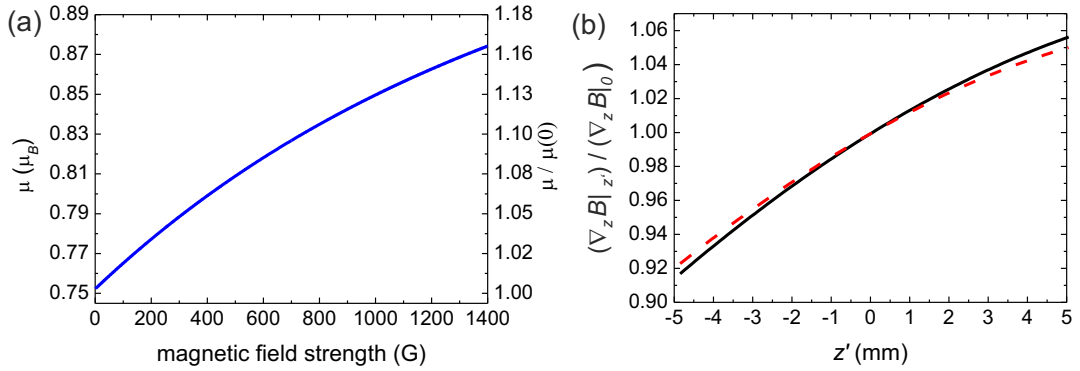

Figure A.3.: (a) Variation of $\mu(B)$ of cesium atoms in the absolute atomic ground states calculated by Eq. (A.15). (b) Sample calculation showing the dependency of $\nabla_z B|_{z'}$ on the vertical position z' of the atom cloud with respect to $\nabla_z B|_0$ at the geometric center of the magnetic bias coils. This calculation is based on typical current configurations of the magnetic bias coils, which are used to reach 500 G (black solid line) and 850 G (red dashed line).

hyperfine Paschen-Back regime[5] and reads as [Bre31]

$$\Delta E = -\frac{\Delta E_{\mathrm{hfs}}}{2(2I+1)} + g_I \mu_B m B \pm \frac{\Delta E_{\mathrm{hfs}}}{2}\sqrt{1+\frac{4mx}{2I+1}+x^2}. \tag{A.15}$$

The fine-structure m_J and nuclear m_I magnetic quantum numbers relate to m via $m = m_I + m_J = m_I \pm 1/2$, where the $\pm$ sign is the same as in Eq. (A.15) and

$$x = \frac{(g_J - g_I)\mu_B B}{\Delta E_{\mathrm{hfs}}}. \tag{A.16}$$

For magnetic field strengths experimentally accessible in our setup $m = m_F$. This can lead to sign ambiguities in the evaluation of Eq. (A.15), therefore it is favorable to use the more direct formula

$$\Delta E = \Delta E_{\mathrm{hfs}} \frac{I}{2I+1} \pm \frac{1}{2}(g_J + 2I g_I)\mu_B B, \tag{A.17}$$

for the two states $m = \pm(I + 1/2)$; sign as in Eq. (A.17).

Magnetic moment in the absolute atomic ground state

Typically, a magnetic gradient field[6] $\nabla_z B$ is applied during the experimental procedure to levitate the atoms against gravity. For this purpose, the gradient

[5] The *Breit-Rabi formula* does not take into account the quadratic Zeeman shift, which results from induced magnetic moments of closed shell electrons. In our case, this effect is negligible.

[6] The z-coordinate refers to the vertical direction.

field has to be adjusted as a function of the magnetic moment $\mu(B)$ in order to fulfill the levitation condition

$$\frac{\partial B}{\partial z} = \frac{mg}{\mu(B)} \xrightarrow{\text{for B=0}} \frac{\partial B}{\partial z} = 31.1\,\frac{\text{G}}{\text{cm}}, \tag{A.18}$$

with the ^{133}Cs mass m and the gravitational acceleration in Innsbruck $g = 9.80636\,\frac{\text{m}}{\text{s}^2}$.

The magnetic moment of atoms in the absolute ground state rises for increasing magnetic field strength from the zero-field value $\mu(0) \simeq 0.75\mu_B$ to $\mu(B) \simeq \mu_B$ in the Paschen-Back regime. This leads to a considerable shift of $\mu(B)$, even with experimentally accessible magnetic field strengths; see Fig. A.3(a).

In the experimental sequence, the levitation field is decreased simultaneously with the increase of $\mu(B)$ for higher magnetic field strengths. For the 800 G (550 G) region, this increase amounts to approximately 11% (8%) in comparison to $\mu(0)$. Experimentally, the adaptation of the levitation field for the 800 G (550 G) region is smaller than expected: $4 \pm 2\%(2 \pm 2\%)$.

This effect might be explained by a misalignment of the trap center relative to the geometric center of the vacuum chamber, in combination with an axial magnetic curvature field C^{Bias}, which is created as a side-effect by the coils that produce the magnetic bias field[7] B^{Bias}. The total magnetic field strength results from the contributions of $B^{\text{Grad.}}(z') = \nabla_z B^{\text{Grad.}}|_0 z'$ of the *Gradient coils* and $B^{\text{Bias}}(z')$, and can be written as

$$\begin{aligned} B(z') &= B^{\text{Bias}}(z') + B^{\text{Grad.}}(z') && \text{(A.19)} \\ &\simeq B^{\text{Bias}}(0) + C^{\text{Bias}} z'^2 + \nabla_z B^{\text{Grad.}}|_0 z'. && \text{(A.20)} \end{aligned}$$

This gives rise to a position-dependent magnetic gradient field according to

$$\nabla_z B|_{z'} = \nabla_z B^{\text{Grad.}}|_0 + 2C^{\text{Bias}} z', \tag{A.21}$$

with $C^{\text{Bias}} z' \ll \nabla_z B^{\text{Grad.}}|_0$. Therefore, the magnetic field gradient necessary for levitation of the atom sample depends on the vertical position of the atom cloud, relative to the geometric center of the magnetic bias coils; see Fig. A.3(b).

A.3. Excited-state manifold

Only the $6\,^2P_{3/2}$ manifold is discussed here, as only this manifold offers closed optical cycle transitions and is therefore relevant to our experimental procedure. Due to the small hyperfine splitting of the $6\,^2P_{3/2}$ states, the **IJ**-coupling breaks down at field strengths as low as about 100 G; see Fig. A.2(b). For the magnetic field strengths that are applied for high-field imaging (between 500 G and 1000 G; see Sec. C.2), the hyperfine Paschen-Back regime is reached and the states are appropriately described in the $|\alpha, LSJm_J Im_I\rangle$ basis. In order to take

[7] These are the so-called *Bias coils*. A description of the different coils is given in Appendix B.

into account residual state mixing effects for the calculation of ΔE, the Hamiltonian $\hat{H}_{\rm hfs} + \hat{H}_B$ is numerically diagonalized in the $|\alpha, LSJm_J Im_I\rangle$ basis. For large magnetic field strengths, the results of this procedure, which are shown in Fig. A.2(b), approach the solutions of Eqs. (A.12) - (A.14).

This diagonalization is simplified by neglecting the small electric quadrupole constant $B_{\rm hfs} = -h \times 0.53(2)$ MHz, which allows us to write the hyperfine interaction Hamiltonian as

$$\hat{H}_{\rm hfs} \simeq \frac{A_{\rm hfs}}{\hbar^2}\hat{\mathbf{I}}\cdot\hat{\mathbf{J}} = \frac{A_{\rm hfs}}{\hbar^2}\big(\hat{I}_z\hat{J}_z + \frac{1}{2}(\hat{I}_+\hat{J}_- + \hat{I}_-\hat{J}_-)\big), \tag{A.22}$$

with the ladder operators defined as $\hat{J}_\pm = \hat{J}_x \pm i\hat{J}_y$ and $\hat{I}_\pm = \hat{I}_x \pm i\hat{I}_y$, leading to off-diagonal matrix elements. The solution involves the diagonalization of one 2×2 matrix ($m'_F = \pm 4$), one 3×3 matrix ($m'_F = \pm 3$) and three 4×4 matrices ($m'_F = 0, \pm 1, \pm 2$), while the $m'_F = \pm 5$ states are obtained directly.

APPENDIX B

MAGNETIC FIELD SYSTEM

Magnetic fields play a major role in achieving Bose-Einstein condensation as well as the observation of (universal) few-body physics due to the tunability of the s-wave scattering length a with the magnetic field strength B in the vicinity of a Feshbach resonance. The publications presented in Chapters 2, 3, 5, 6 and 7 are based on a magnetic field setup restricted to the magnetic low-field region up to 150 G, where a can be tuned between $-2500a_0$ and $1600a_0$ [Web03a].

To accomplish the experimental results presented in Chapter 4 a major upgrade of the magnetic field system was necessary. This new system allows performing measurements in the magnetic high-field region up to 1400 G, with $\sim$ 10 mG stability. The reason for upgrading is the existence of two broad open-channel dominated Feshbach resonances with poles at 549 G and 787 G; see Table F.9. The new setup enables us to exploit the unrestricted tunability of $a(B)$ in the vicinity of these Feshbach resonances.

B.1. Overview

This section gives a short overview of the constituent parts of the upgraded magnetic field setup; see Fig. B.1. The setup is based on paired or single coils, which generate the magnetic field at the geometric center of the vacuum chamber. New components are marked by the symbol (*) and are discussed in this appendix, whereas components that are parts of the previous setup are explained in the PhD theses of my predecessors [Mar08b, Kra06a, Her05].

Bias coils* (see Sec. B.2 and Ref. [Har10])

These coils represent the heart of the new magnetic field setup by producing a stable and homogenous magnetic field up to 1400 G. Basically, the *Bias coils* consist of a modular system of three independent units. Each of these units is composed of one or two coil pairs in Helmholtz configuration and features

individual electronic control, safety installations and water-cooling. This system is described in detail in this appendix.

Curvature coils* (see Sec. B.3 and Ref. [Har10])

The *Bias coils* introduce a small curvature of the magnetic field, due to small inevitable variations from the perfect Helmholtz configuration. Therefore, a set of *Curvature coils* has been implemented, which are capable of correcting for this effect. Moreover, the magnetic field curvature produces trapping and anti-trapping potentials, which can be exploited in future experiments to create a hybrid optical and magnetic trap.

Vertical compensation coils* (see Sec. B.4)

The strong magnetic bias field leads to a remanence effect of the surroundings[1]. To counterbalance this effect, a set of *Vertical Compensation coils* was implemented.

Horizontal compensation coils (see Ref. [Her05])

In order to compensate for stray fields[2], which rotate the magnetic field vector, we use two orthogonally oriented pairs of rectangular coils. These so-called *Horizontal Compensation coils* create a small horizontal bias field.

Gradient coils (see Ref. [Her05])

Besides the magnetic bias coils, all of them in Helmholtz configuration, a pair of *Gradient coils* in Anti-Helmholtz configuration supplies a constant magnetic field gradient, which is essential for several experimental stages. First, these coils provide the quadrupole field for the magneto-optical trap. Furthermore, these coils create a magnetic levitation field, which counteracts gravity; see Sec. A.2. In experiments involving dimers (Chapters 2, 3, 5, and 7) the magnetic field gradient was employed to distinguish between atomic and dimer clouds, see for example Fig. 2.2, by a Stern-Gerlach separation technique.

Supplementary bias coils (see Ref. [Mar08b])

In addition to the strong *Bias coils*, the experimental setup consists of several supplementary bias coils, which offer different ranges of applications.

The electronic controls for the strong *Bias coils* are optimized for large magnetic field ramps of several hundred Gauss. Therefore, a different pair of extra

[1] The origin of this remanence is not unambiguously attributable, as the vacuum chamber is made from non-magnetic stainless steel of grades AISI 316LN (DIN W.-Nr. 1.4429) and AISI 316L (1.4435). Both materials are virtually ferrite-free and specified with a magnetic permeability of $\mu \leq 1.005$ [Web03a].

[2] Such magnetic stray fields can be introduced by electronic devices, such as ion pumps, or magnetized parts in the vicinity of the vacuum chamber.

Helmholtz-coils (the so-called *ExtraHH coils*) is used for small magnetic field ramps of up to 62 G. This pair of coils exhibits switching times of $\tau_{\text{switch}} = 1.5$ ms and is used for Feshbach tuning and molecule production.

To accomplish fast changes of the magnetic field strength, two other coils are used in the experimental setup. First, a pair of small Helmholtz-coils (the so-called *SmallHH coils*) allows for magnetic field jumps of 10 G within a rise time of 300μs. This pair of coils is situated directly on the re-entrant viewports to induce smaller eddy currents. On the upper viewport, an even smaller single coil is placed. This so-called *Booster coil* enables ultra-fast magnetic field jumps of up to 8 G within 500 ns, perfectly suited to perform diabatic magnetic field ramps at molecular avoided level crossings.

A summary of the properties of all the magnetic field coils can be found in Table B.1.

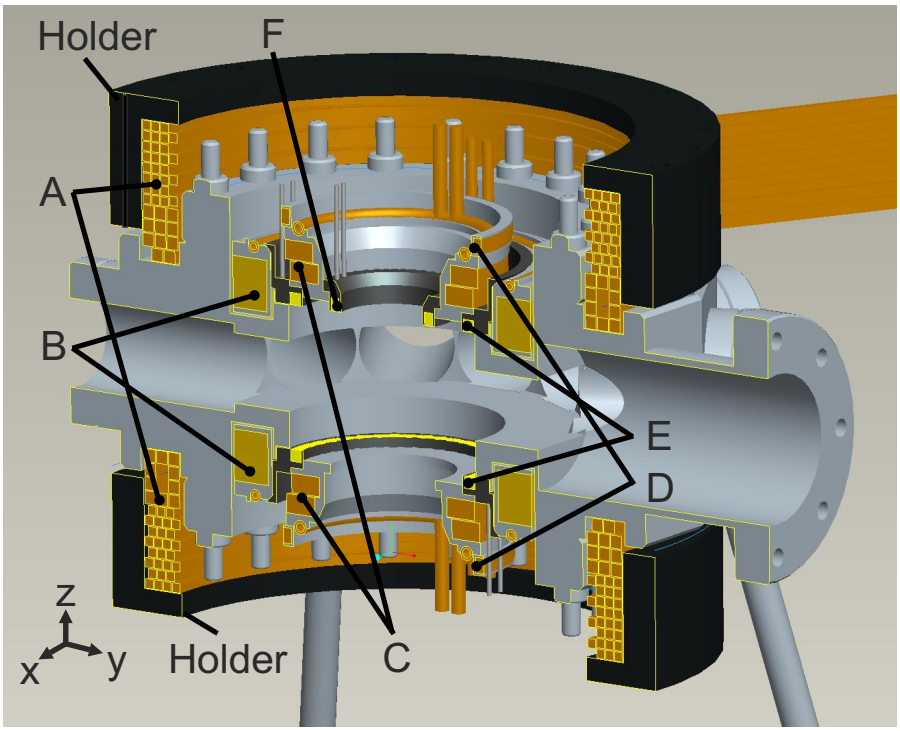

Figure B.1.: Lateral cut through the main vacuum chamber showing the magnetic coil system. The Zeeman-slowed atomic beam enters the chamber from the left viewport along the y-direction. The trapping and cooling stages, which are extensively described in Refs. [Web03a, Her05, Kra06a, Mar08b], take place in the geometrical center of the main chamber. The coils shown in this figure produce a rotational symmetric magnetic field along the z-direction. Note that the *Horizontal Compensation coils* are not shown in this figure. The *Bias coils* (A) consist of three separately controllable sets of coils in Helmholtz-configuration, able to reach a total magnetic field of $\sim$ 1400 G. The coil body (B) contains the *Gradient coils*, which are connected in anti-Helmholtz configuration, and a pair of coils which produces additional magnetic fields up to $\sim$ 60 G (*ExtraHH coils*). A set of *Curvature coils* (C) compensates or increases the magnetic field curvature produced by the *Bias coils*. *Vertical Compensation coils* (D) are used to correct for the magnetization of the chamber and its surroundings. In order to perform fast magnetic field jumps, two coils are mounted directly at the re-entrant viewports, the so-called *SmallHH coils* (E), $\tau_{\text{switch}} \sim 300\,\mu$s, and the single *Booster coil* (F), $\tau_{\text{switch}} \sim 500$ ns.

coil-labeling (see Fig. B.1)	Bias - unit 1 (A)	Bias - unit 2 (A)	Bias - unit 3 (A)	Curvature (C)	Vert. comp. (D)
mean radius (mm)	112	112	112	40	49
mean axial distance (mm)	105	148	185	99	136
max. fields (G)	739	373	295	72	3.7
windings per side	11	14 (2×7)	14 (2×7)	46 (2×23)	23
calibration value[1]	0.924 G/A	0.932 G/A	0.737 G/A	3.6 G/A	0.371 G/V
curvature/current [2] ($mG/cm^2/A$)	-2.0	7.0	10.3	541.2	116.5
max. input values[3]	800 A	400 A	400 A	$\pm$20 A	$\pm$10 V

coil-labeling (see Fig. B.1)	Gradient (B)	ExtraHH (B)	SmallHH (E)	Booster (F)	Horiz. comp.[4]
mean radius (mm)	66		44	24	[5]500
mean axial distance (mm)	74		67	[6]34	400
max. fields	84 G/cm	62 G	10 G	8 G	1 G
windings per side	[7]2×31	48	6	4	70
calibration value	0.836 G/cm/A	6.181 G/V	1.188 G/V	0.254 G/A	0.1 G/V
max. input values[3]	100 A	10 V	8 V	3 V ($\equiv$ 30 A)	$\pm$10 V

Table B.1.: Summary of the magnetic field coils. For a detailed description of the previous magnetic field system (lower part of the table) see Ref. [Her05]. The lower part of the table can also be found in a similar format in Ref. [Mar08b].
[1]The calibration values for the *Bias coils* and the *Vertical compensation coils* are measured, whereas the value for the *Curvature coils* is calculated. The real currents of the *Bias coils* are 10% lower than the input values because of the delivery of wrong precision resistances for the electronic control circuits. The calibration values with these resistances in reference to the input values A′ are: unit 1: 0.840 G/A′, unit 2: 0.847 G/A′ and unit 3: 0.670 G/A′.
[2]The values for the magnetic field curvatures are based on calculations.
[3]These are the max. input values for the experimental control software. For the *Curvature coils*, the feed-back control system introduces a current offset with respect to the input value, which has not yet been corrected.
[4]Taken from Ref. [Web03a].
[5]The value refers to the side length of the rectangular coil.
[6]The distance to the center of the vacuum chamber is given, as the *Booster coil* consists of a single coil mounted on the upper re-entrant viewport of the vacuum chamber.
[7]These two sets of coils are connected in parallel.

B.2. Bias coils

B.2.1. Design

In order to allow the investigation of few-body physics without limitations due to stability or tunability of the s-wave scattering length, a setup of new bias coils has been implemented. These coils consist of three separately controlled units; see Fig. B.2 and Table B.1. Unit 1 almost fulfills the Helmholtz(HH)-configuration and generates a constant magnetic field in the center of the main chamber. Units 2 and 3 deviate slightly from the optimum HH-position and introduce a small magnetic field curvature $C \neq 0$; see Sec. B.2.2. The advantage of this system of individual units is the adjustability of the magnetic field curvature and faster ramping times due to the optimization of the control circuits. Moreover, constructing a single hard coil body was impossible due to geometric reasons, as the legs of the vacuum chamber limit the maximum extension of a single coil body.

Materials

The coils are made of square profile copper tubes (purchased at Eugen Geyer GmbH), which feature square holes for water-cooling. The side lengths of these tubes are 5.5 mm for unit 1 and 4 mm for units 2 and 3. The cooling holes have a side length of 2.7 mm for unit 1 and 2 mm for units 2 and 3. This results in a conducting area cross-section of $A_{\mathrm{cond}} = 23\ \mathrm{mm}^2$ for unit 1 and $A_{\mathrm{cond}} = 12\ \mathrm{mm}^2$ for units 2 and 3. Due to the difference in area cross-sections, unit 1 is able to reach a maximum current of 800 A, whereas for units 2 and 3 the current is restricted to 400 A [3].

The copper tubes are insulated by glass fiber braided sleevings (ETS Favier TPL), with an insulating layer thickness of 0.25 mm. These sleevings feature a dielectric strength of $\sim 0.5 - 1.5$ kV and are specified to a continuous working temperature up to +450°C.

Due to the permeability of the sleeving, each coil was adhered with an epoxy resin (Hysol RE2039/HD3561, Loctite), which features a strong resistance to mechanical impact. The dielectric strength of the epoxy resin is sufficiently large ~ 1.8 kV/mm, but the heat deflection temperature is only +84°C.

Coil configuration

In contrast to thin conducting wires, asymmetries in the wiring process lead to strong magnetic field inhomogeneities for the rather thick copper tubes. Especially, spiraling out windings and, more importantly, asymmetric wire segments resulting from vertical layer transition, would provoke a horizontal magnetic field gradient at the center of the trap. To compensate for this effect, the upper and lower coils are constructed as perfect mirror images of each other, including windings and supply lines.

[3] These restrictions depend on the power supplies in use and the pressure of the cooling water.

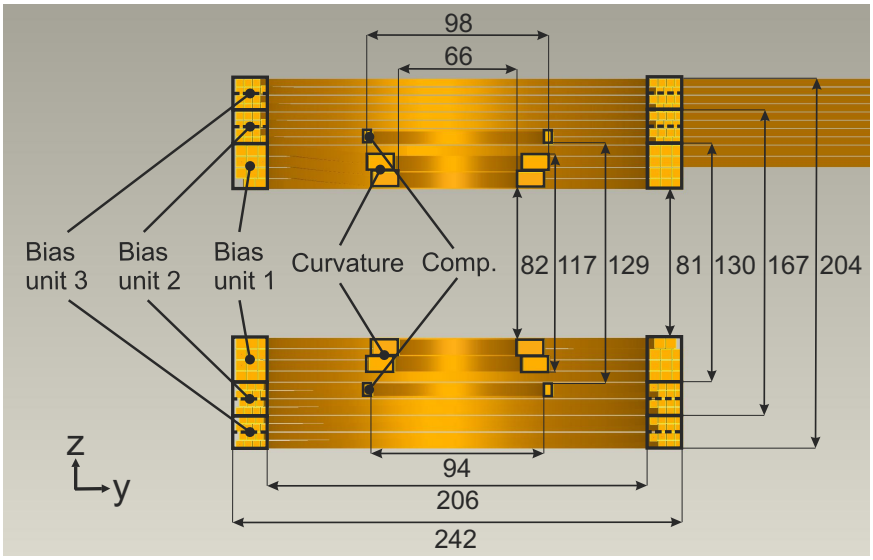

Figure B.2.: Vertical cut showing the design of the newly added coils. The *Bias coils* are separated into the units 1, 2 and 3. Diameters and axial distances are indicated in mm. For the *Bias coils*, the solid rectangular boxes emphasize the different units, whereas the dashed lines indicate the different coils, belonging to the same unit. Likewise, solid boxes point to the *Curvature* and *Vertical compensation coils*. The holders of the coils are not shown in this picture.

Unit 1 features $N_r = 3$ radial and $N_a = 4$ axial windings, which results in a total number of $N = 11$ windings[4]. Units 2 and 3 are geometrically identical and each of them is composed of two coils with $N_r = 4$ and $N_a = 2$, $N = 7$. These two coils are connected electrically in series by a solid copper rod, building up a unit with $N = 14$ windings in total. Although each of the units 2 and 3 is a constituent entity electronically, physically they consist of four separated coils[5]. The main advantage of this design is that water-cooling for all 10 coils is operated in parallel, optimizing the cooling power; see Sec. B.2.3.

The radial extension of all units is 18 mm. The axial extensions are 24.5 mm for unit 1 and 18.5 mm for units 2 and 3, including a 0.5 mm layer of epoxy resin flattening out the horizontal surfaces of the coils.

Mounting

The *Bias coils* are mounted directly onto the main vacuum chamber by a holder made of plastic[6] using the pre-existing screw-holes of the vacuum chamber. The holder has an inner (outer) diameter of 242.5 mm (275 mm) aligning the coil body and a wall thickness in axial direction of 10 mm.

[4] At least one winding is "lost" due to the transition from one layer to another in the winding procedure. The design was optimized to reduce the amount of lost windings to one.
[5] This design was not possible for unit 1 because of geometrical restrictions; see Fig. B.1.
[6] The material of the holder was chosen to prevent eddy currents.

The force acting on the *Bias coils* at maximum magnetic field strength[7] was calculated [Ber87] as ~ 200 N. This relatively small force legitimates the simple mounting structure. No vibrations due to current switching occurred in the experimental cycle.

B.2.2. Curvature and Trap frequencies

The position of the *Bias coils* deviates slightly from the perfect Helmholtz configuration[8], which causes a small magnetic field curvature C.

The definition of C follows from a Taylor series of the magnetic field $\mathbf{B} = (B_z, B_\rho)$, which is created by two circular current loops situated at $z = \pm D$ [Mey05],

$$\begin{aligned} B_z(I) &= \mu_0 I \frac{R^2}{(D^2+R^2)^{3/2}} + \frac{3\mu_0 I}{2}\frac{R^2(4D^2-R^2)}{(D^2+R^2)^{7/2}}(z^2-\rho^2/2)+\dots \\ &= B_{z=0}(I) + C_z(I)(z^2-\rho^2/2)+\dots \qquad \text{(B.1)} \\ B_\rho(I) &= -\frac{3\mu_0 I}{2}\frac{R^2(4D^2-R^2)}{(D^2+R^2)^{7/2}} z\rho + \dots \\ &= -C_\rho(I) z\rho - \dots \qquad \text{(B.2)} \end{aligned}$$

It directly follows that $C_z = C_\rho \equiv C$. For $B_{z=0} \gg C(I)(z^2-\rho^2/2)$ and $B_{z=0} \gg C(I)z\rho$ the magnitude of the magnetic field B is approximately

$$\begin{aligned} B = |\mathbf{B}| &\simeq \sqrt{\left(B_{z=0}(I) + C(I)(z^2-\rho^2/2)\right)^2 + \left(C(I)z\rho\right)^2} \qquad \text{(B.3)} \\ &\simeq B_{z=0}(I) + C(I)(z^2-\rho^2/2). \qquad \text{(B.4)} \end{aligned}$$

The magnetic field curvature $C(I)$ leads to a confinement either in radial or axial direction, in addition to the optical trap, with trapping and anti-trapping frequencies, respectively, given as [Alt07a]

$$\begin{aligned} \nu_\rho^{\mathrm{mag}} &= \frac{1}{2\pi}\sqrt{\frac{\mu(B)}{m}C(I)}, \qquad \text{(B.5)} \\ \nu_z^{\mathrm{mag}} &= \frac{1}{2\pi}\sqrt{-2\frac{\mu(B)}{m}C(I)}. \qquad \text{(B.6)} \end{aligned}$$

Considering the values of Table B.1, the radial trapping frequency[9] can be estimated using the zero-field magnetic moment[10] $\mu(B) \simeq 0.75\mu_B$ as

$$\nu_\rho^{\mathrm{mag}}(\mathrm{Hz}) = 0.0283\left(\frac{\mathrm{Hz}}{\sqrt{\mathrm{A}}}\right)\sqrt{-2I^{\mathrm{unit1}}(A) + 7I^{\mathrm{unit2}}(A) + 10.3I^{\mathrm{unit3}}(A)}. \qquad \text{(B.7)}$$

[7] According to Table B.1

[8] This deviation is inevitable, due to geometric restrictions, which are imposed by the design of the main vaccum chamber.

[9] The vertical anti-trapping frequency is $\nu_z^{\mathrm{mag}} = i \cdot \sqrt{2}\nu_\rho^{\mathrm{mag}}$.

[10] Strictly speaking, the magnetic field dependence of $\mu(B)$ has to be taken into account; see Sec. A.2.

This value can be further increased or decreased using the *Curvature coils*. The trapping frequency at 1000 G is typically at the order of $1.5 - 2$ Hz. In future applications, this allows for the creation of a hybrid optical and magnetic trap.

B.2.3. Water-cooling system

A major feature of the *Bias coils* is the internal water-cooling, which allows current densities exceeding 30 A/mm^2. A Grundfos CRE 3-36 centrifugal pump supplies each of the 10 coils with $p = 10$ bar of water pressure[11]. As the water flow decreases for increasing length of the copper tubes, the water-cooling is connected to the coils in parallel.

The electric power dissipation P in one unit can be estimated as

$$P = \sharp(\text{coils/unit}) \frac{(N \times 2\pi r + l_s)\rho}{A_{\text{cond}}} I^2 \tag{B.8}$$

where r is the mean radius, $l_s = 2 \times 1.5\,\text{m}$ the length of the supply lines of the copper tubes[12] and $\rho = 1.68 \times 10^{-8}\,\Omega\,\text{m}$ the electric conductivity of copper. This results in $P_{\text{max}}^{\text{unit1}} = 10$ kW and $P_{\text{max}}^{\text{unit2,3}} = 7$ kW for the maximum currents given in Table B.1. In our situation, the water flow does not follow the Hagen-Poiseuille equation for laminar flow, due to the fact that the Reynolds number exceeds the critical value of 2300 for the water pressure in use; see Fig. B.3. Therefore, the water flow is in the regime of turbulences[13], where the flow resistance grows quadratically with the flow rate. The measured flow rate f for the large (5.5 mm) and small (4 mm) tubes can be extrapolated[14] by a simple square root fit $f(\text{l/min}) = c_{\text{fl}}\sqrt{p(\text{bar})}$, yielding $c_{\text{fl}}^{5.5\text{mm}} = 0.46\,\frac{\text{l}}{\text{min}}\frac{1}{\sqrt{\text{bar}}}$ and $c_{\text{fl}}^{4\text{mm}} = 0.24\,\frac{\text{l}}{\text{min}}\frac{1}{\sqrt{\text{bar}}}$, respectively. This results in expected flow rates of $f^{5.5\text{mm}} = 1.5$ l/min and $f^{4\text{mm}} = 0.76$ l/min at $p = 10$ bar. Considering the number of coils in each unit, each *Bias coil* unit should feature a water flow of ~ 3 l/min. This simple estimate fits nicely with the optimized set points of the safety flow meters in use, which are set to 2.5 l/min for each unit; see Sec. B.2.5.

The temperature increase in the coils can be calculated by

$$\Delta T = \frac{P}{\rho_{\text{m}} C_{\text{W}} f} \tag{B.9}$$

[11] The maximum water pressure is flow dependent, for 35 l/min it is approximately 20 bar. Apart from this cooling cycle, experimental water-cooling is provided by another 3 bar pump, which is used for the *Gradient* and *Curvature coils*, as well as for the electronic control board of the *Bias coils*, the secondary circuit of the CO_2 chiller, the CO_2 beam dumps and high-power AOMs.

[12] The endings of the copper tubes are routed away from the main chamber, down alongside the optical table and end 10 cm above the floor, where they are connected to the electric and water supplies. That way, a breakage of the water connection does not endanger the optical setup.

[13] In the turbulent regime, convection leads to an efficient heat transfer. Therefore, we assume that the outgoing water is in thermal equilibrium with the coils.

[14] For safety reasons we have not performed water flow rate measurements at 10 bar.

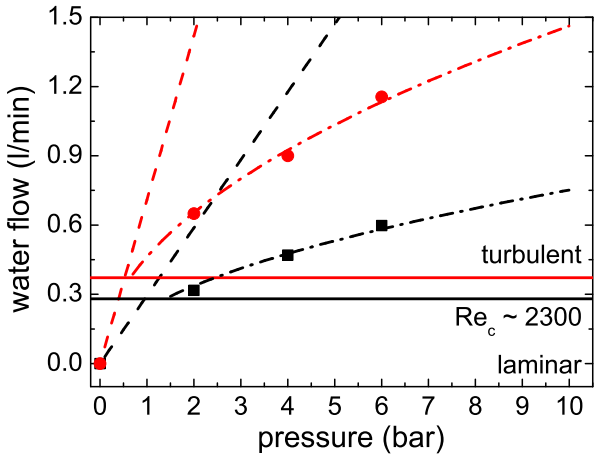

Figure B.3.: Measurements of the water flow rate for 2, 4 and 6 bar. For low pressures, the water flow increases drastically for both the 5.5 mm tube (red dots) and the 4 mm tube (black squares). Already at 2 bars the Reynolds number exceeds the critical number of 2300 (red and black solid lines) and the turbulent flow regime is reached. The dash-dotted lines are a square-root fit for the turbulent regime, which correspond very well with the values of the safety flow meters at 10 bar. The dashed lines mark the expectations for the laminar regime, following the Hagen Poiseuille equation.

with the density $\rho_{\mathrm{m}} = 998.2\ \mathrm{kg/m^3}$ and the specific heat capacity of water $C_{\mathrm{W}} = 4186\ \mathrm{J/kg/K}$. For a magnetic field strength of 1400 G this results in $\Delta T^{\mathrm{unit1}} \sim 48\,^{\circ}\mathrm{C}$ and $\Delta T^{\mathrm{unit2,3}} \sim 33\,^{\circ}\mathrm{C}$.

Optimum temperature condition

In principle, the highest achievable magnetic field strength is limited by the maximum temperature increase $\Delta T \sim 80°\mathrm{C}$ according to Eq. (B.9). The optimum temperature condition is reached when ΔT matches for all units. As the flow rates of the individual units are approximately the same, $f^{\mathrm{unit1}} \sim f^{\mathrm{unit2}} \sim f^{\mathrm{unit3}}$ the optimum condition is obtained for $I^{\mathrm{unit1}} = \frac{5}{3} I^{\mathrm{unit2,3}}$, according to Eq. (B.8)[15]. Together with the value given in Table B.1 this leads to a magnetic field of $B(\mathrm{G}) = 1.94(\mathrm{G/A}) I^{\mathrm{unit1}} = 3.24(\mathrm{G/A}) I^{\mathrm{unit2,3}}$. So for the optimum condition ΔT can be estimated by[16]

$$\Delta T(^{\circ}\mathrm{C}) \sim 6.32 \times 10^{-5} \left(\frac{^{\circ}\mathrm{C}\sqrt{\mathrm{bar}}}{\mathrm{G}^2} \right) \times \frac{\left(B(\mathrm{G})\right)^2}{\sqrt{P(\mathrm{bar})}}, \tag{B.10}$$

[15]The dissipated power is the same for all units for these current configurations.
[16]This temperature increase is in reference to the incoming water temperature $T_0 \sim 16°\mathrm{C}$.

with

$$I^{\text{unit1}}(\text{A}) = \frac{B(\text{G})}{1.94} \qquad \text{and} \qquad I^{\text{unit2,3}}(\text{A}) = \frac{B(\text{G})}{3.24}. \tag{B.11}$$

For 1000 G, this corresponds to a temperature increase of $\Delta T \sim 20°\text{C}$ for a current configuration $I^{\text{unit1}} = 520$ A and $I^{\text{unit2,3}} = 310$ A. Typically, this is the configuration used in the experiment. The applicability of the optimum temperature condition is restricted only due to the current limitations set by the power supplies (800 A/400 A) and the fact that the water pressure should not exceed 16 bar, which is the specified maximum for several of the water connections in use.

B.2.4. Control system

The magnetic field system is operated via a self-made Labview software program. The current control of each *Bias coil* unit is based on an active electronic feedback system, which stabilizes the magnetic field strength to ~ 10 mG. The complete control system leads to a $1/e$-rise time for the *Bias coils* of about 6 ms for a 500 G jump. This value changes moderately for different magnetic field strengths[17].

In this section, the control system of the *Bias coil* units is described in detail; see Fig. B.4.

Control interface

The experimental timing sequence is operated via a real-time control and measurement system (Keithley ADwin-Gold-DA)[18], which is initialized before each experimental cycle by a self-written Labview interface [Web03a]. This Adwin-system is synchronized by a line trigger with the power line to minimize environmental cycle-to-cycle fluctuations [Her05]. The analog channels feature a 16 bit resolution at a voltage range of ± 10 V.

The pre-programmed Adwin-system provides the analog set voltages for the proportional-integral-derivative (PID) controllers, which regulate the currents in the magnetic coil-system. The voltage range $\pm\,10$ V of the analog Adwin outputs thereby corresponds to the full current range of the power supplies. Furthermore, the control system enables a fast switch-off of the coil currents via digitally controlled insulated-gate bipolar transistors (IGBTs).

Feedback control system

In order to achieve a relative magnetic field stability and hence current stability of 10^{-5}, an active feedback system has been implemented. This system con-

[17] In principle, the proportional-integral-derivative (PID) controllers of the feedback control system can be optimized for each magnetic field strength in order to decrease the rise time. However, the experimental procedure does not rely on extremely fast magnetic field jumps, and therefore we keep the calibration of the PIDs fixed.

[18] For the new magnetic-field system, this Adwin-system has been upgraded to three units, due to the limited number of 8 available analog channels per unit.

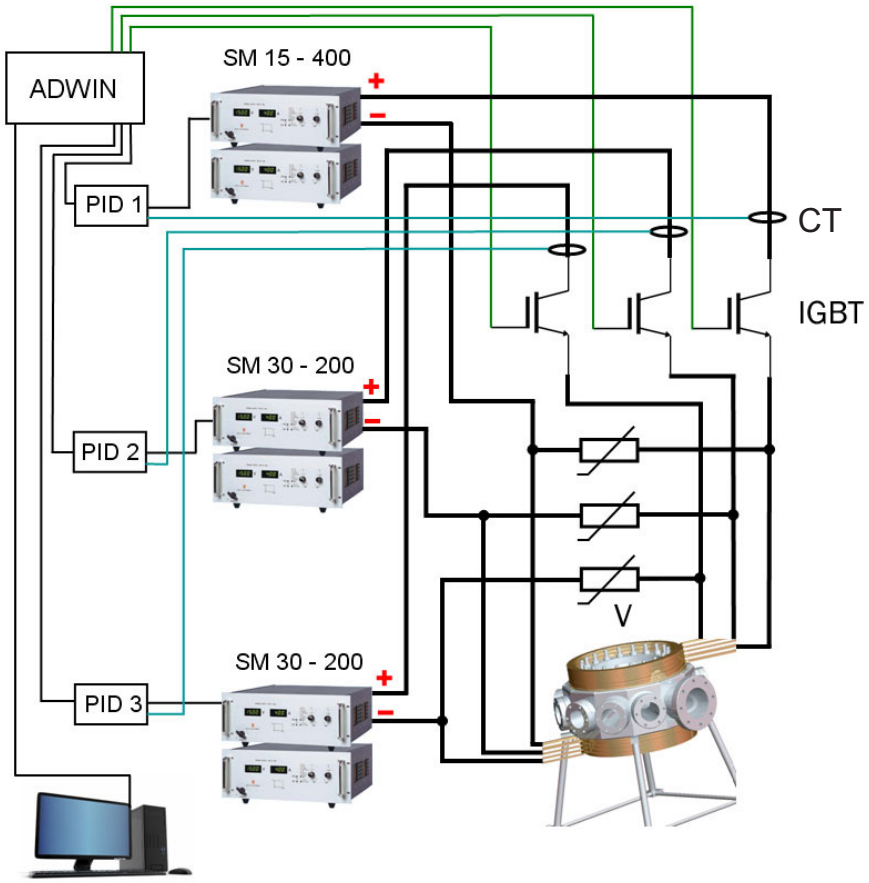

Figure B.4.: Overview of the electronic control system of the *Bias coils*, as explained in the text. Figure taken from Ref. [Har10].

stantly monitors the actual current in each *Bias coil* unit, compares it with the set value from the Adwin and corrects for the deviation.

The actual currents are measured by highly sensitive current transducers (CT), Ultrastab 867-1000IHF Danfysik[19], which offer a current transfer ratio of 1000:1. The transducers feature a thermal stability exceeding 0.5 ppm/K, a response characteristic larger than 100 A/μs and a bandwidth of $0 - 500$ kHz. The output currents of the transducers are converted via precision shunt resistances (VISHAY[20]), which offer a tolerance of 0.1% and a thermal stability of 2 ppm/K.

The self-made PID controllers analyze the deviations of the voltage signals from the shunt resistances with the Adwin set values and generate analog $0-5$ V

[19]The current cords of the *Bias coil* units 2 and 3 pass the current transducers twice in order to increase the accuracy.

[20]After purchasing the resistances, it was realized that their resistance values were 3.3 Ω instead of the 3 Ω ordered. This limits the maximum currents of the power supplies to 730 A and 360 A until the resistances are replaced. Furthermore, the input values of the Labview control software for the *Bias coils* are $\sim 10\%$ higher than the real current values, given in Table B.1

signals, which control the power-supplies via the analog programming input connections.

Power supplies

For each unit, the currents through the *Bias coils* are provided by two parallel connected power supplies of the series SM6000 (DELTA Elektronika)[21] in master-slave configuration.

The two power supplies for unit 1, model SM 15-400, provide a maximum voltage of $V_{\max} = 17$ V and maximum current of $I_{\max} = 400$ A each, resulting in an overall maximum current of $I_{\max}^{\text{unit1}} = 800$ A. For each of the units 2 and 3, two[22] SM 30-200 power supplies are used, with $V_{\max} = 33$ V and $I_{\max} = 200$ A, yielding a total of $I_{\max}^{\text{unit2,3}} = 400$ A.

For the current connections between power supplies, coils and IGBTs, flexible high-current copper connectors (Druisedt Elektrotechnik) are used. These PVC isolated connectors feature cross sections of 400 mm^2 (unit 1) and 150 mm^2 (unit 2 and 3), respectively, which allow a steady-state current-flow without necessitating active cooling.

Fast switch-off

The coil control system includes a fast switch-off routine using IGBTs, which are connected in series with each coil unit. The IGBTs were chosen with regard to the maximum attainable currents, model CM900DU-24NF with $I_{\max} = 900$ A for the circuit of unit 1 and model CM600DU-24NF with $I_{\max} = 600$ A for the circuits of units 2 and 3 (both purchased at POWEREX).

The IGBTs, which are mounted on a water-cooled[23] metal block, close the electric circuits on receiving a +15 V signal. This control-signal is generated by amplification of a TTL high-signal (> 3.5 V) from the Adwin-system. After opening the circuit, the electric power is dissipated via three high-power varistors (V) (EPCOS, B60K275), which are connected in parallel with the coil body and feature a break-through voltage of 700 V at a current of 800 A. In addition, each IGBT is protected by a varistor (EPCOS, S20K385), which is not shown in Fig. B.4.

The switch-off times have been measured in a test setup aside of the main vacuum chamber with a result of 100 μs for a 360 A jump. Within the environ-

[21] We purchased the power supplies with the additional options *Iso Amp Module* and *High Speed Programming*. The *Iso Amp Module* provides galvanic isolation for programming and prevents earth loops, whereas *High Speed Programming* allows rise times of 400 μs ($15-20$ times faster than the normal version) by reducing the output capacitors to 1200 μF (SM 15-400) and 800 μF (SM 30-200), respectively. Primarily, the *High Speed Programming* option was chosen because it enables faster control by the PID, which is necessary for the feedback system.

[22] Operation of unit 2 or 3 with only one SM 15-400 power supply each is not possible, due to the voltage drop over the coils and IGBTs, which exceeds 17 V.

[23] This cooling water is provided by the 3 bar cooling cycle.

ment of the vacuum chamber, eddy currents are expected to increase this time span by an order of magnitude[24].

The main motivation for implementing a fast switch-off routine was to make possible rapid jumps from the magnetic high-field region, where measurements are performed, to the low-field region, where the low-field imaging takes place. However, due to the fact that high-field imaging has been implemented, fast switch-off times are less important. To avoid the risk of damaging the electronic circuits of other coils by high induced voltages, the IGBTs are always switched on during experimental runs.

B.2.5. Safety installments

The major risk of the *Bias coil* system is a malfunction of the 10 bar water-cooling system. In that case, failure to instantly shut off the current could lead to severe damage of the experimental setup. Therefore, several safety arrangements are installed to rapidly shut down the power supplies, if necessary via either the *Interlock* or the *Remote shut down* port of the supplies.

- Interlock
  The interlock connector has 2 inputs which have to be connected in order to turn on the output of the power supplies. As soon as the link between them is interrupted, the power supplies shut down. All water-flow and thermo switch control-elements are connected in series with this link and open the electronic circuit in the event of a failure.

- Remote shut down
  Should the voltage applied to the *Remote shut down* input drop below[25] 4 V, the power supplies shut down. A series of negative temperature resistances (NTCs) and a manual shut down option are electronically connected to a self-made control box, which supplies 5 V as long as the input signals indicate that the system is working properly. This box is explained in detail in Ref. [Har10] and offers the option of implementing another safety system.

Water flow control

The outgoing[26] cooling water flow for each of the *Bias coil* units is constantly controlled by flow meters, which open the electronic safety link of the *Interlock* whenever the flow drops below 2.5 l/min. Another flow meter is checking the overall flow of the whole system. The flow meters have an accuracy of about 10%.

[24] This was never measured due to safety considerations (see text).
[25] The working range lies between 4 V and 12 V.
[26] In this regard, "outgoing" means after passing through the coils.

Temperature control - Thermo switches

The temperature of the coils is monitored by 20 bimetal thermo switches, which interrupt the control link of the *Interlock* if the temperature exceeds 45 ± 5°C. Two switches are mounted on the glass fiber sleeving of each coil, 0.5 m and 1 m away from the coil center. The temperature on the insulation is expected to be slightly lower than of the copper tube itself.

Temperature control - NTCs

In order to have an independent temperature control, at least two NTCs are mounted on the glass fiber sleeving of each coil, 0.15 m away from the coil center. Each of the NTCs is checked independently by a self-made temperature control circuit, using a microcontroller that converts the values of resistance to temperatures. The temperatures are compared with the set value of $T_{\text{set}} = 45$°C. The control box receives a TTL signal, for $T < T_{\text{set}}$ [Har10]. Otherwise the power supplies switch off via *Remote shut down*.

Manual switch-off

In order to increase the temperature stability in the laboratory, the power supplies are located in a separate room. To manually switch off the power supplies in case of an emergency, a control switch in the laboratory is connected to the *Remote shut down* port of the power supplies.

B.2.6. Fabrication process

Several production steps were necessary to build the precise set of coils, composing the *Bias coils*, starting from non-insulated copper tubes. In the following, a short summary of the elaborate fabrication procedure is given. For the utilized materials see Sec. B.2.1.

The copper tubes were delivered in a rolled-up form in lengths of 11 m (unit 1) and 9 m (unit 2 and 3). First, these tubes were straightened out with a moulding press by applying a force of 10 kN on a tube length of one meter. To assure a uniform result, for every 0.5 m that were pressed, the tube was rotated by 90°.

To reverse the effect of cold deformation, the tubes were heated to a temperature of 400°C at an ambient pressure of 3×10^{-1} mbar for the duration of two hours[27], with a subsequent cooling phase of 30 min. This process reduced intrinsic mechanic strains and allowed for a smooth winding of the coils. Due to the low pressure environment, surface oxidation is prevented at this stage. The tubes were cleaned before and after this procedure, using acetone.

[27] For this, we put the copper tubes into a closable pipe of 12 m length, which was connected to a rotary vane pump. The temperature stated above was achieved using heater bands, which were wound around the pipe, and wrapping the entire pipe with several layers of aluminum foil.

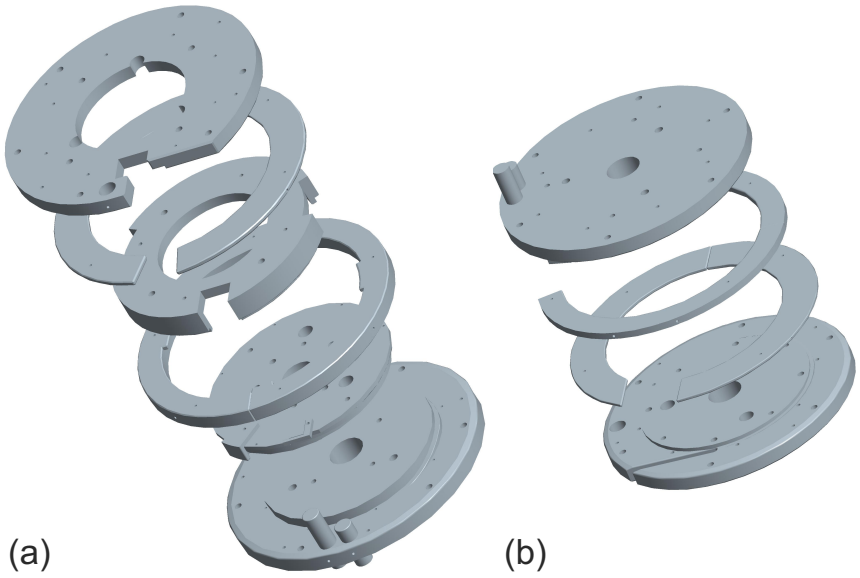

Figure B.5.: *Winding tools* for the fabrication of the *Bias coils* for (a) unit 1 and (b) units 2 and 3. Two mirror-symmetric pairs of tools were used, of which only one tool of each pair is shown here.

In the next step, the tubes were cut to their final lengths, 10 m (unit 1) and 7.5 m (units 2 and 3), and insulated by covering them with glass fibre braided sleevings.

For the winding procedure, special *Winding tools* made of aluminum were constructed for each coil design. The two mirror-symmetric pairs of *Winding tools* for unit 1 and unit 2 and 3, respectively, consist of several parts as shown in Fig. B.5. The modular structure made it possible to adapt the *Winding tools* to each stage of the winding procedure, without the necessitating removal of the copper tubes. These *Winding tools* were modeled using a parametric 3D-CAD software (Pro/Engineer) and generated by a CNC milling machine.

The *Winding tools* were covered with a 0.2 mm thick adhesive foil of teflon to enable easy removal of the coils, after the winding process. Without this foil, not only would the epoxy resin have glued the single windings together, creating a rigid coil body, but the coil would have stuck to the winding tool as well.

For winding the copper tubes, the *Winding tool* was mounted on an electronically adjustable rotary table with a rotation velocity of one turn per minute. Then, an insulated copper tube was attached; half of its length was mounted alongside the rotational axis of the *Winding tool*, while the end of the other half was kept under a tension stress of $\sim$50 N. During the winding procedure, which included several stages, the tube was wetted with epoxy resin and softly hammered onto the channels of the *Winding tool*. Finally, the rotation of the table was reversed and the other half of the copper tube was processed in an analogous way. After 24 h, the epoxy resin reached its final cohesiveness and the finished coil was removed from the *Winding tool*.

B.3. Curvature coils

The main function of the *Curvature coils* is to modify the magnetic field curvature $C(I)$ at the center of the atom trap. For $C(I) > 0$, the radial trapping potential increases according to Eq. (B.5), clearing the way for a large volume hybrid trap, which is a combination of an optical dipole and magnetic trapping potential. On the other hand, applying an anti-curvature, $C(I) < 0$, locally corrects for the magnetic forces that result from the magnetic field curvature produced by the *Bias coils*. This allows to perform, for example, long expansion measurements.

We implemented two symmetric pairs of in series connected coils, deviating from the strong Helmholtz-configuration and therefore producing a considerable magnetic field curvature. These *Curvature coils* consist of 2×23 windings made of varnished copper wires with a rectangular cross section of 1 mm $\times$ 4 mm. The coils are attached to aluminum frames, which feature four cuts in order to reduce eddy currents. The frames for the upper and lower *Curvature coils* are placed near the re-entrant viewports; see Fig. B.2.

The current is provided by a 1.5 kW power supply ($U_{\max} = 52$ V for $I < 30$ A or $U_{\max} = 26$ V for $I > 30$ A), model SM 52 AR 60 (DELTA Elektronika). The power supply is actively controlled by a PID-feedback system analogous to the feedback control of the *Bias coils*, which is described in Sec. B.2.4. The coil current is monitored by a current transducer, model 867-60I (Ultrastab), which is suitable for currents up to 60 A. In contrast to the electronic control circuit of the *Bias coils*, an H-bridge was installed for the *Curvature coils*, which allows reversing the magnetic field and switching between curvature and anti-curvature.

As power dissipation in the *Curvature coils* is lower than in the *Bias Coils*, simple external water cooling tubes made of copper are sufficient. These tubes feature an outer (inner) diameter of 6 mm (4 mm) and are positioned on the outside surfaces of the coil holders. The cooling of the *Curvature coils* operates at a pressure of $\sim$3 bar.

The rise time of the *Curvature coils*, mounted to the main vacuum chamber, was measured as 2 ms (without using the electronic feedback circuit). This results in an inductance of $L = 200\,\mu$H with a calculated resistance of $\sim 100\,\mathrm{m}\Omega$.

It has been experimentally observed that an axial misalignment $\delta\rho^{\mathrm{Curv}}$ of the *Curvature coils*, relatively to the *Bias coils*, leads to a shift of the center of the radial magnetic trap according to

$$\Delta\rho^{\mathrm{mag}}_{\mathrm{center}} = \frac{C^{\mathrm{Curv}}(I^{\mathrm{Curv}})}{C^{\mathrm{Bias}}(I^{\mathrm{Bias}}) + C^{\mathrm{Curv}}(I^{\mathrm{Curv}})}\delta\rho^{\mathrm{Curv}}. \tag{B.12}$$

For large magnetic field curvatures resulting from the *Curvature coils* $C^{\mathrm{Curv}}(I^{\mathrm{Curv}}) \gg C^{\mathrm{Bias}}(I^{\mathrm{Bias}})$, the center of the magnetic trap shifts to the radial center of the *Curvature coils* $\Delta\rho^{\mathrm{mag}}_{\mathrm{center}} \to \delta\rho^{\mathrm{Curv}}$. If the absolute value of the anti-curvature produced by the *Curvature coils* approaches the curvature of the *Bias coils*, $C^{\mathrm{Curv}}(I^{\mathrm{Curv}}) + C^{\mathrm{Bias}}(I^{\mathrm{Bias}}) \to 0$, the atoms are pushed outwards radially.

Besides for variation of the magnetic field curvature, we also use the *Curvature coils* for the determination of dimer binding energies by rf magnetic field modulation spectroscopy; see Sec. F.3.1.

B.4. Vertical compensation coils

In order to enable small bi-directional alterations of the magnetic field strength, a pair of *Vertical compensation coils* was implemented. They consist of 23 windings of round copper wire with a thinkness of 1 mm, mounted on a PVC-frame. These coils are not in perfect Helmholtz configuration. However, the resulting magnetic field curvature does not have a noticeable effect on the atom cloud, due to the low currents in use.

The *Vertical compensation coils* are connected to a bi-directional power supply, model HighFiness BCS 3/15, with $I_{\max} = 3$ A and $U_{\max} = 15$ V, which is controlled directly by the Adwin-system. The circuit also includes a $5\,\Omega$-resistance (Arcol), which is connected in series.

The main task of these coils is to compensate for remanent magnetization[28] of the vacuum chamber and surroundings, which limits the minimal magnetic field strengths achievable in the experiment. This is especially important during the Raman sideband cooling stage [Web03a, Ker00, Tre01], where we reverse the current in the *Vertical compensation coils* in order to reach the necessary fields strengths of ~ 200 mG.

[28]Increasing the magnetic field strength to 1000 G leads to a strong remanent magnetization of unknown origin of $1-2$ G. So far, we observed no independent fading of this remanence.

APPENDIX C

IMAGING AT HIGH MAGNETIC FIELDS

The findings presented in this thesis are based on precise knowledge of the characteristic properties of the atom cloud and the trapping potential, such as atom number, temperature and trap frequencies. These properties are derived from the atom cloud spatial density distribution, which is obtained by means of *absorption imaging* [Ket99]. This standard technique in cold atom experiments is performed by illumination of the atoms with resonant light, either while the atoms are trapped (*in-situ*) or after their release from the trap. In this process, the atoms scatter photons of the imaging light, generating a shadow image, which is mapped on a charge-coupled device (CCD) chip[1].

For measurements performed in the magnetic low-field region, an imaging setup was used that allows taking pictures at zero field. This setup was adapted later on for magnetic field strengths up to ~ 20 G. The low-field setup is outlined in the theses of former PhD students working on the experiment; see Refs. [Web03a, Her05, Kra06a, Mar08b]. However, the low-field imaging setup is of limited use for experiments in the magnetic high-field region as it involves magnetic field ramps spanning up to 1000 G. Such ramps lead to additional atom loss and an increase of the sample temperature, thereby inhibiting accurate investigation of few-body phenomena in the high-field region.

Therefore, a new high-field imaging setup, as described in Sec. C.2, has been implemented to overcome this problem. The selection of the appropriate imaging and repumper[2] transitions, based on the level structure of cesium atoms described in Appendix A, is explained in Sec. C.1. In Sec. C.3, the image analysis, used to identify the properties of the atom cloud, is summarized.

[1] This is in contrast to fluorescence imaging, where the scattered light is collected.

[2] Actually, the repumper performs a state transfer before the imaging starts and is subsequently switched off. No repumping light is necessary during the imaging process, as there is no noteworthy leakage from the closed imaging cycle transitions in the magnetic high-field region. Still, to avoid confusion, the laser preparing the initial state for the imaging cycle is referred to as repumper.

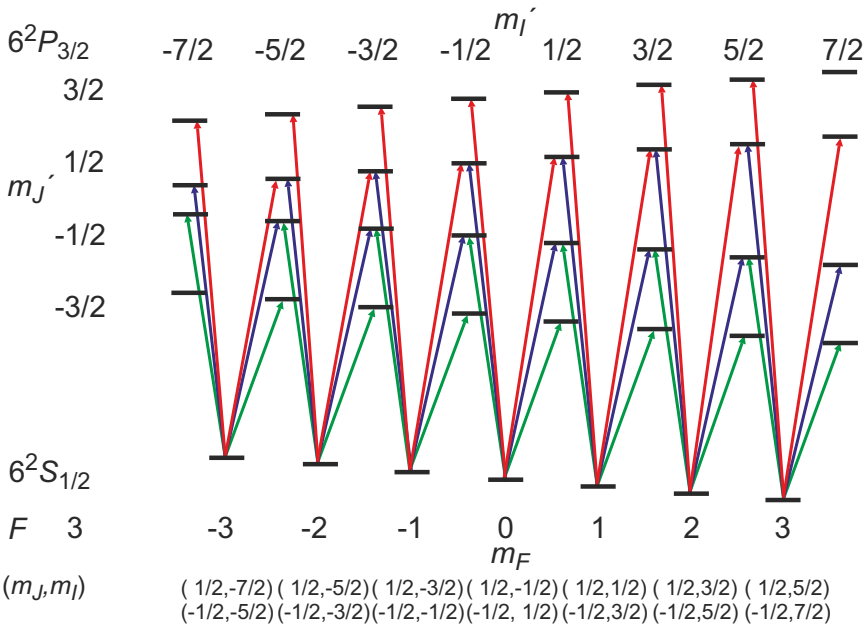

Figure C.1.: Transitions between the $F = 3$ hyperfine ground states and the $6\,^2P_{3/2}$ excited states at high magnetic fields. The states are labeled according to their set of good quantum numbers, which differ for the ground (F, m_F) and excited states (m_J, m_I). Colors indicate the polarizations of light for the optical transitions: red σ^+, blue π and green σ^-. At the bottom of the figure the quantum numbers (m_J, m_I), which contribute to the specific $|F = 3, m_F\rangle$ state, are listed. Typically, the atom sample to be imaged is initially in the $|F = 3, m_F = 3\rangle$ state, which offers no closed optical transitions, due to the decay to $F = 4$ (not shown).

C.1. Optical cycling transitions

Absorption imaging requires a closed optical transition between two accessible states, meaning that there is no or only negligible leakage to other states. As explained in Appendix A, F and m_F remain good quantum numbers for the ground state manifold in the magnetic high-field region. However, that is not the case for the $6\,^2P_{3/2}$ manifold, where the states are identified by m_J and m_I for magnetic fields above ~ 200 G. The different optical D_2 transitions starting from either $F = 3$ or $F = 4$ in the ground state manifold are shown in Figs. C.1 and C.2. The D_1 transitions do not offer any closed optical cycles.

A summary of the implemented high-field repump and imaging transitions is shown in Fig. C.3. First, the atoms are transferred from the $|F = 3, m_F = 3\rangle$ to the $|F = 4, m_F = 4\rangle$ state by the repumper light, which is resonant on the $|F = 3, m_F = 3\rangle \rightarrow |m_J' = 1/2, m_I' = 7/2\rangle$ σ_+-transition. The majority of atoms subsequently decay to the $|F = 4, m_F = 4\rangle$ state. A small leakage to the $|F = 4, m_F = 3\rangle$ dark state decreases the total number of imaged atoms by 6%, which is taken into account for the imaging analysis. The imaging cycle

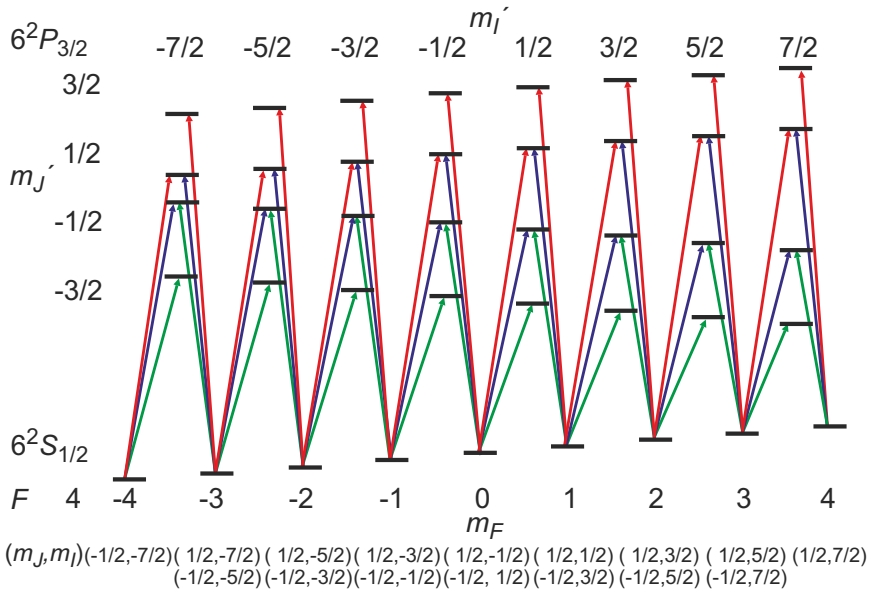

Figure C.2.: Transitions between the $F = 4$ hyperfine ground state and excited states at high magnetic field strengths. The color coding and labeling are the same as for Fig. C.1. Starting from $F = 4$, there are two closed transitions suitable for imaging: $|F = 4, m_F = 4\rangle \rightarrow |m_J' = 3/2, m_I' = 7/2\rangle$ and $|F = 4, m_F = -4\rangle \rightarrow |m_J' = -3/2, m_I' = -7/2\rangle$.

is performed on the $|F = 4, m_F = 4\rangle \rightarrow |m_J' = 3/2, m_I' = 7/2\rangle$ σ_+-transition. Details of the imaging and repumper transitions, such as the calculation of the repumper leakage, are given below.

Imaging transition

Transitions from $F = 3$ do not offer closed cycles, due to the inevitable leakage to $F = 4$. In contrast, the $F = 4$ hyperfine level features two closed optical transition cycles that are suitable for absorption imaging, namely, a σ^+ transition: $|F = 4, m_F = 4\rangle \rightarrow |m_J' = 3/2, m_I' = 7/2\rangle$ and a σ^- transition: $|F = 4, m_F = -4\rangle \rightarrow |m_J' = -3/2, m_I' = -7/2\rangle$. In analogy to the low-field setup, the transition used in the experiment is the σ^+-transition, which involves atoms initially brought to the $|F = 4, m_F = 4\rangle$ state.

The Zeeman shift of the states involved in the transition leads to a strong magnetic field dependence of the transition frequency. In comparison to the magnetic zero-field imaging frequency of the $|F = 4 \rightarrow F' = 5\rangle$ transition [Web03a, Her05, Kra06a, Mar08b], this accounts for a shift of ~ 1.40 MHz/G, which amounts to about 1.4 GHz at 1000 G; see Fig. C.4(a). The technical implementation of laser-locking is described in Sec. C.2.

The optical cross section σ_0 for this closed transition and light intensities I

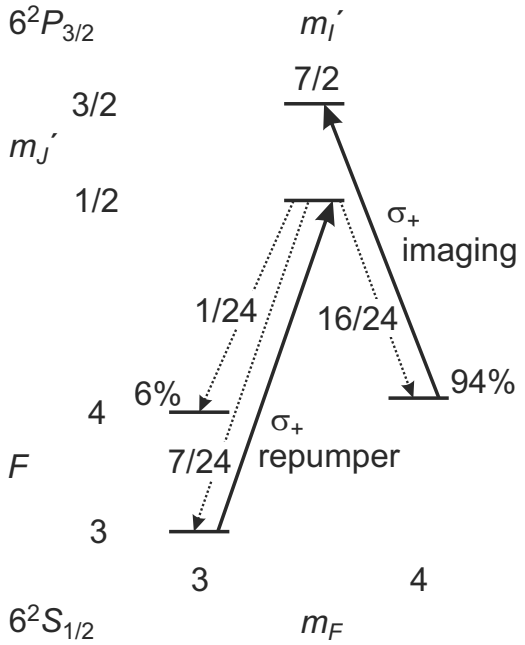

Figure C.3.: Repumper and imaging transitions in the magnetic high-field region. The solid lines indicate those transitions, which both involve σ_+ polarization, whereas the dotted lines represent the possible decay channels from $|m'_J = 1/2, m'_I = 7/2\rangle$. The numbers indicate the relative transition strengths for these decays, calculated by using the expression given in Eq. (C.12). A fraction of 6% of the atoms will end up in the $|F = 4, m_F = 3\rangle$ state, which is a dark state for the repumping light.

well below the saturation intensity[3] I_s is given on resonance as [Foo05]

$$\sigma_0 = \frac{3\lambda^2}{2\pi} = 3.469 \times 10^{-9}\,\mathrm{cm}^2. \tag{C.1}$$

Other states are of negligible significance for the imaging transition, as the energetically nearest transition, $|F = 4, m_F = 4\rangle \rightarrow |m'_J = 1/2, m'_I = 7/2\rangle$, is a π-transition and detuned by more than 1 GHz from the imaging transition at magnetic fields strengths exceeding 500 G.

Repumper transition

The imaging cycle requires the atoms to be in the $|F = 4, m_F = 4\rangle$ state initially, but most of our experiments are performed with atoms in the $|F = 3, m_F = 3\rangle$ state. Therefore, a state transfer is required. For reasons of efficiency, this transfer is carried out via an optical instead of a microwave transition.

As the $|F = 4, m_F = 4\rangle$ stretched state is uniquely related to the quantum numbers $(m_J = 1/2, m_I = 7/2)$, the repumper transition has to involve either

[3]The saturation intensity is defined as $I_s = \frac{\pi h c \gamma}{3\lambda^3}$, which is 1.1 mW/cm^2 for the D_2-transition of cesium. For the values of λ and γ see Table A.1; c denotes the velocity of light.

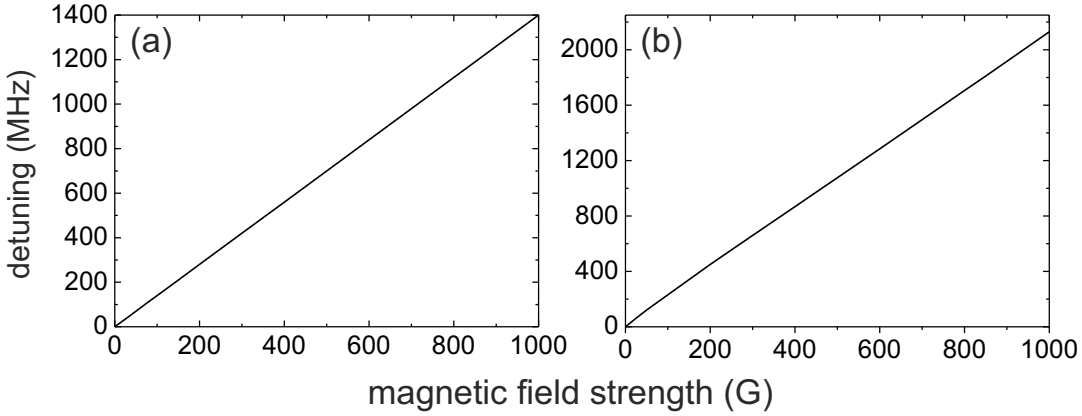

Figure C.4.: Frequency detuning of the (a) imaging and (b) repumper transitions in the magnetic high-field region. The detunings are in reference to the transition frequencies of the adiabatically connected zero-field states. Note that the actual detunings of the beat-lock presented in Sec. C.2 differ by an offset from the one given in this figure. This is due to the fact that the frequencies of the repumper and imaging reference light for beat-locking are not the transition frequencies of the adiabatically connected zero-field states. (a) The frequency shift of the imaging transition $|F = 4, m_F = 4\rangle \rightarrow |m'_J = 3/2, m'_I = 7/2\rangle$ in comparison to the zero-field imaging transition $|F = 4 \rightarrow F' = 5\rangle$ [Web03a, Her05, Kra06a, Mar08b] amounts to 1.40 MHz/G. (b) For the repumper transition $|F = 3, m_F = 3\rangle \rightarrow |m'_J = 1/2, m'_I = 7/2\rangle$, the resonance frequency changes by 2.12 MHz/G compared to the $|F = 3 \rightarrow F' = 4\rangle$ transition.

the excited state $|m'_J = 1/2, m'_I = 7/2\rangle$ or $|m'_J = -1/2, m'_I = 7/2\rangle$; see Fig. C.1. This follows from the selection rules for optical transitions, $\Delta m_J = 0, \pm 1$ and $\Delta m_I = 0$. As derived below, the $|m'_J = 1/2, m'_I = 7/2\rangle$ state offers a more efficient transfer to the $|F = 4, m_F = 4\rangle$ state.

The repumper transition has been chosen by comparing the strengths and leakages of the transition process. The transition strength is proportional to the square of the dipole matrix element $|d^{ge}|^2$, which connects the excited state[4] $|\alpha', J'm'_J I'm'_I\rangle$ with the ground state $|\alpha, JIFm_F\rangle$ according to

$$d^{ge} = q_e \langle \alpha, JIFm_F | \epsilon \, \mathbf{r} | \alpha', J'm'_J I'm'_I \rangle, \tag{C.2}$$

with the electron charge q_e. Interestingly, d_q^{ge} involves a different set of good quantum numbers for the excited state and the ground state. By writing the polarization unit vector ϵ in the basis related to $\sigma_\pm$ and π-transitions [Foo05]

$$\epsilon = \underbrace{\epsilon_{-1} \frac{\mathbf{e_x} - i\mathbf{e_y}}{\sqrt{2}}}_{\sigma_-} + \underbrace{\epsilon_0 \mathbf{e_z}}_{\pi} + \underbrace{\epsilon_{+1} \left(- \frac{\mathbf{e_x} + i\mathbf{e_y}}{\sqrt{2}} \right)}_{\sigma_+}, \tag{C.3}$$

[4]The quantum numbers L and S are omitted for simplification.

the product $\epsilon\,\mathbf{r}$ can be expressed in terms of the spherical harmonics $Y_{l,m}$ as

$$\epsilon\,\mathbf{r} = r\sum_{q=-1}^{1}\epsilon_q Y_{1,q} =: \sum_{q=-1}^{1} r_q. \tag{C.4}$$

This allows us to treat each element of $d_{ge} = \sum_{q=-1}^{1} d_{ge}^{q}$ separately,

$$d_q^{ge} = q_e\langle\alpha, JIFm_F|r_q|\alpha', J'm'_J I'm'_I\rangle. \tag{C.5}$$

The ground state can be expanded using the *Clebsch-Gordan coefficients* as

$$|\alpha, JIFm_F\rangle = \sum_{m_J=-J}^{J}\sum_{m_I=-I}^{I}\underbrace{\langle Jm_J Im_I|JIFm_F\rangle}_{\text{Clebsch}-\text{Gordan coefficients}}|\alpha, Jm_J Im_I\rangle, \tag{C.6}$$

where the Clebsch-Gordan coefficients can be expressed in terms of the *Wigner* $3j$ *symbols* by

$$\langle Jm_J Im_I|JIFm_F\rangle = (-1)^{-J+I-m_F}\sqrt{2F+1}\begin{pmatrix} J & I & F \\ m_J & m_I & -m_F\end{pmatrix}. \tag{C.7}$$

As the electric dipole operator does not act on the nuclear spin, Eq. (C.5) can be simplified by considering only transitions with $I = I'$ and $m_I = m'_I$, which leads to

$$d_q^{ge} = q_e\sum_{m_J=-J}^{J}(-1)^{-J+I-m_F}\sqrt{2F+1}\begin{pmatrix} J & I & F \\ m_J & m_I & -m_F\end{pmatrix}\langle\alpha, Jm_J|r_q|\alpha', J'm'_J\rangle. \tag{C.8}$$

Using the *Wigner-Eckart theorem*, the factor to the right in Eq. (C.8) can be written as a product of a Clebsch-Gordan coefficient and a *reduced matrix element* [Sak94],

$$\begin{aligned}\langle\alpha, Jm_J|r_q|\alpha', J'm'_J\rangle &= \\ &= \langle J'm'_J 1q|J'1Jm_J\rangle\frac{\langle\alpha J||r||\alpha' J'\rangle}{\sqrt{2J'+1}} \qquad (C.9)\\ &= (-1)^{-J'+1-m_J}\frac{\sqrt{2J+1}}{\sqrt{2J'+1}}\begin{pmatrix} J' & 1 & J \\ m'_J & q & -m_J\end{pmatrix}\langle\alpha J||r||\alpha' J'\rangle. \qquad (C.10)\end{aligned}$$

Therefore, the dipole matrix element is given as

$$\begin{aligned} d_q^{ge} &= q_e\sum_{m_J=-J}^{J}(-1)^{-J+I-m_F-J'+1-m_J}\frac{\sqrt{2F+1}\sqrt{2J+1}}{\sqrt{2J'+1}} \\ &\quad\cdot\begin{pmatrix} J & I & F \\ m_J & m_I & -m_F\end{pmatrix}\begin{pmatrix} J' & 1 & J \\ m'_J & q & -m_J\end{pmatrix}\langle\alpha J||r||\alpha' J'\rangle. \end{aligned} \tag{C.11}$$

This can be further simplified by the properties of the Wigner $3j$-symbols. As the first $3j$-symbol is non-zero only for a particular m_J, the sum is reduced to a single term. Moreover, as we are only interested in the relative line strength between different transitions, it is sufficient to compare the factor given below, which is proportional to $|d^{ge}|^2$:

$$(2F+1)\left[\begin{pmatrix} J & I & F \\ m_J & m_I & -m_F \end{pmatrix}\begin{pmatrix} J' & 1 & J \\ m'_J & q & -m_J \end{pmatrix}\right]^2. \tag{C.12}$$

The results for the branching ratios of the possible decay channels reveal that the $|F=3, m_F=3\rangle \rightarrow |m'_J=1/2, m'_I=7/2\rangle$ transition leads to a loss of 6% into the $|F=4, m_F=3\rangle$ dark state; see Fig. C.3. The alternative transition $|F=3, m_F=3\rangle \rightarrow |m'_J=-1/2, m'_I=7/2\rangle$ exhibits less favorable transition strengths, with a loss of 12% to the $|F=4, m_F=3\rangle$ state. Therefore, the first transition was implemented experimentally.

The transition frequency changes in dependence of the magnetic field by 2.12 MHz/G, which is shown in Fig. C.4. Off-resonant scattering by σ_- polarized[5] light is suppressed as the energy difference between different m'_J states exceeds 1 GHz at a magnetic field strength of 500 G. However, the nearest π-transition, which is to the $|m'_J=1/2, m'_I=5/2\rangle$ state, is only detuned by 25 MHz from the repumper transition. In principle, this could cause some losses. For this reason, the repumper light is, within the experimental uncertainty, purely σ_+/σ_- polarized.

C.2. Absorption imaging setup

In this section, the laser setup and locking scheme as well as the configuration of the imaging setup is described. An overview is given in Fig. C.5.

Laser setup and locking scheme

The light for the new imaging system at high magnetic field strengths is provided by two 852 nm laser diodes (SDL-5411-G1), which are both frequency stabilized using a Littrow-type extended cavity setup [Ric95, Tha01].

The imaging laser is referenced via beat-lock [Sch99] to the so-called *master laser*. This *master laser* is the heart of the entire diode laser system as it supplies the reference light for the MOT- and Zeeman lasers, both stabilized via beat-lock, and the Raman cooling lattice laser, which is stabilized by injection-lock [Sie86, MR99]. A description of the diode laser system can be found in the PhD and diploma theses of my predecessors in Refs. [Mar03, Web03a, Her05, Kra06a, Mar08b]. The *master laser* is frequency stabilized, 160 MHz red-detuned to the $|F=4\rangle \rightarrow |F'=5\rangle$ zero-field transition by modulation transfer spectroscopy (MTS) [Raj80, Ber01] and features a frequency width of about 100 kHz.

[5] As described in Sec. C.2, we use linear polarized light with a polarization orthogonal to the quantization axis. This corresponds to a superposition of σ_+ and σ_- polarized light.

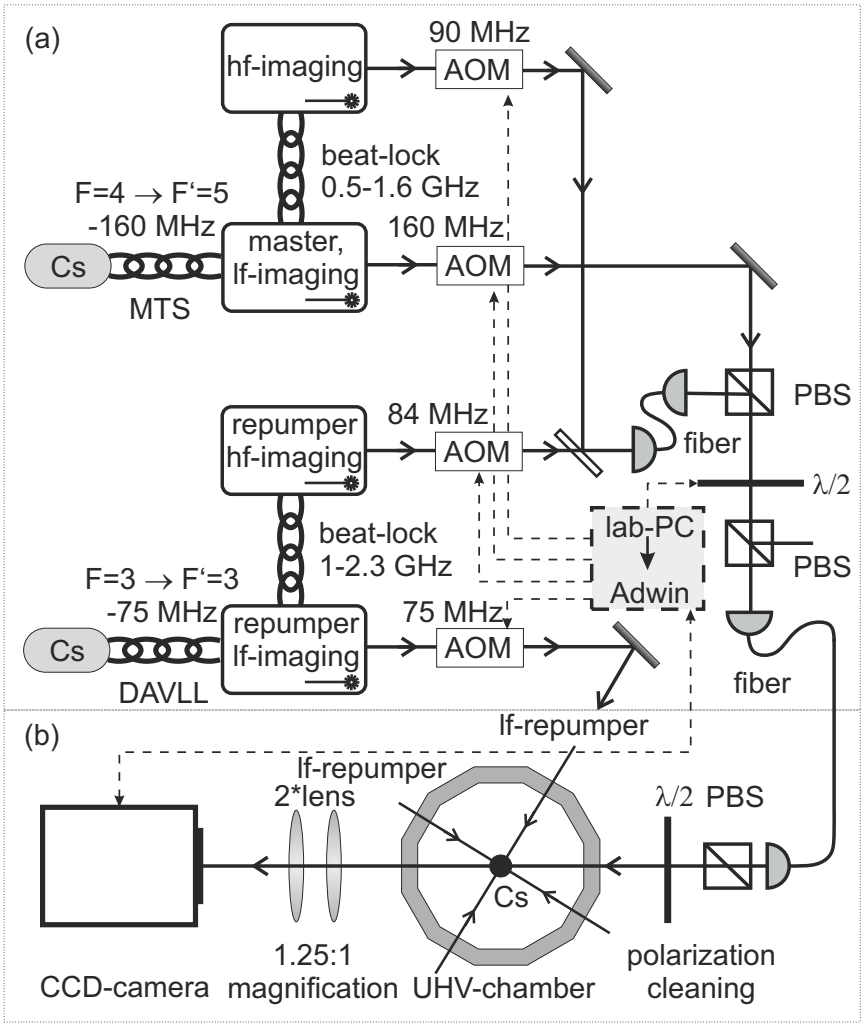

Figure C.5.: Schematic overview of the high and low-field imaging system containing (a) the laser setup and locking scheme as well as (b) the imaging configuration. The solid lines show the light beam paths and the symbolic chains refer to a locking system of two elements. (a) The low-field (lf) lasers for repumping and imaging, respectively, are locked to cesium vapor cells (Cs) via either modulation transfer spectroscopy (MTS) or dichroic-atomic-vapor laser lock (DAVLL). The corresponding transitions and detunings are given in the figure. The high-field (hf) lasers are locked to the low-field lasers via beat-locking with a detuning in the order of a GHz. The imaging and repumper light beams are controlled by means of acousto-optical modulators (AOMs) via the experimental control system, consisting of lab computer (PC) and Adwin. The high-field imaging and repumper light beams are overlapped at a non-polarizing beam splitter. An electronic rotatable $\lambda/2$-plate allows switching between high- and low-field imaging. (b) The imaging and repumper beams, with the exception of the low-field repumper beam, are linearly polarized, in orthogonal direction to the magnetic bias field (quantization axis). The shadow image of the atoms is imaged with a 1.25:1 magnification, produced by a two-lens system, on the CCD-chip of the camera. The data is read out by the experimental control system. Note that the MOT repumper is used as the repumper for low-field imaging as well. Therefore, it illuminates the atoms from six different sides (only four shown in the figure).

A fast photo detector, exhibiting a maximum cutoff frequency[6] of 1.6 GHz, is used for beat-locking. This photo detector is able to bridge the large frequency gap of 0.7-1.5 GHz between the *master laser* frequency and the $|F = 4, m_F = 4\rangle \rightarrow |m'_J = 3/2, m'_I = 7/2\rangle$ high-field imaging transitions. The tunability of the frequency offset is provided by voltage adjustment of the voltage-controlled oscillator (VCO) (ZX95-1300S+, Mini-Circuits) of the beat lock circuit via the lab computer. This tunability allows to bring the imaging light into resonance for magnetic field strengths ranging from about 400-1000 G. The locked imaging laser inherits the narrow-band characteristic of the *master laser* and has a linewidth of about 200 kHz.

The setup of the repumper laser for high-field imaging is similar to that of the imaging laser. One difference, however, is the fact that the repumper resonantly couples atoms from the $F = 3$ hyperfine level. Therefore, the laser is locked, via beat-lock, to the MOT repumper, which itself is locked via dichroic-atomic-vapor laser lock (DAVLL) [Cor98] in the middle between the $|F = 3\rangle \rightarrow |F' = 2\rangle$ and the $|F = 3\rangle \rightarrow |F' = 3\rangle$ transitions, detuned 75 MHz from both. The MOT repumper is also used as repumper for the zero-field imaging. Due to this locking method, the MOT repumper has a large capture range, at the expense of a rather broad linewidth of about 3.5 MHz [Kra06a], which leads to a similar linewidth for the imaging repumper. In principle, the narrow-band Zeeman repumper laser[7], which is locked 200 MHz red-detuned to the cesium $|F = 3\rangle \rightarrow |F' = 3\rangle$ transition line by modulation transfer spectroscopy, could have been used as a reference as well. However, this would make the imaging system more susceptible to frequency drifts.

Because of the larger detuning of the repumper beat-lock (2.12 MHz/G) in comparison to the one for the imaging (1.40 MHz/G), a photo diode with integrated amplification circuit featuring a cutoff frequency of 2.3 GHz (UPD-200-SP, Alphalas) was implemented in the electronic beat-lock circuit, as well as a VCO (ZX95-2500W+, Mini-Circuits) suitable for large beating frequencies.

Imaging configuration

Both the imaging and the repumper beams pass through computer controlled AOMs, which shift the frequencies of the beams by 90 MHz and 84 MHz, respectively. After being matched in polarization, the beams are overlapped in propagation direction at a non-polarizing beam splitter before they are coupled to a polarization-maintaining single-mode optical fiber; see Fig. C.5. This is in contrast to the low-field imaging setup, where the repumper light for the MOT, which illuminates the atom cloud from six different directions[8], provides the light for the imaging repumper as well.

[6] This frequency is not limited by the photodiode (S5973, Hamamatsu) itself, but by the self-made photodiode amplifier circuit.

[7] This laser also provides the pump light for the Raman sideband cooling. For this, the frequencies are shifted by acusto-optic modulators (AOMs) in order to obtain the appropriate frequencies for both means.

[8] Counter propagating along the three distinct spatial axes [Mar03].

In order to facilitate switching between magnetic high-field and low-field imaging, the out-coupled high-field imaging (and repumper) light is overlapped with the low-field imaging light at a polarizing beam splitter (PBS). The low- and high-field imaging beams differ by 90° in their linear polarization direction, which makes it possible to choose the appropriate imaging light via a computer controlled rotatable $\lambda/2$-plate in combination with a PBS. Another polarization-maintaining single-mode optical fiber transports the imaging light to a side viewport of the main vacuum chamber. At the entrance of the vacuum chamber, the light is purely linear polarized[9], in orthogonal direction to the magnetic quantization axis, with a beam-diameter of about 1.5 cm. The power available for the experiment is 1.5 mW for the repumper and 150 μW for the imaging beam. This results in an intensity of approximately 0.08 mW/cm^2 for the imaging beam, which is well below the saturation intensity.

The shadow of the atom cloud is focused by two lenses[10] onto the CCD chip of the camera (Theta System SIS-99/PH, 1024×1024 pixels, 14 bit resolution), outside the vacuum chamber. The lens setup features a calculated diffraction limited resolution of 5 μm. The measured pixel size corresponds to 6.02(2) μm [Web03a, Her05].

The imaging sequence is controlled by triggering the AOMs for the imaging and repumper light and the exposure time of the CCD chip. In contrast to low-field imaging, where the low-field repumper light is active during the imaging cycle, this is not possible for the high-field setup, as the CCD chip is situated along the path of the high-field repumper beam[11]. Hence, the CCD chip is only triggered simultaneously with the imaging beam after the repumping beam is switched off. The sequence begins with 50 μs of illumination of the atom cloud with the repumper light, which we checked to be sufficiently long to saturate the transfer of atoms to the $|F = 4, m_F = 4\rangle$ state. After 1.5 ms the imaging light is switched on for a duration of 200 μs, generating the shadow picture of the atoms. After 1 s of waiting time a background image without atoms is taken by another 200 μs of illumination. Both pictures are read out using a Labview interface and analyzed with a Matlab program.

C.3. Diagnostics

The diagnostic methods for determining the particle number and sample temperature are described in Ref. [Web03a] and are summarized here. Prior to this, the effective absorption cross section is derived, which is an essential input value for the image analysis.

[9] For this, the polarization is cleaned with a PBS and a $\lambda/2$-plate in front of the viewport.

[10] The lens system consists of a 40 mm diameter, $f = 200$ mm achromatic doublet (Linos Photonics 322293 NIR-ARB2), which is positioned 200 mm from the trap center, and a 50 mm diameter, $f = 250$ mm achromat (Thorlabs LAC376-B) [Web03a].

[11] As discussed before, the imaging and repumper light beams are coupled in the same fiber.

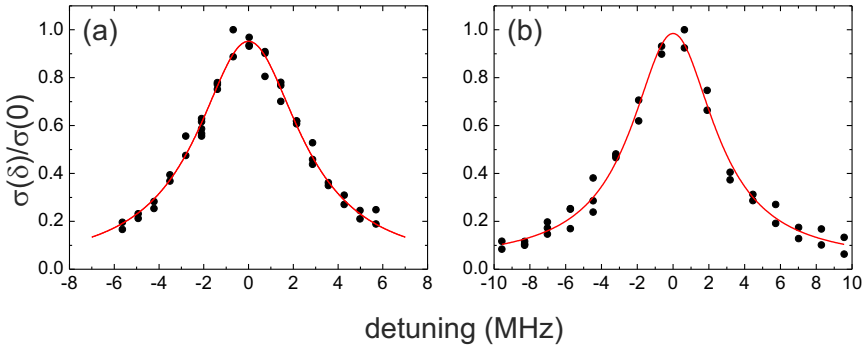

Figure C.6.: Scan of the relative effective absorption cross section $\sigma(\delta)/\sigma(0)$ to determine the resonance frequency at (a) 556 G and (b) 881 G. The Lorentzian fits according to Eq. (C.14) yield a width of 5.6(3) MHz in both cases.

Absorption cross section

The absorption cross section σ_0 given in Eq. (C.1) is only valid for resonant light. In our imaging setup, the light is not exclusively σ_+ polarized, contributing the resonant part, but linearly polarized, which is an equal mixture of σ_+ and σ_-. Therefore, the effective absorption cross section is reduced by a factor of 1/2 [Geh03].

In order to correctly derive the total particle number, it has to be considered that not all atoms are imaged, but only those that have been successfully transferred to the $|F = 4, m_F = 4\rangle$ state by the repumper light. In Sec. C.1, this is calculated to amount to a fraction of 0.94 of the total number of particles.

Therefore, the effective absorption cross section is

$$\sigma = \sigma_0 \times \underbrace{1/2}_{\text{polarization}} \times \underbrace{0.94}_{\text{leakage}} = 1.632 \times 10^{-9}\,\text{cm}^2. \tag{C.13}$$

For the experiments, we ensure that the imaging light is resonant by scanning the detuning δ from resonance. The off-resonant effective absorption cross section $\sigma(\delta)$ is

$$\sigma(\delta) = \frac{\sigma}{1 + (2\delta/\gamma)^2}, \tag{C.14}$$

with the linewidth for the D_2 transition $\gamma = 5.22$ MHz, as listed in Table A.1. Sample scans of the detuning at 556 G and 881 G are shown in Fig. C.6. In both cases, the linewidths were measured to be 5.6(3) MHz, not far from the theoretical zero-field linewidth.

Note that due to the linear polarization used in the imaging setup, the effective saturation intensity[12] is increased by a factor of 2, $I_{s,\text{eff}} = 2I_s \simeq 2.2$ mW/cm^2.

[12] For laser intensities I_L not small in comparison to I_s, the optical pumping effect to the excited state can be taken into account by using $\sigma(I_L, \delta) = \frac{\sigma_0}{1+I_L/I_{s,\text{eff}}+(2\delta/\gamma)^2}$.

Determination of the particle number

The particle number of a thermal atom cloud can be calculated by using a simple method. The measured intensity I (in pixels) of the atom shadow image is given as

$$I(y,z) = I_{\mathrm{bg}}(y,z)\underbrace{\exp(-\sigma\eta(y,z))}_{T(y,z)}, \tag{C.15}$$

with the intensity $I_{\mathrm{bg}}(y,z)$ of the background picture. Here, the column density $\eta(y,z)$ is the density $n(x,y,z)$ integrated over the imaging beam direction x, $\eta(y,z) = \int n(x,y,z)dx$. The transmission function $T(y,z)$ (in pixels) is derived by dividing the atom image by the background picture. Using σ from Eq. (C.13), the column density is calculated as

$$\eta(y,z) = -\frac{\ln T(y,z)}{\sigma}. \tag{C.16}$$

A fit of $\eta(y,z)$ with a two-dimensional Gaussian distribution,

$$\eta(y,z) = \hat{\eta}\exp\left[-\left(\frac{y-\overline{y}}{w_y}\right)^2 - \left(\frac{z-\overline{z}}{w_z}\right)^2\right], \tag{C.17}$$

yields the $1/e$-widths $w_{y,z}$, the center of the cloud $(\overline{y},\overline{z})$ and $\hat{\eta}$. These fitted parameters, together with the pixel size $l = 6.02(2)\,\mu$m, allow to calculate the particle number N_{fit} as

$$N_{\mathrm{fit}} = \pi l^2 w_y^2 w_z^2 \hat{\eta}. \tag{C.18}$$

Temperature measurement

The temperature of the atom cloud is measured via time-of-flight technique [Ket99]. For this, the expansion time t after release from the trap is varied between $10 - 70$ ms for successive repetitions of experimental runs[13], and the $1/e$-widths $w_{y,z}(t)$ are fitted according to

$$w_{y,z}(t) = \sqrt{w_{y,z}(0) + 2\sigma_{v_y,v_z}^2 t^2}. \tag{C.19}$$

The Gaussian widths σ_{v_y,v_z} of the velocity distribution are related to the temperature T via

$$\sigma_{v_y,v_z} = \sqrt{\frac{k_B T}{m}}. \tag{C.20}$$

The temperatures derived from σ_{v_y} and σ_{v_z} differ slightly, due to the fact that after release from the optical dipole trap, magnetic trapping and/or anti-trapping forces influence the atom trajectories. In the magnetic high-field region, this is mainly caused by horizontal trapping and vertical anti-trapping forces produced by the *Bias coils*, as discussed in Sec. B.2.2. Limiting the expansion times decreases the size of this error. In the magnetic low field region, the magnetic levitation field[14] leads to a transversal force as described in Ref. [Her05].

[13] Without the magnetic levitation field, t is limited to 30 ms by the size of the CCD chip.

[14] The temperature measurements related to the publications presented in Chapters 2, 3, 5 and 7 were performed without a supporting magnetic leviation field.

APPENDIX D

MICROWAVE TRANSITIONS

In principle, microwave (MW) transitions connect states of different hyperfine levels of the same (ground- or excited-state) manifold. Besides state transfers, microwave radiation can be used in a similar manner as rf radiation for the creation of trapping potentials [Spr94, Ago89].

In Sec. D.1, the application of microwave radiation in our experimental setup is discussed. Sec. D.2 describes the newly implemented microwave setup for the magnetic high-field region.

D.1. Applications

Magnetic field calibration

For the publications presented in this PhD thesis, the magnetic field strength B was calibrated by directly probing the atom sample by means of microwave spectroscopy. This method is based on the magnetic field dependent variation of transition frequencies within the ground-state manifold due to the Zeeman effect, as described in Sec. A.2.

For this, a hyperfine transition from the initial $|F = 3, m_F = 3\rangle$ to the $|F = 4, m_F = 4\rangle$ state is probed by a 5 ms microwave pulse. In our experiment, transitions with $\Delta m_F = +1$ are preferred[1] due to the tilting of the microwave horn relatively to the vertical magnetic field axis. However, we observe $\Delta m_F = -1, 0$ transitions as well (see Chapter 3), which allows to increase the calibration range for the magnetic field strength (see Fig. D.3). After a waiting time of ~ 100 ms, atoms in the excited state are lost due to inelastic two-body collisions[2]. The microwave frequency is scanned and the remaining atom number is recorded in subsequent experimental runs. If the microwave frequency matches the atomic

[1] According to the selection rules for magnetic dipole transitions, $\Delta m_F = 0, \pm 1$.

[2] For a non-zero magnetic levitation field, the atoms in different states spatially separate because of the difference in magnetic moment $\Delta\mu(B)$, thereby allowing shorter waiting times for the calibration procedure.

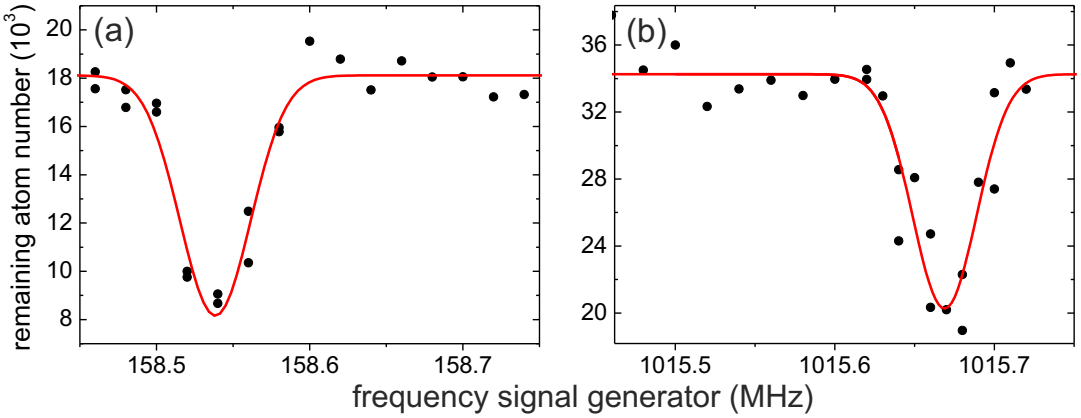

Figure D.1.: Samples of typical calibration measurements of the magnetic field strength in the high-field region. The microwave drives a hyperfine transition $|F = 3, m_F = 3\rangle \rightarrow |F = 4, m_F = 4\rangle$, leading to a loss-resonance. The resonance frequency is determined by a Gaussian fit. From this value the magnetic field strength is obtained using the *Breit-Rabi formula*. The horizontal axis corresponds to the frequency ν_{SG} of a signal generator, which is electronically mixed with a 10.5 GHz oscillator (see Sec. D.2). In these measurements, only the blue sideband is resonant ($\nu = 10.5\,\mathrm{GHz} + \nu_{\mathrm{SG}}$). The transition frequencies and linewidths (FWHM) are (a) $\nu_{\mathrm{SG}} = 158.535(2)$ MHz, $\Delta\nu = 55(5)$ kHz and (b) $\nu_{\mathrm{SG}} = 1015.669(2)$ MHz, $\Delta\nu = 45(5)$ kHz. This results in a magnetic field strength of 586.225(1) G for (a) and 920.712(1) G for (b).

hyperfine transition frequency ν_0, a loss resonance can be observed; see Fig. D.1. From this transition frequency, the magnetic field strength is determined using the *Breit-Rabi formula* (Eq. (A.15)).

The width of the loss resonance $\Delta\nu$ is a measure for the stability of the magnetic field system $\delta B_{\mathrm{noise}}$, provided that no magnetic gradient (levitation) field is applied. Then, $\delta B_{\mathrm{noise}}$ can be estimated as

$$\delta B_{\mathrm{noise}} = \frac{h}{\Delta\mu(B)}\Delta\nu \simeq \frac{4}{7}\frac{h}{\mu_B}\Delta\nu. \tag{D.1}$$

In case of a magnetic gradient (levitation) field being applied, the linewidth of the loss resonance increases according to[3]

$$\Delta\nu \simeq \frac{\Delta\mu(B)}{h}\frac{\partial B}{\partial z}w_z^{\mathrm{FWHM}} \simeq \frac{7}{4}\frac{\mu_B}{h}\frac{\partial B}{\partial z}w_z^{\mathrm{FWHM}}. \tag{D.2}$$

The FWHM-width w_z^{FWHM} in vertical direction (which is the direction of the gradient field) is given by [Gri00a]

$$w_z^{\mathrm{FWHM}} = 2\sqrt{2\ln 2}\sigma_z \quad \text{with} \quad \sigma_z = \frac{1}{\omega_z}\sqrt{\frac{k_B T}{m}}, \tag{D.3}$$

[3]In this context, the effect of the magnetic field curvature is negligible.

for a thermal atom cloud confined in a harmonic potential with a vertical trapping frequency $\nu_z = \omega_z/(2\pi)$. Note that, strictly speaking, the terms on the right in Eqs. (D.1) and (D.2) are only valid in the anomalous Zeeman-regime.

Up to now, the magnetic field calibration measurements in the magnetic high-field region have been performed with a supporting levitation field of 8 G/cm. These measurements show linewidths of $45 - 55$ kHz (FWHM), which sets a limit for the magnetic field noise of $\delta B_{\mathrm{noise}} < 20$ mG, corresponding to a relative stability of the total magnetic field strength of $< 2 \times 10^{-5}$; see Fig. D.1.

Purification of dimer samples

Fast removal of the atoms is necessary for experiments on pure dimer samples, as atom-dimer relaxation losses limit the lifetime considerably (see Chapter 2). In experiments which are focused on dimer-dimer processes (see Chapters 5 and 7), microwave transitions are utilized for removing remaining atoms after dimers have been created via Feshbach association. For this, the atoms are first transferred from the $|F = 3, m_F = 3\rangle$ to the $|F = 4, m_F = 4\rangle$ state via an adiabatic passage, performed by a slight variation of the magnetic field while a short microwave pulse is applied. Finally, the atoms are pushed out of the trap by illumination with the low-field imaging light, which operates at the $|F = 4, m_F = 4\rangle \rightarrow |F' = 5, m'_F = 5\rangle$ transition.

State-selective creation of atom-dimer samples

For the publication presented in Chapter 3, ultracold exchange reactions in different atom-dimer samples are analyzed. For this, the atoms are prepared in the $|F = 4, m_F = 2, 3, 4\rangle$ hyperfine states by a microwave state transfer via an adiabatic passage.

Binding energy measurements

In the publication of my former colleagues [Mar07a], microwave transitions are used to obtain the binding energies of the weakly bound open-channel s-wave state in dependence of the magnetic field strength. For this purpose, a sample of s-wave dimers is prepared, and the transition frequency to another weakly bound dimer state, belonging to the closed-channel $|F = 3, m_F = 3\rangle + |F = 4, m_F = 4\rangle$ potential, is measured. From this *bound-bound* transition frequency, the binding energy of the open-channel s-wave state is determined.

A drawback of this method, however, is the fact that it demands a sufficiently large dimer sample, as well as knowledge of the binding energy of the molecular state in the closed-channel. Therefore, newer measurements (see Appendix F.3) are performed by using radio-frequency magnetic-field modulation spectroscopy as explained in Appendix E.

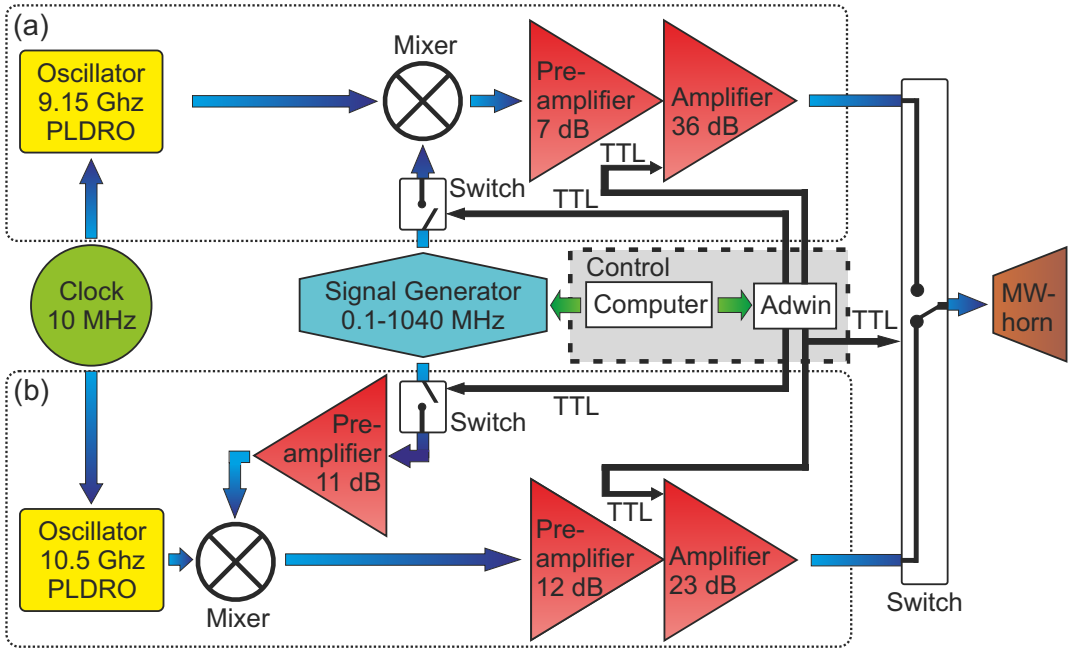

Figure D.2.: Schematic of the microwave setup for (a) the low-field region (lf) [Mar08b] and (b) the high-field region (hf). The two setups are similar and described simultaneously. A commercial 10 MHz Rb-clock is the reference for a phase locked dielectric resonator oscillator (PLDRO, lf: 9.15 GHz, hf: 10.5 GHz). The (hf: amplified) signal created by a signal generator is mixed with the carrier frequency from the PLDRO in order to create sidebands. The carrier and sidebands are amplified and out-coupled via a microwave-horn. The switches and amplifiers are controlled by digital logic pulses from the real-time control system (Adwin), which is programmed in the beginning of each experimental cycle via the lab computer. The frequency and amplitude of the out-coupled microwave signal are controlled by the signal generator, which is connected to the lab computer via a GPIB interface.

D.2. Microwave setup

The microwave setup consists of two parts, which are separately optimized to drive transitions in either the magnetic low-field or high-field region; see Fig. D.2. The low-field setup is limited to microwave transitions with a maximum transition frequency of 10.19 GHz[4], which allows to drive $|F = 3, m_F = 3\rangle \rightarrow |F = 4, m_F = 4\rangle$ transitions up to $\sim$ 400 G. As calibration measurements for the magnetic high-field region of up to 1000 G are necessary, a new high-field setup has been implemented. The low-field setup is described in the PhD thesis of my former colleague [Mar08b].

For the high-field setup, we use a phase locked dielectric resonator oscilla-

[4]The value of 10.19 GHz results from a phase locked dielectric resonator oscillator with a frequency of 9.15 GHz mixed with the output of a $0.1 - 1040$ MHz signal generator.

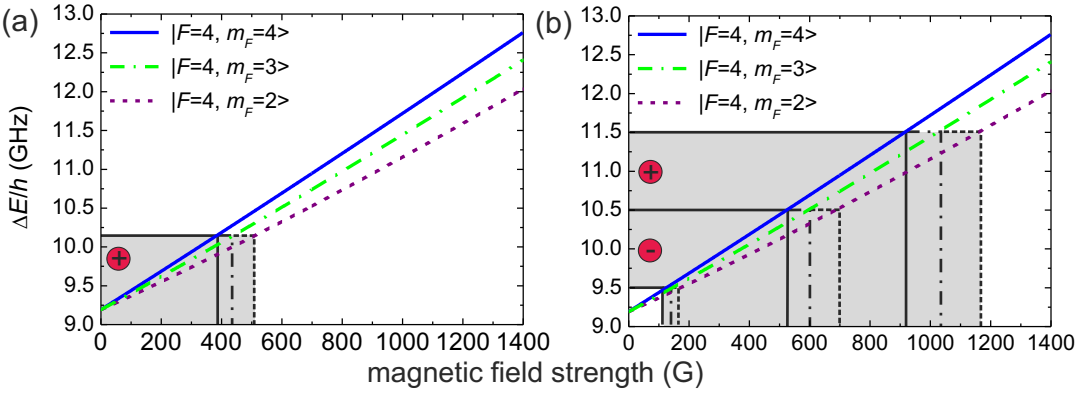

Figure D.3.: Microwave frequencies for the $|F = 3, m_F = 3\rangle \rightarrow |F = 4, m_F = 2, 3, 4\rangle$ transitions calculated with Eq. (A.15). The figures visualize the regions where (a) the low-field and (b) the high-field setup are applicable. The signs indicate the regions accessible for the blue ("+") and red ("-") sideband. The legend denotes the final states.

tor (PLDRO) from Amplus Communications (AM-4000-1005), which provides a carrier frequency of 10.5 GHz[5]. For phase locking, a 10 MHz reference signal from a commercial Rb-clock (Stanford Research Systems) is used. The carrier frequency is electronically mixed (frequency mixer SIM-153, Mini-Circuits) with the amplified sinusoidal signal from a programmable signal generator (HP8657A, $0.1 - 1040$ MHz). The signal generator is programmed via GBIP by the lab computer, and a digitally controlled switch (ZMSW-1211, Mini-Circuits) allows to vary the duration of the microwave pulse during the experimental sequence. A pre-amplifier (ZX60-14012L+, Mini-Circuits) prepares the signal amplitude for efficient mixing.

The microwave transitions are driven by the tunable sidebands, which are created in the mixing process. The signal (carrier + sidebands) is amplified in a two-step process including a pre-amplifier (ZX60-14012L+, Mini-Circuits) and a power-amplifier (KU 1012 MM, Kuhne electronic). A high-power switch (MSP2TA-18, Mini-Circuits) allows to switch between the low-field and high-field microwave setup. The TTL signal for the operation of this switch controls the power-amplifier[6] as well. The final signal is transferred to a microwave-horn, which is used as an out-coupler to irradiate the microwave into free space. The horn is mounted on top of the central chamber, slightly tilted, at a distance of about 5 cm from the atom cloud.

The frequency and power of the microwave radiation is controlled via the signal generator. The tunability of the two main sidebands allows to cover a range of 10.5 ± 1.04 GHz. Taking into account the low-field setup, $|F = 3, m_F = 3\rangle \rightarrow |F = 4, m_F = 4\rangle$ transitions can be performed at magnetic field

[5]The exact carrier frequency is 10.499 999 27(5) GHz.

[6]The amplifier is only switched on several ms before and after the microwave pulse for noise-reduction.

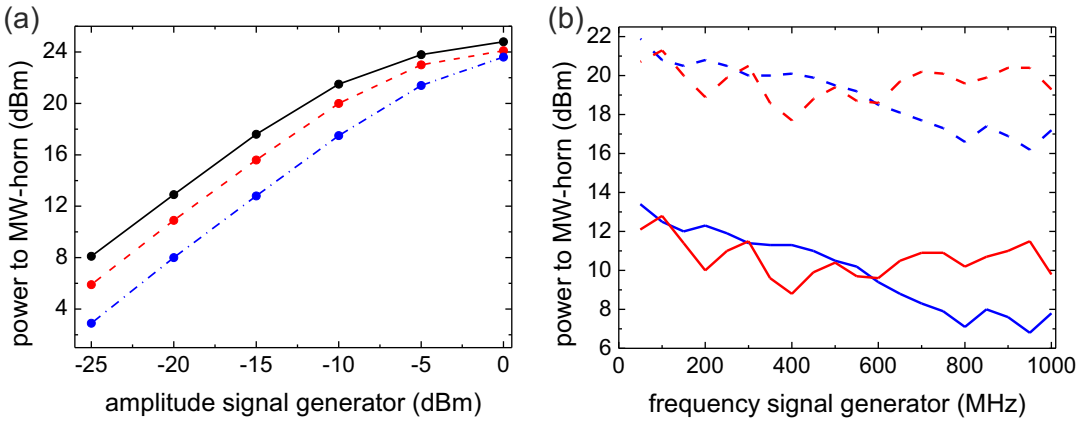

Figure D.4.: Power feed to the microwave horn in dependence on the amplitude and frequency of the signal from the signal generator. (a) The microwave power is over a wide range linear with the amplitude of the signal, with a saturation for large powers (blue sidebands - black solid line: 100 MHz, red dashed line: 500 MHz, blue dash-dotted line: 1000 MHz). (b) The microwave power of the main sidebands for two different input powers (solid line: -20 dBm, dashed line: -10 dBm). The red sidebands (red) remain more or less on the same level, whereas the blue sidebands (blue) show a decrease for larger frequencies.

strengths up to 900 G; see Fig. D.3. The carrier frequency is sufficiently off-resonant that it does not perturb the transitions. Although weaker, transitions to $|F = 4, m_F = 2, 3\rangle$ are possible and increase the range for magnetic field strength calibration up to $\sim$ 1200 G. Fig. D.4 shows the dependence of the microwave output power on the amplitude and frequency of the input signal.

APPENDIX E

RADIO-FREQUENCY SPECTROSCOPY

Radio-frequency (rf) radiation is a versatile tool for experiments with ultracold atoms and molecules. The alignment of the radiation with respect to the quantization axis set by the magnetic bias field allows to differentiate between tranversal and longitudinal rf radiation, as outlined in Sec. E.1. A theoretical introduction to rf magnetic field modulation spectroscopy, which is based on longitudinal rf radiation, is given in Sec. E.2. Sec. E.3 presents a method to precisely determine binding energies by rf magnetic field modulation spectroscopy. The experimental implementation of the rf setup is described in Sec. E.4.

E.1. Transversal and longitudinal rf radiation

The experimental utilization of rf radiation is based on the coupling of the oscillating magnetic radiation field $\mathbf{B}_{\mathrm{rf}}(t)$ with the magnetic dipole operator[1] $\hat{\mu}$ of the particles involved. The alignment of $\mathbf{B}_{\mathrm{rf}}$ in reference to the magnetic bias field $\mathbf{B}$ allows to differentiate between *transversal* ($\mathbf{B}_{\mathrm{rf}}(t) \perp \mathbf{B}$) and *longitudinal* ($\mathbf{B}_{\mathrm{rf}}(t) \| \mathbf{B}$) rf radiation.

Rf spectroscopy techniques, based on a transversal $\mathbf{B}_{\mathrm{rf}}(t)$, were employed to dissociate (*bound-free transition*) and associate (*free-bound transition*) Feshbach molecules [Reg03b, Osp06, Bar05, Zir08b, Kle08, Chi05a]. They were also used to measure the pairing gap in a strongly interacting Fermi gas [Chi04a] and the mean-field interaction energy of a Fermi gas [Reg03a]. Furthermore, this technique was successfully applied to determine the energy of Efimov trimers in a spin mixture of fermionic ^{6}Li [Lom10b, Nak11]. The coherent interaction of atoms with transversal rf radiation allows the creation of trapping potentials [Zob01, Col04, Les06, Hof06] and the manipulation of Feshbach resonances similar to an optical Feshbach resonance [Han10, Kau09, Tsc10].

[1] The magnetic dipole operator $\hat{\mu}$ relates to the angular momentum operators by $\hat{\mu} = -\frac{\mu_B}{\hbar}(\hat{\mathbf{L}} + g_S\hat{\mathbf{S}} + g_I\hat{\mathbf{I}})$ (see Eq. (A.2)), which reduces for the ground-state manifold to $\hat{\mu} = -\frac{\mu_B}{\hbar} g_F \hat{\mathbf{F}}$ in the magnetic field region investigated.

Application of a longitudinal $\mathbf{B}_{\mathrm{rf}}(t)$ has recently been proven to be a powerful method for determining bound state energies and controllable atom-to-molecule, and vice-versa, state transfers [Tho05b, Web08, Lan09b, Tha09, Bea10, Pas10, Gro10, Han07, Ber07, Ber06]. Moreover, with this method state transfers between different molecular bound states (*bound-bound transition*) were performed [Lan08a][2].

Longitudinal rf excitation is experimentally achieved by an rf modulation of the magnetic bias field. Therefore, the application of this method for means of spectroscopy is referred to as *rf magnetic field modulation spectroscopy* in the following.

Note that the interaction Hamiltonian $H_{\mathrm{rf}}(t)$ describing a longitudinal $\mathbf{B}_{\mathrm{rf}}(t)$ is diagonal in the bare states basis, whereas for transversal excitations, it has off-diagonal elements. Therefore, the effectiveness of a longitudinal magnetic field modulation relies on an additional interchannel coupling mechanism. In contrast to a transversal $\mathbf{B}_{\mathrm{rf}}(t)$, which couples states with different projections of the total magnetic moment quantum number, the longitudinal rf modulation conserves this quantum number.

E.2. Model for rf magnetic field modulation spectroscopy

In this section, the association of dimers in an ultracold cloud of thermal atoms by rf magnetic field modulation is described by a simple model, which is based on an approach given in Ref. [Bea10]. Note that in contrast to Ref. [Bea10], where the radiation field is quantized, the model given here treats the field classically.

The frequency related to the association process allows to determine the binding energy E_b of the dimers. It is assumed that only the continuum states of two free atoms $|\mathrm{at}, E_{\mathrm{rel}}\rangle$ with relative (collision) energy E_{rel} and the molecular state $|\mathrm{mol}\rangle$ are involved in the process. The rf modulation field $\mathbf{B}_{\mathrm{rf}}(t) = \mathbf{B}_{\mathrm{rf}} \cos(\omega_{\mathrm{rf}} t)$, with modulation amplitude $\mathbf{B}_{\mathrm{rf}}$ and frequency $\nu_{\mathrm{rf}} = \omega_{\mathrm{rf}}/(2\pi)$, is parallel to the quantization axis defined by the magnetic bias field $\mathbf{B}$.

The complete Hamiltonian $\hat{H}(t)$, including the rf modulation, takes the form

$$\hat{H}(t) = \hat{H}_0 + \hat{W} + \hat{H}_{\mathrm{rf}}(t), \tag{E.1}$$

which is given in matrix representation in the bare state basis $(|\mathrm{at}, \mathrm{E}_{\mathrm{rel}}\rangle, |\mathrm{mol}\rangle)$ as

$$\hat{H}(t) = \begin{pmatrix} \hat{H}_{0,\mathrm{at}} + \hat{H}_{\mathrm{rf}}(t) & \hat{W} \\ \hat{W} & \hat{H}_{0,\mathrm{mol}} + \hat{H}_{\mathrm{rf}}(t) \end{pmatrix}. \tag{E.2}$$

[2] *Bound-bound transitions* that we carried out to measure the energy difference of the $4d(4)$ and the $6g(6)$ cesium molecular states at an avoided level crossing are published in Ref. [Hut08]. Note that the molecular states are labeled according to their quantum numbers $f\ell(m_f)$, with $f = |\mathbf{F}_1 + \mathbf{F}_2|$ and ℓ being the rotational quantum number of the relative motion of atom 1 and 2.

The Hamiltonians $\hat{H}_{0,\mathrm{at}}$ and $\hat{H}_{0,\mathrm{mol}}$ describe the bare state energies of two atoms and a molecule, respectively, including the magnetic field dependence of the Zeeman energy. The time-dependent Hamiltonian describing the effect of the rf field $\hat{H}_{\mathrm{rf}}(t) = -\hat{\mu}\cdot\mathbf{B}_{\mathrm{rf}}\cos(\omega_{\mathrm{rf}}t)$ commutes with $\hat{H}_0$. The interchannel coupling is given by $\hat{W}$, which contains all coupling mechanisms that could principally lead to the appearance of Feshbach resonances, for example, the strong electronic interaction or the weak relativistic spin-spin and second-order spin-orbit interactions [Köh06b]. This off-diagonal interchannel coupling determines the width (coupling strength) Γ_0 of the related Feshbach resonance [Chi10],

$$\Gamma_0(E_{\mathrm{rel}}) = 2\pi|\langle \mathrm{mol}|\hat{W}|\mathrm{at}, E_{\mathrm{rel}}\rangle|^2. \tag{E.3}$$

Eq. (E.1) suggests a bifocal perspective, depending on which of the contributing Hamiltonians are analyzed first. When starting with $\hat{H}_0 + \hat{W}$, the resulting coupled states are no longer eigenstates of $\hat{H}_{\mathrm{rf}}(t)$. These eigenstates are, in turn, coupled by the interaction Hamiltonian $\hat{H}_{\mathrm{rf}}(t)$. This approach is discussed in Refs. [Lan09a, Lan08a].

Another way to look at Eq. (E.1) is to first consider $\hat{H}_0 + \hat{H}_{\mathrm{rf}}(t)$, followed by the coupling related to $\hat{W}$. The temporal periodicity of $\hat{H}_{\mathrm{rf}}(t)$ gives rise to the creation of sidebands, which interact according to $\hat{W}$. The subsequent discussion is based upon this approach, which is valid in the linear Zeeman regime [Bea10, Pas10]. Note that the Hamiltonian of Eq. (E.1) can also be analyzed using a Floquet approach [Shi65].

We adopt the convention that an energy of zero corresponds to the energy of two free atoms in the incoming (open) channel in the limit of zero collision energy $E_{\mathrm{rel}} = 0$. Now, the energies of the uncoupled time-independent two-atom and dimer states are given as

$$\big(\hat{H}_{0,\mathrm{at}} + \hat{H}_{\mathrm{rf}}(t)\big)\widetilde{|\mathrm{at}, \mathrm{E}_{\mathrm{rel}}\rangle} = \big(E_{\mathrm{rel}} - 2\mu^{\mathrm{at}}B_{\mathrm{rf}}\cos(\omega_{\mathrm{rf}}t)\big)\widetilde{|\mathrm{at}, \mathrm{E}_{\mathrm{rel}}\rangle}, \tag{E.4}$$

$$\big(\hat{H}_{0,\mathrm{mol}} + \hat{H}_{\mathrm{rf}}(t)\big)\widetilde{|\mathrm{mol}\rangle} = \big(-E_b(B) - \mu^{\mathrm{mol}}B_{\mathrm{rf}}\cos(\omega_{\mathrm{rf}}t)\big)\widetilde{|\mathrm{mol}\rangle}, \tag{E.5}$$

where μ^{at} and μ^{mol} are the magnetic moment of the atoms and dimers, respectively. We define the magnetic field dependent binding energy $E_b(B)$ to be positive for a real bound state. The tilde indicates the eigenstates of $\hat{H}_0 + \hat{H}_{\mathrm{rf}}(t)$. The time-dependent states are given as

$$\widetilde{|\mathrm{at}, E_{\mathrm{rel}}(t)\rangle} = |\mathrm{at}, E_{\mathrm{rel}}\rangle \cdot \exp\Big[-\frac{i}{\hbar}\big(E_{\mathrm{rel}} - 2\mu^{\mathrm{at}}B_{\mathrm{rf}}\cos(\omega_{\mathrm{rf}}t)\big)\,t\Big], \tag{E.6}$$

$$\widetilde{|\mathrm{mol}(\mathrm{t})\rangle} = |\mathrm{mol}\rangle \cdot \exp\Big[-\frac{i}{\hbar}\big(-E_b(B) - \mu^{\mathrm{mol}}B_{\mathrm{rf}}\cos(\omega_{\mathrm{rf}}t)\big)\,t\Big]. \tag{E.7}$$

The coupling strength Γ can be calculated according to the Fermi golden rule

[Nap94] as

$$\Gamma(E_{\rm rel}) = 2\pi\left|\langle\widetilde{\rm mol(t)}|\hat{W}|{\rm at},\widetilde{E_{\rm rel}(t)}\rangle\right|^2\delta(\Delta E_{if}) \tag{E.8}$$

$$= 2\pi\Big|\langle{\rm mol}|\hat{W}|{\rm at},{\rm E_{rel}}\rangle \cdot\exp\big[-\frac{i}{\hbar}(E_{\rm rel}+E_b(B)-\Delta\mu B_{\rm rf}\cos(\omega_{\rm rf}t))t\big]\Big|^2\delta(\Delta E_{if}). \tag{E.9}$$

Here, $\Delta\mu = 2\mu_{\rm at}-\mu_{\rm mol}$ is the difference of magnetic moments, and the delta function assures that the energy in the process is conserved, with ΔE_{if} referring to the difference in the eigenenergies of the initial and final states $|\widetilde{\rm at},\widetilde{E_{\rm rel}}\rangle$ and $|\widetilde{\rm mol}\rangle$.

The expression above can be simplified by replacing $\cos(\omega_{\rm rf}t)t$ with its time-average, which is reasonable for frequencies $\omega_{\rm rf}\gg 2\pi/t$,

$$\langle\cos(\omega_{\rm rf}t)\,t\rangle_t = \frac{1}{t}\int_0^t\cos(\omega_{\rm rf}t')\,t'dt' \tag{E.10}$$

$$= \frac{\sin(\omega_{\rm rf}t)}{\omega_{\rm rf}}+\frac{\cos(\omega_{\rm rf}t)}{\omega_{\rm rf}^2t}-\frac{1}{\omega_{\rm rf}^2t} \tag{E.11}$$

$$\xrightarrow{\omega_{\rm rf}t\gg1} \frac{\sin(\omega_{\rm rf}t)}{\omega_{\rm rf}}. \tag{E.12}$$

The time-dependent factor $\exp\big[-\frac{i}{\hbar}(E_{\rm rel}+E_b(B))\,t-\Delta\mu B_{\rm rf}\frac{\sin(\omega_{\rm rf}t)}{\omega_{\rm rf}}\big]$ can be developed into a series of Bessel functions J_N using the *Jacobi - Anger expansion*

$$e^{iz\sin(\omega_{\rm rf}t)} = \sum_{N=-\infty}^{\infty}e^{iN\omega_{\rm rf}t}J_N(z), \tag{E.13}$$

which corresponds to the creation of sidebands energetically shifted from the bare states by $\pm N\hbar\omega_{\rm rf}$.

Putting this into Eq. (E.9), it follows

$$\Gamma(E_{\rm rel}) = 2\pi\Big|\langle{\rm mol}|\hat{W}|{\rm at},{\rm E_{rel}}\rangle \cdot\sum_{N=-\infty}^{\infty}J_N\left(\frac{\Delta\mu B_{\rm rf}}{\hbar\omega_{\rm rf}}\right)\exp\big[-\frac{i}{\hbar}(E_{\rm rel}+E_b(B)-N\hbar\omega_{\rm rf})\,t\big]\Big|^2\cdot\delta(\Delta E_{if}). \tag{E.14}$$

From the phase factors of the infinite sum we can read the energy difference as

$$\Delta E_{if} = E_{\rm rel}+E_b(B)-N\hbar\omega_{\rm rf}, \tag{E.15}$$

which has to be zero due to energy conservation, $\delta(\Delta E_{if})$, hence,

$$E_b(B) = N\hbar\omega_{\rm rf}-E_{\rm rel}, \tag{E.16}$$

where N can be identified as the rf photon number. Since for our ultracold atom sample[3] $E_{\mathrm{rel}} \ll \hbar\omega_{\mathrm{rf}}$, this resonance condition is only fulfilled for a certain $N = N_{\mathrm{res}}$. Therefore, the series of Bessel functions in Eq.(E.14) can be reduced to one term, leading to the the final result

$$\Gamma(E_{\mathrm{rel}}) = 2\pi \left| \langle \mathrm{mol}|\hat{W}|\mathrm{at}, \mathrm{E_{rel}}\rangle \cdot J_{N_{\mathrm{res}}}\left(\frac{\Delta\mu B_{\mathrm{rf}}}{\hbar\omega_{\mathrm{rf}}}\right)\right|^2 \tag{E.17}$$

$$= \Gamma_0(E_{\mathrm{rel}}) \left| J_{N_{\mathrm{res}}}\left(\frac{\Delta\mu B_{\mathrm{rf}}}{\hbar\omega_{\mathrm{rf}}}\right)\right|^2, \tag{E.18}$$

using the Feshbach coupling strength Γ_0 (Eq.(E.3)). Typically, $N_{\mathrm{res}} = 1$ in the experiments. However, for large modulation amplitudes two-photon transitions ($N_{\mathrm{res}} = 2$) are observed as well.

To summarize, the rf field leads to a sinusoidal time-modulation of the eigenenergies of the system, due to the periodic modulation of the Zeeman energies of the states. This modulation creates sidebands shifted by an energy of $N\hbar\omega_{\mathrm{rf}}$. When one of these sidebands energetically coincides with the dimer state, an *assisted* Feshbach resonance is induced by $\hat{W}$. The coupling strength depends on the bare Feshbach coupling strength Γ_0, the applied rf amplitude B_{rf}, the frequency $\nu_{\mathrm{rf}} = \omega_{\mathrm{rf}}/(2\pi)$ and the magnetic moment difference $\Delta\mu$. For both approaches, the one discussed in Refs. [Lan09a, Lan08a] as well as the one presented here, the coupling efficiency decreases with increasing ν_{rf}, corresponding to the decrease of the open-channel contribution to the bound state. Note that as the coupling strength Γ is a result of the interchannel interaction $\hat{W}$, states of the same molecular potential cannot be coupled by rf magnetic field modulation.

E.3. Determination of binding energies

In this section, the method for precise determination of the dimer binding energy in a *free-bound transition* by magnetic field modulation spectroscopy, performed on a thermal atom sample, is described. This method is based on fitting a theoretically derived line shape of the atom loss to the experimental data [Web08, Kle08, Bea10].

Experimentally, we obtain $E_b(B)$ by either varying the modulation frequency ν_{rf} at fixed magnetic field strength B (*frequency scan*) or by changing B, and thereby $E_b(B)$, while fixing ν_{rf} (*magnetic field scan*). The finite temperature of the sample leads to a distribution of E_{rel} in the harmonic trap, resulting in broad and asymmetric loss signals; see Fig. E.1.

As outlined in Sec. E.2, dimers are produced in a process referred to as an *assisted* Feshbach resonance when the resonance condition for the rf modulation frequency ν_{rf}, which is stated in Eq. (E.16), is fulfilled. These dimers exhibit a relatively short lifetime τ_D, due to atom-dimer relaxation to deeply bound

[3] $T = 50$ nK, which is a typical temperature of the atoms sample, corresponds to $\omega_{\mathrm{rf}} \sim 2\pi \times 1$ kHz.

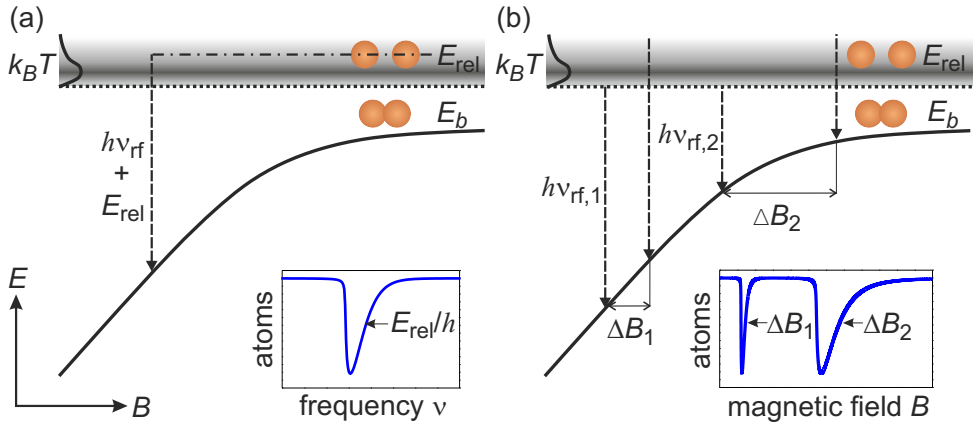

Figure E.1.: Determination of $E_b(B)$ by (a) a *frequency scan* or (b) a *magnetic field scan*. This illustration shows exemplary the energies of the states involved in an atom-dimer association process as a function of B for a thermal sample. The dotted horizontal line depicts the zero-energy threshold of two atoms at rest, $E_{\mathrm{rel}} = 0$. The finite temperature T leads to a Maxwellian distribution of E_{rel}, illustrated by the shaded area above the zero-energy threshold. The solid line depicts the binding energy E_b of a weakly bound dimer state. For decreasing B the dimer state takes on the closed-channel bound state character. For increasing B, the coupling of the closed-channel dimer state to the weakly bound open-channel state of Cs in $|F = 3, m_F = 3\rangle$ with $E_b \simeq 10$ kHz leads to a curvature of E_b until the dimer state is of purely open-channel character. (a) For a *frequency scan*, B is fixed and ν_{rf} is varied. Atom losses occur if the resonance condition of Eq. (E.16) is fulfilled, which is typically the case for $N_{\mathrm{res}} = 1$. The distribution of E_{rel} leads to an asymmetric line shape of the loss signal. (b) For a *magnetic field scan*, ν_{rf} is fixed and B is varied. The width of the loss signal depends on $\Delta\mu(B)$; note the difference of ΔB for $\nu_{\mathrm{rf},1}$ and $\nu_{\mathrm{rf},2}$ in the inset. The insets illustrate exemplary the line shapes of loss signals in an atom-dimer association process; arrows indicate the width of the resonances. The application of a magnetic gradient field, as well as the existence of magnetic field noise, increase the width and symmetrize the line shape of the loss signal.

dimers. Typically, three particles are lost in this process, $n_l = 3$ (see Chapter 2). Additionally, dimers can leave the trap, resulting in $n_l = 2$, because of a mismatch of μ_{mol} and the levitation field, which is optimized for atoms[4]. For large atom-dimer elastic cross-sections, avalanche effects as described in Ref. [Zac09] can occur, causing $n_l > 3$. The fitting procedure is independent of the definite value of n_l, as long as $n_l > 0$.

Typically, τ_D is much smaller than the dimer association time, therefore, the association process results in a reduction of the atom number N_{at} according to

$$\frac{dN_{\mathrm{at}}}{dt} = -n_l K_2(\nu_{\mathrm{rf}}, E_b(B)) \frac{N_{\mathrm{at}}^2}{V_{\mathrm{eff}}}, \tag{E.19}$$

[4]In the case that $\Delta\mu \simeq 0$, dimers may remain trapped.

with the effective volume[5] $V_{\text{eff}} = (4\pi k_B T/(m\bar{\omega}^2))^{3/2}$. Eq. (E.19) is valid for a 3D harmonic trap with the geometric mean of the trap frequencies $\bar{\omega} = (\omega_x\omega_y\omega_z)^{1/3}$. The two-body loss rate is introduced as K_2, assuming a two-body density dependence; however, this does not necessarily mean that two particles are lost from the trap. Other loss processes, such as three-body recombination, are neglected in this treatment[6].

The loss process is similar to the one treated in the theory for photoassociation line shapes in Refs. [Nap94, Jon06, Web08, Bea09]. For a thermal sample, K_2 is proportional to[7]

$$K_2(\nu_{\text{rf}}, E_b(B)) \propto \int_0^\infty \frac{\Gamma_D\,\Gamma(E_{\text{rel}})\,e^{-\frac{E_{\text{rel}}}{k_B T}}}{\big(h\nu_{\text{rf}} - (E_{\text{rel}} + E_b(B))\big)^2 + \big(\Gamma_{\text{tot}}(E_{\text{rel}})/2\big)^2} dE_{\text{rel}}, \quad \text{(E.20)}$$

with $\Gamma_D = \hbar/\tau_D$ and the total width defined as $\Gamma_{\text{tot}}(E_{\text{rel}}) = \Gamma_D + \Gamma(E_{\text{rel}})$. Eq. (E.20) assumes a thermal distribution of the atoms $f(E_{\text{rel}}) \propto \exp(-E_{\text{rel}}/(k_B T))$, which leads to a broadening and asymmetry of the association spectrum. The probability of transitions from atom pairs to the dimer states is taken into account by convolution with a Lorentzian distribution.

Generally, atoms are converted to dimers when $\nu_{\text{rf}} = (E_{\text{rel}} + E_b)/h$, which is reflected in the denominator of Eq. (E.20). As our focus is mainly on the determination of $E_b(B)$, it is sufficient to understand the relative line strength for a fixed set of experimental parameters during a measurement, which allows to apply the following simplifications.

The loss process is typically much faster then the association process, $\Gamma_D \gg \Gamma(E_{\text{rel}})$, so it can be assumed that $\Gamma_{\text{tot}} \simeq \Gamma_D$, independent of E_{rel}.

According to Eq. (E.17), $\Gamma(E_{\text{rel}})$ depends on the bare Feshbach coupling strength, $\Gamma_0(E_{\text{rel}})$[Mie00], which features an energy dependence given by the Wigner threshold-law $\Gamma_0(E_{\text{rel}}) \propto E_{\text{rel}}^{(2\ell+1)/2}$, with ℓ being here the quantum number of the incoming partial wave [Wig48]. For ultracold collisions $\ell = 0$, resulting in $\Gamma_0(E_{\text{rel}}) \propto \sqrt{E_{\text{rel}}}$. In principle, due to variations of ν_{rf}, $\Delta\mu$ and ${}^8B_{\text{rf}}$, the coupling strength $\Gamma(E_{\text{rel}})$ changes during a measurement according to the Bessel function in Eq. (E.17). However, for the limited range where Eq. (E.16) is fulfilled, this effects can be neglected[9], $\Gamma \propto \Gamma_0$.

[5] The effective volume follows from the two-body loss equation, which is defined for the particle density n as $\dot{n} = -n_l K_2 n^2$. This equation transforms to Eq. (E.19) after integration over the volume in a 3D harmonic trap.

[6] Three-body recombination plays a minor role, as rf-association is typically performed at small (and positive) values of the s-wave scattering length.

[7] The density of states, which is related to the distribution of the relative energies E_{rel}, is a constant for a 3D harmonic potential as shown in Ref. [Kle08].

[8] For a *frequency scan* ν_{rf} is scanned and B_{rf} changes due to the variation of the impedance in the coils. In a *magnetic field scan* $\Delta\mu$ varies slightly in the vicinity of a molecular avoided crossing.

[9] This has been experimentally verified by comparing *frequency scans* and *magnetic field scans*, which show the same outcome; see Sec. F.3.1.

Therefore, Eq. (E.20) can be written as

$$K_2(\nu_{\rm rf}, E_b(B)) \simeq C_{\rm loss} \int_0^\infty \frac{\sqrt{E_{\rm rel}} e^{-\frac{E_{\rm rel}}{k_B T}}}{\left(h\nu_{\rm rf} - (E_{\rm rel} + E_b(B))\right)^2 + (\Gamma_{\rm tot}/2)^2} dE_{\rm rel}. \quad \text{(E.21)}$$

The coefficient $C_{\rm loss}$ incorporates the parameters that are assumed to be almost constant during a measurement.

The two-body loss coefficient $K_2(\nu_{\rm rf}, E_b(B))$ is related to the atom number $N_{\rm at}(\nu_{\rm rf}, B, t_{\rm rf})$ via the solution of Eq. (E.19),

$$N_{\rm at}(\nu_{\rm rf}, B, t_{\rm rf}) = \frac{N_{\rm at,0}}{1 + \frac{N_{\rm at,0}}{V_{\rm eff}} n_l K_2(\nu_{\rm rf}, E_b(B)) t_{\rm rf}}, \quad \text{(E.22)}$$

with the initial particle number[10] $N_{\rm at,0} = N_{\rm at}(\nu_{\rm rf}, B, 0)$ and $t_{\rm rf}$ being the association pulse time. The factors n_l, $V_{\rm eff}$ and $C_{\rm loss}$ can be combined into an overall loss factor $C'_{\rm loss} = n_l C_{\rm loss}/V_{\rm eff}$. The temperature T can be either fitted or determined by a separate measurement, and $N_{\rm at,0}$ can be taken from the off-resonant wings of the loss signal.

In order to obtain $E_b(B)$, the experimentally obtained loss signal can be fitted with the theoretical loss signal by

$$N_{\rm at}(\nu_{\rm rf}, B, t_{\rm rf}) = \quad \text{(E.23)}$$
$$N_{\rm at,0}\left(1 + C'_{\rm loss} N_{\rm at,0} t_{\rm rf} \int_0^\infty \frac{\sqrt{E_{\rm rel}} e^{-\frac{E_{\rm rel}}{k_B T}}}{\left(h\nu_{\rm rf} - (E_{\rm rel} + E_b(B))\right)^2 + (\Gamma_{\rm tot}/2)^2} dE_{\rm rel}\right)^{-1},$$

with the fitting parameters $C'_{\rm loss}$, $\Gamma_{\rm tot}$ and $E_b(B)$.

Simplified determination of the binding energy

A simplified determination of $E(B)$ is possible if the line shape features the asymmetric pattern related to the thermal distribution [Jon06]. According to Eq. (E.21), for $K_2(\nu_{\rm rf}, E_b(B))$ each collision energy $E_{\rm rel}$ contributes a Lorentzian centered at $\nu_{\rm rf} = (E_{\rm rel} + E_b(B))/h$ with an amplitude $\propto \sqrt{E_{\rm rel}} \exp[-E_{\rm rel}/(k_B T)]$. It is easily calculated that the largest contribution to the line comes from $E_{\rm rel} = k_B T/2$. Therefore, $E_b(B)$ can be determined in a *frequency scan* by

$$E_b(B) = h\nu_{\rm rf,max} - \frac{k_B T}{2}, \quad \text{(E.24)}$$

with $\nu_{\rm rf,max}$ being the modulation frequency at which the atom loss features a maximum[11].

[10] Assuming that the number of atoms at $t = 0$ is independent of $\nu_{\rm rf}$ and B.

[11] In Ref. [Tho05b], this shift has been measured in a ^{85}Rb sample resulting in $h\nu_{\rm rf,max} - E_b(B) = 0.60(2) k_B T$.

Effects of variations of the magnetic bias field

So far, effects on the line shape due to variations of the magnetic bias field δB have not been taken into consideration. Such variations not only broaden the loss signals but also lead to more symmetric line shapes for $\Delta\mu\delta B > k_B T$.

The main contributions are the magnetic gradient field, which leads to $\delta B_{\mathrm{grad}} = \frac{\partial B}{\partial z} w_z^{\mathrm{FWHM}}$ with the FWHM-width given in Eq. (D.3) [12], and magnetic field noise $\delta B_{\mathrm{noise}}$, which is below 20 mG for measurements in the magnetic high-field region. The effect of magnetic field curvature is negligible in comparison to the magnetic levitation field.

For an accurate determination of $E_b(B)$, the magnetic field variations have to be taken into account by convolution of Eq. (E.21) with an adequate distribution function representing δB.

Effects of magnetic field dependent magnetic moments

Here, the influence of a magnetic field dependence of $\Delta\mu$ on the derivation of the dimer binding energy is discussed. If the binding energy exhibits a quadratic dependence on the magnetic field with $\partial^2 E_b/\partial B^2 = 2\eta$, the time-modulated $E_b(B)$ is given as

$$E_b(B, B_{\mathrm{rf}}, t) = E_b(B) + \frac{\partial E}{\partial B} B_{\mathrm{rf}} \cos(\omega_{\mathrm{rf}} t) + \eta (B_{\mathrm{rf}} \cos(\omega_{\mathrm{rf}} t))^2. \tag{E.25}$$

Averaging this expression over a period leads to

$$\langle E_b(B_{\mathrm{bias}}, B_{\mathrm{rf}}) \rangle_t = E_b(B_{\mathrm{bias}}) + \frac{1}{2} \eta B_{\mathrm{rf}}^2, \tag{E.26}$$

which causes an effective shift of the measured binding energy in dependence of the modulation amplitude B_{rf}. Eq. (E.16) has then to be corrected for this shift resulting in[13]

$$E_b(B) = N\hbar\omega_{\mathrm{rf}} - E_{\mathrm{rel}} - \frac{1}{2}\eta B_{\mathrm{rf}}^2. \tag{E.27}$$

E.4. Rf magnetic field modulation setup

Here, the rf setup for the determination of dimer binding energies in the magnetic high-field region is described (see Fig. E.2), which differs only slightly from the low-field setup.

The implemented rf setup allows to perform rf magnetic field modulation spectroscopy for measuring E_b of weakly bound dimer states. For this, a sinusoidal signal for the rf association process is created by a signal generator (Agilent arbitrary waveform generator, 33250A, 80 MHz) which is programmed by the experimental software via a computer interface (General Purpose Interface Bus).

[12] This corresponds to a variation of $\delta B_{\mathrm{grad}} \sim 50$ mG for the binding energy measurements in the high-field region (reported in Sec. F.3.1).

[13] This effect has been measured in Ref. [Web08].

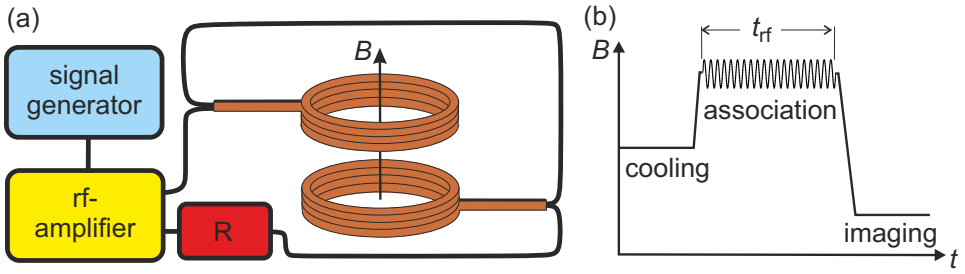

Figure E.2.: (a) Experimental setup for the rf magnetic field modulation spectroscopy. The signal generator, which is programmed via the experimental control computer (not shown), is connected to an rf amplifier, which allows to achieve sufficiently high currents in the *Curvature coils* to produce $B_{\mathrm{rf}} \sim 3$ G. The electric circuit includes four 1 Ω-resistances (R), which are connected in series. (b) Timing procedure for the rf modulation spectroscopy. The magnetic field B is ramped from the evaporation field to a magnetic field, where the dimer association is performed by application of a magnetic field modulation for a time t_{rf}. Then, the remaining atom fraction is imaged via absorption imaging at the imaging field.

The adjustable parameters are the modulation time t_{rf}, the modulation amplitude B_{rf} and the frequency ν_{rf}. The signal generator is connected to a 25 W radio-frequency amplifier (FLL25, Frankonia)[14]. The amplifier drives the current in the *Curvature coils*[15], which are connected in series with $4 \times 1\,\Omega$ high power resistances (Arcol, 300 W). This setup allows to measure binding energies exceeding $h \times 1$ Mhz.

Fig. E.3 shows the current in the *Curvature coils* as well as the amplitude of the magnetic field modulation B_{rf} as a function of the input power and frequency of the signal generator.

As the efficiency of the rf amplifier decreases significantly for frequencies below 50 kHz, for measurements in the low-frequency regime the use of an audio amplifier (LM4780, National Semiconductor) is advantageous.

[14]For safety reasons, a 20 dB attenuator is placed between the frequency generator and the rf amplifier.

[15]The *Curvature coils* are used due to their favorable properties concerning inductance and magnetic field strength as described in Sec. B.3 and listed in Table B.1.

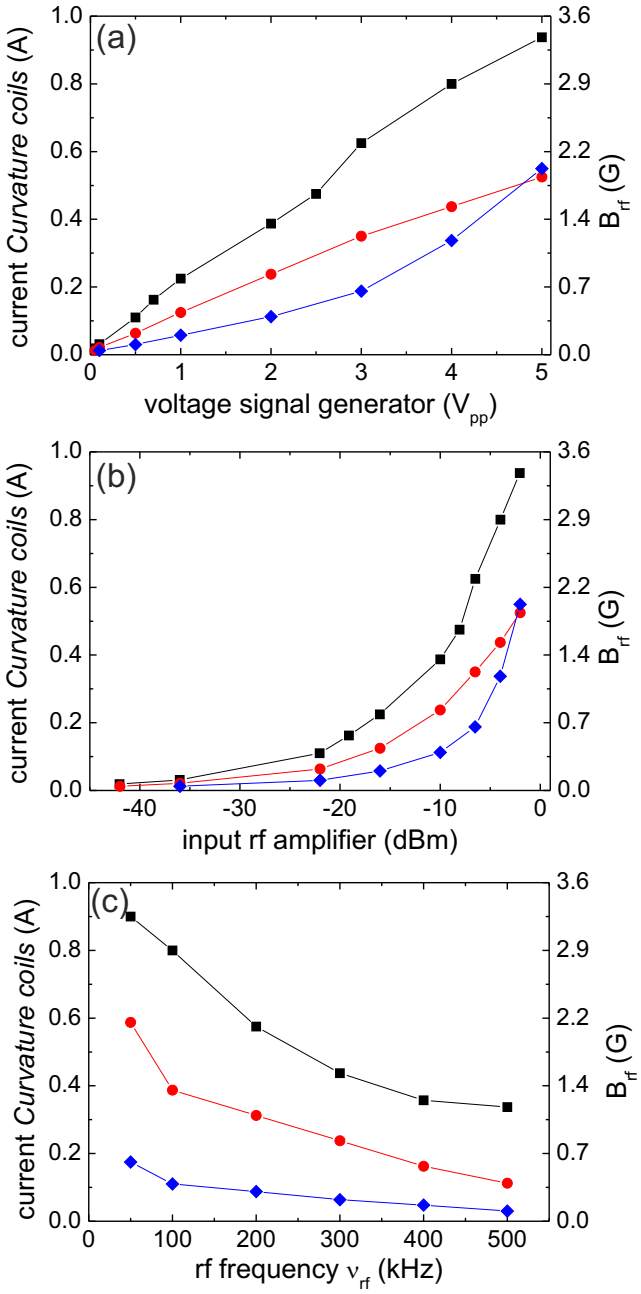

Figure E.3.: Current in the *Curvature Coils* and B_{rf} as a function of the amplitude and frequency of the signal generator. (a) The current and B_{rf} are shown in dependence of the peak-to-peak voltage ($\mathrm{V_{pp}}$), set at the signal generator. A 20 dB attenuator, placed between the output of the signal generator and the input of the rf amplifier, reduces the input signal strength for the rf amplifier. (b) The same data as (a), but as a function of the signal input power of the rf amplifier after attenuation. The data presented in (a) and (b) correspond to (■) $\nu_{\mathrm{rf}} = 100$ kHz, (●) $\nu_{\mathrm{rf}} = 300$ kHz and (♦) $\nu_{\mathrm{rf}} = 500$ kHz. Figure (c) visualizes the dependence of the current and B_{rf} on ν_{rf} for (♦) 0.5 $\mathrm{V_{pp}}$ (−22 dBm), (●) 2 $\mathrm{V_{pp}}$ (−10 dBm) and (■) 4 $\mathrm{V_{pp}}$ (−4 dBm). Voltage and power refer to the output of the signal generator and the input of the rf amplifier, respectively.

APPENDIX F

TWO-BODY SCATTERING PROPERTIES

The interpretation of few-body phenomena relies on precise knowledge of the underlying two-body scattering physics. Especially the relation between the magnetic field strength B, being the experimentally accessible parameter, and the s-wave scattering length a, which is the quantity used in universal theories, is of utmost importance. The results presented in Chapters 2, 3, 5, 6 and 7, are based on accurate experiments and analyses of the scattering properties in the magnetic low-field region ($B < 150$ G); see Ref. [Chi10] and references therein. Contrary to the low-field region, the high-field region has not been experimentally investigated in the literature, until now. In this appendix a study of the cesium scattering properties in the magnetic high-field region is presented[1].

An overview of the Feshbach resonances at the low- and high-field region is given in Sec. F.1. Initially, for the study of the high-field region, the positions of several narrow Feshbach resonances, which result from $\ell > 0$ states, are determined by trap-loss spectroscopy [Chi10]; see Sec. F.2. In a second set of experiments, binding energies of weakly bound dimer states ($\ell \geq 0$) are measured via rf-spectroscopy[2]; see Sec. F.3. Based on these results, the s-wave scattering length and the properties of the broad s-wave Feshbach resonances are derived by a coupled-channel calculation performed by J. Hutson and P. Julienne [Hut11].

F.1. Overview of the cesium Feshbach resonances

Essentially, the scattering properties of cesium in the absolute ground state $|F = 3, m_F = 3\rangle$ are governed by three broad s-wave Feshbach resonances with poles at $B_0 = -12$ G, 549 G and 787 G [Chi10, Chi04b][3]; see Fig. F.1. These s-wave Feshbach resonances stem from molecular s-wave states belonging to different atom-atom scattering hyperfine potentials.

[1] The data presented in this appendix will be published soon [Ber11a].
[2] This method is described in Appendix E.
[3] The determination of the exact values of the resonance poles is described in this appendix.

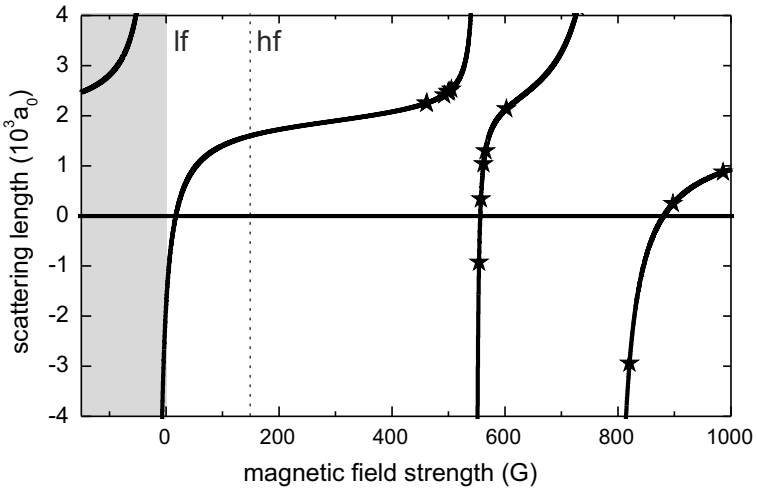

Figure F.1.: Overview of the magnetic field dependence of the s-wave scattering length for atoms in the $|F = 3, m_F = 3\rangle$ state, obtained by considering only the s-wave Feshbach resonances with poles at -12 G, 549 G and 787 G. The graph is the result of a coupled-channel calculation performed by J. Hutson and P. Julienne [Hut11], which is based on the experimental data presented in Sec. F.2 and F.3. The grey area marks the region that is only accessible with the $|F = 3, m_F = -3\rangle$ state. The dashed vertical line separates the so-called low-field region (lf) of up to 150 G, which was accessible with the old experimental setup, from the high-field (hf) region. The new experimental setup allows to reach magnetic field strengths up to 1400 G. The stars represent Feshbach resonances in the high-field region caused by states with rotational orbital angular momenta $\ell > 0$. The positions of these resonances were obtained by Feshbach spectroscopy; see Table F.1.

The low-field resonance ($B_0 = -12$ G) is created by a molecular state of the ($F_1 = 4, F_2 = 4, f = |\mathbf{F}_1 + \mathbf{F}_2| = 6$) potential and features a width of $\Delta = 29$ G. Moreover, cesium features many narrow resonances stemming from the coupling to higher-order rotational angular momentum ($\ell > 0$) states, resulting from weak relativistic spin-spin and second-order spin-orbit interactions; see Fig. F.2. An overview of the low-field scattering properties and the binding energies of weakly bound dimers is given in Figs. F.2 and F.3.

We investigated the scattering properties of cesium in the absolute ground state $|F = 3, m_F = 3\rangle$ in the vicinity of the entrance-channel dominated s-wave Feshbach resonances in the high-field region. The 549 G-resonance is generated by an s-wave molecular state belonging to the ($F_1 = 3, F_2 = 4, f = 7$) potential. The 787 G-resonance stems from a ($F_1 = 3, F_2 = 4, f = 6$) state. Several narrow and overlapping Feshbach resonances have been identified, resulting from the coupling to states with $\ell > 0$; see Fig. F.1. Note that Feshbach resonances are only induced by molecular states with the same Zeeman sublevel $M = m_f + m_\ell = 6$ as the entrance-channel ($m_{F_{1,2}} = 3$).

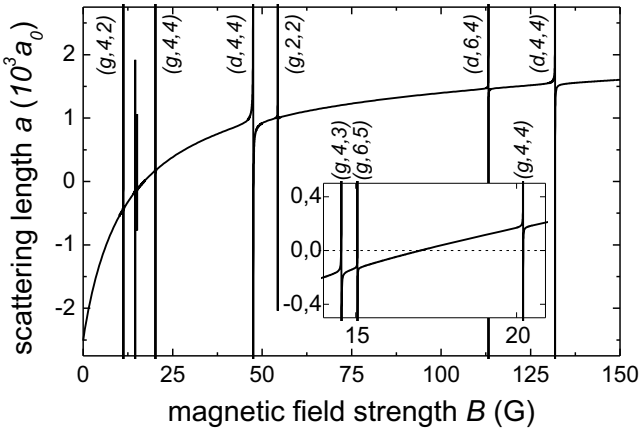

Figure F.2.: s-wave scattering length in the magnetic low-field region. The labeling refers to the molecular states $(\ell, f = |\mathbf{F}_1 + \mathbf{F}_2|, m_f)$, which cause the Feshbach resonances. The inset shows a zoom-in of the region of the zero crossing of a connected to the broad low-field s-wave Feshbach resonance. Note that the 20.1 G resonance is actually located at 19.8 G [Mar05]. Taken from [Chi04b].

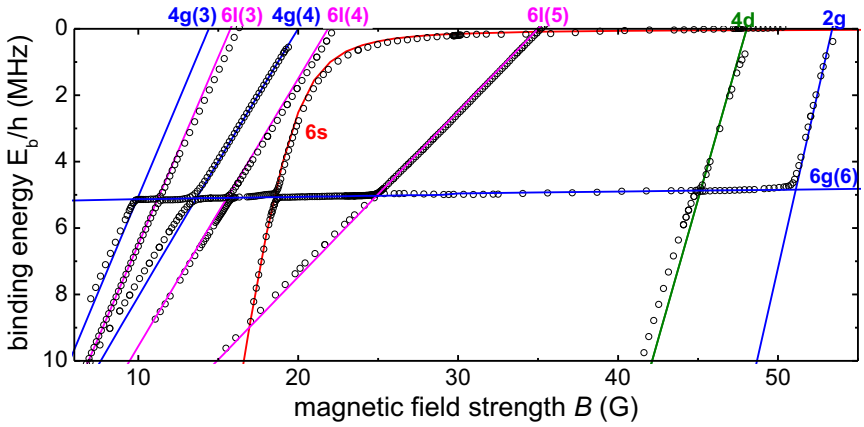

Figure F.3.: Binding energies of the weakly bound Feshbach molecules in the magnetic low-field region. The experimental data points were obtained by magnetic moment spectroscopy and microwave spectroscopy [Mar07a]. The state labeling is according to the quantum numbers $f\ell(m_f)$, with $m_f = 6 - m_\ell$ omitted if $m_f = f$ and $m_\ell = \ell$. The solid lines represent s, d, g and l-wave states. These lines are obtained from a theoretical model derived at the NIST. Taken from [Mar07a].

In the following, molecular states are labeled either according to their quantum numbers ($f\ell m_f$) or by the capital letters given in Table F.1, if the quantum state is not unambiguously identified yet. Furthermore, Feshbach resonances are labeled according to the molecular states that cause the resonances.

F.2. Feshbach spectroscopy

The idea of Feshbach spectroscopy is based on the general a^4-scaling [Web03c, Fed96b, Nie99, Esr99, Bed00] of three-body recombination losses. If two-body losses are sufficiently supressed[4], which is the case for atoms in the absolute ground state, three-body losses are typically the main cause for particle loss[5]. Therefore, poles of Feshbach resonances can be determined by scanning the magnetic field strength, with a fixed hold time, for atom loss maxima. This method is generally referred to as trap-loss spectroscopy. Furthermore, zero-crossings of a appear as loss-minima, allowing to experimentally determine the width of the resonances. However, for especially narrow resonances the resolution is not sufficient to precisely determine the zero-crossings[6].

Unfortunately, this method is not applicable to accurately determine the properties of the broad s-wave Feshbach resonances. The exact position of the pole is obscured by the unitarity limit [D'I04], which sets a temperature dependent limit on atom losses; see Fig. F.4. The ascending slope of $a(B)$ at the zero-crossing, on the other hand, is too small to clearly identify a minimum in losses. Therefore, the properties of the s-wave Feshbach resonances are determined via binding energy measurements; see Sec. F.3.

Sample preparation

The sample preparation down to the μK-regime is similar to the one given in the PhD theses of my former colleagues and described in detail in Refs. [Web03a, Her05, Kra06a, Mar08b]. In brief, the experimental sequence includes several standard cooling and trapping techniques. First, atoms from the Zeeman-slowed atomic beam are accumulated in a magneto-optical trap for 13 s. Then, the MOT is compressed, by linearly tuning the gradient field from 8 G/cm to 33 G/cm within 35 ms. In this stage, the frequency of the MOT beams is adjusted simultaneously. This process is experimentally optimized without determination of the definite value of the detunings. After a 5 ms optical molasses phase, where the MOT coils are switched off, the atoms are loaded into an optical lattice, where Raman-sideband cooling [Web03a, Ker00, Tre01] is performed for 6.5 ms. At this stage of the experiment, the sample size amounts to $N \simeq 1.5 \times 10^7$ Cs

[4] In our experimental setup, one-body losses are negligible due to the ultra-high vacuum conditions.

[5] Normally, n-body losses for $n > 3$ are small in the absence of resonances. Nevertheless, the loss maximum is always at the pole of the resonance, which follows from the general scaling $L_n \propto a^{3n-5}$ [Meh09].

[6] The main effects limiting the resolution are magnetic field noise and the magnetic gradient field.

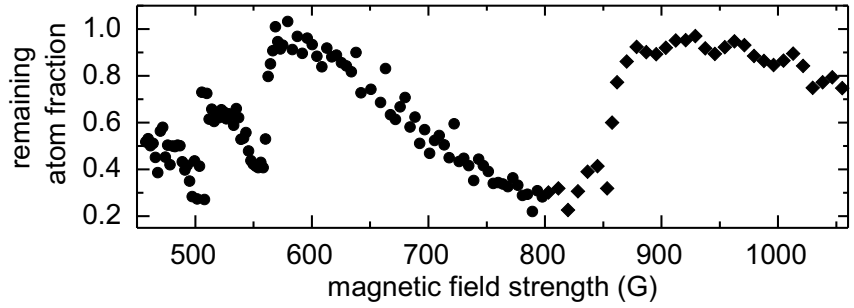

Figure F.4.: Feshbach scan from 450 G to 1050 G showing particle loss due to the two broad high-field *s*-wave Feshbach resonances at 549 G and 787 G, as well as several *d*-wave resonances at $\sim$ 500 G. The experimental setup for these measurements is equal to the one used for binding energy measurements, described in Sec. F.3.1. The dots refer to an evaporation field at 558.7 G and the diamond symbols to an evaporation field at 894 G. Both measurements are performed with a $T = 50$ nK sample in a 1064 nm crossed optical dipole trap. For the scan, the hold time was 500 ms, leading to a maximum particle number of 8×10^4. The *d*-wave resonances are not resolved in this plot, and the main contribution comes from the resonance connected to the $7d6$ state with $\Delta = 4.5$ G; see Ref. [Fer11]. The widths of the *s*-wave Feshbach resonances do not allow to accurately determine the Feshbach resonance parameters by method of Feshbach spectroscopy. Narrow resonances are not shown in this plot due to the step size of the magnetic field scan.

atoms in the $|F = 3, m_F = 3\rangle$ state at a temperature of $\sim 1\,\mu$K. The sample is transferred into a large volume far-off resonant dipole trap [Gri00a], which is generated by two crossed 100 W-CO_2 (Coherent-DEOS GEM-100L) beams with waists of about $600\,\mu$m. As the trap by itself is not strong enough to hold the atoms against gravity, an additional magnetic gradient field of 31 G/cm is applied to levitate the atoms. After 2 s of plain evaporation, resulting to $N \simeq 5 \times 10^6$ and a temperature of slightly below $1\,\mu$K, the CO_2 trap is spatially overlapped by a tightly focused crossed dipole trap. For this trap, a 1064 nm fibre laser (IPG Laser GmbH, 10 W) is used, with waists at the center of the trap of 40 μm (*Dimple 1*-beam) and 250 μm (*Dimple 2*-beam)[7].

The sample is further cooled down by 6.5 s of forced evaporation in the magnetic low-field region[8]. For this purpose, the intensity of *Dimple 1* is reduced from 60 mW to 3.5 mW in an almost exponential ramp within these 6.5 s . The intensity of *Dimple 2* is first linearly increased from 0 to 400 mW within the first half second, and then decreased to 300 mW within the last 3 s of the evaporation scheme. The switching-off process of the two CO_2 lasers starts at $t = 1.5$ s of the evaporation stage. One of the CO_2 lasers is abruptly switched off, whereas

[7] The names of the two lasers refer to the so-called "dimple-trick" discussed in Ref. [Web03a].

[8] At the time of these measurements, the high-field imaging has not yet been installed. Therefore, evaporation was performed in the magnetic low-field region.

the other one is ramped down to zero within 2 s. During the whole evaporation scheme the s-wave scattering length is adjusted by slowly varying the magnetic field in order to optimize the thermalization rate with respect to inelastic losses. After 0.7 s of plain evaporation, which make sure that the sample is in thermal equilibrium, we end up with 10^5 thermal atoms at a temperature of 70 nK.

In order to decrease the widths of the measured loss resonances, the levitation field is reduced to 8 G/cm, while simultaneously recompressing the optical trap. This is performed by increasing the intensity of *Dimple 1* to 40 mW within 1 s. Also, the ellipticity of the trap is modified by a rapid spatial horizontal oscillation of *Dimple 1* using an AOM at a frequency of about 100 kHz, so that the trap size along *Dimple 2* is increased by a factor 1.5. This method is mentioned in Chapter 5 and discussed in Ref. [Sch07]. After this adiabatic reshaping of the trap the temperature increases to about 120 nK.

The magnetic field scans are performed by ramping up to the desired value B_{scan} in the magnetic high-field region within 10 ms. After a hold time t_{hold}, which has been experimentally optimized for each measurement series and lies between 0.25 s and 1 s, the magnetic fields are ramped to zero within 30 ms. The remaining atom cloud is imaged in time-of-flight absorption imaging after 16 ms of expansion. Note that ramping over the broad Feshbach resonances leads to a significant heating effect and additional atom losses. The magnetic field calibration is carried out by $|F = 3, m_F = 3\rangle \rightarrow |F = 4, m_F = 4\rangle$ microwave transitions as explained in Appendix D.

Results of the Feshbach spectroscopy

The results of the Feshbach spectroscopy are given in Table F.1 and the loss resonances obtained are shown in Fig. F.5.

In the magnetic field regions that are discussed below[9], supplementary measurements increased the accuracy of the positions of poles and zero-crossings. As these measurements were carried out after the high-field imaging setup was implemented, the sample preparation is similar to the one described in Sec. F.3.1.

In the magnetic region ranging from 490 G to 506 G, four d-wave Feshbach resonances, stemming from the following molecular states, were identified: $7d4$, $7d6$, $7d7$ and $7d5$; see Fig. F.6. The properties of the $7d6$ resonance have been calculated by J. Hutson and P. Julienne [Hut11], based on the experimental data. According to these calculations, $B_0 = 495.06$ G and $\Delta = 4.5$ G. The large width of this resonance enabled us to identify an Efimov resonance at its shoulder, see Ref. [Fer11]. For the other d-wave resonances $\Delta < 1$ G.

The s-wave Feshbach resonance centered at 549 G features an overlapping g-wave Feshbach resonance, with $B_0 = 554.06$ G and $\Delta = 330$ mG; see resonance "G" in Table F.1. This resonance leads to a splitting of the Efimov scenario, as reported in Chapter 4. The parameters for this resonance are derived from an

[9] The analysis of Efimov resonances, which were observed in these regions, is based on accurate knowledge on $a(B)$. Therefore, precise data on Feshbach resonance poles and zero-crossings in these regions is of utmost importance.

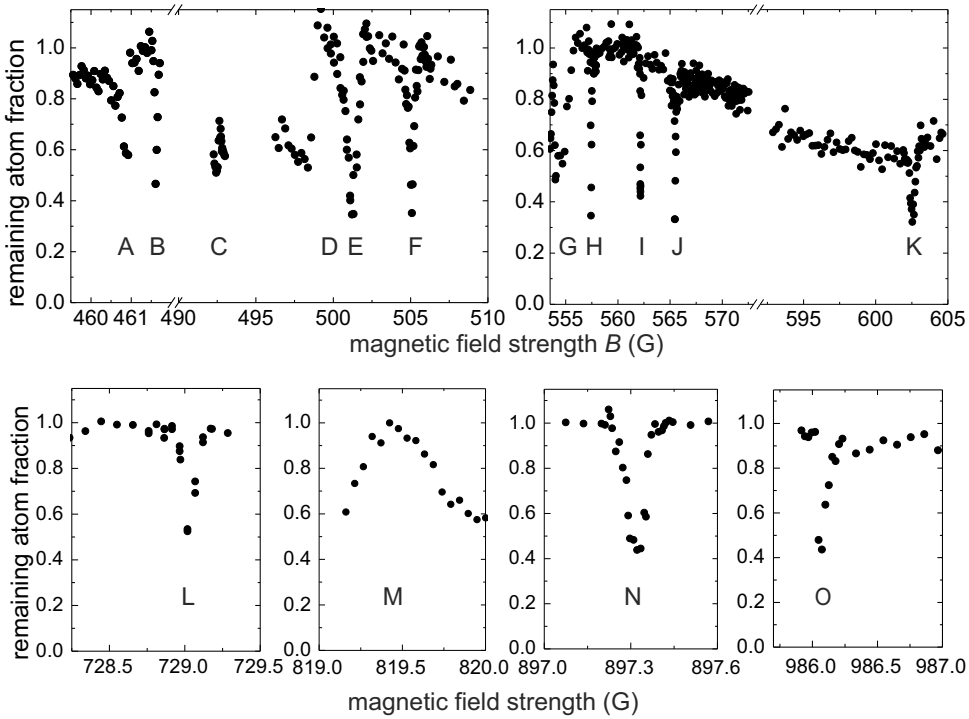

Figure F.5.: Collection of resonances obtained by Feshbach spectroscopy. We use capital letters to label the resonances. For the resonances "D" and "M" only loss minima have been obtained. The "G" resonance is broadened due to the existence of an Efimov resonance at the Feshbach resonances shoulder; see Chapter 4. A remaining atom fraction of 1 corresponds to about 3×10^4 atoms.

accurate Feshbach scan across the resonance, which is shown in Fig. F.7(a).

Overlapping the broad s-wave Feshbach resonance centered at 787 G, we find a d-wave resonance with $B_0 = 820.37$ G and $\Delta = 0.96$ G. It features an Efimov resonance at 818.89 G; see Ref. [Fer11]. Fig. F.7(b) shows the measurements for the determination of the loss minimum and maximum of this Feshbach resonance.

F.3. Binding energy measurements

This section treats binding energy measurements of weakly bound dimers. The binding energies are derived by radio-frequency magnetic-field modulation spectroscopy. This technique is described in Appendix E.

In Sec. F.3.1, measurements on the weakly bound dimer states in the high-field regions at 550 G and 880 G are presented. Some unpublished data for the magnetic low-field region, which is included for the refinement of the $a(B)$ conversion, is given in Sec.F.3.2.

assignment		loss	loss
$f\ell m_f(F_1,F_2)\nu$	Fig. F.5	maximum (G)	minimum (G)
$5d4$(3,4) -6	A	460.86(5)	
	B	461.62(5)	
$7d4$(3,4) -6	C	492.45(3)	492.63(3)
$7d6$(3,4) -6	D		499.40(10)
$7d7$(3,4) -6	E	501.24(3)	
$7d5$(3,4) -6	F	505.07(3)	
$6g3$(3,3) -3	G	554.06(2)	553.73(2)
	H	557.45(3)	
	I	562.17(3)	
	J	565.48(3)	
$3g$(3,4)	K	602.54(3)	
$5g$(3,4) -6	L	729.03(3)	
$6d6$(3,4) -6	M	820.37(22)	819.41(2)
	N	897.33(3)	
	O	986.08(3)	

Table F.1.: Results of the Feshbach spectroscopy. The assignment relates the Feshbach resonances to the molecular states which cause the resonance. If known, the quantum numbers are noted, including the vibrational quantum number ν. Some of the resonances that are not assigned by quantum numbers are supposedly caused by i-wave ($\ell = 6$) states. For further discussion all resonances are labeled by a capital letter ("A"-"O"). The loss minimum of the $6g3$ resonance and the loss maximum of the $6d6$ resonance result from separate measurements; see Fig. F.7. For these measurements, the evaporation scheme is similar to the one described in Sec. F.3.1.

F.3.1. Measurements in the magnetic high-field region

The dimer energies in magnetic high-field regions are investigated by performing *free-bound transitions*, particularly focussing on the energies of the s-wave Feshbach molecules in the universal regime.

Sample preparation

The sample preparation is equal to the one described for Feshbach spectroscopy, up to the trapping stage in the crossed CO_2-trap; see Sec. F.2. However, the high-field imaging setup (see Appendix C) was implemented before the measurements presented in this section were performed. Therefore, to benefit from this technical improvement, which allows to perform evaporation and imaging in the high-field region, the sequence is modified accordingly.

At the beginning of the CO_2-trapping stage, the magnetic field is linearly ramped within 10 ms to the magnetic high-field regime, either the 550 G or 800 G region, crossing the broad s-wave Feshbach resonances. Due to the μK-

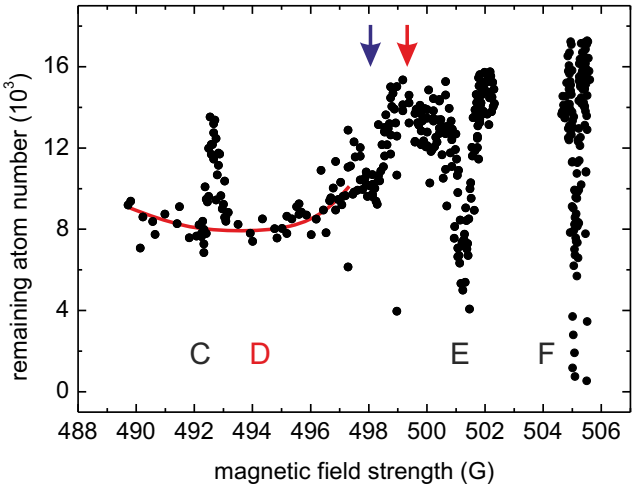

Figure F.6.: *d*-wave Feshbach resonances in the 500 G region, obtained by Feshbach spectroscopy. The capital letters label the resonances according to Table F.1. The solid line is a guide to the eye to indicate the broad *d*-wave resonance with $B_0 = 495$ G, which is masked by the unitarity limit, and the zero-crossing at 499 G (red arrow). In the vicinity of this resonance, an Efimov loss maximum was identified at 498 G (blue arrow). This measurement was performed with a 50 nK sample prepared similarly to the method described in Sec. F.3.1.

temperature of the sample, three-body losses are unitarity limited and, hence, relatively low while crossing the resonances at this stage of the preparation sequence. During the ramp, the magnetic levitation field is adapted to the magnetic moment of the atoms, which varies considerably for this large change of the magnetic bias field; see Sec. A.2. After 2 s of plain evaporation, the atoms are loaded into a tightly focused 1064 nm crossed dipole trap. The laser, trap parameters and ramping schemes for the evaporation procedure are almost the same as for the sample preparation discussed in Sec. F.2. In contrast to Sec. F.2, however, the atoms remain fully levitated and there is no change of the ellipticity of the trap. After 15 s of forced evaporation, with the CO_2s being switched off during the first five seconds, the optical beam powers of *Dimple 1* and *Dimple 2* are 3.5 mW and 300 mW, respectively. The last stage of evaporation ends at a magnetic field strength of 558.7 G ($a \approx 700\,a_0$) or 894 G ($a \approx 300\,a_0$). The 894 G value corresponds to the Efimov minimum reported in Chapter 4. With this procedure, a non-condensed sample of $3-5\times10^4$ atoms[10] at a temperature of about 50 nK is achieved.

For rf magnetic field modulation spectroscopy, we perform *frequency scans* and *magnetic field scans*, as described in Sec. E.2, to minimize systematic errors. The experimental setup for rf magnetic field modulation spectroscopy is described in Sec. E.4. Both scanning methods show consistent results. Typically, the rf modulation signal is applied for a variable duration of $t_{\mathrm{rf}} = 0.1 - 1$ s in

[10] In the lowest atomic Zeeman state $|F = 3, m_F = 3\rangle$.

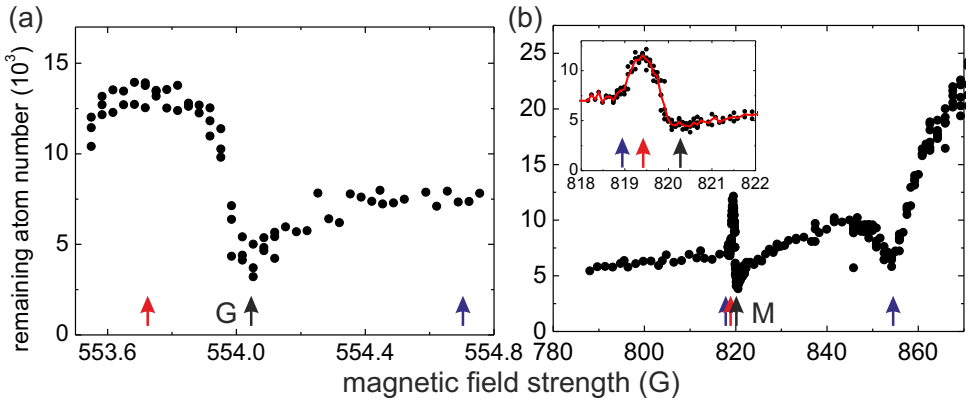

Figure F.7.: Precise magnetic field scan of the region of the overlapping (a) g-wave Feshbach resonance with $B_0 = 554.06$ G and (b) d-wave resonance with $B_0 = 820.37$ G. The positions of the poles and zero-crossings are indicated with a black and red arrow, respectively. Each of these overlapping Feshbach resonances features Efimov loss resonances (blue arrows). The sample preparation for both measurements is similar to the one described in Sec. F.3.1. (a) The Feshbach scan across the g-wave resonance is performed with a 30 nK sample. This g-wave resonance leads to a splitting of the Efimov scenario as described in Chapter 4, with Efimov loss resonances at 553.30 G (not shown) and 554.71 G. (b) The parameters of the d-wave Feshbach resonance are derived from an accurate scan with a 30 nK atom sample. Besides the Efimov loss resonance at 853.07 G (reported in Chapter 4), there exists another Efimov loss resonance on the shoulder of the d-wave Feshbach resonance at 818.19 G; see Ref. [Fer11]. The inset shows a magnification of the d-wave Feshbach resonance.

a frequency range of $\nu_{\mathrm{rf}} = 50 - 1500$ kHz and with an amplitude of $B_{\mathrm{rf}} = 0.5 - 3$ G. The modulation time and amplitude are experimentally optimized with respect to the signal-to-noise ratio for each individual frequency region. Then, the magnetic field is ramped to the imaging field, where the remaining atom number is recorded by absorption imaging after release from the trap, see Appendix C.

Discussion of the results

Here, our high-field data on dimer binding energies E_b in the interval $h \times 20\,\mathrm{kHz} < |E_b| < h \times 2000\,\mathrm{kHz}$ are presented. Note that $E_b > 0$ is defined for a real bound state, and $E_b < 0$ corresponds to a closed-channel bound state embedded in the continuum of the open channel.

Due to an avoided crossing, both in the 550 G and 800 G region, the s-wave closed-channel states are adiabatically connected to the s-wave open-channel bound state, which features $E_b \sim h \times 10$ kHz. Therefore, E_b approaches the open-channel bound state energy for $B > B_0 + \Delta$.

For $E_b < h \times 200$ kHz, the s-wave states exhibit a large open-channel contri-

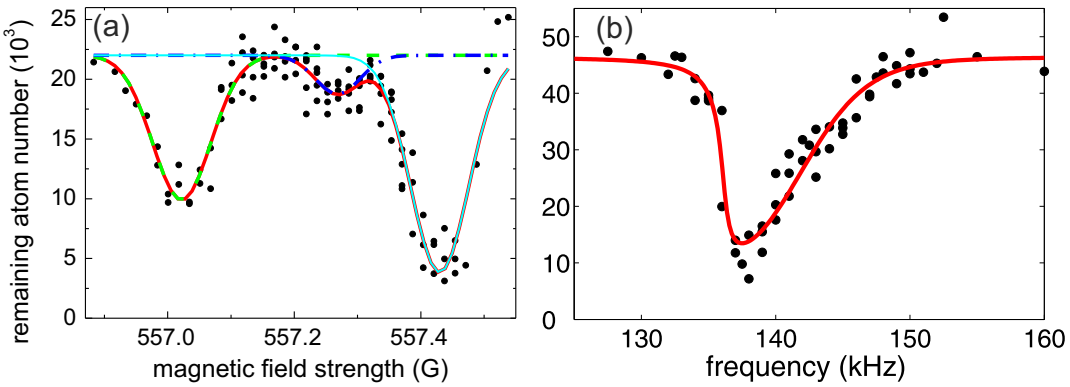

Figure F.8.: Typical rf magnetic field modulation spectroscopy loss signals. (a) A *magnetic field scan* for $\nu_{\mathrm{rf}} = 400$ kHz shows three loss resonances in the 550 G region in the vicinity of an avoided crossing of the 7s6 state and the "H" state. The loss resonance at 557.05 G results from the state with mainly s-wave character (green dashed line), whereas the resonance at 557.30 G stems from the state dominated by the "H" state (blue dash-dotted line). The third resonance at 557.45 G (turquoise solid line) is the bare Feshbach resonance related to the "H" state. The (red) solid line illustrates the envelope of the loss resonances. (b) In the 800 G region, an asymmetric loss signal with an onset at $\nu_{\mathrm{rf}} = 137$ kHz is exemplified, which is obtained via a *frequency scan* for $B_{\mathrm{rf}} = 911.69$ G.

bution. Therefore, the magnetic moment difference $\Delta\mu$ between the atomic and the molecular state is small and the data is treated according to the method explained is Sec. E.3, including magnetic field variations. In this regime, we observe asymmetric line shapes, stemming from the finite temperature of the sample, see Fig. F.8.

For $E_b > h \times 200$ kHz, the increased closed-channel contribution leads to a strong magnetic field dependence of E_b due to the large $\Delta\mu$. Those data are dominated by the magnetic field fluctuations of $\delta B_{\mathrm{noise}} < 20$ mG and the influence of the magnetic levitation field, $\delta B_{\mathrm{grad}} \sim 50$ mG. Therefore, symmetric loss signals of increased widths are observed, which is why data with $E_b > h \times 200$ kHz are fitted by a simple Gaussian function, see Fig. F.8.

For molecular states with $\ell > 0$, broad and symmetric loss signals are observed, due to the large values of $\Delta\mu$. Hence, the loss resonances are fitted by a Gaussian for all E_b, for the same reasons as stated above.

The results for the 550 G region are shown in Fig. F.9. Interestingly, an avoided crossing between the s-wave state ($7s6$) and the "H" state influences E_b in the range between $h \times 200$ kHz and $h \times 500$ kHz. The results for the bare state and coupling regions are summarized in Tables F.2 and F.3. The binding energies for the "G" state ($6g3$) and the "I" state are listed in Tables F.4 and F.5.

Fig. F.10 presents the findings in the 880 G region. There, an even stronger avoided crossing of the closed-channel s-wave state ($6s6$) and the open-channel

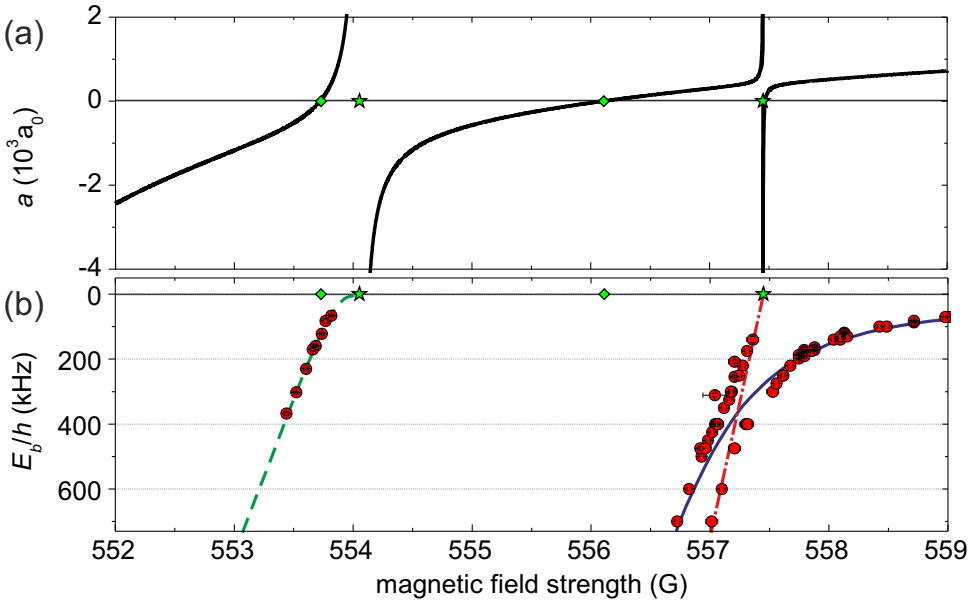

Figure F.9.: (a) s-wave scattering length and (b) binding energy measurements for the weakly bound molecular spectrum in the 550 G region. (a) The s-wave scattering length is derived from a coupled-channel calculation based on the binding energy measurements [Hut11]. The ($\star$)-symbols indicate the poles of the Feshbach resonances and the ($\blacklozenge$)-symbols the zero-crossings. (b) The dots show the results of binding energy measurements, which are obtained by rf magnetic field modulation spectroscopy. The lines indicate the molecular energy level, neglecting the avoided crossing between the s-wave state (blue solid line) and the "H" state (red dash-dotted line). The dashed line illustrates the binding energy of the "G" state ($6g3$).

s-wave state is observed, compared to the 550 G region. A small avoided crossing with the "N" state affects the data between 505 and 509 kHz. The results are summarized in Table F.6, while results for the "M" state ($6d6$) can be found in Table F.7.

F.3.2. Measurements in the magnetic low-field region

The near-threshold[11] molecular energy structure of cesium in the low-field region was already investigated by means of microwave spectroscopy, magnetic moment spectroscopy [Mar07a] and rf magnetic field modulation spectroscopy via *free-bound transitions* [Lan09b].

In order to increase the accuracy of the coupled-channel calculation, data (which has not yet been published) was collected in the low-field region. The measurements focussed on the precise determination of binding energies of the

[11]Note that the threshold refers to the open-channel $|F = 3, m_F = 3\rangle + |F = 3, m_F = 3\rangle$ asymptote for large inter-particle distances.

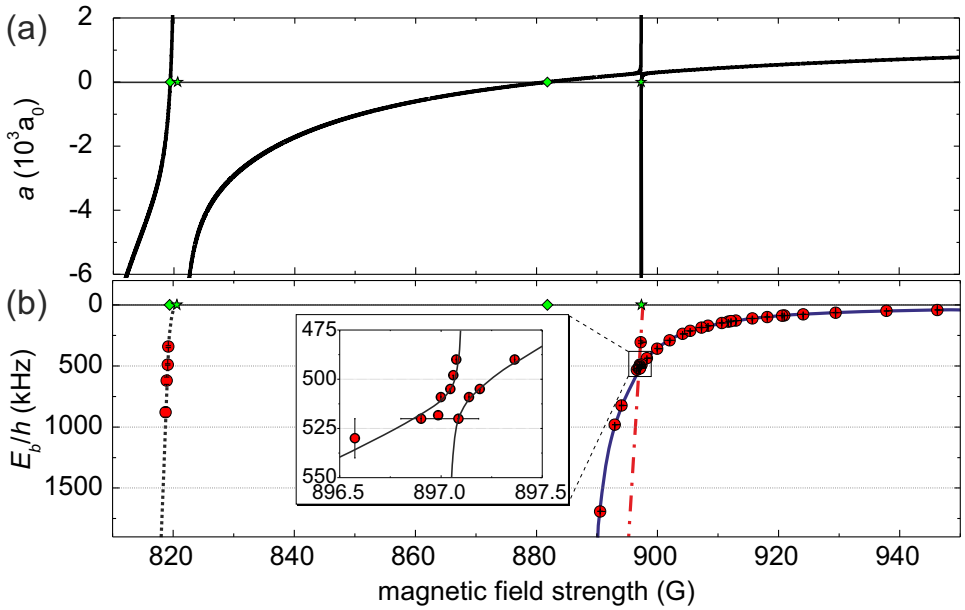

Figure F.10.: (a) *s*-wave scattering length and (b) binding energy measurements for the weakly bound molecular spectrum in the 880 G region. (a) The *s*-wave scattering length is derived from a coupled-channel calculation based on the binding energy measurements [Hut11]. The (⋆)-symbols indicate the poles of the Feshbach resonances and the (⧫)-symbols the zero-crossings. (b) The dots show the results of binding energy measurements, which are obtained by rf magnetic field modulation spectroscopy. Lines indicate the molecular energy level, neglecting the narrow avoided crossing between the *s*-wave state (blue solid line) and the "N" state (red dash-dotted line). The inset illustrates a magnification of this avoided crossing, with lines to guide the eye. The dotted line displays the binding energy of the "M" state ($6d6$).

universal *s*-wave dimer state at a magnetic field of around 30 G. In contrast to Ref. [Lan09b], the binding energies of the weakly bound *s*-wave state were obtained via *bound-free transitions* in *frequency scans*. In this process, dimers are dissociated by a transition to the free atom continuum.

Sample preparation

The preparation procedure for an ultracold sample of thermal dimers in the halo *s*-wave state is outlined in Chapters 2 and 5 and described in detail in Ref. [Mar07a]. Principally, the experimental setup for the rf magnetic field modulation spectroscopy, as well as the timing sequence, are similar to those described in Sec. E.4, the difference being that an audio amplifier (LM4780, National Semiconductor) drives the current in the *Small HH coils*[12] to produce

[12]The *Curvature coils* have not been implemented into the experimental setup at the time these measurements were performed.

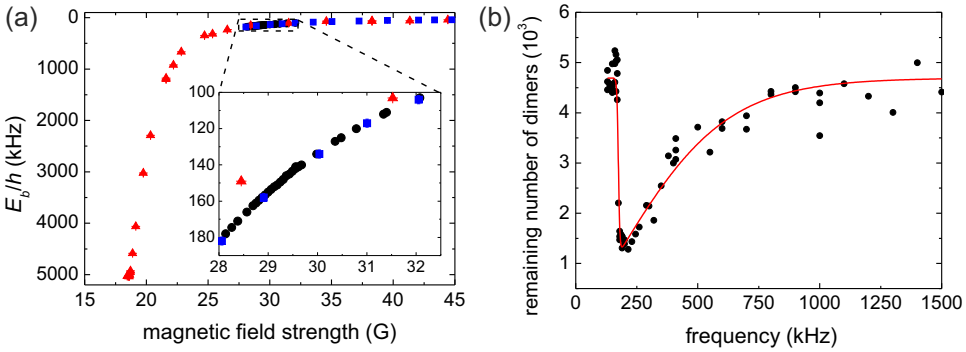

Figure F.11.: (a) Binding energy measurements in the magnetic low-field region. The figure includes three different sets of data, which match very well. The (red) triangles are obtained via micro-wave spectroscopy [Mar07a], whereas the other data are derived by rf magnetic field modulation spectroscopy. The (blue) squares show *free-bound transition* obtained in a neighboring lab [Lan09b]. The (black) dots indicate the new data, which were extensively recorded by probing *bound-free transitions* in the region between 100 kHz and 200 kHz. (b) Sample dimer loss signal for a *bound-free transition* obtained in a *frequency scan* with $B = 28.3$ G, $t_{\mathrm{rf}} = 25$ ms and $B_{\mathrm{rf}} = 0.6$ G. The data points demonstrate the strongly asymmetric line shape, featuring a sharp onset and a large high-energy tail, greatly exceeding the width of a *free-bound transition* as depicted in Fig. F.8. The solid line exemplifies an asymmetric Gaussian fit to guide the eyes.

the magnetic field modulation. The ultracold dimer sample is exposed to an rf magnetic field modulation at the probe magnetic field B for several ms, which dissociates the dimers into free atoms with kinetic energy E_{rel}. The dissociation procedure is more efficient than dimer association, as it does not depend on the availability of a collision partner. The dissociated atoms are either lost from the trap due to their kinetic energy, which exceeds the trap depth, or because of atom-dimer relaxation, leading to additional dimer loss. After a Feshbach ramp, which dissociates the dimers into atoms without considerable loss, the remaining atoms are imaged.

Discussion of the results

The newly obtained spectroscopy data for the magnetic low-field region are presented in Table F.8 and Fig. F.11(a). Due to the nature of *bound-free transitions*, the line shape does not result from the initial temperature of the dimer sample, but from the transition probability to the continuum state with kinetic energy E_{rel} [Bar05]. This leads to an asymmetric loss signal, featuring a large width and a sharp onset, see Fig. F.11(b), where the binding energy is obtained by determination of the onset of the loss signal.

The data presented in Table F.8 conform with the one of Ref. [Lan09b].

F.4. Determination of the scattering length

The s-wave scattering length in different magnetic field regions is derived by least-square fitting of a full coupled-channel calculation, which is based on optimization of the s-, d- and g-wave Cs-Cs scattering potentials, to the experimentally obtained data. These data include the dimer binding energies[13] as well as the Feshbach resonance poles and zero-crossings reported in this appendix. This coupled-channel calculation, which was performed by J. Hutson and P. Julienne [Hut11], yields the parameters of the previously unexplored high-field s-wave Feshbach resonances and a refinement of the low-field s-wave Feshbach resonance. The parameters are given in Table F.9 and the resulting $a(B)$ is presented in Fig. F.12. Table F.10 lists the (theoretically derived) Feshbach parameters of the resonances with $\ell > 0$ that are shown in Fig. F.12. Knowledge of $a(B)$ was the crucial element for the analysis of the recombination loss measurements in Chapter 4.

[13]The fit involves, besides the data presented in this appendix, the low-field data of Refs. [Mar07a, Lan09b].

s-wave state ($7s6$)			
below avoided crossing		above avoided crossing	
B(G)	E_b/h(kHz)	B(G)	E_b/h(kHz)
561.86(2)	24(1)	556.82(3)	600(2)
560.87(2)	31(1)	556.72(2)	700(2)
560.73(2)	32(1)	556.71(5)	800(2)
560.45(2)	35(1)	556.53(5)	900(2)
560.12(2)	40(1)	556.47(5)	1000(2)
559.80(2)	45(1)	556.29(10)	1200(2)
559.53(2)	55(1)		
558.99(2)	70(1)		
558.71(2)	84(1)		
558.44(2)	100(2)		
558.13(2)	123(2)		
558.12(2)	130(2)		
558.07(2)	140(2)		
557.88(2)	170(2)		
557.85(2)	175(2)		
557.79(2)	175(2)		
557.79(2)	188(2)		

at the avoided crossing			
"left" branch		"right" branch	
B(G)	E_b/h(kHz)	B(G)	E_b/h(kHz)
557.28(3)	220(2)	557.66(2)	220(2)
557.24(2)	250(2)	557.62(2)	221(2)
557.24(3)	250(2)	557.60(2)	250(2)
557.21(2)	254(6)	557.61(2)	250(2)
557.17(2)	300(2)	557.56(2)	275(2)
557.18(2)	300(2)	557.53(5)	300(2)
557.16(2)	325(2)	557.30(5)	400(2)
557.12(2)	350(2)	557.21(5)	475(2)
557.07(3)	400(2)		
557.05(2)	400(2)		
557.04(2)	400(2)		
557.02(2)	425(2)		
556.98(2)	450(2)		
556.92(2)	475(2)		
556.96(5)	475(2)		
556.93(3)	500(2)		

Table F.2.: Binding energies $E_b(B)$ of the s-wave state ($7s6$) in the 550 G region. The Table includes values for the s-wave state outside the avoided crossing with the "H" state (upper part) and both branches within the avoided crossing region (lower part). The state that, for increasing binding energies, connects the "H" state with the s-wave state is referred to as the "left" branch, and vice versa as the "right" branch.

"H" state			
above atom threshold		below atom threshold	
B(G)	E_b/h(kHz)	B(G)	E_b/h(kHz)
557.72(2)	-300(2)	557.36(5)	140(10)
557.70(2)	-300(2)	557.31(2)	175(2)
557.69(5)	-275(2)	557.12(2)	600(5)
557.65(2)	-275(2)	557.09(2)	602(5)
557.61(2)	-175(2)	557.01(5)	700(2)

Table F.3.: Binding energies $E_b(B)$ of the "H" state, which causes the Feshbach resonance at $B_0 = 557.45$ G, outside the avoided crossing region with the s-wave $(7s6)$ state.

"G" state $(6g3)$	
B(G)	E_b/h(kHz)
553.82(2)	65(20)
553.77(2)	83(20)
553.74(2)	122(20)
553.69(2)	160(20)
553.66(2)	170(20)
553.60(2)	230(20)
553.52(2)	302(20)
553.44(2)	368(20)

Table F.4.: Binding energies $E_b(B)$ of the "G" state $(6g3)$, which generates the Feshbach resonance at $B_0 = 554.06$ G.

"I" state	
B(G)	E_b/h(kHz)
562.01(2)	208(6)
561.92(3)	279(6)
561.84(2)	402(6)

Table F.5.: Binding energies $E_b(B)$ of the "I" state, which generates the Feshbach resonance at $B_0 = 562.17$ G.

s-wave state ($6s6$)			
B(G)	E_b/h(kHz)	B(G)	E_b/h(kHz)
946.21(3)	40(1)	907.23(2)	184(2)
937.81(3)	49(1)	905.35(2)	212(2)
929.41(3)	63(1)	904.13(3)	235(2)
923.97(2)	76(1)	902.00(2)	289(2)
920.93(3)	85(2)	899.93(3)	356(2)
920.52(2)	87(2)	898.25(2)	434(2)
918.06(2)	98(2)	897.03(2)	498(2)
915.60(2)	110(2)	896.99(2)	516(2)
912.95(3)	127(2)	896.57(3)	538(5)
912.10(2)	133(2)	894.06(2)	821(5)
911.69(3)	137(2)	892.94(2)	977(5)
910.58(2)	146(2)	890.54(2)	1689(5)
908.33(3)	169(2)		
at the avoided crossing			
B(G)	E_b/h(kHz)	B(G)	E_b/h(kHz)
"left" branch		"right" branch	
897.02(2)	505(2)	897.16(2)	505(2)
897.10(2)	509(2)	896.97(2)	509(2)

Table F.6.: Binding energies $E_b(B)$ of the s-wave state ($6s6$) around 900 G, including four data points (505 and 509 kHz) in the region of an avoided crossing with the "N" state. The "N" state causes the Feshbach resonance at $B_0 = 897.33$ G.

"M" state ($6d6$)			
above atom threshold		below atom threshold	
B(G)	E_b/h(kHz)	B(G)	E_b/h(kHz)
819.98(2)	-848(20)	819.18(2)	342(20)
820.00(2)	-777(20)	819.12(2)	488(20)
819.98(2)	-774(20)	818.92(5)	620(30)
819.89(2)	-642(20)	818.75(5)	878(40)
819.90(2)	-625(20)		
819.76(2)	-502(20)		
819.69(2)	-492(20)		
819.77(2)	-476(20)		
819.62(2)	-452(20)		

Table F.7.: Binding energies $E_b(B)$ of the "M" state ($6d6$), which causes the Feshbach resonance at $B_0 = 820.37$ G.

s-wave state ($6s6$)			
B(G)	E_b/h(kHz)	B(G)	E_b/h(kHz)
28.13(1)	178(1)	29.37(1)	146(1)
28.26(1)	175(1)	29.43(1)	145(1)
28.38(1)	171(1)	29.49(1)	144(1)
28.56(1)	166(1)	29.55(1)	142(1)
28.69(1)	163(1)	29.55(1)	141(1)
28.75(1)	161(1)	29.61(1)	141(1)
28.81(1)	160(1)	29.67(1)	140(1)
28.87(1)	158(1)	29.98(1)	134(1)
28.93(1)	157(1)	30.36(1)	127(1)
29.00(1)	155(1)	30.48(1)	125(1)
29.06(1)	154(1)	30.79(1)	120(1)
29.12(1)	152(1)	31.34(1)	112(1)
29.18(1)	151(1)	31.40(1)	111(1)
29.24(1)	150(1)	32.08(1)	103(1)
29.30(1)	148(1)		

Table F.8.: Binding energies $E_b(B)$ of the s-wave state ($6s6$) in the low-field region around 30 G.

assignment	pole (G)	width (G)	zero-crossing (G)	
$f\ell m_f(F_1, F_2)\nu$	theory	theory	theory	experiment
$6s6$(4,4) -7	-12.34	29.48	17.14	17.13(1)
$7s6$(3,4) -6	548.79	7.40	556.19	556.26(10)
$6s6$(3,4) -6	786.84	93.82	880.66	880.9(3)

Table F.9.: Feshbach resonance parameters of the low-field and high-field s-wave Feshbach resonances, obtained by a coupled-channel calculation [Hut11]. The experimental value for the low-field zero-crossing is taken from Ref. [Gus08a], while for the high-field resonances, they are derived from the collapse of a Bose-Einstein condensate [Zen11].

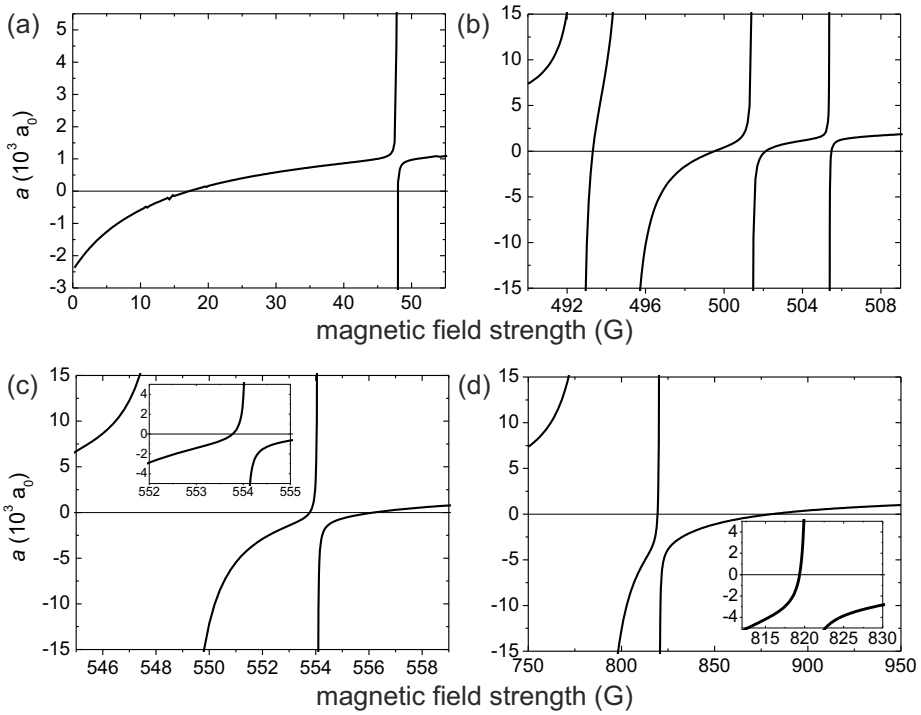

Figure F.12.: Results of the coupled-channel calculation for the s-wave scattering length a for various magnetic field regions [Hut11]. The conversion $a(B)$ is based on experimental data derived by Feshbach spectroscopy and binding energy measurements. The calculation for these plots includes only states with $\ell \leq 4$. (a) In the magnetic low-field region, a is governed by the low-field s-wave Feshbach resonance. The $4d4$ state causes a Feshbach resonance at 47.79 G. Several g-wave resonances are not indicated in this plot; see Fig. F.2. (b) The region around 500 G is dominated by multiple d-wave resonances, of which the $7d6$ (with $\Delta = 4.5$ G) has the strongest effect. (c) In the region of the 550 G s-wave Feshbach resonance, the $6g3$ state induces an overlapping Feshbach resonance. The inset magnifies the region of the g-wave zero-crossing. (d) The large 800 G s-wave Feshbach resonance is overlapped by the $6d6$ Feshbach resonance. The inset magnifies the zero-crossing of the d-wave resonance. The states labeled with "H" and "N" do not appear in the calculation, which strongly indicates that these resonances stem from states with $\ell > 4$.

assignment $f\ell m_f$	pole (G) theory	width (G) theory	loss max. (G) experiment	loss min. (G) experiment
$4d4$	47.79	0.18	47.78(1)	47.94(1)
$7d4$	492.68	0.63	492.45(3)	492.63(3)
$7d6$	495.04	4.48	-	499.4(1)
$7d7$	501.44	0.68	501.24(3)	-
$7d5$	505.37	0.10	505.07(3)	-
$6g3$	554.07	-0.32	554.06(2)	553.73(2)
$6d6$	820.33	-0.97	820.37(22)	819.41(2)

Table F.10.: Parameters of the d- and g-wave Feshbach resonances that are shown in Fig. F.12 derived by a coupled-channel calculation [Hut11] in comparison to the experimental values obtained by Feshbach spectroscopy. The experimental high-field data are taken from Table F.1, whereas the ones for the low-field d-wave resonance at 47.78 G are taken from Ref. [Lan09b]. A horizontal line indicates that no data is available. Note that the theoretical values for the d-wave resonances in the 500 G region feature a larger uncertainty, as no binding energy measurements are yet available in this region.

BIBLIOGRAPHY

[Adh81] S. K. Adhikari and A. C. Fonseca, *Four-body Efimov effect in a Born-Oppenheimer model*, Phys. Rev. D **24**, 416 (1981).

[Adh88] S. Adhikari, A. Delfino, T. Frederico, I. Goldman, and L. Tomio, *Efimov and Thomas effects and the model dependence of three-particle observables in two and three dimensions*, Phys. Rev. A **37**, 3666 (1988).

[Ago89] C. C. Agosta, I. F. Silvera, H. T. C. Stoof, and B. J. Verhaar, *Trapping of Neutral Atoms with Resonant Microwave Radiation*, Phys. Rev. Lett. **62**, 2361 (1989).

[Ale93] E. B. Alexandrov, M. P. Chaika, and G. I. Khvostenko (Eds.), *Interference of Atomic States*, Springer Verlag, Berlin, 1993.

[Alt07a] A. Altmeyer, *Collective oscillations of an ultracold quantum gas in the BEC-BCS crossover regime*, Ph.D. thesis, University of Innsbruck (2007).

[Alt07b] A. Altmeyer, S. Riedl, M. J. Wright, C. Kohstall, J. Hecker Denschlag, and R. Grimm, *Dynamics of a strongly interacting Fermi gas: The radial quadrupole mode*, Phys. Rev. A **76**, 033610 (2007).

[Ama71] R. Amado and J. Noble, *On Efimov's effect: a new pathology of three-particle systems*, Phys. Lett. B **35**, 25 (1971).

[Ama72] R. D. Amado and J. V. Noble, *Efimov's effect: A new pathology of three-particle systems. II*, Phys. Rev. D **5**, 1992 (1972).

[Ama73] R. D. Amado and F. C. Greenwood, *There Is No Efimov Effect for Four or More Particles*, Phys. Rev. D **7**, 2517 (1973).

[And81] S. V. Andreev, V. I. Balykin, V. S. Letokhov, and V. G. Minogin, *Radiative slowing and reduction of the energy spread of a beam of*

sodium atoms to 1.5K in an oppositely directed laser beam, JETP Lett. **34**, 442 (1981).

[And95] M. H. Anderson, J. R. Ensher, M. R. Matthews, C. E. Wieman, and E. A. Cornell, *Observation of Bose-Einstein condensation in dilute atomic vapor*, Science **269**, 198 (1995).

[Ari77] E. Arimondo, M. Inguscio, and P. Violino, *Experimental determinations of the hyperfine structure in the alkali atoms*, Rev. Mod. Phys. **49**, 31 (1977).

[Ari92] E. Arimondo, W. D. Phillips, and F. Strumia (Eds.), *Laser Manipulation of Atoms and Ions*, North Holland, Amsterdam, 1992, Proceedings of the International School of Physics "Enrico Fermi", Course CXVIII, Varenna, 9-19 July 1991.

[Arl98] J. Arlt, P. Bance, S. Hopkins, J. Martin, S. Webster, A. Wilson, K. Zetie, and C. J. Foot, *Suppression of collisional loss from a magnetic trap*, J. Phys. B **31**, L321 (1998).

[Arn97] M. Arndt, M. B. Dahan, D. Guéry-Odelin, M. Reynolds, and J. Dalibard, *Observation of a Zero-Energy Resonance in Cs-Cs Collisions*, Phys. Rev. Lett. **79**, 625 (1997).

[Axi43] B. M. Axilrod and E. Teller, *Interaction of the van der Waals Type Between Three Atoms*, J. Chem. Phys. **11**, 299 (1943).

[Bac00] I. Baccarelli, G. Delgado-Barrio, F. Gianturco, T. Gonzalez-Lezana, S. Miret-Artes, and P. Villarreal, *Searching for Efimov states in triatomic systems: The case of $LiHe_2$*, Europhys. Lett. **50**, 567 (2000).

[Bal85] V. I. Balykin, V. S. Letokhov, V. G. Minogin, Y. V. Rozhdestvensky, and A. I. Sidorov, *Radiative collimation of atomic beams through two-dimensional cooling of atoms by laser-radiation pressure*, J. Opt. Soc. Am. B **2**, 1776 (1985).

[Bal88a] V. I. Balykin, V. S. Letokhov, Y. B. Ovchinnikov, and A. I. Sidorov, *Quantum-state-selective mirror reflection of atoms by laser light*, Phys. Rev. Lett. **60**, 2137 (1988).

[Bal88b] V. I. Balykin, V. S. Letokhov, Y. B. Ovchinnikov, A. I. Sidorov, and S. V. Shulga, *Channeling of atoms in a standing spherical light-wave*, Optics Lett. **13**, 958 (1988).

[Bar05] M. Bartenstein, A. Altmeyer, S. Riedl, R. Geursen, S. Jochim, C. Chin, J. Hecker Denschlag, R. Grimm, A. Simoni, E. Tiesinga, C. J. Williams, and P. S. Julienne, *Precise determination of ^6Li cold collision parameters by radio-frequency spectroscopy on weakly bound molecules*, Phys. Rev. Lett. **94**, 103201 (2005).

[Bar09] G. Barontini, C. Weber, F. Rabatti, J. Catani, G. Thalhammer, M. Inguscio, and F. Minardi, *Observation of heteronuclear atomic Efimov resonances*, Phys. Rev. Lett. **103**, 043201 (2009).

[Bea09] Q. Beaufils, A. Crubellier, T. Zanon, B. Laburthe-Tolra, É. Maréchal, L. Vernac, and O. Gorceix, *Feshbach resonances in d-wave collisions*, Phys. Rev. A **79**, 032706 (2009).

[Bea10] Q. Beaufils, A. Crubellier, T. Zanon, B. Laburthe-Tolra, É. Maréchal, L. Vernac, and O. Gorceix, *Radio-frequency association of molecules: an assisted Feshbach resonance*, Eur. Phys. J. D **56**, 99 (2010).

[Bed99a] P. Bedaque, H.-W. Hammer, and U. van Kolck, *Renormalization of the three-body system with short-range interactions*, Phys. Rev. Lett. **82**, 463 (1999).

[Bed99b] P. Bedaque, H.-W. Hammer, and U. van Kolck, *The three-boson system with short-range interactions*, Nucl. Phys. A **646**, 444 (1999).

[Bed00] P. F. Bedaque, E. Braaten, and H.-W. Hammer, *Three-body recombination in Bose gases with large scattering length*, Phys. Rev. Lett. **85**, 908 (2000).

[Ber87] T. Bergemann, G. Erez, and H. J. Metcalf, *Magnetostatic trapping fields for neutral atoms*, Phys. Rev. A **35**, 1535 (1987).

[Ber01] F. Bertinetto, P. Cordiale, G. Galzerano, and E. Bava, *Frequency Stabilization of DBR Diode Laser Against Cs Absorption Lines at 852 nm Using the Modulation Transfer Method*, IEEE Transactions on Instrumentation and Measurement **50**, 490 (2001).

[Ber06] J. F. Bertelsen and K. M. lmer, *Molecule formation in optical lattice wells by resonantly modulated magnetic fields*, Physical Review A (Atomic, Molecular, and Optical Physics) **73**, 013811 (2006).

[Ber07] J. F. Bertelsen and K. Mølmer, *Association of heteronuclear molecules in a harmonic oscillator well*, Phys. Rev. A **76**, 043615 (2007).

[Ber11a] M. Berninger, A. Zenesini, B. Huang, H.-C. Nägerl, F. Ferlaino, R. Grimm, P. S. Julienne, and J. M. Hutson, *High magnetic-field scattering properties of ultracold Cs atoms* (2011), in preparation.

[Ber11b] M. Berninger, A. Zenesini, B. Huang, W. Harm, H.-C. Nägerl, F. Ferlaino, R. Grimm, P. S. Julienne, and J. M. Hutson, *Universality of the Three-Body Parameter for Efimov States in Ultracold Cesium*, Phys. Rev. Lett. **107**, 120401 (2011).

[Bet35a] H. Bethe and R. Peierls, *Quantum Theory of the Diplon*, Proc. Roy. Soc. A **148**, 146 (1935).

[Bet35b] H. Bethe and R. Peierls, *The Scattering of Neutrons by Protons*, Proc. Roy. Soc. A **149**, 176 (1935).

[Bla52] J. M. Blatt and V. F. Weisskopf, *Theoretical Nuclear Physics*, Wiley, New York, 1952.

[Blo08] I. Bloch, J. Dalibard, and W. Zwerger, *Many-body physics with ultracold gases*, Rev. Mod. Phys. **80**, 885 (2008).

[Bra95] C. C. Bradley, C. A. Sackett, J. J. Tollett, and R. G. Hulet, *Evidence of Bose-Einstein condensation in an atomic gas with attractive interactions*, Phys. Rev. Lett. **75**, 1687 (1995).

[Bra01] E. Braaten and H.-W. Hammer, *Three-body recombination into deep bound states in a Bose gas with large scattering length*, Phys. Rev. Lett. **87**, 160407 (2001).

[Bra03] E. Braaten and H.-W. Hammer, *Universality in the three-body problem for ^{4}He atoms*, Phys. Rev. A **67**, 042706 (2003).

[Bra04] E. Braaten and H. W. Hammer, *Enhanced dimer relaxation in an atomic and molecular Bose-Einstein condensate*, Phys. Rev. A **70**, 042706 (2004).

[Bra06] E. Braaten and H.-W. Hammer, *Universality in few-body systems with large scattering length*, Phys. Rep. **428**, 259 (2006).

[Bra07] E. Braaten and H.-W. Hammer, *Resonant dimer relaxation in cold atoms with a large scattering length*, Phys. Rev. A **75**, 052710 (2007).

[Bra09a] E. Braaten and H.-W. Hammer, *Erratum: Resonant dimer relaxation in cold atoms with a large scattering length [Phys. Rev. A 75, 052710 (2007)]*, Phys. Rev. A **79** (2009).

[Bra09b] E. Braaten, H.-W. Hammer, D. Kang, and L. Platter, *Three-body recombination of ^{6}Li atoms with large negative scattering lengths*, Phys. Rev. Lett. **103**, 073202 (2009).

[Bra10] E. Braaten, H.-W. Hammer, D. Kang, and L. Platter, *Efimov physics in ^{6}Li atoms*, Phys. Rev. A **81**, 013605 (2010).

[Bre31] G. Breit and I. I. Rabi, *Measurement of Nuclear Spin*, Phys. Rev. **38**, 2082 (1931).

[Brü05] R. Brühl, A. Kalinin, O. Kornilov, J. P. Toennies, G. C. Hegerfeldt, and M. Stoll, *Matter wave diffraction from an inclined transmission grating: Searching for the elusive ^{4}He trimer Efimov state*, Phys. Rev. Lett. **95**, 063002 (2005).

[Car09] L. D. Carr, D. DeMille, R. V. Krems, and J. Ye, *Cold and ultracold molecules: Science, technology and applications*, New J. Phys. **11**, 055049 (2009).

[Chi00] C. Chin, V. Vuletić, A. J. Kerman, and S. Chu, *High resolution Feshbach spectroscopy of cesium*, Phys. Rev. Lett. **85**, 2717 (2000).

[Chi01] C. Chin, *Cooling, collisions and coherence of cold cesium atoms in a trap*, Ph.D. thesis, Stanford University (2001).

[Chi04a] C. Chin, M. Bartenstein, A. Altmeyer, S. Riedl, S. Jochim, J. Hecker Denschlag, and R. Grimm, *Observation of the Pairing Gap in a Strongly Interacting Fermi Gas*, Science **305**, 1128 (2004).

[Chi04b] C. Chin, V. Vuletić, A. J. Kerman, S. Chu, E. Tiesinga, P. J. Leo, and C. J. Williams, *Precision Feshbach spectroscopy of ultracold* Cs_2, Phys. Rev. A **70**, 032701 (2004).

[Chi05a] C. Chin and P. S. Julienne, *Radio-frequency transitions on weakly bound ultracold molecules*, Phys. Rev. A **71** (2005).

[Chi05b] C. Chin, T. Kraemer, M. Mark, J. Herbig, P. Waldburger, H.-C. Nägerl, and R. Grimm, *Observation of Feshbach-like resonances in collisions between ultracold molecules*, Phys. Rev. Lett. **94**, 123201 (2005).

[Chi10] C. Chin, R. Grimm, P. S. Julienne, and E. Tiesinga, *Feshbach resonances in ultracold gases*, Rev. Mod. Phys. **82**, 1225 (2010).

[Chu98] S. Chu, *Nobel Lecture: The manipulation of neutral particles*, Rev. Mod. Phys. **70**, 685 (1998).

[Col04] Y. Colombe, E. Knyazchyan, O. Morizot, B. Mercier, V. Lorent, and H. Perrin, *Ultracold atoms confined in rf-induced two-dimensional trapping potentials*, Europhys. Lett. **67**, 593 (2004).

[Cor77] A. Corney (Ed.), *Atomic and Laser Spectroscopy*, Oxford University Press Inc., New York, 1977.

[Cor98] K. L. Corwin, Z.-T. Lu, C. F. Hand, R. J. Epstein, and C. E. Wieman, *Frequency-stabilized diode laser with the Zeeman shift in an atomic vapor*, Appl. Opt. **37**, 3295 (1998).

[CT98] C. N. Cohen-Tannoudji, *Nobel Lecture: Manipulating atoms with photons*, Rev. Mod. Phys. **70**, 707 (1998).

[Cub03] J. Cubizolles, T. Bourdel, S. J. J. M. F. Kokkelmans, G. V. Shlyapnikov, and C. Salomon, *Production of Long-Lived Ultracold* Li_2 *Molecules from a Fermi Gas*, Phys. Rev. Lett. **91**, 240401 (2003).

[Dan07] J. G. Danzl, *Towards optical spectroscopy of ultracold cesium molecules*, Diploma thesis, University of Innsbruck (2007).

[Dan08] J. G. Danzl, E. Haller, M. Gustavsson, M. J. Mark, R. Hart, N. Bouloufa, O. Dulieu, H. Ritsch, and H.-C. Nägerl, *Quantum Gas of Deeply Bound Ground State Molecules*, Science **321**, 1062 (2008).

[Dan10] J. G. Danzl, M. J. Mark, E. Haller, M. Gustavsson, R. Hart, J. Aldegunde, J. M. Hutson, and H.-C. Nägerl, *An ultracold high-density sample of rovibronic ground-state molecules in an optical lattice*, Nature Phys. **6**, 265 (2010).

[Dav95] K. B. Davis, M. O. Mewes, M. R. Andrews, N. J. van Druten, D. S. Durfee, D. M. Kurn, and W. Ketterle, *Bose-Einstein condensation in a gas of sodium atoms*, Phys. Rev. Lett. **75**, 3969 (1995).

[Dei08] J. Deiglmayr, A. Grochola, M. Repp, K. Mörtlbauer, C. Glück, J. Lange, O. Dulieu, R. Wester, and M. Weidemüller, *Formation of Ultracold Polar Molecules in the Rovibrational Ground State*, Physical Review Letters **101**, 133004 (2008).

[DeM99] B. DeMarco and D. S. Jin, *Onset of Fermi Degeneracy in a Trapped Atomic Gas*, Science **285**, 1703 (1999).

[D'I04] J. P. D'Incao, H. Suno, and B. D. Esry, *Limits on Universality in Ultracold Three-Boson Recombination*, Phys. Rev. Lett. **93**, 123201 (2004).

[D'I05a] J. P. D'Incao and B. D. Esry, *Manifestations of the Efimov effect for three identical bosons*, Phys. Rev. A **72**, 032710 (2005).

[D'I05b] J. P. D'Incao and B. D. Esry, *Scattering length scaling laws for ultracold three-body collisions*, Phys. Rev. Lett. **94**, 213201 (2005).

[D'I06a] J. P. D'Incao and B. D. Esry, *Enhancing the observability of the Efimov effect in ultracold atomic gas mixtures*, Phys. Rev. A **73**, 030703(R) (2006).

[D'I06b] J. P. D'Incao and B. D. Esry, *Mass dependence of ultracold three-body collision rates*, Phys. Rev. A **73**, 030702 (2006).

[D'I08] J. P. D'Incao and B. D. Esry, *Suppression of molecular decay in ultracold gases without Fermi statistics*, Phys. Rev. Lett. **100**, 163201 (2008).

[D'I09a] J. P. D'Incao and B. D. Esry (2009), in preparation.

[D'I09b] J. P. D'Incao and B. D. Esry, *Ultracold Three-Body Collisions near Overlapping Feshbach Resonances*, Phys. Rev. Lett. **103**, 083202 (2009).

[D'I09c] J. P. D'Incao, C. H. Greene, and B. D. Esry, *The short-range three-body phase and other issues impacting the observation of Efimov physics in ultracold quantum gases*, J. Phys. B: At. Mol. Opt. Phys. **42**, 044016 (2009).

[D'I09d] J. P. D'Incao, J. von Stecher, and C. H. Greene, *Universal four-boson states in ultracold molecular gases: Resonant effects in dimer-dimer collisions*, Phys. Rev. Lett. **103**, 033004 (2009).

[Don02] E. A. Donley, N. R. Clausen, S. T. Thompson, and C. E. Wieman, *Atom-molecule coherence in a Bose-Einstein condensate*, Nature **417**, 529 (2002).

[Dür04] S. Dürr, T. Volz, A. Marte, and G. Rempe, *Observation of Molecules Produced from a Bose-Einstein Condensate*, Phys. Rev. Lett. **92** (2004).

[Efi70] V. Efimov, *Energy levels arising from resonant two-body forces in a three-body system*, Phys. Lett. B **33**, 563 (1970).

[Efi71] V. Efimov, *Weakly-bound states of three resonantly-interacting particles*, Sov. J. Nucl. Phys. **12**, 589 (1971).

[Efi72] V. Efimov, *Level spectrum of three resonantly interacting particles*, Sov. Phys. JETP Lett. **16**, 34 (1972).

[Efi73] V. Efimov, *Energy levels of three resonantly interacting particles*, Nucl. Phys. A **210**, 157 (1973).

[Efi79] V. Efimov, *Low-energy properties of three resonantly interacting particles*, Sov. J. Nuc. Phys. **29**, 546 (1979).

[Efi81] V. Efimov, *Qualitative treatment of three-nucleon properties*, Nucl. Phys. A **362**, 45 (1981).

[Efi90] V. Efimov, *Is a qualitative approach to the three-body problem useful?*, Comm. Nucl. Part. Phys. **19**, 271 (1990).

[Esr96] B. D. Esry, C. D. Lin, and C. H. Greene, *Adiabatic hyperspherical study of the helium trimer*, Phys. Rev. A **54**, 394 (1996).

[Esr99] B. D. Esry, C. H. Greene, and J. P. Burke, *Recombination of Three Atoms in the Ultracold Limit*, Phys. Rev. Lett. **83**, 1751 (1999).

[Esr06] B. D. Esry and C. H. Greene, *Quantum physics: A ménage à trois laid bare*, Nature **440**, 289 (2006).

[Esr07] B. D. Esry (2007), private communication.

[Fad61] L. Faddeev, *Scattering theory for a three particle system*, Zh. Eksp. Teor. Fiz. **39**, 1459 (1961).

[Fan35] U. Fano, *Sullo spettro di assorbimento dei gas nobili presso il limite dello spettro d'arco*, Nuovo Cimento **12**, 154 (1935).

[Fan61] U. Fano, *Effects of configuration interaction on intensities and phase shifts*, Phys. Rev. **124**, 1866 (1961).

[Fan05] U. Fano, G. Pupillo, A. Zannoni, and C. W. Clark, *On the absorption spectrum of noble gases at the arc spectrum limit*, J. Res. Natl. Inst. Stand. Technol. **110**, 583 (2005).

[Fat00] F. K. Fatemi, K. M. Jones, and P. D. Lett, *Observation of Optically Induced Feshbach Resonances in Collisions of Cold Atoms*, Phys. Rev. Lett. **85**, 4462 (2000).

[Fed93] D. V. Federov and A. S. Jensen, *Efimov Effect in Coordinate Space Faddeev Equations*, Phys. Rev. Lett. **71**, 4103 (1993).

[Fed94] D. V. Fedorov, A. S. Jensen, and K. Riisager, *Efimov States in Halo Nuclei*, Phys. Rev. Lett. **73**, 2817 (1994).

[Fed96a] P. O. Fedichev, Y. Kagan, G. V. Shlyapnikov, and J. T. M. Walraven, *Influence of nearly resonant light on the scattering length in low-temperature atomic gases*, Phys. Rev. Lett. **77**, 2913 (1996).

[Fed96b] P. O. Fedichev, M. W. Reynolds, and G. V. Shlyapnikov, *Three-Body recombination of ultracold atoms to a weakly bound s level*, Phys. Rev. Lett. **77**, 2921 (1996).

[Fer08] F. Ferlaino, S. Knoop, M. Mark, M. Berninger, H. Schöbel, H.-C. Nägerl, and R. Grimm, *Collisions between tunable halo dimers: Exploring an elementary four-body process with identical bosons*, Phys. Rev. Lett. **101**, 023201 (2008).

[Fer09a] F. Ferlaino, S. Knoop, M. Berninger, W. Harm, J. P. D'Incao, H.-C. Nägerl, and R. Grimm, *Evidence for universal four-body states tied to an Efimov trimer*, Phys. Rev. Lett. **102**, 140401 (2009).

[Fer09b] F. Ferlaino, S. Knoop, and R. Grimm, *Cold Molecules: Theory, Experiment, Applications*, chap. Ultracold Feshbach molecules, Taylor & Francis, 2009.

[Fer10] F. Ferlaino, S. Knoop, M. Berninger, M. Mark, H.-C. Nägerl, and R. Grimm, *Collisions of ultracold trapped cesium Feshbach molecules*, Laser Phys. **20**, 23 (2010).

[Fer11] F. Ferlaino, A. Zenesini, M. Berninger, B. Huang, H.-C. Nägerl, and R. Grimm, *Efimov Resonances in Ultracold Quantum Gases*, arXiv: 1108.1909 (2011).

[Fes58] H. Feshbach, *United theory of nuclear reations*, Ann. Phys. **5**, 357 (1958).

[Fes62] H. Feshbach, *United theory of nuclear reations II*, Ann. Phys. **19**, 287 (1962).

[Flo09] S. Floerchinger, R. Schmidt, and C. Wetterich, *Three-body loss in lithium from functional renormalization*, Phys. Rev. A **79**, 053633 (2009).

[Foo05] C. J. Foot (Ed.), *Atomic Physics*, Oxford University Press Inc., New York, 2005.

[Fri01] N. Friedman, A. Kaplan, D. Carasso, and N. Davidson, *Observation of Chaotic and Regular Dynamics in Atom-Optics Billiards*, Phys. Rev. Lett. **86**, 1518 (2001).

[Gao04] B. Gao, *Binding energy and scattering length for diatomic systems*, J. Phys. B: At. Mol. Opt. Phys. **37**, 4273 (2004).

[Geh03] M. E. Gehm, *Preparation of an optically-trapped degenerate Fermi gas of ^{6}Li: Finding the route to degeneracy*, Ph.D. thesis, Duke University (2003).

[Gio08] S. Giorgini, L. P. Pitaevskii, and S. Stringari, *Theory of ultracold atomic Fermi gases*, Rev. Mod. Phys. **80**, 1215 (2008).

[GO98] D. Guéry-Odelin, J. Söding, P. Desbiolles, and J. Dalibard, *Is Bose-Einstein condensation of atomic cesium possible?*, Europhys. Lett. **44**, 25 (1998).

[Gog08] A. O. Gogolin, C. Mora, , and R. Egger, *Analytical solution of the bosonic three-body problem*, Phys. Rev. Lett. **100**, 140404 (2008).

[Gre03] M. Greiner, C. A. Regal, and D. S. Jin, *Emergence of a Molecular Bose-Einstein Condensate from a Fermi Gas*, Nature **426**, 537 (2003).

[Gre11] C. Greene (2011), private communication.

[Gri90] R. Grimm, Y. B. Ovchinnikov, A. I. Sidorov, and V. S. Letokhov, *Observation of a strong rectified dipole force in a bichromatic standing light wave*, Phys. Rev. Lett. **65**, 1415 (1990).

[Gri93] G. F. Gribakin and V. V. Flambaum, *Calculation of the scattering length in atomic collisions using the semiclassical approximation*, Phys. Rev. A **48**, 546 (1993).

[Gri00a] R. Grimm, M. Weidemüller, and Y. B. Ovchinnikov, *Optical dipole traps for neutral atoms*, Adv. At. Mol. Opt. Phys. **42**, 95 (2000).

[Gri00b] R. Grisenti, W. Schöllkopf, J. Toennies, G. Hegerfeldt, T. Köhler, and M. Stoll, *Determining the bond length and binding energy of the helium dimer by diffraction from a transmission grating*, Phys. Rev. Lett. **85**, 2284 (2000).

[Gro09] N. Gross, Z. Shotan, S. Kokkelmans, and L. Khaykovich, *Observation of universality in ultracold ^7Li three-body recombination*, Phys. Rev. Lett. **103**, 163202 (2009).

[Gro10] N. Gross, Z. Shotan, S. Kokkelmans, and L. Khaykovich, *Nuclear-Spin-Independent Short-Range Three-Body Physics in Ultracold Atoms*, Phys. Rev. Lett **105**, 103203 (2010).

[Gus08a] M. Gustavsson, *A quantum gas with tunable interactions in an optical lattice*, Ph.D. thesis, University of Innsbruck (2008).

[Gus08b] M. Gustavsson, E. Haller, M. J. Mark, J. G. Danzl, G. Rojas-Kopeinig, and H.-C. Nägerl, *Control of interaction-induced dephasing of Bloch oscillations*, Phys. Rev. Lett. **100**, 080404 (2008).

[Ham07a] H.-W. Hammer, T. A. Lähde, and L. Platter, *Effective-range corrections to three-body recombination for atoms with large scattering length*, Phys. Rev. A **75**, 032715 (2007).

[Ham07b] H.-W. Hammer and L. Platter, *Universal properties of the four-body system with large scattering length*, Eur. Phys. J. A **32**, 113 (2007).

[Han06] G. J. Hanna and D. Blume, *Energetics and structural properties of three-dimensional bosonic clusters near threshold*, Phys. Rev. A **74**, 063604 (2006).

[Han07] T. M. Hanna, T. Köhler, and K. Burnett, *Association of molecules using a resonantly modulated magnetic field*, Physical Review A (Atomic, Molecular, and Optical Physics) **75**, 013606 (2007).

[Han10] T. M. Hanna, E. Tiesinga, and P. S. Julienne, *Creation and manipulation of Feshbach resonances with radiofrequency radiation*, New J. Phys. **12**, 083031 (2010).

[Har10] W. Harm, *Entwicklung und Aufbau eines Magnetspulensystems für Experimente an ultrakalten Cäsium-Atomen*, Diploma thesis, University of Innsbruck (2010).

[Hel09] K. Helfrich and H. W. Hammer, *Resonant atom-dimer relaxation in ultracold atoms*, Europhys. Lett. **86**, 53003 (2009).

[Her03] J. Herbig, T. Kraemer, M. Mark, T. Weber, C. Chin, H.-C. Nägerl, and R. Grimm, *Preparation of a pure molecular quantum gas*, Science **301**, 1510 (2003).

[Her05] J. Herbig, *Quantum-degenerate cesium: Atoms and molecules*, Ph.D. thesis, University of Innsbruck (2005).

[Hof06] S. Hofferberth, I. Lesanovsky, B. Fischer, J. Verdu, and J. Schmiedmayer, *Radiofrequency-dressed-state potentials for neutral atoms*, Nature Phys. **2**, 710 (2006).

[Huc09] J. H. Huckans, J. R. Williams, E. L. Hazlett, R. W. Stites, and K. M. O'Hara, *Three-body recombination in a three-state Fermi gas with widely tunable interactions*, Phys. Rev. Lett. **102**, 165302 (2009).

[Hud08] E. R. Hudson, N. B. Gilfoy, S. Kotochigova, J. M. Sage, and D. DeMille, *Inelastic Collisions of Ultracold Heteronuclear Molecules in an Optical Trap*, Physical Review Letters **100**, 203201 (2008).

[Hun08] C.-L. Hung, X. Zhang, N. Gemelke, and C. Chin, *Accelerating evaporative cooling of atoms into Bose-Einstein condensation in optical traps*, Phys. Rev. A **78**, 011604(R) (2008).

[Hut08] J. M. Hutson, E. Tiesinga, and P. S. Julienne, *Avoided crossings between bound states of ultracold cesium dimers*, Phys. Rev. A **78**, 052703 (2008).

[Hut11] J. M. Hutson and P. Julienne (2011), private communication.

[Ina08] Y. Inada, M. Horikoshi, S. Nakajima, M. Kuwata-Gonokami, M. Ueda, and T. Mukaiyama, *Collisional properties of p-wave Feshbach molecules*, Phys. Rev. Lett. **101**, 100401 (2008).

[Ing08] M. Inguscio, W. Ketterle, and C. Salomon (Eds.), *Ultra-cold Fermi Gases*, IOS Press, Amsterdam, 2008, Proceedings of the International School of Physics "Enrico Fermi", Course CLXIV, Varenna, 20-30 June 2006.

[Jen04] A. S. Jensen, K. Riisager, D. V. Fedorov, and E. Garrido, *Structure and reactions of quantum halos*, Rev. Mod. Phys. **76**, 215 (2004).

[JL10] M. Jona-Lasinio and L. Pricoupenko, *Three Resonant Ultracold Bosons: Off-Resonance Effects*, Phys. Rev. Lett. **104**, 023201 (2010).

[Joc03a] S. Jochim, M. Bartenstein, A. Altmeyer, G. Hendl, S. Riedl, C. Chin, J. Hecker Denschlag, and R. Grimm, *Bose-Einstein Condensation of Molecules*, Science **302**, 2101 (2003).

[Joc03b] S. Jochim, M. Bartenstein, A. Altmeyer, G. Hendl, C. Chin, J. Hecker Denschlag, and R. Grimm, *Pure Gas of Optically Trapped Molecules Created from Fermionic Atoms*, Phys. Rev. Lett **91**, 240402 (2003).

[Jon06] K. M. Jones, E. Tiesinga, P. D. Lett, and P. S. Julienne, *Ultracold photoassociation spectroscopy: Long-range molecules and atomic scattering*, Reviews of Modern Physics **78**, 483 (2006).

[Jul08] P. Julienne and E. Tiesinga (2008), private communication.

[Kau09] A. M. Kaufman, R. P. Anderson, T. M. Hanna, E. Tiesinga, P. S. Julienne, and D. S. Hall, *Radio-frequency dressing of multiple Feshbach resonances*, Phys. Rev. A **80**, 050701(R) (2009).

[Kaz90] A. Kazantsev, G. Surdutovich, and V. Yakovlev, *Mechanical Action of Light on Atoms*, World Scientific, Singapore, 1990.

[Ker00] A. J. Kerman, V. Vuletić, C. Chin, and S. Chu, *Beyond Optical Molasses: 3D Raman Sideband Cooling of Atomic Cesium to High Phase-Space Density*, Phys. Rev. Lett. **84**, 439 (2000).

[Ket99] W. Ketterle, D. S. Durfee, and D. M. Stamper-Kurn, *Making, probing and understanding Bose-Einstein condensates*, Proceedings of the International School of Physics - Enrico Fermi **67** (1999), arXiv:cond-mat/9904034.

[Kle08] C. Klempt, T. Henninger, O. Topic, M. Scherer, L. Kattner, E. Tiemann, W. Ertmer, and J. J. Arlt, *Radio-frequency association of heteronuclear Feshbach molecules*, Phys. Rev. A **78**, 061602(R) (2008).

[Kno08] S. Knoop, M. Mark, F. Ferlaino, J. G. Danzl, T. Kraemer, H.-C. Nägerl, and R. Grimm, *Metastable Feshbach Molecules in High Rotational States*, Phys. Rev. Lett. **100**, 083002 (2008).

[Kno09] S. Knoop, F. Ferlaino, M. Mark, M. Berninger, H. Schöbel, H.-C. Nägerl, and R. Grimm, *Observation of an Efimov-like trimer resonance in ultracold atom-dimer scattering*, Nature Phys. **5**, 227 (2009).

[Kno10] S. Knoop, F. Ferlaino, M. Berninger, M. Mark, H.-C. Nägerl, R. Grimm, J. P. D'Incao, and B. D. Esry, *Magnetically controlled exchange process in an ultracold atom-dimer mixture*, Phys. Rev. Lett. **104**, 053201 (2010).

[Köh05] T. Köhler, E. Tiesinga, and P. S. Julienne, *Spontaneous Dissociation of Long-Range Feshbach Molecules*, Physical Review Letters **94**, 020402 (2005).

[Köh06a] T. Köhler (2006), private communication.

[Köh06b] T. Köhler, K. Góral, and P. S. Julienne, *Production of cold molecules via magnetically tunable Feshbach resonances*, Rev. Mod. Phys. **78** (2006).

[Kot00] S. Kotochigova, E. Tiesinga, and P. S. Julienne, *Relativistic ab initio treatment of the second-order spin-orbit splitting of the $a^3\Sigma_u^+$ potential of rubidium and cesium dimers*, Phys. Rev. A **63**, 012517 (2000).

[Kra04] T. Kraemer, J. Herbig, M. Mark, T. Weber, C. Chin, H.-C. Nägerl, and R. Grimm, *Optimized production of a cesium Bose-Einstein condensate*, Appl. Phys. B **79**, 1013 (2004).

[Kra06a] T. Kraemer, *Few-body interactions in an ultracold gas of cesium atoms*, Ph.D. thesis, University of Innsbruck (2006).

[Kra06b] T. Kraemer, M. Mark, P. Waldburger, J. G. Danzl, C. Chin, B. Engeser, A. D. Lange, K. Pilch, A. Jaakkola, H.-C. Nägerl, and R. Grimm, *Evidence for Efimov quantum states in an ultracold gas of caesium atoms*, Nature **440**, 315 (2006).

[Kre08] R. Krems, *Cold controlled chemistry*, Phys. Chem. Chem. Phys. **10**, 4079 (2008).

[Kre09] R. V. Krems, B. Friedrich, and W. C. Stwalley (Eds.), *Cold Molecules: Theory, Experiment, Applications*, Taylor & Francis, 2009.

[Lan65] L. D. Landau and E. M. Lifshitz, *Quantum Mechanics (Course of theoretical physics)*, Pergamon Press, Oxford, 1965.

[Lan08a] F. Lang, P. van der Straten, B. Brandstätter, G. Thalhammer, K. Winkler, P. S. Julienne, R. Grimm, and J. Hecker Denschlag, *Cruising through molecular bound-state manifolds with radiofrequency*, Nature Phys. **4**, 223 (2008).

[Lan08b] F. Lang, K. Winkler, C. Strauss, R. Grimm, and J. Hecker Denschlag, *Ultracold Triplet Molecules in the Rovibrational Ground State*, Phys. Rev. Lett. **101**, 133005 (2008).

[Lan09a] F. Lang, *Coherent transfer of ultracold molecules: From weakly to deeply bound*, Ph.D. thesis, University of Innsbruck (2009).

[Lan09b] A. D. Lange, K. Pilch, A. Prantner, F. Ferlaino, B. Engeser, H.-C. Nägerl, R. Grimm, and C. Chin, *Determination of atomic scattering lengths from measurements of molecular binding energies near Feshbach resonances*, Phys. Rev. A **79**, 013622 (2009).

[Lee06] T.-G. Lee, N. Balakrishnan, R. C. Forrey, P. C. Stancil, D. R. Schultz, and G. J. Ferland, *State-to-state rotational transitions in H_2 + H_2 collisions at low temperatures*, The Journal of Chemical Physics **125**, 114302 (2006).

[Lee07] M. D. Lee, T. Köhler, and P. S. Julienne, *Excited Thomas-Efimov levels in ultracold gases*, Phys. Rev. A **76** (2007).

[Leo00] P. J. Leo, C. J. Williams, and P. S. Julienne, *Collision properties of ultracold ^{133}Cs atoms*, Phys. Rev. Lett. **85**, 2721 (2000).

[Les06] I. Lesanovsky, T. Schumm, S. Hofferberth, L. M. Andersson, P. Krüger, , and J. Schmiedmayer, *Adiabatic radio-frequency potentials for the coherent manipulation of matter waves*, Phys. Rev. A **73**, 033619 (2006).

[Let68] V. S. Letokhov, *Narrowing of Doppler width in a standing light wave*, JETP Lett. **7**, 272 (1968).

[Let07] V. S. Letokhov, *Laser Control of Atoms and Molecules*, Oxford University Press, 2007.

[Lew07] M. Lewenstein, A. Sanpera, V. Ahufinger, B. Damski, A. Sen, and U. Sen, *Ultracold atomic gases in optical lattices: mimicking condensed matter physics and beyond*, Adv. Phys. **56**, 243 (2007).

[Lim77] T. K. Lim, S. K. Duffy, and W. C. Damer, *Efimov state in the ^4He trimer*, Phys. Rev. Lett. **38**, 341 (1977).

[Lom10a] T. Lompe, T. B. Ottenstein, F. Serwane, K. Viering, A. N. Wenz, G. Zürn, and S. Jochim, *Atom-Dimer Scattering in a Three-Component Fermi Gas*, Phys. Rev. Lett **105**, 103201 (2010).

[Lom10b] T. Lompe, T. B. Ottenstein, F. Serwane, A. N. Wenz, G. Zürn, and S. Jochim, *Radio-Frequency Association of Efimov Trimers*, Science **330**, 940 (2010).

[Luo93] F. Luo, G. C. McBane, G. Kim, C. F. Giese, and W. R. Gentry, *The weakest bond: Experimental observation of helium dimer*, The Journal of Chemical Physics **98**, 3564 (1993).

[Mar03] M. Mark, *Bose-Einstein-Kondensation von Cäsium*, Diploma thesis, University of Innsbruck (2003).

[Mar05] M. Mark, T. Kraemer, J. Herbig, C. Chin, H.-C. Nägerl, and R. Grimm, *Efficient creation of molecules from a cesium Bose-Einstein condensate*, Europhys. Lett. **69**, 706 (2005).

[Mar07a] M. Mark, F. Ferlaino, S. Knoop, J. G. Danzl, T. Kraemer, C. Chin, H.-C. Nägerl, and R. Grimm, *Spectroscopy of ultracold trapped cesium Feshbach molecules*, Phys. Rev. A **76**, 042514 (2007).

[Mar07b] M. Mark, T. Kraemer, P. Waldburger, J. Herbig, C. Chin, H.-C. Nägerl, and R. Grimm, *Stückelberg Interferometry with Ultracold Molecules*, Phys. Rev. Lett. **99** (2007).

[Mar08a] B. Marcelis, S. J. J. M. F. Kokkelmans, G. V. Shlyapnikov, and D. S. Petrov, *Collisional properties of weakly bound heteronuclear dimers*, Phys. Rev. A **77**, 032707 (2008).

[Mar08b] M. Mark, *Exploring ultracold trapped cesium Feshbach molecules*, Ph.D. thesis, University of Innsbruck (2008).

[Mas08] P. Massignan and H. T. C. Stoof, *Efimov states near a Feshbach resonance*, Phys. Rev. A **78**, 030701 (2008).

[Meh09] N. P. Mehta, S. T. Rittenhouse, J. P. D'Incao, J. von Stecher, and C. H. Greene, *General theoretical description of N-body recombination*, Phys. Rev. Lett. **103**, 153201 (2009).

[Mey05] T. P. Meyrath, *Experiments with Bose-Einstein Condensation in an Optical Box*, Ph.D. thesis, University of Texas at Austin (2005).

[Mie96] F. H. Mies, C. J. Williams, P. S. Julienne, and M. Krauss, *Estimating bounds on collisional relaxation rates of spin-polarized Rb-87 atoms at ultracold temperatures*, J. Res. Natl. Inst. Stand. Technol. **101**, 521 (1996).

[Mie00] F. H. Mies, E. Tiesinga, and P. S. Julienne, *Manipulation of Feshbach resonances in ultracold atomic collisions using time-dependent magnetic fields*, Phys. Rev. A **61**, 022721 (2000).

[Mil01] V. Milner, J. L. Hanssen, W. C. Campbell, and M. G. Raizen, *Optical Billiards for Atoms*, Phys. Rev. Lett. **86**, 1514 (2001).

[Min87] V. G. Minogin and V. S. Letokhov, *Laser Light Pressure on Atoms*, Gordon and Breach, New York, 1987.

[Moe96] A. J. Moerdijk, B. J. Verhaar, and T. M. Nagtegaal, *Collisions of dressed ground-state atoms*, Phys. Rev. A **53**, 4343 (1996).

[Mon93] C. R. Monroe, E. A. Cornell, C. A. Sackett, C. J. Myatt, and C. E. Wieman, *Measurement of Cs-Cs elastic scattering at T=30 μK*, Phys. Rev. Lett. **70**, 414 (1993).

[MR99] M. G. und M. Rosenbluh, *Injection Locking of a Diode Laser Locked to a Zeeman Frequency Stabilized Laser Oscillator*, Opt. Comm. **170**, 269 (1999).

[Muk04] T. Mukaiyama, J. R. Abo-Shaeer, K. Xu, J. K. Chin, and W. Ketterle, *Dissociation and decay of ultracold sodium molecules*, Phys. Rev. Lett. **92**, 180402 (2004).

[Näg06] H.-C. Nägerl, T. Kraemer, M. Mark, P. Waldburger, D. J. G., B. Engeser, A. D. Lange, K. Pilch, A. Jaakkola, C. Chin, and R. Grimm, *Experimental Evidence for Efimov Quantum States*, in: C. Roos,

H. Häffner, and R. Blatt (Eds.), *20th International Conference on Atomic Physics: Quantum Optics and Spectroscopy, Innsbruck, Austria, 16 - 21 Jul 2006*, American Institute of Physics, 2006.

[Nai09] P. Naidon and M. Ueda, *Possible Efimov Trimer State in a Three-Hyperfine-Component Lithium-6 Mixture*, Phys. Rev. Lett. **103**, 073203 (2009).

[Nai11] P. Naidon and M. Ueda, *The Efimov effect in lithium 6*, C.R. Physique **12**, 13 (2011).

[Nak10] S. Nakajima, M. Horikoshi, T. Mukaiyama, P. Naidon, and M. Ueda, *Nonuniversal Efimov Atom-Dimer Resonances in a Three-Component Mixture of ^6Li*, Phys. Rev. Lett **105**, 023201 (2010).

[Nak11] S. Nakajima, M. Horikoshi, T. M. P. Naidon, and M. Ueda, *Measurement of an Efimov Trimer Binding Energy in a Three-Component Mixture of ^6Li*, Phys. Rev. Lett. **106**, 143201 (2011).

[Nap94] R. Napolitano, J. Weiner, C. J. Williams, and P. S. Julienne, *Line Shapes of High Resolution Photoassociation Spectra of Optically Cooled Atoms*, Phys. Rev. Lett. **73**, 1352 (1994).

[Nau87] H. W. L. Naus and J. A. Tjon, *The Efimov effect in a four-body system*, Few-Body Syst. **2**, 121 (1987).

[Ni08] K.-K. Ni, S. Ospelkaus, M. H. G. de Miranda, A. Pe'er, B. Neyenhuis, J. J. Zirbel, S. Kotochigova, P. S. Julienne, D. S. Jin, and J. Ye, *A High Phase-Space-Density Gas of Polar Molecules*, Science **322**, 231 (2008).

[Nie97] E. Nielsen, D. V. Fedorov, and A. S. Jensen, *Three-body halos in two dimensions*, Phys. Rev. A **56**, 3287 (1997).

[Nie99] E. Nielsen and J. H. Macek, *Low-energy recombination of identical bosons by three-body collisions*, Phys. Rev. Lett. **83**, 1751 (1999).

[Nie01] E. Nielsen, D. Fedorov, A. Jensen, and E. Garrido, *The three-body problem with short-range interactions*, Phys. Rep. **347**, 373 (2001).

[Nie02] E. Nielsen, H. Suno, and B. D. Esry, *Efimov resonances in atom-diatom scattering*, Phys. Rev. A **66**, 012705 (2002).

[Nis11] Y. Nishida and S. Tan, *Liberating Efimov physics from three dimensions*, arXiv: 1104.2387 (2011).

[Osp06] C. Ospelkaus, S. Ospelkaus, L. Humbert, P. Ernst, K. Sengstock, and K. Bongs, *Ultracold Heteronuclear Molecules in a 3D Optical Lattice*, Phys. Rev. Lett. **97** (2006).

[Osp10a] S. Ospelkaus, K.-K. Ni, G. Quéméner, B. Neyenhuis, D. Wang, M. H. G. de Miranda, J. L. Bohn, J. Ye, and D. S. Jin, *Controlling the hyperfine state of rovibronic ground-state polar molecules*, Phys. Rev. Lett. **104**, 030402 (2010).

[Osp10b] S. Ospelkaus, K.-K. Ni, D. Wang, M. H. G. de Miranda, B. Neyenhuis, G. Quemener, P. S. Julienne, J. L. Bohn, D. S. Jin, and J. Ye, *Quantum-state controlled chemical reactions of ultracold potassium-rubidium molecules*, Science **327**, 853 (2010).

[Ott08] T. B. Ottenstein, T. Lompe, M. Kohnen, A. N. Wenz, and S. Jochim, *Collisional stability of a three-component degenerate Fermi gas*, Phys. Rev. Lett. **101**, 203202 (2008).

[Pas10] B. Pasquiou, G. Bismut, Q. Beaufils, A. Crubellier, E. Maréchal, P. Pedri, L. Vernac, O. Gorceix, and B. Laburthe-Tolra, *Control of dipolar relaxation in external fields*, Phys. Rev. A **81**, 042716 (2010).

[Pet04a] D. S. Petrov, *Three-boson problem near a narrow Feshbach resonance*, Phys. Rev. Lett. **93**, 143201 (2004).

[Pet04b] D. S. Petrov, C. Salomon, and G. V. Shlyapnikov, *Weakly bound molecules of fermionic atoms*, Phys. Rev. Lett. **93**, 090404 (2004).

[Pet05] D. S. Petrov, C. Salomon, and G. V. Shlyapnikov, *Scattering properties of weakly bound dimers of fermionic atoms*, Phys. Rev. A **71** (2005).

[Pet08] D. Petrov and G. Shyapnikov (2008), private communication.

[Phi68] A. Phillips, *Consistency of the low-energy three-nucleon observables and the separable interaction model*, Nucl. Phys. A **107**, 209 (1968).

[Phi98] W. D. Phillips, *Nobel Lecture: Laser cooling and trapping of neutral atoms*, Rev. Mod. Phys. **70**, 721 (1998).

[Pla04] L. Platter, H.-W. Hammer, and U.-G. Meißner, *Four-boson system with short-range interactions*, Phys. Rev. A **70**, 052101 (2004).

[Pla08] L. Platter and J. R. Shepard, *Scaling functions applied to three-body recombination of ^{133}Cs atoms*, Phys. Rev. A **78**, 062717 (2008).

[Pla09] L. Platter, C. Ji, and D. R. Phillips, *Range corrections to three-body observables near a Feshbach resonance*, Phys. Rev. A **79**, 022702 (2009).

[Pol09a] S. E. Pollack, D. Dries, and R. G. Hulet, *Universality in three- and four-body bound states of ultracold atoms*, Science **326**, 1683 (2009).

[Pol09b] S. E. Pollack, D. Dries, M. Junker, Y. P. Chen, T. A. Corcovilos, and R. G. Hulet, *Extreme Tunability of Interactions in a ^7Li Bose-Einstein Condensate*, Phys. Rev. Lett. **102**, 090402 (2009).

[Qué08] G. Quéméner and N. Balakrishnan, *Vibrational energy transfer in ultracold molecule-molecule collisions*, Phys. Rev. A **77**, 030704(R) (2008).

[Raf97] R. J. Rafac and C. E. Tanner, *Measurement of the ^{133}Cs $6p^2P_{1/2}$ state hyperfine structure*, Phys. Rev. A **56**, 1027 (1997).

[Raj80] R. K. Raj, D. Bloch, J. J. Snyder, G. Camy, and M. Ducloy, *High-Frequency Optically Heterodyned Saturation Spectroscopy Via Resonant Degenerate Four-Wave Mixing*, Phys. Rev. Lett. **44**, 1251 (1980).

[Reg03a] C. A. Regal and D. S. Jin, *Measurement of Positive and Negative Scattering Lengths in a Fermi Gas of Atoms*, Phys. Rev. Lett. **90** (2003).

[Reg03b] C. A. Regal, C. Ticknor, J. L. Bohn, and D. S. Jin, *Creation of Ultracold Molecules from a Fermi Gas of Atoms*, Nature **424**, 47 (2003).

[Ric95] L. Ricci, M. Weidemüller, T. Esslinger, A. Hemmerich, C. Zimmermann, V. Vuletic, W. König, and T. Hänsch, *A compact grating-stabilized diode laser system for atomic physics*, Opt. Commun. **117**, 541 (1995).

[Rus29] H. N. Russell, A. G. Shenstone, and L. A. Turner, *Report on notation for atomic spectra*, Phys. Rev. **33**, 900 (1929).

[Ryc04] D. Rychtarik, B. Engeser, H.-C. Nägerl, and R. Grimm, *Two-Dimensional Bose-Einstein Condensate in an Optical Surface Trap*, Phys. Rev. Lett. **92** (2004).

[Sak94] J. J. Sakurai and S. F. Tuan (Eds.), *Modern Quantum Mechanics*, Addison-Wesley Publishing Company, Inc., 1994.

[Sch94] W. Schöllkopf and J. P. Toennies, *Nondestructive Mass Selection of Small van der Waals Clusters*, Science **266**, 1345 (1994).

[Sch96] W. Schöllkopf and J. P. Toennies, *The nondestructive detection of the helium dimer and trimer*, J. Chem. Phys. **104**, 1155 (1996).

[Sch99] U. Schünemann, H. Engler, R. Grimm, M. Weidemüller, and M. Zielonkowski, *Simple scheme for tunable frequency offset locking of two lasers*, Rev. Sci. Instrum. **70**, 242 (1999).

[Sch07] H. Schöbel, *Ultrakalte Cs_2-Moleküle in einer optischen Dipolfalle mit kontrollierbarer Elliptizität*, Diploma thesis, University of Innsbruck (2007).

[Shi65] J. H. Shirley, *Solution of the Schrödinger Equation with a Hamiltonian Periodic in Time*, Phys. Rev. **138**, B979 (1965).

[Sie86] A. E. Siegmann (Ed.), *Lasers*, University Science Books, Mill Valley, 1986.

[Sim81] I. Simenog and A. Sitnichenko, *Effect of long-range interaction in a three-body system with short-range forces*, Doklady Academy of Sciences of the Ukrainian SSR **11**, 74 (1981).

[Sø02] O. Sørensen, D. V. Fedorov, and A. S. Jensen, *Correlated Trapped Bosons and the Many-Body Efimov Effect*, Phys. Rev. Lett. **89**, 173002 (2002).

[Söd98] J. Söding, D. Guéry-Odelin, P. Desbiolles, G. Ferrari, and J. Dalibard, *Giant spin relaxation of an ultracold cesium gas*, Phys. Rev. Lett. **80**, 1869 (1998).

[Sol03] P. Soldán, M. T. Cvitaš, and J. M. Hutson, *Three-body nonadditive forces between spin-polarized alkali-metal atoms*, Phys. Rev. A **67**, 054702 (2003).

[Spr94] R. J. C. Spreeuw, C. Gerz, L. S. Goldner, W. D. Phillips, S. L. Rolston, C. I. Westbrook, M. W. Reynolds, and I. F. Silvera, *Demonstration of Neutral Atom Trapping with Microwaves*, Phys. Rev. Lett. **72**, 3162 (1994).

[Sta06] P. Staanum, S. D. Kraft, J. Lange, R. Wester, and M. Weidemüller, *Experimental Investigation of Ultracold Atom-Molecule Collisions*, Phys. Rev. Lett. **96** (2006).

[Ste03] D. A. Steck, *Cesium D Line Data*, available online at http://steck.us/alkalidata, revision 1.6 (2003).

[Ste09] J. von Stecher, J. P. D'Incao, and C. H. Greene, *Signatures of universal four-body phenomena and their relation to the Efimov effect*, Nature Phys. **5**, 417 (2009).

[Ste10] J. von Stecher, *Weakly bound cluster states of Efimov character*, J. Phys. B: At. Mol. Opt. Phys. **43**, 101002 (2010).

[Ste11] J. von Stecher, *Universal Five- and Six-Body Droplets Tied to an Efimov Trimer*, arXiv: 1106.2319 (2011).

[Str03] K. E. Strecker, G. B. Partridge, and R. G. Hulet, *Conversion of an Atomic Fermi Gas to a Long-Lived Molecular Bose Gas*, Phys. Rev. Lett. **91**, 080406 (2003).

[Stw78] W. C. Stwalley, *Long-range molecules*, Contemp. Phys. **19**, 65 (1978).

[Stw04] W. C. Stwalley, *Collisions and reactions of ultracold molecules*, Can. J. Chem. **82**, 709 (2004).

[Sun02] H. Suno, B. D. Esry, C. H. Greene, and J. J. P. Burke, *Three-body recombination of cold helium atoms*, Phys. Rev. A **65**, 042725 (2002).

[Sya06] N. Syassen, T. Volz, S. Teichmann, S. Dürr, and G. Rempe, *Collisional decay of ^{87}Rb Feshbach molecules at 1005.8 G*, Phys. Rev. A **74**, 062706 (2006).

[Sya08] N. Syassen, D. M. Bauer, M. Lettner, T. Volz, D. Dietze, J. J. Garcia-Ripoll, J. I. Cirac, G. Rempe, and S. Dürr, *Strong dissipation inhibits losses and induces correlations in cold molecular gases*, Science **320**, 1329 (2008).

[Tan88] C. E. Tanner and C. Wieman, *Precision measurement of the hyperfine structure of the ^{133}Cs $6P_{3/2}$ state*, Phys. Rev. A **38**, 1616 (1988).

[Tha01] G. Thalhammer, *Frequenzstabilisierung von Diodenlasern bei 850, 854 und 866 nm mit Linienbreiten im Kilohertz-Bereich*, Diploma thesis, University of Innsbruck (2001).

[Tha06] G. Thalhammer, K. Winkler, F. Lang, S. Schmid, R. Grimm, and J. Hecker Denschlag, *Long-lived Feshbach molecules in a three-dimensional optical lattice*, Phys. Rev. Lett. **96** (2006).

[Tha09] G. Thalhammer, G. Barontini, J. Catani, F. Rabatti, C. Weber, A. Simoni, F. Minardi, and M. Inguscio, *Collisional and molecular spectroscopy in an ultracold Bose-Bose mixture*, New J. Phys. **11**, 055044 (2009).

[The04] M. Theis, G. Thalhammer, K. Winkler, M. Hellwig, G. Ruff, R. Grimm, and J. H. Denschlag, *Tuning the Scattering Length with an Optically Induced Feshbach Resonance*, Phys. Rev. Lett. **93**, 123001 (2004).

[Tho35] L. H. Thomas, *The interaction between a neutron and a proton and the structure of H^3*, Phys. Rev. **47**, 903 (1935).

[Tho05a] S. T. Thompson, E. Hodby, and C. E. Wieman, *Spontaneous dissociation of ^{85}Rb Feshbach molecules*, Phys. Rev. Lett. **94**, 020401 (2005).

[Tho05b] S. T. Thompson, E. Hodby, and C. E. Wieman, *Ultracold molecule production via a resonant oscillating magnetic field*, Physical Review Letters **95**, 190404 (2005).

[Thø08a] M. Thøgersen, D. V. Fedorov, and A. S. Jensen, *N-body Efimov states of trapped bosons*, Europhys. Lett. **83**, 30012 (2008).

[Thø08b] M. Thøgersen, D. V. Fedorov, and A. S. Jensen, *Universal properties of Efimov physics beyond the scattering length*, Phys. Rev. A **78**, 020501(R) (2008).

[Tjo75] J. A. Tjon, *Bound states of ^{4}He with local interactions*, Phys. Lett. B **56**, 217 (1975).

[Tre01] P. Treutlein, K. Y. Chung, and S. Chu, *High-brightness atom source for atomic fountains*, Phys. Rev. A **63**, 051401(R) (2001).

[Tsc10] T. V. Tscherbul, T. Calarco, I. Lesanovsky, R. V. Krems, A. Dalgarno, , and J. Schmiedmayer, *rf-field-induced Feshbach resonances*, Phys. Rev. A **81**, 050701(R) (2010).

[Ude99] T. Udem, J. Reichert, R. Holzwarth, and T. W. Hänsch, *Absolute Optical Frequency Measurement of the Cesium D_1 Line with a Mode-Locked Laser*, Phys. Rev. Lett. **82**, 3568 (1999).

[Ude00] T. Udem, J. Reichert, T. W. Hänsch, and M. Kourogi, *Absolute optical frequency measurement of the cesium D_2 line*, Phys. Rev. A **62**, 031801(R) (2000).

[Wan09] Y. Wang and B. D. Esry, *Efimov trimer formation via ultracold four-body recombination*, Phys. Rev. Lett. **102**, 133201 (2009).

[Wan11a] Y. Wang, J. P. D'Incao, and B. D. Esry, *Ultracold three-body collisions near narrow Feshbach resonances*, Phys. Rev. A **83**, 042710 (2011).

[Wan11b] Y. Wang, J. P. D'Incao, and C. H. Greene, *Efimov Effect for Three Interacting Bosonic Dipoles*, Phys. Rev. Lett. **106** (2011).

[Web03a] T. Weber, *Bose-Einstein condensation of optically trapped cesium*, Ph.D. thesis, University of Innsbruck (2003).

[Web03b] T. Weber, J. Herbig, M. Mark, H.-C. Nägerl, and R. Grimm, *Bose-Einstein condensation of cesium*, Science **299**, 232 (2003).

[Web03c] T. Weber, J. Herbig, M. Mark, H.-C. Nagerl, and R. Grimm, *Three-body recombination at large scattering lengths in an ultracold atomic gas*, Phys. Rev. Lett. **91** (2003).

[Web08] C. Weber, G. Barontini, J. Catani, G. Thalhammer, M. Inguscio, and F. Minardi, *Association of ultracold double-species bosonic molecules*, Phys. Rev. A **78**, 061601(R) (2008).

[Wei99] J. Weiner, V. S. Bagnato, S. Zilio, and P. S. Julienne, *Experiments and theory in cold and ultracold collisions*, Rev. Mod. Phys. **71**, 1 (1999).

[Wen09] A. N. Wenz, T. Lompe, T. B. Ottenstein, F. Serwane, G. Zürn, and S. Jochim, *Universal trimer in a three-component Fermi gas*, Phys. Rev. A **80**, 040702(R) (2009).

[Wes93] P. H. Westfall and S. S. Young, *Resampling-Based Multiple Testing*, John Wiley and Sons, New York, 1993.

[Wig48] E. P. Wigner, *On the Behavior of Cross Sections Near Thresholds*, Phys. Rev. **73**, 1002 (1948).

[Wil09] J. R. Williams, E. L. Hazlett, J. H. Huckans, R. W. Stites, Y. Zhang, and K. M. O'Hara, *Evidence for an excited-state Efimov trimer in a three-component Fermi gas*, Phys. Rev. Lett. **103**, 130404 (2009).

[Xu03] K. Xu, T. Mukaiyama, J. R. Abo-Shaeer, J. K. Chin, D. E. Miller, and W. Ketterle, *Formation of Quantum-Degenerate Sodium Molecules*, Phys. Rev. Lett. **91** (2003).

[Yam06] M. T. Yamashita, L. Tomio, A. Delfino, and T. Frederico, *Four-boson scale near a Feshbach resonance*, Europhys. Lett. **75**, 555 (2006).

[Yam07] M. Yamashita, T. Frederico, and L. Tomio, *Three-boson recombination at ultralow temperatures*, Phys. Lett. A **363**, 468 (2007).

[Zac08] M. Zaccanti, G. Modugno, C. D'Errico, M. Fattori, G. Roati, and M. Inguscio (2008), talk at DAMOP, 27-31 May 2008, State College, Pennsylvania, USA.

[Zac09] M. Zaccanti, B. Deissler, C. D'Errico, M. Fattori, M. Jona-Lasinio, S. Müller, G. Roati, M. Inguscio, and G. Modugno, *Observation of an Efimov spectrum in an atomic system*, Nature Phys. **5**, 586 (2009).

[Zah06] N. Zahzam, T. Vogt, M. Mudrich, D. Comparat, and P. Pillet, *Atom-Molecule Collisions in an Optically Trapped Gas*, Phys. Rev. Lett. **96** (2006).

[Zen11] A. Zenesini, M. Berninger, B. Huang, S. Besler, H.-C. Nägerl, F. Ferlaino, and R. Grimm, *Creation of Bose Einstein condensates of cesium at high magnetic fields* (2011), to be published.

[Zir08a] J. J. Zirbel, K.-K. Ni, S. Ospelkaus, J. P. D'Incao, C. E. Wieman, J. Ye, and D. S. Jin, *Collisional Stability of Fermionic Feshbach Molecules*, Physical Review Letters **100**, 143201 (2008).

[Zir08b] J. J. Zirbel, K.-K. Ni, S. Ospelkaus, T. L. Nicholson, M. L. Olsen, P. S. Julienne, C. E. Wieman, J. Ye, and D. S. Jin, *Heteronuclear molecules in an optical dipole trap*, Phys. Rev. A **78**, 013416 (2008).

[Zob01] O. Zobay and B. M. Garraway, *Two-Dimensional Atom Trapping in Field-Induced Adiabatic Potentials*, Phys. Rev. Lett. **86**, 1195 (2001).

[Zwi03] M. W. Zwierlein, C. A. Stan, C. H. Schunck, S. M. F. Raupach, S. Gupta, Z. Hadzibabic, and W. Ketterle, *Observation of Bose-Einstein Condensation of Molecules*, Phys. Rev. Lett. **91**, 250401 (2003).

ACKNOWLEDGMENTS

I would like to thank all the people who made the accomplishments of the past years possible.

First of all, I want to express my sincere gratitude to my advisor Rudi Grimm, who gave me the opportunity to work in such a scientifically stimulating environment. He fostered an open atmosphere and his guidance of the group encouraged intellectual exchange by internal group discussions and participation in conferences. During my whole time here in Innsbruck, he always supported me in scientific and non-scientific matters. His ideas and explanations in discussions of scientific as well as technical topics were essential for the successful achievements presented in this thesis. Furthermore, I want to thank him for his confidence in me, giving me so much freedom in working on these experiments.

I want to thank the diploma and PhD students, postdocs and assistants with whom I experienced an exciting time working together in the lab during these past years. At the beginning of my time here, Michael Mark, who was about to finish his PhD, explained to me in his genuine tyrolean way the experimental setup. Not only did he introduce me to the mysteries of the setup, but we also often had nice chats about topics unrelated to physics. At this time, Harald Schöbel was a diploma student working on the experiment, with whom I implemented the new optical trap design. I spent many long evenings in the lab together with the postdocs Francesca Ferlaino and Steven Knoop, collecting data. Even though we could never completely agree on the background music in the lab, we enjoyed a nice and fruitful teamwork. I thank Francesca for the intriguing discussions and especially for keeping me up-to-date on the research progress of experimental groups all around the world. Her good eye for the design of presentations was always helpful for the preparation of my conference talks. During the critical phase of reconstructing the experiment, I was fortunate to be supported by diploma student Walter Harm and postdoc Alessandro Zenesini. Walter's technical skills were a great help for constructing the magnetic coil system, and he also became a good friend outside of the workplace. I really enjoyed the time spent working with him. Alessandro's straightforward attitude was very helpful for efficient implementation of the magnetic high-field setup, as well as for the realization of the most recent experiments. He and diploma

student Stefan Besler constructed the optical lattice, which in the near future will yield new results on few-body phenomena systems with reduced dimensions. Additionally, Stefan's recent optimization of the lab software program will facilitate the data analysis considerably. My successor, Bo Huang, made important contributions to the implementation of the high-field imaging system and now takes over the experiment, which I am sure will be in good hands. I also enjoyed our discussions about physics a lot. I would like to thank Hanns-Christoph Nägerl for technical support and his essential contributions to writing the articles.

For helping with the design of the magnetic coil system, I express my gratitude to Gerhard Hendl. During numerous discussions he helped to develop a concept which worked out straight away.

I also want to thank the mechanical workshop for the technical support. In particular, Anton Schönherr and Helmut Jordan made major contributions to the construction of the magnetic coil system.

Moreover, I thank all former and present colleagues of our group for the scientific and non-scientific interchange of ideas. With many of them I've been spending a wonderful time in Innsbruck - also outside of the university.

Thanks to the secretaries on the 4^{th} floor, Christine Götsch-Obmascher, Karin Köhle, Ingeborg Kaindl, Nicole Jorda, Patricia Moser, Renate Rupprechter and Sabine Hofer, for taking care of administrative issues. I also enjoyed many nice conversations with them.

Furthermore, I want to say a big thank you to all my friends, who always supported me over all these years, and, in particular, Georg for proofreading this thesis. I warmly thank Simone for her constant motivation and her patient understanding for the many nights I spent at work.

From the bottom of my heart I want to express my gratitude to my parents, who were always there for me and supported me in every possible way.